High-Resolution Experiments and Computations on Mixing of Turbulent Buoyant Round Free Jets in Uniform and Stratified Environments

by

Sunming Qin

A dissertation submitted in partial fulfillment
of the requirements for the degree of
Doctor of Philosophy
(Nuclear Engineering and Radiological Sciences)
in the University of Michigan
2020

Doctoral Committee:

Professor Annalisa Manera, Co-Chair
Associate Research Scientist Dr. Victor Petrov, Co-Chair
Associate Professor Elia Merzari, Pennsylvania State University
Dr. W. David Pointer, Oak Ridge National Laboratory
Professor Xiaodong Sun
Assistant Professor Aaron Towne

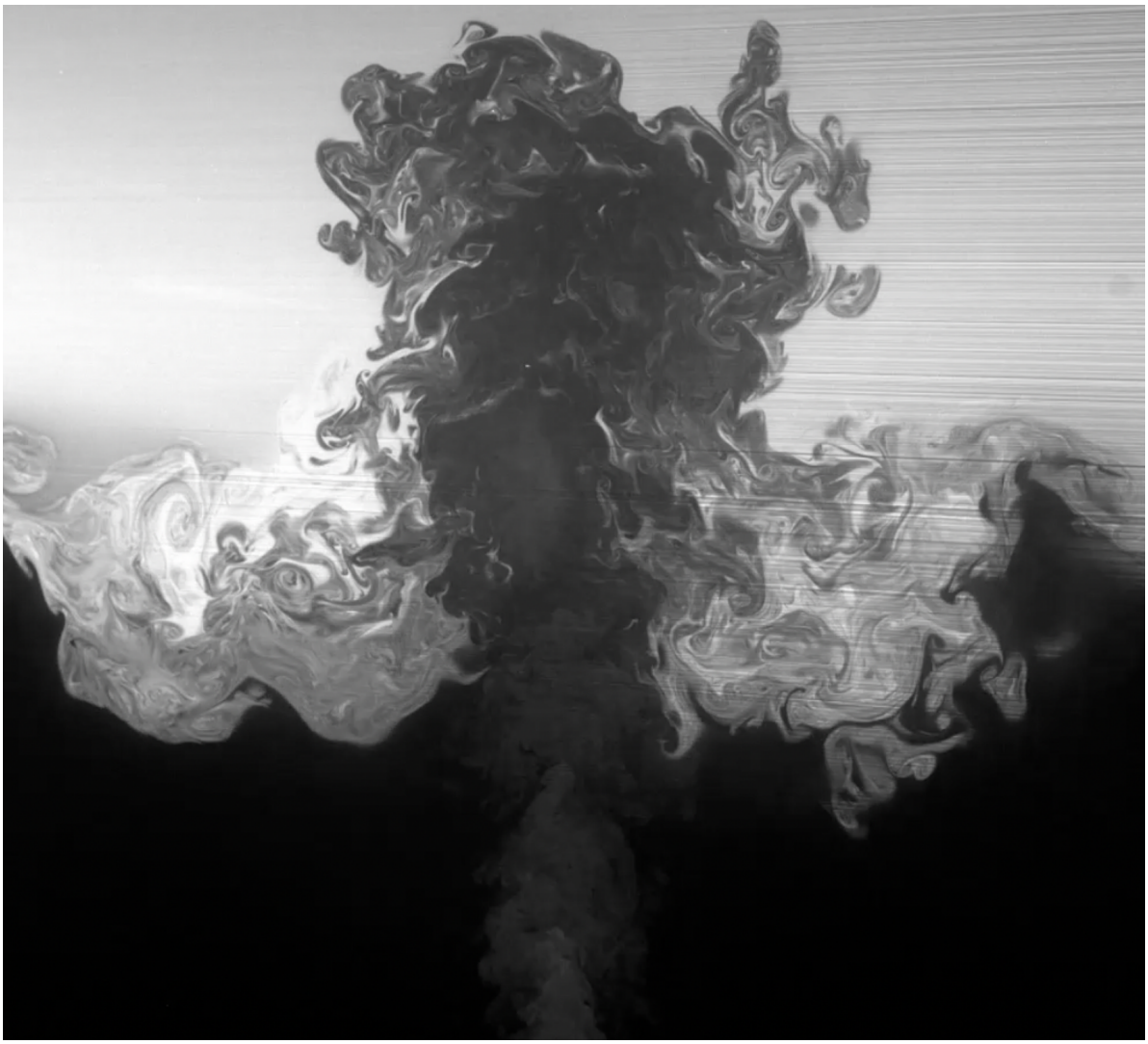

The refractive-index matched turbulent jet penetrating a sharp density interface.

sunming@umich.edu
ORCID ID: 0000-0002-2850-0387

Dedication

To **Turbulence**, the most important unsolved problem of classical physics yet.

ACKNOWLEDGEMENTS

First of all, I would like to express my sincere appreciation for the tremendous supports from my advisors Professor Annalisa Manera and Dr. Victor Petrov. Thank you for the patient guidance whenever I need through all these years. Thank you for giving me the trust and freedom in learning and trying new ideas. The experience of working with you will always be part of my precious memory during my lifespan.

Second, I would like to thank my doctoral committee members. Thank you for the advice to help me polish the dissertation work. In particular, I would like to thank Prof. Xiaodong Sun for his valuable suggestions and perpetual encouragement. Without all the help and patience from the committee, finishing this degree would have been an impossible mission.

I am very thankful to all of my colleagues at the Experimental and Computational Multiphase Flow Laboratory (ECMFL) for so many helpful discussions and assistance with the experimental work, especially Dr. Benedikt Krohn, who always inspires me with the beauty of turbulence and supports me whenever I need. Special thanks to John Downing, Julio Diaz and Daniel Nunez, you are my most reliable allies for all the up and down from the very beginning of my PhD journey. We are a great team, amazing and cheerful. I will never forget all those fantastic conversations we had, especially during the coffee breaks and table tennis games. I would also like to thank all of my friends who work diligently in Cooley, ERB and NEL, as well as all of my roommates who used to be in Ann Arbor and now being scattered all over the world. You will be missed and I will be always available by your side.

What's more, I am sincerely grateful to my family that is over 7,000 miles away in China, especially my parents, for their ineffable love and support. You are the harbor with

the lighthouse, guiding me through the darkness and taking good care of me. It was your words that gave me courage and vitality whenever I am facing obstacles and thinking of giving up. I must have saved the whole universe to have you as my parents for this life. I love you forever!

Last but not least, the work was made possible by the generous funding support from U.S. Department of Energy Nuclear Energy University Program (NEUP) with the Project No. 14-6552, as well as the Rackham Graduate Student Research Grant and Predoctoral Fellowship program from the University of Michigan.

TABLE OF CONTENTS

LIST OF FIGURES

Figure

LIST OF TABLES

Table

LIST OF APPENDICES

Appendix

LIST OF ABBREVIATIONS

AHTR Advanced High Temperature Reactor

CFD Computational Fluid Dynamics

DESTROJER **DE**nsity **S**tratified **T**urbulent **RO**und free **J**et **E**xpe**R**iment

DNS Direct Numerical Simulation

ECCS Emergency Core Cooling Systems

ECMFL Experimental and Computational Multiphase Flow Laboratory

FF flatness factor

FHR Fluoride salt-cooled High-temperature Reactor

Fr Froude Number

GPU Graphics Processing Unit

LDV Laser Doppler Velocimetry

LES Large Eddy Simulations

LWR Light Water Reactor

NEUP Nuclear Energy University Program

NS Navier-Stokes

PDF probability density function

PIRT Phenomena Identification and Ranking Table

PIV Particle Image Velocity

PLIF Planar Laser-induced Fluorescence

PSD Power Spectral Density

PWR Pressurized Water Reactor

PTS Pressurized Thermal Shock

RANS Reynolds-Averaged Navier-Stokes

Re Reynolds number

RPV reactor pressure vessel

RI Refractive Index

RIM Refractive Index Matching

RKE Realizable $k - \epsilon$

RSS root-sum-square

RST Reynolds Stress Transport

SBO station blackout

SF skewness factor

SGDH Standard Gradient-Diffusion Hypothesis

SNR signal-to-noise ratio

SFR Sodium-cooled Fast Reactor

TKE Turbulent Kinetic Energy

ABSTRACT

Fluid jets interacting with stratified environments play an essential role in the safety of several nuclear reactor designs. In the containment of some power plants like a Light Water Reactor (LWR), fluid jets dominate the transport and mixing of gaseous species and consequent hydrogen distribution in case of a severe accident. The mixing phenomena in the containment are driven by buoyant high-momentum injections (jets) and low momentum injection plumes. Mixing near the postulated break is initially dominated by high flow velocities, while plumes with moderate flow velocities are instead relevant in the break compartment during the long-term pressurization phase, or in any of the apertures between two connected compartments if the mass flows are sufficiently high and the density differences between efflux and ambient are sufficiently low. Phenomena of interest include free plumes (as produced by the efflux from the break compartment in a larger room or directly from a break flow), wall plumes (such those produced by low mass flows through inter-compartment apertures), and propagating stratification fronts in the ambient (for any stably stratified conditions). These phenomena have been highly ranked for nuclear reactor safety analyses. For example, during a Pressurized Thermal Shock (PTS) scenario in a Pressurized Water Reactor (PWR), the interaction between the cold injection plume of the Emergency Core Cooling Systems (ECCS) and the stratified fluid present in the cold (or hot) leg is important to determine the time evolution of the temperature at the inlet of the reactor pressure vessel (RPV) and therefore the potential to cause a thermal shock on the RPV wall. All the above phenomena can be characterized by the interaction of buoyant jets with stratified environments.

In stratified layers, baroclinic forces create a significant redistribution of turbulent kinetic energy and scales, which leads to anisotropy. This important physical phenomenon is highly three dimensional. Results reported in the literature have shown that the turbulence models currently implemented in Computational Fluid Dynamics (CFD) commercial software (e.g. ANSYS-CFX, STAR-CCM+, and FLUENT) tend to overestimate thermal stratification and underestimate turbulent mixing when buoyancy effects become dominant with respect to momentum effects. Because of the local isotropy assumptions used in most subgrid-scale models, even Large Eddy Simulations (LES) might fail to reproduce thermal stratification when buoyant jets interact with stratified environments. In order to gain insight into the relevant physical phenomena and improve the existing models for the buoyancy-driven flows, it is pivotal to establish a database of high-resolution experiments for turbulent buoyant jet flow fields in the presence of uniform and stratified environments. To shed new light on this crucial phenomenon, non-intrusive optical methods of flow visualization, like Particle Image Velocity (PIV) and Planar Laser-induced Fluorescence (PLIF), are applied to obtain highly-resolved velocity and concentration fields. However, high-resolution measurements of turbulent jet flows with density differences are extremely challenging because tiny changes in density correspond with changes in refractive indices, yielding blurred images. Refractive indices must precisely match (up to 0.0002) throughout the mixing process.

The experiments in this dissertation make use of a novel Refractive Index Matching (RIM) methodology based on mixing behaviors of ternary-component systems that was developed in our research group. This technique has allowed to perform experiments with density differences up to about 8.6% (3 times larger than previously published in the open literature). Implementing a high-fidelity synchronized PIV/PLIF system combined with the new RIM technique, a novel high-resolution experimental database for the mixing of turbulent buoyant jets in both uniform and stratified environments has been built. The experimental data are analyzed to extract fundamental features of buoyant jets in stratified environments and to assess and improve the predictive capabilities of the current CFD models.

As a brief outline, after the motivation and background of the research work is discussed in Chapter I, more details on the measurement techniques and experimental setups are provided in Chapter II. In Chapter III, the novel methodology for Refractive Index Matching (RIM) is introduced and explained based on mixing behaviors of ternary-component systems, successfully achieving density differences up to about 9% (3 times larger than previously achieved). In order to verify the experimental setup and establish a set of reference cases, experiments have been performed also for non-buoyant turbulent jets in uniform environments. The turbulence statistics as well as the mean flow field and the time-dependent behavior of the jet mixing have been investigated in Chapter IV. In Chapter V, the mixing process of turbulent buoyant jets in non-uniform environments has been characterized, including comparisons with the reference uniform cases and available datasets published in the literature. The assessment of the performance of CFD Reynolds-Averaged Navier-Stokes (RANS) models against the novel experimental database established in this dissertation is summarized in Chapter VI. For this study the commercial CFD code STAR-CCM+ has been used. Finally, a summary of the dissertation conclusions as well as recommendations for future work are provided in Chapter VII.

CHAPTER I

Introduction

Categorized as one of the canonical flows, the turbulent round jet flow has been investigated extensively by the researchers both experimentally and computationally during the past century. Due to its characteristics of momentum transport in free shear layers created by Kelvin-Helmholtz instabilities, this type of jet is relevant to a wide range of industrial applications ranging from nuclear reactor safety analysis to rocket designs for aerospace research. This dissertation is aimed at gaining physical insight into the turbulent mixing process for a turbulent round free jet flow interacting with uniform and stratified environments. Providing a high-resolution high-fidelity experimental database, this work can potentially contribute to the validation and further advancement of CFD models related to, but not limited to, nuclear reactor core design and safety analysis. In this chapter, the motivation for this study is discussed in brief. The theoretical background is also illustrated as the foundations for the analyses, which will be presented in this dissertation in the following chapters.

1.1 Motivation and Background

Turbulence is almost everywhere in our daily life, contributing to heat, mass and momentum transfer over a large scale range, from molecular to interstellar. Turbulent round free jets are among one of the most common flow types in technical applications, and have been extensively studied by the research community for over 90 years since the jet engine

Figure 1.1: A turbulent jet from a factory chimney. Reprinted from [1]

Figure 1.2: This photo taken from a drone shows a column of ash shooting up from the Mayon volcano, seen from the city of Legazpi in Albay province, south of Manila, Jan. 24, 2018. Reprinted from [2]

research in the 1920s. Jets are relevant in a large number of geophysical and engineering applications, such as emissions from chimneys (see Figure 1.1) and dispersion of pollutants, volcanic eruptions into the atmosphere (see Figure 1.2), emergency spraying systems for fire safety, powerful waterjets that can cut through bulletproof glasses, etc. Experiments on jet interacting with density stratifications have been conducted in many fields, such as the atmospheric, oceanographic and other hydrodynamic sciences. During the last several decades, many researches have been dedicating to the study of plumes, jets and fountains([30], [31], [32], and [33]). The interaction between axisymmetric flows and sharp density interfaces has been widely investigated using both liquids and gaseous mixtures. Mott and Woods [34] investigated the mixing of two-layer and linear stratifications with turbulent positively buoyant plumes using water and salt solutions. Dehmani et al. [35] proposed a series of velocity and turbulence measurements on positively buoyant plumes across strong stratifications with air-helium jets. Lin and Linden [36] studied the entrainment of a fountain at a steady density interface. Friedman and Katz [37] quantified the jet penetration height in a two phase medium. Several other experimental works are devoted to the buoyant jet structural analyses in the stratified environment (e.g. Bloomfield and Kerr [38], Ansong et al. [39]) and on the mixing behavior at the density interface (e.g. Baines [40], Ermanyuk and Flor [41], and Guyez et al. [42]).

In the field of nuclear engineering, free jets and the associated turbulent mixing processes with density differences also play a significant role during accident scenarios [43]. In nuclear power plants, the last barrier to prevent radioactive releases into the environment is the containment building. It is extremely crucial to understand and predict the complicated thermal-hydraulics phenomena which occur in the containment atmosphere in case of severe accidents. As demonstrated by the Three Mile Island accident in 1979 and Fukushima Daiichi nuclear disaster in 2011, overheating in the reactor core can cause a reaction between the water and the zircaloy to generate hydrogen gases, which is a serious threat since the mixture of hydrogen and oxygen is highly flammable and explosive. Owing to the lightweight of

hydrogen, it will accumulate in the upper region of the containment, leading to the formation of a stratified region in the containment atmosphere. By investigating the heat and mass transfer in buoyancy-driven flows, as Deri et al. [44] mentioned in their study with Helium and air, features can be designed to break the stratification in the containment building, such as sprays injection and gas jets.

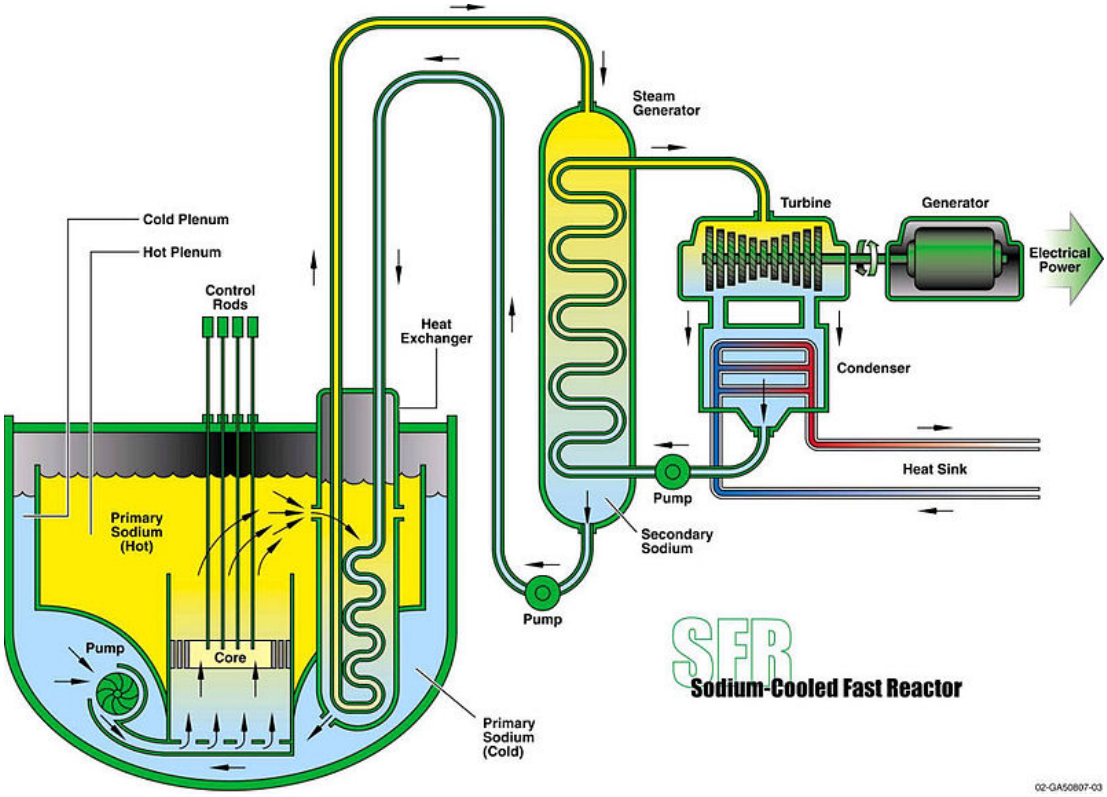

Figure 1.3: The schematic of a Sodium-cooled Fast Reactor. Reprinted from [3]

Additionally, Thermal mixing and stratification phenomena with liquids in large pools play an important role in the safety and operation of several advanced Gen-IV reactor systems. For example, in the pool-type Sodium-cooled Fast Reactor (SFR) systems, as illustrated in Figure 1.3, thermal stratification occurs in the pool upper plenum. Because of the sodium heated up in the reactor core, buoyant jets are formed at the core outlet that disturb the stratified layer present in the pool upper plenum. Core channels in the SFR are typically hydro-dynamically isolated so that considerable temperature variations might exist at the exit of adjacent fuel assemblies. The interaction between the buoyant jets and

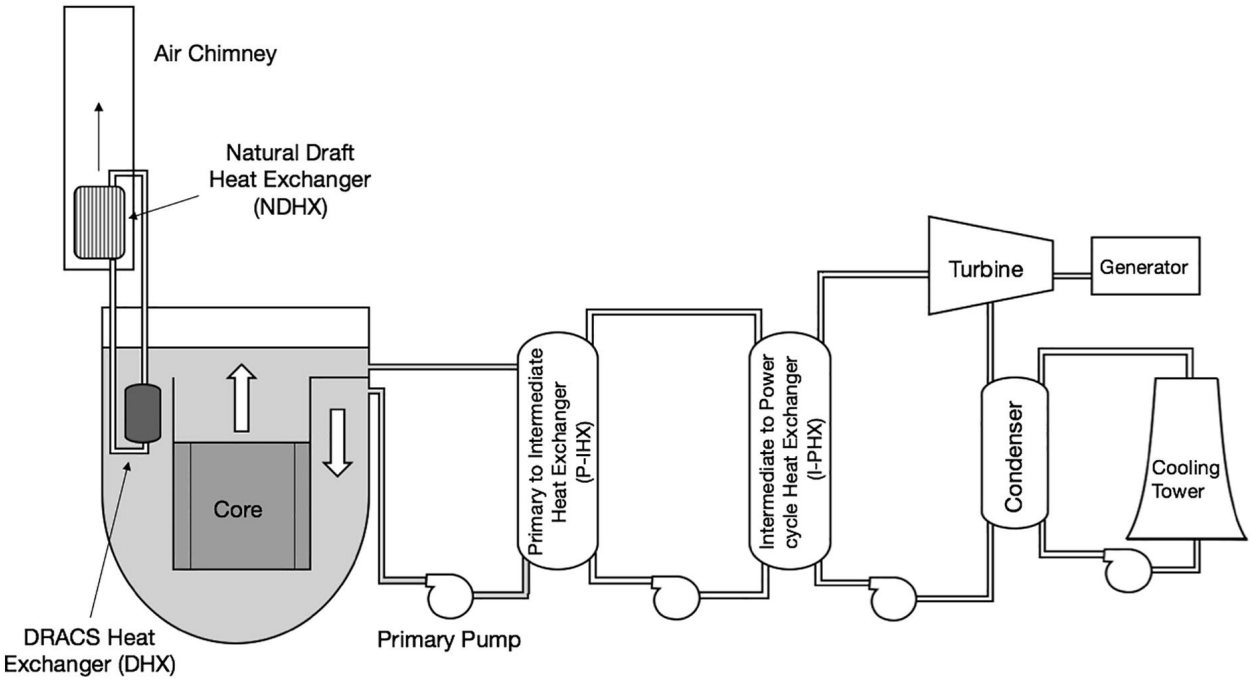

Figure 1.4: The schematic of the AHTR system and heat transfer paths. Reprinted from [4]

thermal stratification needs to be characterized in order to understand and predict the temperature distribution in the pool. This because the temperature distribution in the hot pool will affect the heat transfer from the primary loop to the secondary loop through the heat exchanger presents in the upper section of the pool. The stratification in the pool will also affect the natural circulation flow-rate through the core that is established in case of a loss of flow accident. The thermal imbalance between parallel core jets combined with turbulence fluctuations in the flow might also result in oscillating thermal loads on the upper plenum structures, which is known as thermal striping. Similar issues exist in other types of reactor designs such as Advanced High Temperature Reactor (AHTR) mentioned by Varma et al. [4]. AHTR is a conceptual design of a Fluoride salt-cooled High-temperature Reactor (FHR) that utilizes molten FLiBe salt as its primary coolant. A system schematic is shown in Figure 1.4. Lin et al. [45] performed a thermal-hydraulics phenomena identification and ranking table (TH-PIRT) study for two major events, namely station blackout (SBO) and simultaneous withdrawal of all control rods. The research reported that upper plenum mixing with

pluming and stratification is critical to quantify the thermal load on the reactor vessel and hot-leg salt temperature but that not enough knowledge on these is available yet.

All the phenomena mentioned above depend on the interactions of turbulent buoyant jets with uniform and non-uniform environments, which are ranked high in importance but low in knowledge base. As a matter of fact, despite turbulent buoyant jets and their interaction with uniform and non-uniform environments have received considerable attention from the scientific community, due to the general complexities for experimental setup and the limitation of measurement techniques, the influence of density variations during a turbulent buoyant jet mixing process has not been fully understood yet. Therefore, it is of great significance to better characterize the turbulent buoyant jet mixing process in liquids with both experimental and computational methods, motivating the work carried out in this dissertation.

1.2 Experimental Discovery

A turbulent jet is a flow produced by a continuous source of momentum. As the jet issues into a quiescent environment, it will eventually entrain the receiving fluid and spread in the radial direction with downstream distance until all the initial momentum gets dissipated into heat through viscous effects. Several experimental techniques have been used to investigate turbulent jets. In 1956, Laurence [46] applied hot-wire anemometry techniques to study high Reynolds number subsonic jets, leading to a thorough investigation in terms of velocity profiles, turbulent intensities, and velocity spectra of turbulent jet flow. Since then the experimental techniques have matured allowing more extensive measurements. Such experimental techniques includes optical flow-field measurement techniques like Particle Image Velocity (PIV) and Planar Laser-induced Fluorescence (PLIF) (see Chapter II for more details). Given the wide range of existing experimental discoveries in the literature, the research in turbulent jet flows has diverged into multiple approaches and topics. In this section, the most common and popular topics are selected and summarized as follows.

1.2.1 Initial conditions and self-similarity

In the case of a turbulent round free jet, turbulence is generated at the jet boundary and diffuses towards the axis such that the width of the mixing zone increases with downstream distance. The mean velocity profile at the jet exit is determined by the jet nozzle geometry: a contraction nozzle produces a top-hat velocity profile shown in Figure 1.5; a pipe nozzle produces a fully developed turbulent pipe flow profile, respectively. The initial instability modes, created by the jet at its source, produce the flow structures in the shear layer (or mixing zone). The resulting vortices will roll-up and then pair-up, engulfing the liquid in the surroundings in the transition zone. As the flow travels further downstream, the jet flow transits into the fully developed region till all the jet momentum gets dissipated into heat at the molecular scale due to the effect of viscosity.

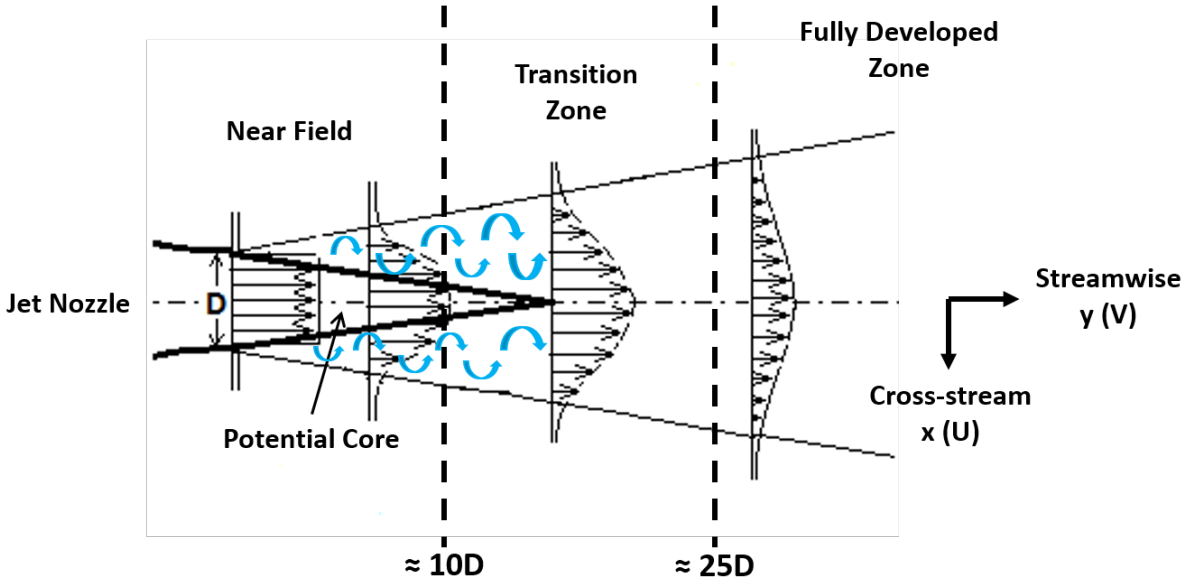

Figure 1.5: Schematic of a free jet issuing from a smooth-contraction nozzle. Adapted from [5].

In the near-field region of the jet, initial velocity profiles and their fluctuations can be easily captured using PIV to measure the instantaneous velocity fields, and therefore the velocity fluctuations and their statistics, including turbulent intensities and Reynolds stresses. With regards to jets with steady inlet conditions, it has been found that the jet

inlet boundary conditions will affect both the near- and far-field of the turbulent jet flows [8]. According to Nathan et al. [47], only the jet inlet conditions will affect both the near-field and downstream flows because the influence of initial conditions contributes to the underlying structures of turbulent motions that are carried from the jet nozzle throughout the flow, i.e., "a jet never forgets."

Traveling with the jet and after about 25 jet diameter away from the nozzle (see Figure 1.5), the jet reaches a fully developed state. Hrycak et al. [48] showed that the velocity profiles, after being normalized by the centerline velocities, are independent from the Reynolds number in the turbulent flow region for an axisymmetric jet. According to Hussein et al. [24], the centerline axial mean velocity also decays linearly with the axial distance away from the jet nozzle. For the fully developed (self-similar) region, the relation between the jet exit velocity V_0 and the centerline velocity $V_c(x)$ at a specific downstream location can be expressed as:

$$\frac{V_0}{V_c(x)} = \frac{1}{K_v}\left(\frac{y}{D} - \frac{y_{0,v}}{D}\right) \tag{1.1}$$

where D is the jet diameter, $y_{0,v}$ is defined as the jet virtual origin for the centerline velocity decay, and K_v as the jet centerline velocity decay constant. George and Arndt [49] mentioned in their study on the self-preservation in jets that both y_0 and B may depend on the inlet boundary conditions of the jet (i.e., the jet nozzle shapes and initial boundary conditions). Also Pope [50] reports that, according to empirical observations for the self-similar region, with the proper scaling, the profiles of jet mean velocity and normal stresses become self-similar, independent of the particular downstream location along the axis of the jet.

Later in Chapter IV and V, detailed experimental results on turbulent jets discharged into uniform and non-uniform environments and comparisons with the literature for the jet self-similar region will be presented in terms of the jet virtual origin and decay constants as well as the self-similarity behavior.

1.2.2 Entrainment

During the mixing process, the jet engulfs the surrounding fluid that maintains the momentum flow rate but causes the radial-wise spreading of the jet to increase with the downstream distance from the jet origin. This is known as the entrainment of the jet. To characterize the spreading rate of the jet, the jet half-width distance, $r_{1/2}$, defined as the radial position where the velocity has dropped to half the centerline velocity, is plotted against the downstream distance from the jet inlet, as shown in Figure 1.6.

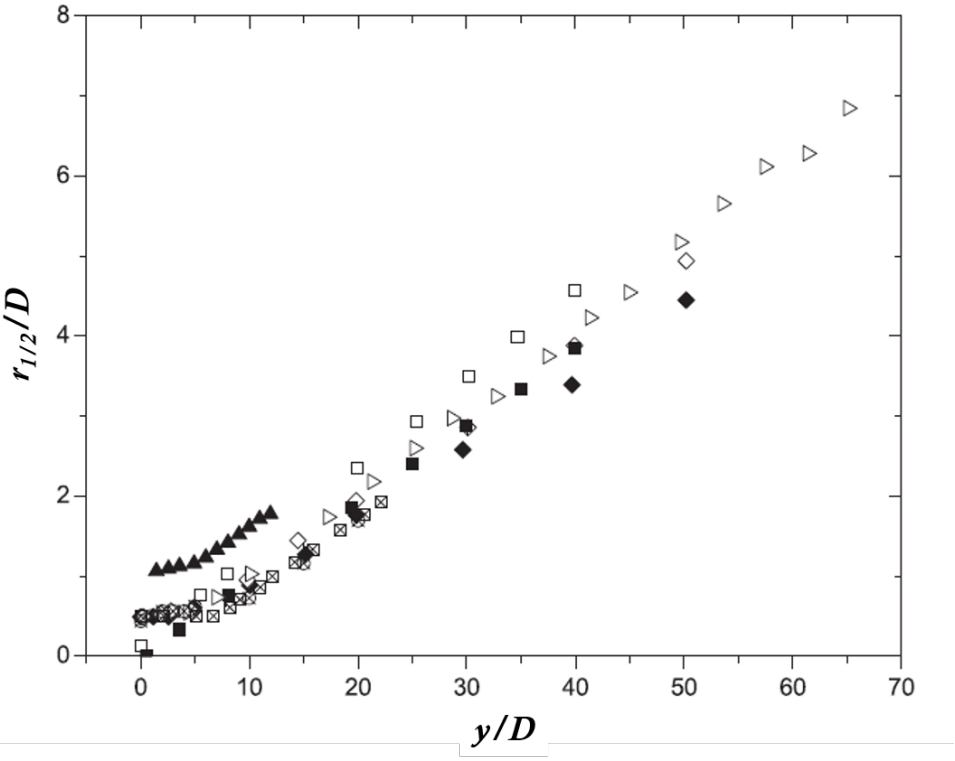

Figure 1.6: Axial evolution of the jet half-width. Reprinted from [6]. Legend: ⊠ Quinn and Militzer [7]; □ Mi et al., contraction nozzle [8]; ■ Mi et al., pipe nozzle [8]; ▷ Mi et al., orifice nozzle [8]; ♢ Xu and Antonia, contraction nozzle [9]; ♦ Xu and Antonia, pipe nozzle [9]; ▲ Iqbal and Thomas [10]; ⊗ Fellouah and Pollard [11].

In Figure 1.6, the jet half-width normalized by the jet diameter found in previous studies (Quinn and Militzer [7], Mi et al. [8], Xu and Antonia [9], Iqbal and Thomas [10], and Fellouah and Pollard [11]) are summarized and plotted along downstream distances y/D. It can be noticed that the spreading rate of $r_{1/2}$ increases linearly with downstream distance

beyond the potential core (around 15D away from the jet inlet, see Figure 1.5), as the equation below indicated:

$$\frac{r_{1/2}}{D} = K_r \left(\frac{y}{D} - \frac{y_{0,r}}{D} \right) \tag{1.2}$$

where D is the jet inlet diameter, $y_{0,r}$ is defined as the jet virtual origin characterized by the jet half-width, and K_r as the spread rate for jet half-width. These constants will be investigated using the experimental results for uniform and stratified jets in Chapters IV and V, with detailed comparisons with literature findings.

1.2.3 Spectral analysis

The turbulent mixing process is directly related to the inertia of the turbulent eddies. Because a range of eddy sizes are present in a turbulent flow, each characterized by its own time scale, a turbulent velocity signal is rich in frequencies.Therefore, the velocity spectrum provides information about the contributions to the intensity of velocity signals from various length scales (eddy sizes). Kolmogorov in 1941 [51] proposed that the velocity spectrum in the inertial sub-range of eddy scales should follow the form of:

$$E(\kappa) = C\epsilon^{2/3}\kappa^{-5/3} \tag{1.3}$$

where C is known as the Kolmogorov constant ($C \approx 1.5$ if turbulence isotropy is assumed) and $\kappa = 2\pi/\lambda_k$ is the wave-number associated to the eddy scales, with the definition of the Kolmogorov length scale λ_k. According to Fellouah and Pollard [11], while the -5/3 slope is associated with the range of frequencies in which the energy cascade of 3D turbulence is dominated by inertial transfer, as hypothesized by Kolmogorov, the -3 slope reflects what may be expected for two-dimensional turbulence flows, and the -7 slope characterizes the dissipation range at the near-field region where viscous forces dominate, as shown in Figure 1.7. The normalized axial velocity spectra $E_{11}(\kappa_1)/\left(\lambda_k u_{\lambda_k}^2\right)$ are plotted versus normalized wave numbers $\kappa_1\lambda_k$ to characterize the relationship between the various length scales and the

energy intensities, with the definition of the Kolmogorov velocity scale u_{λ_k} correspondingly.

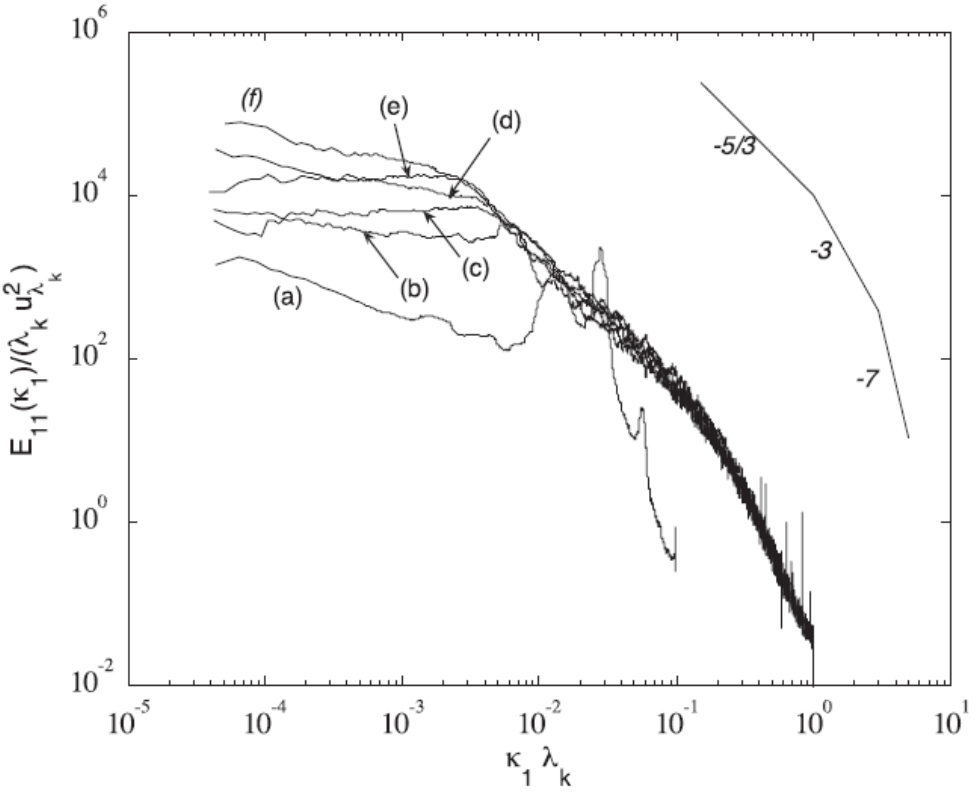

Figure 1.7: Velocity spectra of streamwise centerline velocity u and Re=30,000. (a) x/D=1, (b) x/D=3, (c) x/D=5, (d) x/D=10, (e) x/D=15, and (f) x/D=20. Reprinted from [11]

1.2.4 Coherent structures

Another way turbulent flows are analyzed is in terms of so-called coherent structures. Coherent structures have been studied over the last four decades to understand and describe turbulent flows (see for example Becker and Massaro [52] and Dimotakis et al. [53]). However, the research community has not yet come up with an accepted definition for coherent structures. In this dissertation Robinson's description [54] is adopted: "a coherent motion is defined as a three-dimensional region of the flow over which at least one fundamental flow variable (velocity components, density, temperature, etc.) exhibits significant correlation with itself or with another variable over a range of space and/or time that is significantly larger than the smallest local scales of the flow."

Since a single turbulent round free jet is implemented in this dissertation, a simple method, namely two-point correlations, are applied to identify those structures that give insight into the mass and momentum transports in large scales. The general form of a two-point correlation can be expressed as follows:

$$R_{a',b'} = \frac{\overline{a'_x b'_0}}{\sqrt{\overline{a'_0 b'_0} \cdot \overline{a'_x b'_x}}} \tag{1.4}$$

where $R_{a',b'}$ describes the spatially distributed influence of the variance of a component a'_x in the interrogation plane to the variance of a reference component b'_0 at a certain location of the flow domain.

1.3 Computational Fluid Dynamics (CFD) Approach

Though the physics of the turbulent jets has long been known to be governed by Navier-Stokes (NS) equations, analytical solutions exist only for limited cases due to the non-linear property of these equations. Tollmien [55], as first of many theoretical investigations of turbulent jets, modeled the circular jets based on Prandtl's mixing-length theory. Over the years, more complex turbulence models have been developed and the growing computational resources have allowed direct integration of the NS equations. Therefore Computational Fluid Dynamics (CFD) simulations has become a complementary tool to experiments to gain physical insight into the behavior of turbulent flows.

Among the numerical approaches that can be used to gain more physical insight are, Direct Numerical Simulation (DNS) and Large Eddy Simulations (LES) have been used by different researchers to simulate turbulent round jets (Zhang et al. [56], Salkhordeh et al. [57], Bisoi et al. [58], Lai and Socolofsky [59], Wang P. et al. [60] and Wang Z. et al. [61]). While DNS consists in integrating the NS equations with a mesh and time step sufficiently low to resolve all scales of turbulence down to the Kolmogorov scale, in LES the space averaging of the NS equations is performed to filter out the smallest (viscous)

scales, which therefore needs explicit modeling. While DNS and LES are excellent research tools, these methods are still not commonly employed for practical engineering applications due to their high computational expense. As a compromise between fidelity and efficiency, Reynolds-Averaged Navier-Stokes (RANS) approach has been prevailing as a tool to study practical engineering problems involving turbulent jets, which will be mainly emphasized in this study. Examples of simulation results for a turbulent jet flow using these three simulation approaches are illustrated in Figure 1.8 (it can be noticed that the results from LES and DNS are transient in nature, therefore the images in the figure correspond to one specific time snapshot, while RANS yields results for the mean flow field). As far as typical modeling processes, Figure 1.9 from André Bakker's lectures summarizes the differences between these CFD modeling approaches: DNS resolves all scales of motion, all the way down to the Kolmogorov scale. LES is next up and resolves most of the scales, with the smallest eddies being modeled. RANS is on the other end of the spectrum from DNS, where only the large-scale eddies are resolved and the remaining scales are modeled.

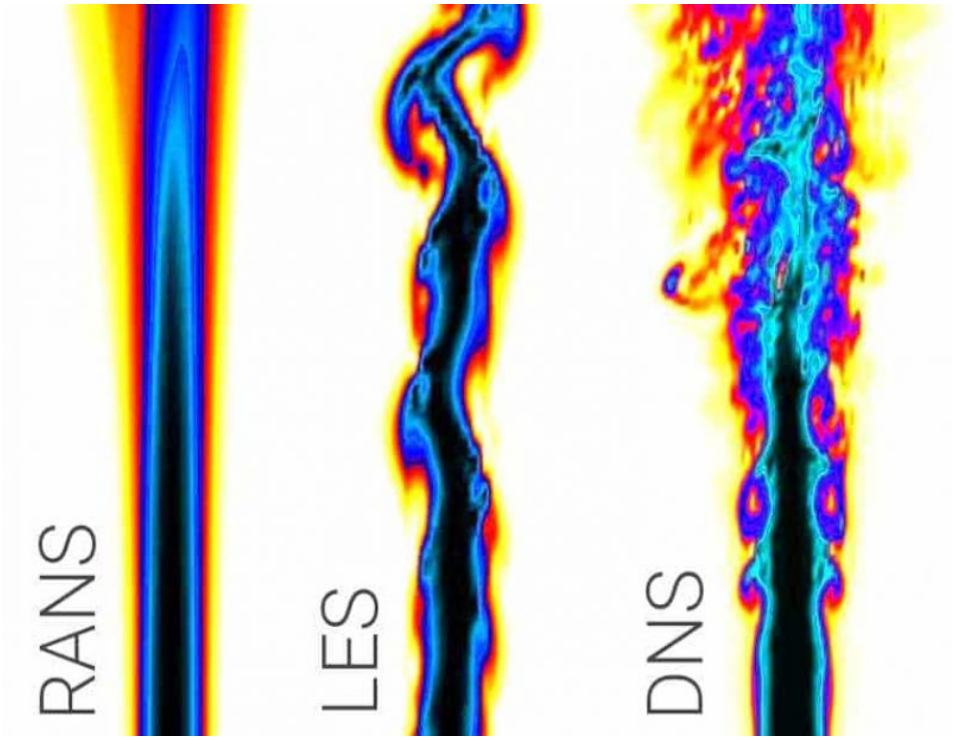

Figure 1.8: CFD modeling of a turbulent jet using different approaches. Reprinted from [12].

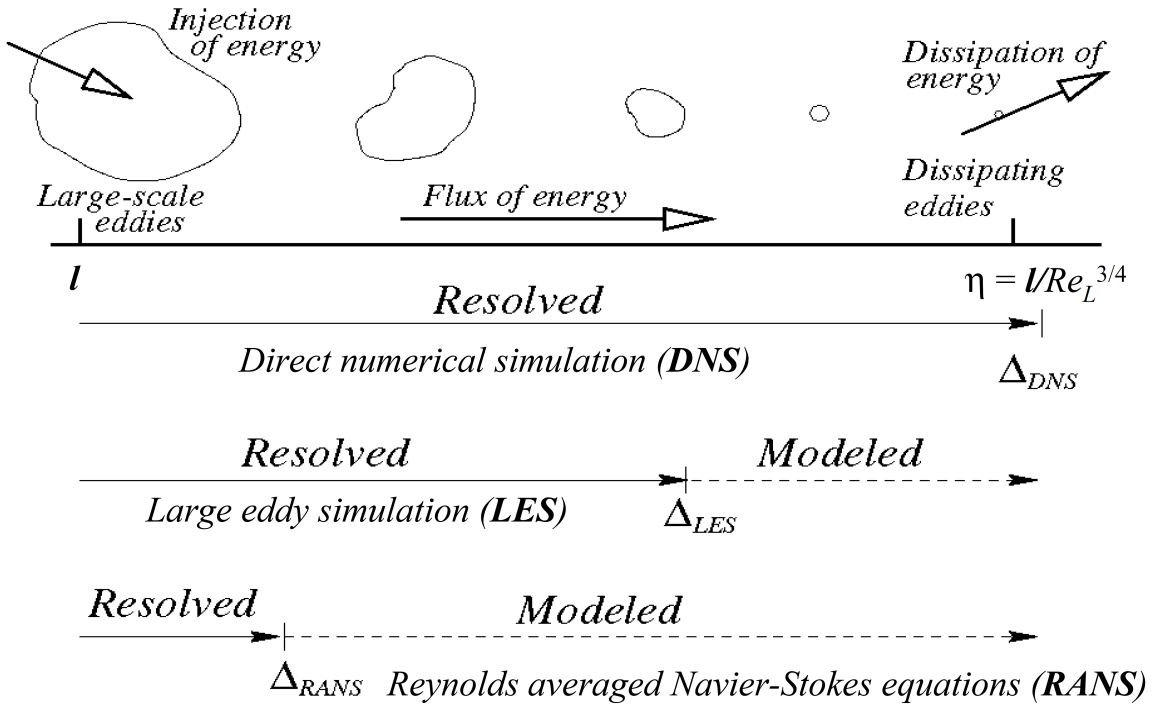

Figure 1.9: Modeling domains with respect to eddy sizes in the turbulent flow for different CFD approaches. Reprinted from [13].

1.3.1 Reynolds averaged Navier-Stokes (RANS)

Based on Reynolds decomposition, which consist in decomposing time-dependent instantaneous variables into a time-averaged mean component and a fluctuating component [62], the RANS approach solves for the mean values of the time-dependent variables characterizing the flow field. The time-averaged NS equations with Continuity equations, in the format of Einstein notation, are presented below:

$$\frac{\partial \rho}{\partial t} + \frac{\partial \rho U_j}{\partial x_j} = 0 \tag{1.5a}$$

$$\frac{\partial \rho U_j}{\partial t} + \frac{\partial \rho U_i U_j}{\partial x_j} = \frac{\partial P}{\partial x_i} + \frac{\partial}{\partial x_j}\left[\mu\left(\frac{\partial U_i}{\partial x_j} + \frac{\partial U_j}{\partial x_i}\right) - \frac{2}{3}\mu\frac{\partial U_k}{\partial x_k}\delta_{ij} - \rho\overline{u_i' u_j'}\right] + g_i\left(\rho - \rho_0\right) \tag{1.5b}$$

$$\frac{\partial \rho C}{\partial t} + \frac{\partial \rho C U_j}{\partial x_j} = \frac{\partial}{\partial x_j}\left(\Gamma\frac{\partial C}{\partial x_j}\right) - \frac{\partial}{\partial x_j}\left(\rho\overline{u_j' c'}\right) \tag{1.5c}$$

where ρ is density, μ is dynamic viscosity, Γ is molecular diffusivity, C is the mean scalar with its fluctuation represented by c' and U is the mean velocity with its fluctuation u'.

The correlation of the velocity fluctuations $\rho\overline{u_i' u_j'}$ in Equation 1.5b is known as the Reynolds stresses or momentum fluxes, and is identified as the source of turbulent transport and mixing. The appearance of this term in the Reynolds averaged NS equations make the system of equations under-determined and requires the introduction of closure relations. Turbulence modeling is required to determine appropriate closures for the Reynolds stresses $\rho\overline{u_i' u_j'}$ in the momentum equation as well as for the turbulent scalar fluxes $\rho\overline{u_j' c'}$ in the scalar transport equation 1.5c.

There are a considerable number of models for the Reynolds stresses. One of the most common approaches is to relate the Reynolds stresses to the mean velocity gradients by using the so-called Boussinesq Eddy viscosity approximation given by:

$$-\rho\overline{u_i' u_j'} = \nu_t\left(\frac{\partial U_i}{\partial x_j} + \frac{\partial U_j}{\partial x_i}\right) - \frac{2}{3}\rho k\delta_{ij} \tag{1.6}$$

where ν_t is the turbulent eddy viscosity, $k = \frac{1}{2}\overline{u_i' u_i'}$ is the Turbulent Kinetic Energy (TKE),

and δ_{ij} is the Kronecker delta. As for modeling the turbulent scalar fluxes $\rho\overline{u_j'c'}$, the prominent approximation method is based on the Standard Gradient-Diffusion Hypothesis (SGDH), which assumes local thermodynamic equilibrium and use the Erdogan theorem by relating the flux with its mean gradient. According to the SGDH, the turbulent scalar fluxes are assumed to be proportional to the gradient of the mean scalar field employing a turbulent diffusion coefficient Γ_t:

$$-\rho\overline{u_j'c'} = \rho\Gamma_t\frac{\partial C}{\partial x_j} \tag{1.7}$$

1.3.2 Challenges and limitations

Several turbulence models based on the Eddy viscosity approximation have been extensively used to simulate the behavior of round free jets in a uniform environment. For example, a comparison of simulation results with experiments can be found in the studies by Heschl et al. [63], Ghahremanian and Moshfegh [64], Aziz et al. [65] and Miltner et al. [66]). Researchers have also performed investigations and optimizations of turbulence models parameters, as in [7], [67] and [68]. Results from these past works have shown that the $k-\epsilon$ model, one of the most used eddy viscosity models, can nevertheless give reasonable predictions of turbulent round jet, even though the model tends to overpredicts the jet spreading rate.

However, the performance of the RANS turbulence models has not been extensively investigated for turbulent jets in the presence of density differences, which are relevant in reactor safety scenarios for LWRs as well as for advanced reactors. The presence of density gradients would cause enhancement or suppression of turbulence production. Petrov and Manera [69] pointed out that current RANS models result in an overestimation of thermal stratification and an underestimation of turbulent mixing when buoyancy effects dominate mass transportation in the flow. According to Nunez [70], RANS simulations yield under- and over-production of the Reynolds stresses depending on the sign of the

density gradients. Because most subgrid-scale models assume local isotropy, even Large Eddy Simulation (LES) cannot adequately capture the behavior of a buoyant jet in the presence of thermal stratification. Efforts to take into account buoyant effects in turbulence models has resulted in the implementation of additional source terms for turbulence production and dissipation ([71], [72], [73], and [74]).

However, the capability of RANS turbulence models to correctly predict turbulent buoyant round jets has not been fully evaluated due to the lack of detailed experimental data. As discussed in Chapter VI, the novel experimental results obtained within this dissertation for both uniform and non-uniform turbulent jets can be utilized to assess the predictive capability of the Realizable $k-\epsilon$ (RKE) and Reynolds Stress Transport (RST) models for turbulent round buoyant jets, identify the reasons for discrepancies, and provide recommendations to potentially improve the CFD RANS models predictive capabilities.

CHAPTER II

Experimental Setup and Uncertainty Quantification

This chapter describes the high-resolution experimental measurement techniques and facilities that have been used to generate the high-fidelity experimental database discussed in this dissertation. In order to gain insights into the mechanism of turbulent mixing in both uniform and density difference cases, two facilities, equipped with non-intrusive optical flow measurement methods were designed and constructed. The sources of uncertainties associated with the measurements are discussed and quantified as well.

2.1 Instrumentation and Measurement Techniques

With advances in the development of high-frequency pulsed lasers and high-speed cameras, non-intrusive optical methods have gained more and more popularity for turbulent flows visualization in the scientific community. Synchronized Particle Image Velocity (PIV) and Planar Laser-induced Fluorescence (PLIF) systems has been widely applied to obtain instantaneous velocity- and scalar-fields with high spatial and temporal resolutions.

2.1.1 Particle Image Velocimetry (PIV)

Developed in the early 1980s, Particle Image Velocity (PIV) is a non-intrusive optical measurement technique that provides instantaneous velocity vector fields in a cross-section of a flow field [75]. With standard PIV systems only two velocity components are measured,

but the use of a stereoscopic approach (so-called stereo-PIV) permits all three velocity components to be recorded at the same time in a selected 2D cross-section. The resolution of PIV measurements is comparable to that of CFD simulations, therefore this type of measurements is very well suited for CFD models validation.

The measurements discussed in this dissertation have been carried out with a typical 2D PIV system setup, illustrated in Figure 2.1. The setup makes use of a laser and appropriate optics to create a thin sheet of light, illuminating tracer particles mixed with the working fluid. For water applications, the seeding particles are typically polystyrene, polyamide, or hollow glass spheres. These particles are very small in size (usually in the range 5 to 100 micrometers in diameter) and neutrally buoyant in the specific working fluid, following the flow satisfactorily. One high-speed digital camera is used to track the motion of these particles by detecting the reflected laser light from those tracers.

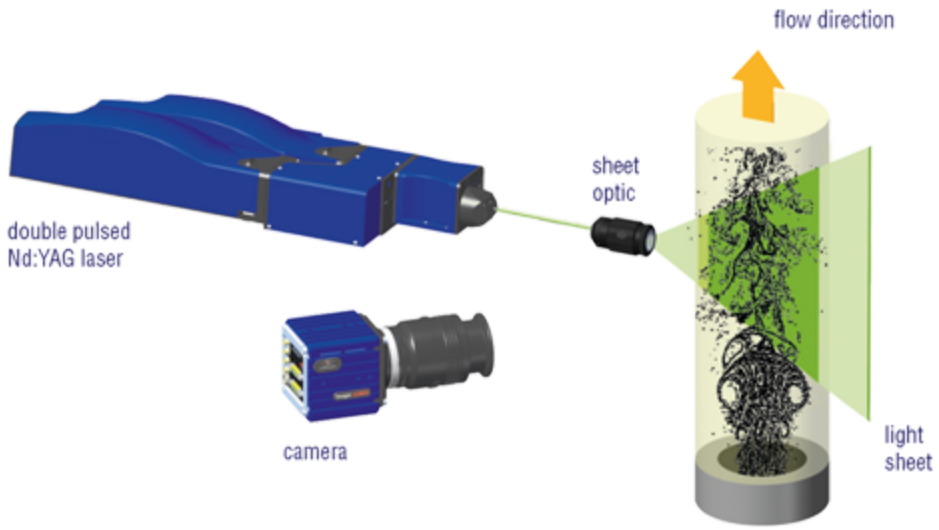

Figure 2.1: An illustration of a 2D PIV system setup according to LaVision®. Reprinted from [14]

In principle, by visualizing the motion of a individual tracer particle across multiple time frames, one could easily compute the velocity components u_i associated to that single particle by taking the ratio of the particle displacement Δx_i and the time interval Δt over which the

displacement occurred:

$$u_i = \frac{\Delta x_i}{\Delta t} \tag{2.1}$$

For the PIV measurements, nevertheless, with Δt still depends on the images acquisition rate, the determination of the particles displacement is required to be done using cross-correlation techniques. This because, one pair of PIV raw particle images, as shown in Figure 2.2, usually contain hundreds of thousands of illuminated particles, and each experimental campaign inevitably requires numerous particle image pairs to be processed.

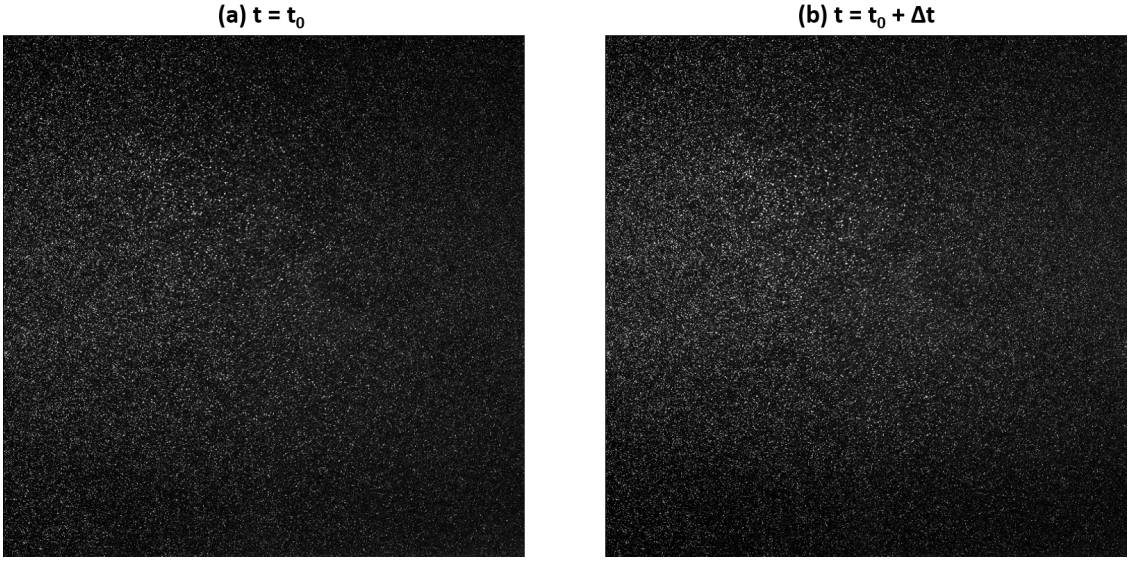

Figure 2.2: Sample of one PIV image pair taken (a) at t = t_0 and (b) at t = $t_0 + \Delta t$.

Before cross-correlation algorithms can be applied, PIV image calibration is necessary to map the particle displacement information from pixels to physical length scale (e.g. millimeters) and to correct for image distortions due to the viewing angle of the measurement plane and the optical aberration from the camera lens. The image calibration is performed by means of calibration targets. Shown in Figure 2.3 are two calibration targets, which are manufactured with high precision to provide a grid of equidistant marks. in Figure 2.3(a) the calibration target used for the near-field measurements (close to the jet inlet) is reported. This target has dimensions of 50 mm × 50 mm and overall 41 × 41 dots; each dot has a diameter of about 0.1 mm. The larger target shown in Figure 2.3(b) is used for the self-similar

region (further downstream from the jet inlet) and has a dimension of 200 mm × 200 mm and in total 324 dots.

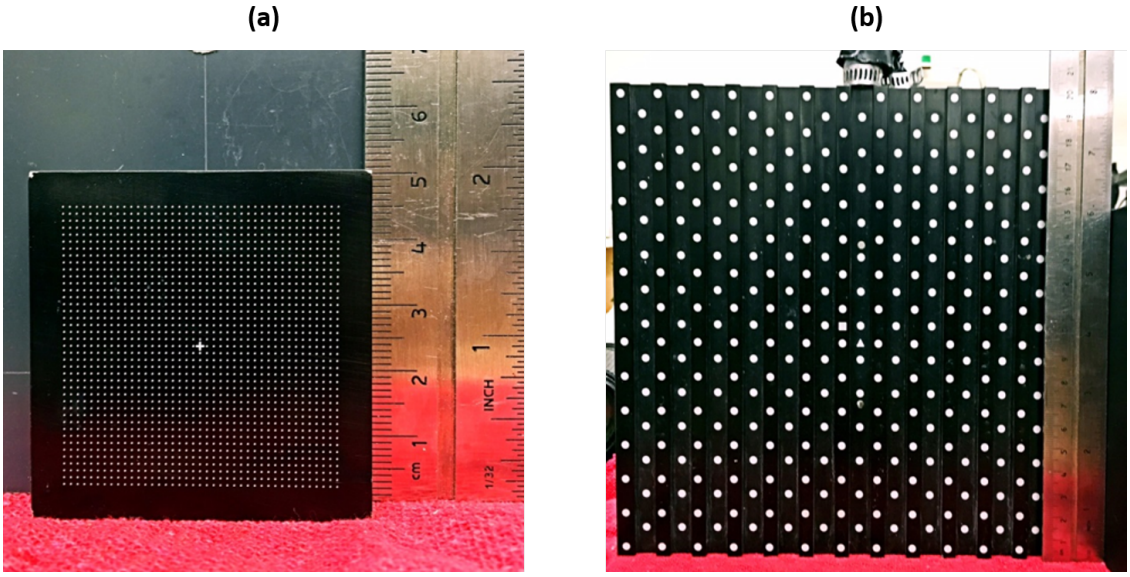

Figure 2.3: Calibration targets used for (a) near-field regions and (b) self-similar regions.

In Figure 2.4(a) the calibration target holder is reported, specifically designed to have a 12.7 mm pin that matches the diameter of the jet nozzle. When inserting the holder into the nozzle, the calibration target can fit tightly into the target holder, allowing to accurately align the front surface of the calibration target with the jet center. There is a slot milled on the target holder which can be used to rotate the holder from a distance. Inserting an adjustable aluminum bar into the slot, the orientation of the calibration target can be well controlled from outside the tank, as illustrated in Figure 2.4(b). As for the measurements in the far-field region, a T-shape holder was manufactured as shown in Figure 2.5(a), on which the calibration target is fastened by L brackets that can be slid up and down along the slot of the aluminum structure, giving a wide range of adjustments along the jet axis. After inserting the calibration target in the tank filled with water, a pendulum and a 3D printed piece, which have a precise center of the jet on the top surface, can be utilized to align the target's front surface with the center of the nozzle, as shown in Figure 2.5(b). A similar calibration target holder has been designed and manufactured for the miniDESTROJER

facility as well.

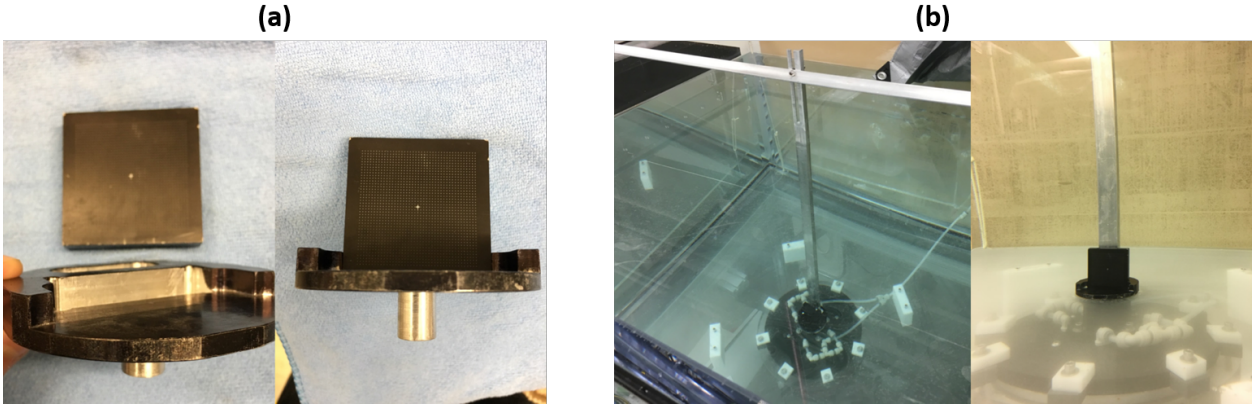

Figure 2.4: (a) Calibration target and its holder which can fit in the 12.7 mm diameter nozzle for DESTROJER facility, and (b) Rotation mechanisms to adjust the orientation of the calibration target.

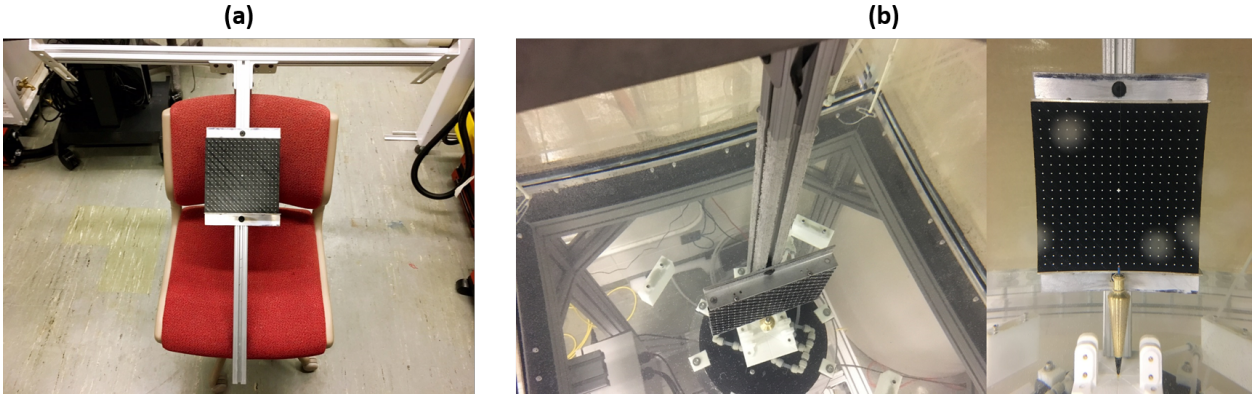

Figure 2.5: (a) Calibration system for far-field experiments in DESTROJER facility, and (b) Alignment of the calibration system in the one-cubic-meter tank.

Once the images of the calibration target are used to correct the PIV raw images, these can be post-processed to extract the velocity field. In order to efficiently post-process the PIV images for velocity field information, the images are divided into small areas, so-called interrogation windows, as illustrated in Figure 2.6. The cross-correlation algorithm scans the interrogation windows from the two images one by one to determine the average particle displacements within a specific interrogation window. After all these steps, the local velocity vector can be computed applying Equation 2.1 for the average particle displacement.

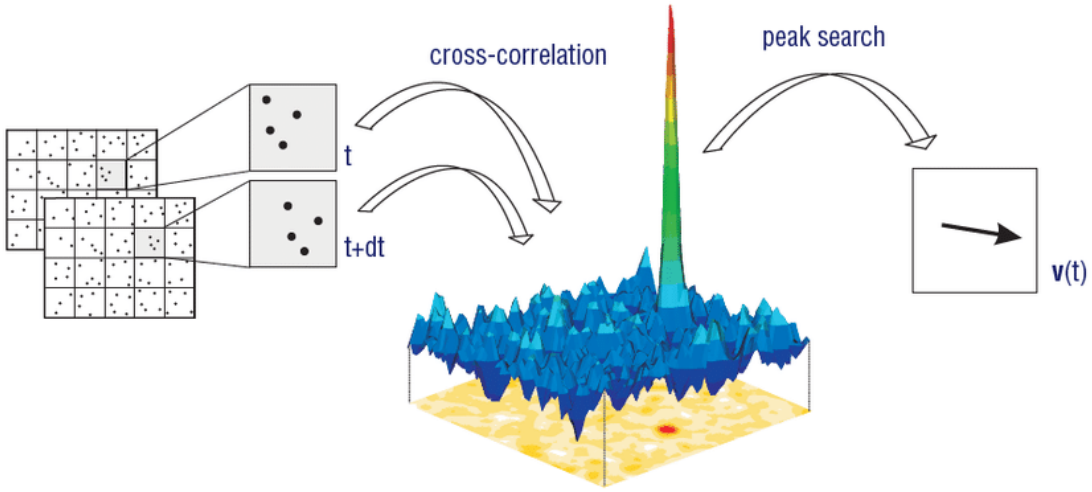

Figure 2.6: Block-matching cross-correlation technique used in PIV. The position of the highest peak in the correlation plane indicates the most likely displacement vector. Reprinted from [15]

.

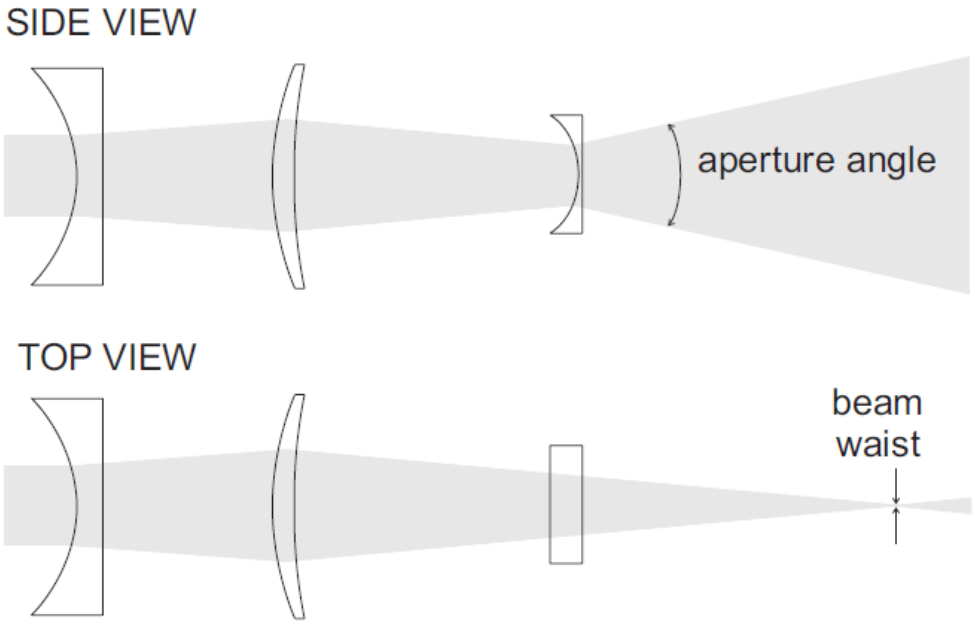

Figure 2.7: Lens configurations of the laser sheet formation. Reprinted from [16]

The experiments reported in this dissertation at Experimental and Computational Multiphase Flow Laboratory (ECMFL) have been carried out with a 2D PIV system using a high-speed double pulsed Nd:YLF laser (Photonics Industries International Inc., Model No. DM30-527-DH) with a maximum pulse frequency of 10 kHz at a wavelength of 527 nm and 70 mJ energy per pulse. The optics of the laser system (LaVision, Item No. 1108405) include a combination of two spherical lenses to focus the original laser beam, while a third planar concave lens is used to form a light sheet that is aligned to the vertical mid-plane of the jet, as shown in Figure 2.7. The eye of the PIV system is a Phantom Miro LAB M340 high-speed CMOS camera with 2,560 $\times$ 1,600 pixels (4MP), achieving 800Hz as the maximum frame rate at full resolution. The laser and camera systems communication is controlled by a LaVision's high-speed Synchronizer with the model No. 1108075. Since the working fluids used in the experiments reported in this dissertation are water or aqueous solutions, the seeding particles for the PIV measurements are chosen to be 10 μm glass hollow sphere particles having the density of $1.10 \pm 0.05\ g/cm^3$.

2.1.2 Planar Laser-induced Fluorescence (PLIF)

While PIV is used to measure the velocity field, another non-intrusive optical flow visualization technique, Planar Laser-induced Fluorescence (PLIF), is typically used to measure species concentration, mixtures fraction and temperature measurements in liquid and gaseous flows. Developed as a molecule specific visualization method, PLIF imaging has a high spatial and temporal resolution. For mixing studies, typically one of the fluids is marked with a tracer compound, whereas the other is fresh fluid. The working principle is illustrated in Figure 2.8: a laser light sheet illuminates a thin plane in the flow. The tracer particles in the fluid absorb some of the light and, as a result, get excited to a higher electronic energy state. In the subsequent return to a lower energy state, a part of the excess energy is released as light at a longer wavelength, commonly known as Fluorescence. Dyes typically employed for measurements in liquids are Rhodamine-6G (for concentration measurements), and Rho-

damine B (for temperature measurements), while Ketones such as acetone are regularly used for characterizing gas phase flows.

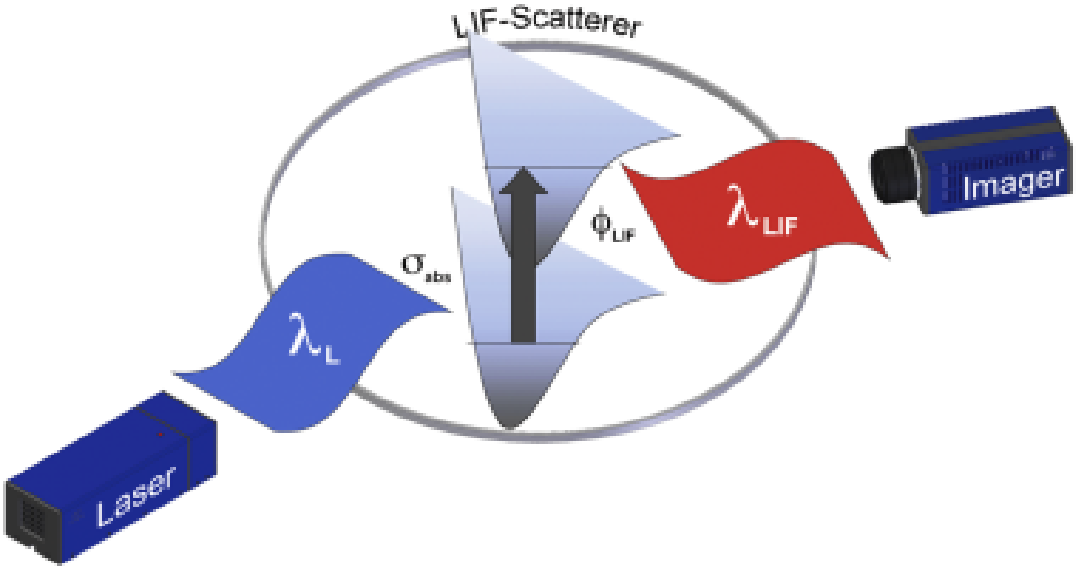

Figure 2.8: PLIF principle: absorption of a laser photon followed by emission of a fluorescence photon from the excited state. Reprinted from [17]

Rhodamine-6G, as shown in Figure 2.9, is a highly fluorescent rhodamine family dye. It is often used as a tracer dye within water to determine the rate and direction of flow and transport. Rhodamine dye has an $S_1 - S_0$ absorption around the 500-550 nm region, with the maximum at 530 nm. On the other hand, it has a fluorescence region from 550 to 590 nm with a peak at 565 nm (see Figure 2.10).

In this thesis, the PLIF technique makes use of the fluorescence property of Rhodamine-6G as the tracer to characterize the scalar field (mixing scalar) of the jet flow. The experimental setup consists of illuminating a particular region in the flow (see Figure 2.11) with a pulsed laser plane (wavelength 532 nm), which acts on the tracer molecules (Rhodamine-6G) exciting and causing the same to emit fluorescent signals. Images are captured by a CMOS digital camera equipped with a light filter permeable to the particles emission wavelength (570 nm), enabling the mapping of the flow through the correlation between the intensity of the emitted radiation and the concentration of the tracer, previously established by a

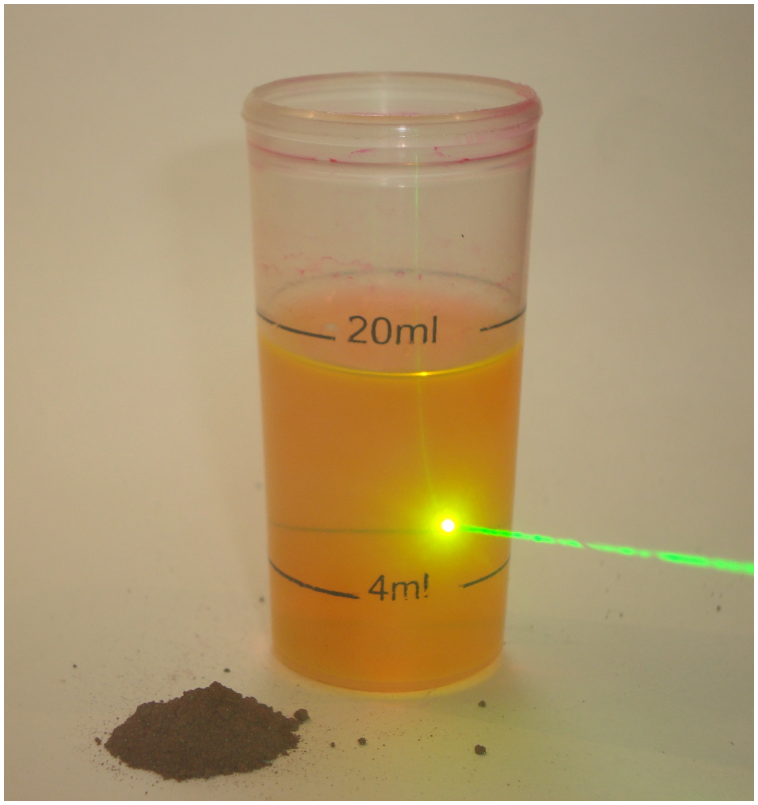

Figure 2.9: Rhodamine-6G chloride powder mixed with methanol, emitting yellow light under green laser illumination. Reprinted from [18]

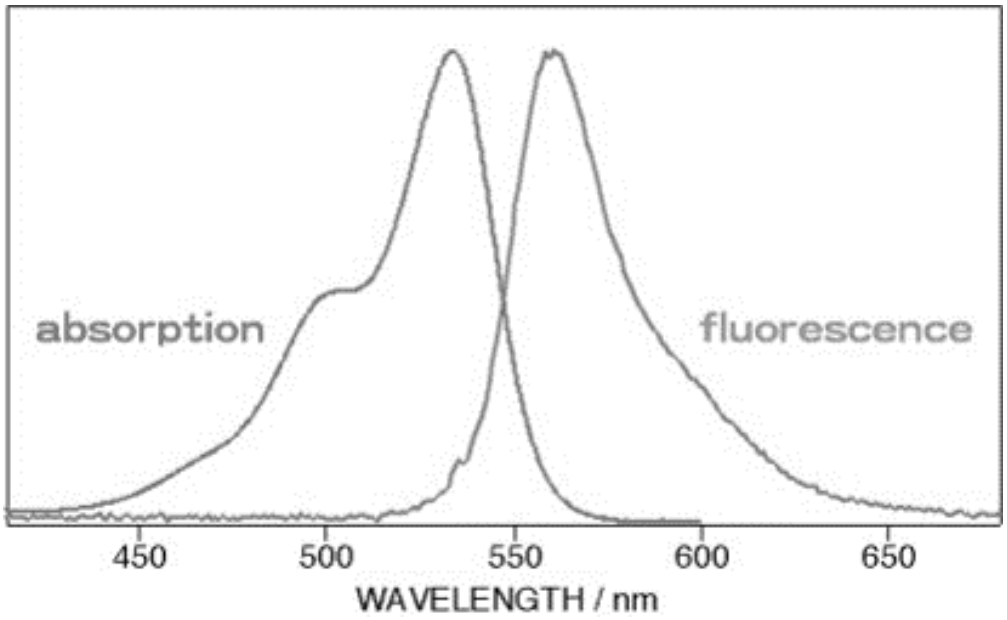

Figure 2.10: The absorption and fluorescence spectra of Rhodamine-6G. Reprinted from [19]

calibration curve. With a precise time controller, the PLIF technique can be combined with PIV measurements, leading to a synchronized measurement of both the velocity and scalar fields.

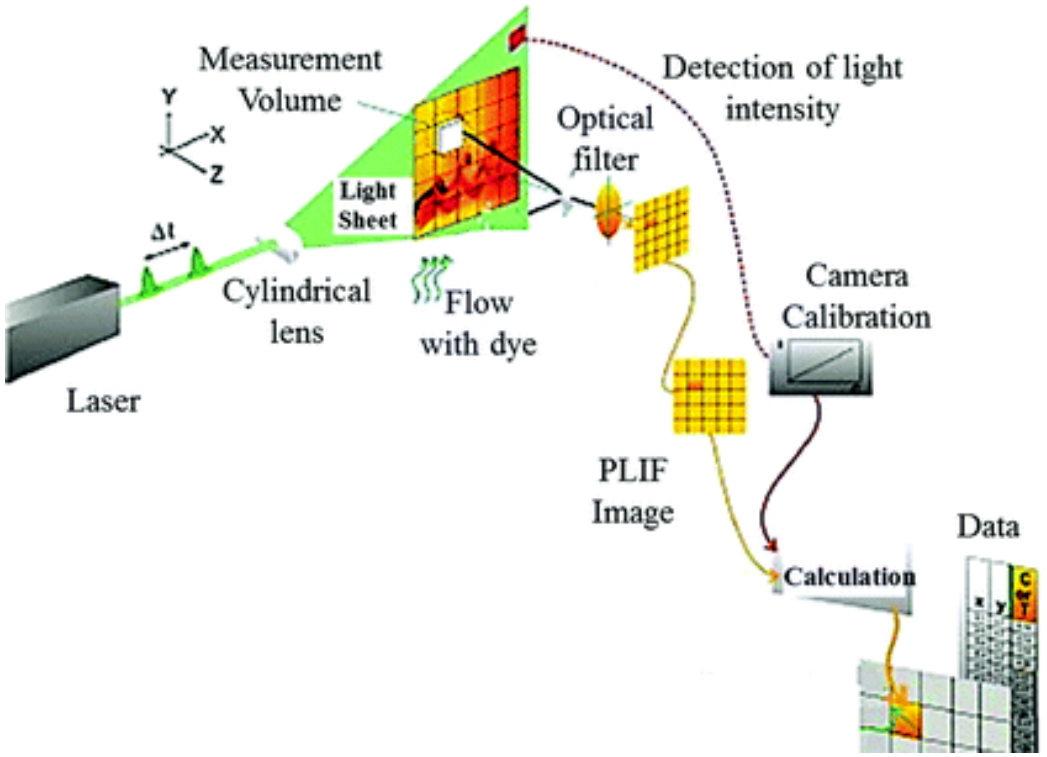

Figure 2.11: Schematic representation of PLIF apparatus according to DANTEC®. Reprinted from [20]

2.2 DESTROJER Facility

An experimental water jet facility was designed and built at ECMFL to study a round axisymmetric incompressible vertical jet in uniform environments, named **DE**nsity **S**tratified **T**urbulent **RO**und free **J**et **E**xpe**R**iment (DESTROJER) facility. A photograph of the facility is reported in Figure 2.12. A simplified schematic of DESTROJER is shown in Figure 2.13, depicting the imaging system setup and the regions of interest for the flow measurements. The axial jet flow is driven with a piston that is powered by a Dynamic Motor Motion 86M-DHT-A6MK1AC Servo engine. The servo drive prevents motor vibration to introduce

undesired fluctuations in the flow, resulting in a precisely controllable and repeatable inlet velocity profile. An in-house software was implemented using JAVA to control the servo motor for the jet. The graphical interface of the software developed to accurately control the motor speed is shown in Figure 2.14.

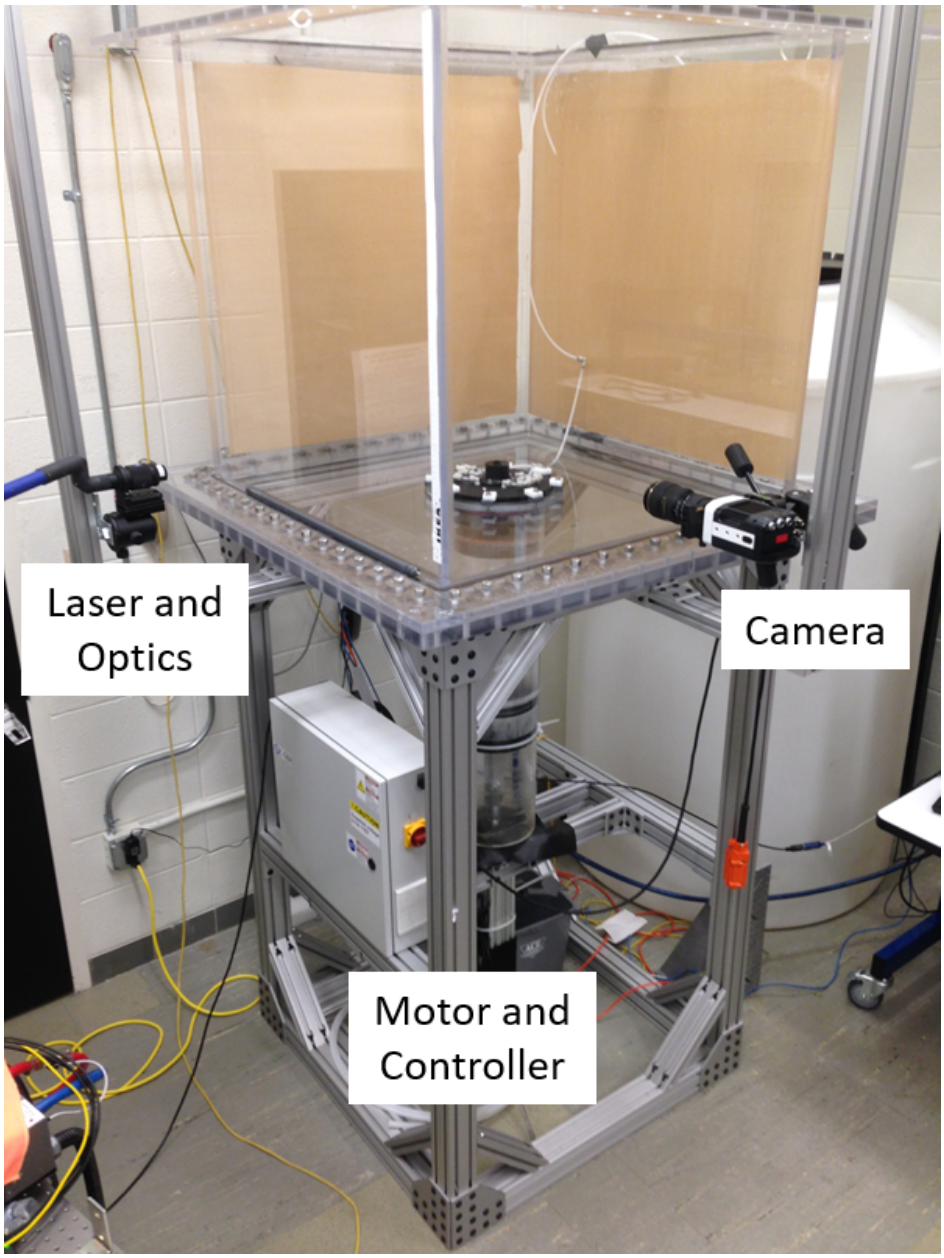

Figure 2.12: Photograph of the DESTROJER facility.

After being pushed through a 200.7 mm diameter cylindrical chamber, the fluid passes through the first contraction with an exit diameter of 50.8 mm. Then the flow is finally

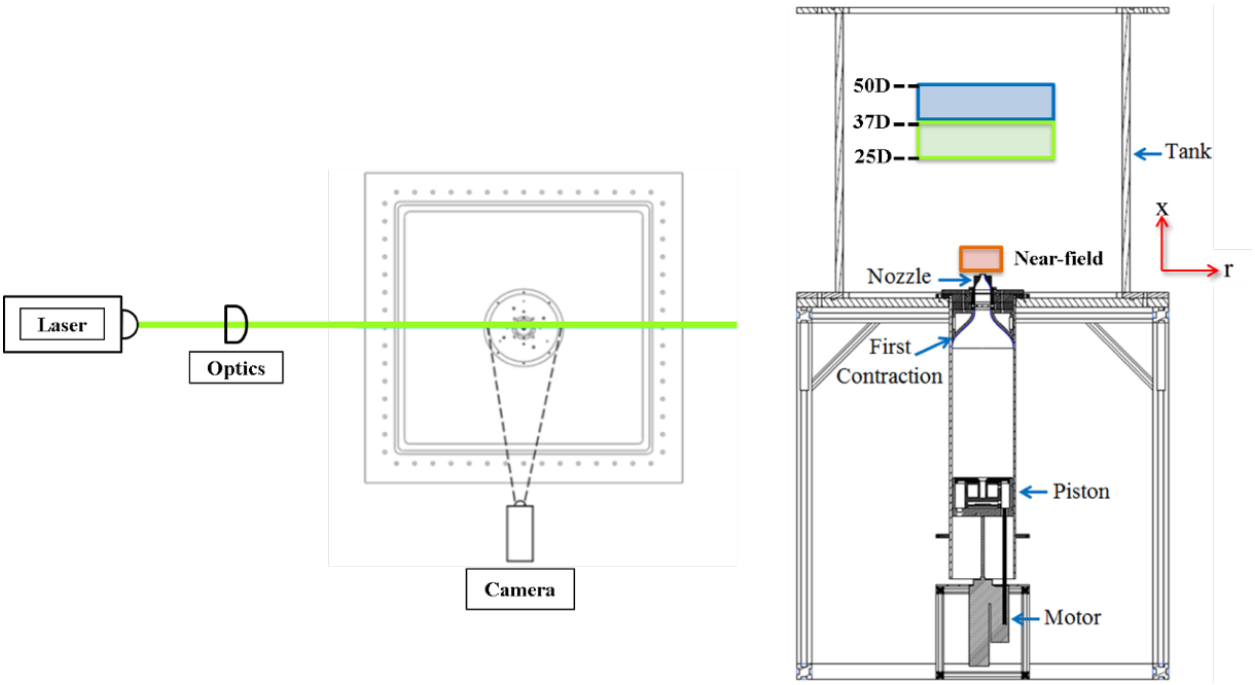

Figure 2.13: (right) Front view of DESTROJER facility with details shown on the right. PIV measurements are taken in the near-field region, indicated by the red area. For the self-similar regions, measurements are separated into two regions of interest, green and red areas, respectively. (left) Shown on the left is the top view of the configurations of the imaging and laser systems.

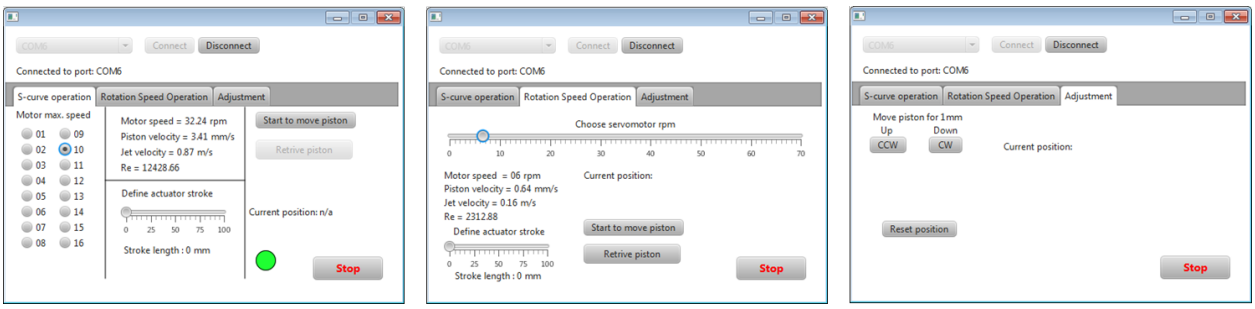

Figure 2.14: GUI to control the servo-motor of the jet injection system at UM.

directed out of a contoured jet nozzle with a diameter of D = 12.7 mm into a 1 m × 1 m × 1 m cubic tank which is made of acrylic glass for optical access. A detailed design of the first and second nozzle contraction profile is provided in Figure 2.15. Because the tank width to nozzle diameter is equal to 78, it is ensured that no direct interaction between the jet and the side walls exist.

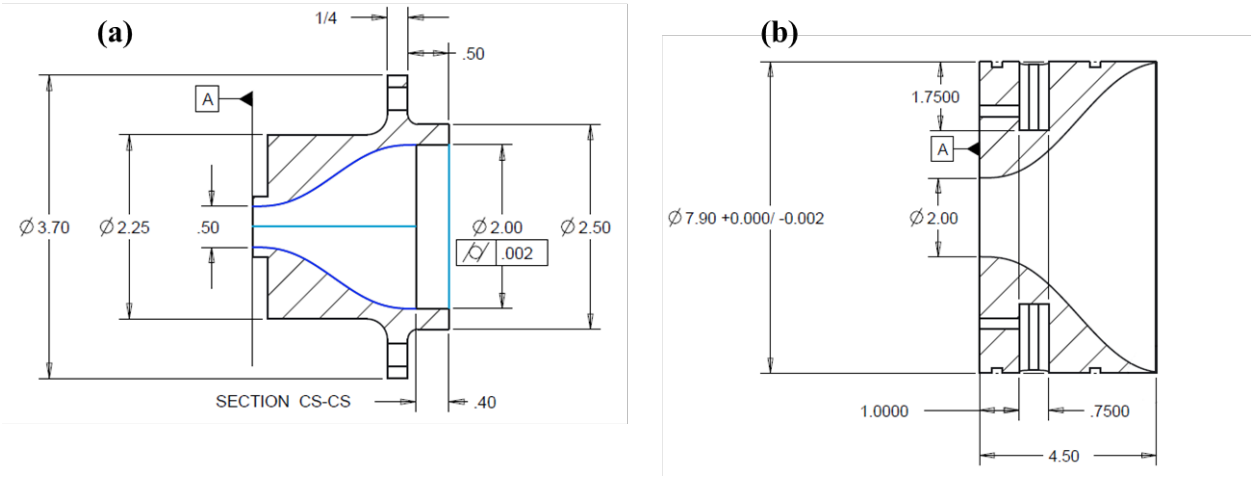

Figure 2.15: Contraction profiles for (a) the jet nozzle, and (b) the first contraction

2.3 miniDESTROJER Facility

In order to study the influence of density gradients on turbulence dynamics, aqueous solutions with specific density and refractive index need to be prepared. Since repeating the experiments with density variations in the one-cubic meter tank is time-consuming and expensive, and in order to be able to investigate also scaling effects, a scaled-down facility was designed and built. This facility has the advantage to considerable shorten the preparation time and to decrease the amount of chemicals needed for the solutions. The CAD drawing for the scaled facility, named miniDESTROJER is reported in Figure 2.16. The test section is characterized by a tank size of 300 mm × 300 mm × 300 mm and a jet inlet diameter of 2 mm. The corresponding tank size-to-nozzle ratio is 150, ensuring the flow is still an unconfined free jet. The axial jet flow is driven by the same servo-engine-driven piston as

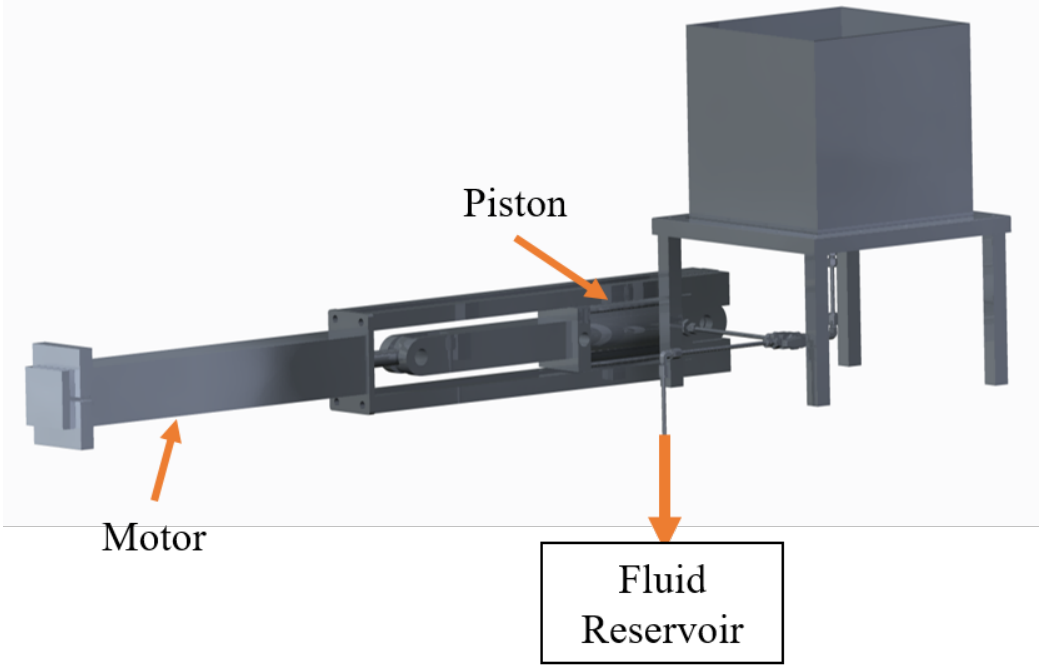

Figure 2.16: CAD drawing for miniDESTROJER facility.

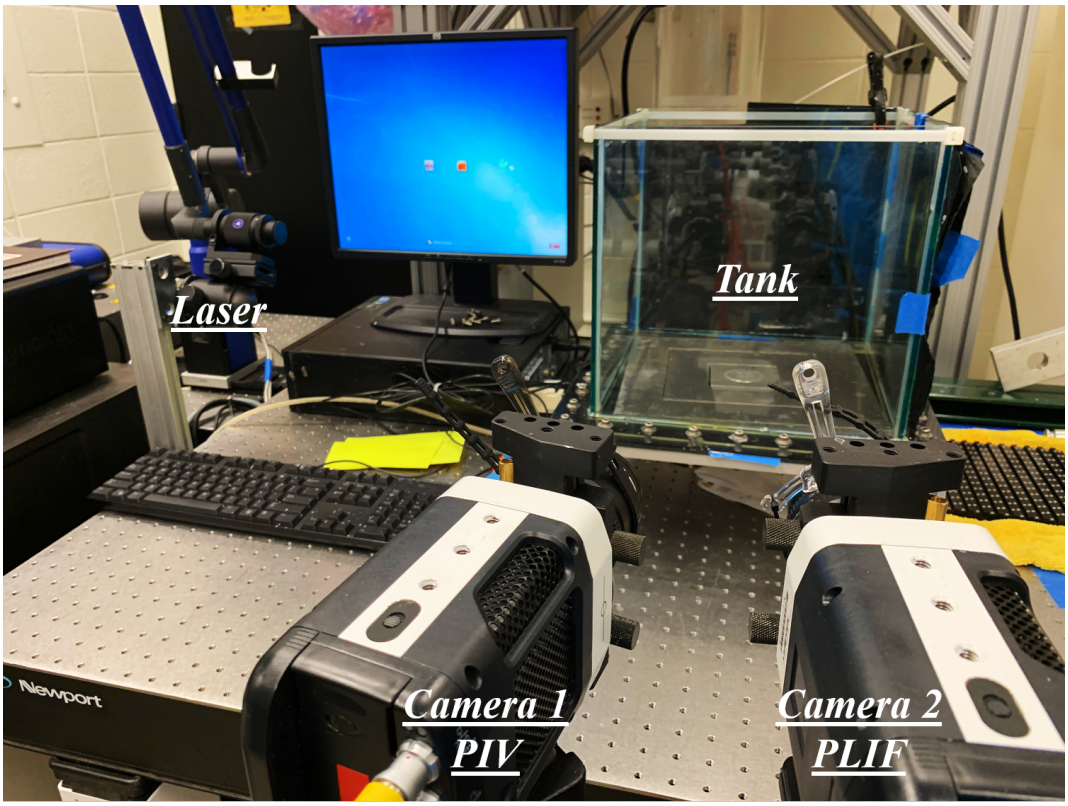

Figure 2.17: Photograph of the miniDESTROJER facility.

the DESTROJER facility, for a precisely controllable and repeatable inlet velocity profile. The inlet region has an entrance length L of 25 jet-diameter ($L/D = 25$) to establish a fully-developed turbulent flow, upstream of the jet inlet. A two-direction valve is mounted at the bottom, to allow discharge of the fluids to the disposal bottle underneath the tank at the end of an experiment.

To gain optical access to the entire jet flow domain, the walls of the tank are made of glass (see Figure 2.17). The laser located in the left illuminates the vertical mid-plane of the jet, while the high-speed cameras for the PIV/PLIF systems are utilized to measure the synchronized velocity and mixing scalar fields in the turbulent round free jet.

2.4 Data Processing

For the PIV analysis, the computer software LaVision®'s DaVis 8.4 [76] is used on a Graphics Processing Unit (GPU) to compute the vector fields by using a direct normalized correlation. A multi-pass approach was applied with an initial interrogation window of 64 $\times$ 64 pixels^2 with a 50% overlap for the first two passes, and a final interrogation of 32 $\times$ 32 pixels^2, with a 75% overlap for the last three passes. A high accuracy model for image reconstruction in the final passes is used. Particle diameters in the PIV recordings are about 4 pixels, usually leading to peak locking and limiting the accuracy of the PIV cross-correlation algorithm. Therefore, in order to avoid a bias error introduced by peak locking [27], the Whittaker-Shannon interpolation method [77] was applied to reconstruct the vector fields in the final pass. Based on these settings and the locations of the PIV equipment, this results in an effective spatial resolution of 200 - 800 μm for the velocity field.

As for the PLIF analysis, the laser sheet inhomogeneities and intensity absorption towards the PLIF tracer were first corrected with the sheet geometry based on edge detection and ray-tracing methods. The absorption correction was then implemented by computing the molar extinction coefficient for the laser light decaying according to Beer-Lambert law [78]. The light intensity $I(L)$ after passing an absorption length L along a laser beam-line is

defined as the reciprocal value of the molar extinction coefficient α and the concentration of the absorbing molecule c:

$$I(L) = I_0 \cdot e^{-\alpha c L} \tag{2.2}$$

Finally, the normalized scalar field c_{norm} was computed using the following equation:

$$c_{\text{norm}} = \frac{c_i - c_0}{c_{\text{full}} - c_0} \tag{2.3}$$

where c_i is the measured fluorescence signal strength, and c_{full} and c_0 are two reference (calibration) measurements taken with a tank completely filled with Rhodamine-6G homogeneously distributed in the flow, and with no tracer respectively.

Once the instantaneous velocity field is measured, turbulent statistics can be computed by appropriate averaging. The ensemble-averaged quantities are calculated according to:

$$\overline{u} = \frac{1}{N} \sum_{i=1}^{N} u_i \tag{2.4}$$

where N is the overall number of the recorded samples of the instantaneous field and u_i denotes the instantaneous streamwise component of the velocity vector. Equivalent averaging is applied to the crosswise velocity component and the mixing scalar. Higher-order terms like the normal components of the Reynolds stress tensor are calculated according to the variance of the velocity components:

$$\overline{u'u'} = \frac{1}{N-1} \sum_{i=1}^{N} (u_i - \overline{u})^2 \tag{2.5}$$

Equations 2.4 and 2.5 shown above can then be applied for solving $\overline{v}$, $\overline{c}$, $\overline{v'v'}$, and $\overline{c'c'}$.

The shear stress component $\overline{u'v'}$ are computed using the concept of covariance between two quantities:

$$\overline{u'v'} = \frac{1}{N-1} \sum_{i=1}^{N} (u_i - \overline{u})(v_i - \overline{v}) \tag{2.6}$$

By mapping the data sets of the synchronized velocity and scalar fields to match the spatial resolution of both PIV and PLIF techniques, turbulent fluxes $\overline{u'c'}$ and $\overline{v'c'}$ can also be estimated as follows:

$$\overline{u'c'} = \frac{1}{N-1}\sum_{i=1}^{N}(u_i - \overline{u})(c_i - \overline{c}) \tag{2.7}$$

$$\overline{v'c'} = \frac{1}{N-1}\sum_{i=1}^{N}(v_i - \overline{v})(c_i - \overline{c}) \tag{2.8}$$

Since the turbulent free jet flow is axisymmetric, the radial-components $\overline{v'v'}$ are assumed to comparable to the spanwise-components $\overline{w'w'}$ along the centerline. Therefore, the Turbulent Kinetic Energy (TKE) can be computed according to:

$$k = \frac{1}{2}(\overline{u'u'} + 2 \cdot \overline{v'v'}) \tag{2.9}$$

2.5 Measurement Uncertainties

For all measured values, uncertainty quantifications is of great importance to determine the confidence in the results. The detected sources of uncertainty within the conducted experiments can be categorized in uncertainties in manufacturer's specifications, limitations in the accuracy of the applied measurement systems, uncertainties associated to the data processing algorithms, and statistical uncertainties. In this section, the uncertainties from the facility geometry and laser alignments are not taken into account, efforts focusing on the data processing algorithms and statistical uncertainties. Each individual source of uncertainties then can be combined to estimate the intervals of confidence for the presented results. For any variable x_i, the uncertainty can be represented in general as the combination of the measured quantity x_i(measured) and the uncertainty term $\sigma(x_i)$ as shown in Equation 2.10:

$$x_i = x_i(\text{measured}) + \sigma(x_i) \tag{2.10}$$

Kline and McClintock [79] mentioned that the uncertainty can be estimated with good approximation using the root-sum-square (RSS) combination of the effects of each independent input, and the overall uncertainty in the result $\sigma(R)$ can be propagated by the RSS method including the uncertainties from each variable $\sigma(x_i)$ as shown in Equation 2.11:

$$\sigma(R) = \sqrt{\sum_{i=1}^{N} \left(\frac{\partial R}{\partial x_i} \, \sigma(x_i) \right)^2} \tag{2.11}$$

For the velocity field measurements carried out using PIV, the first uncertainty source is associated with the relative error due to the drag of seeding particles $\sigma_{\text{drag}}(u)$ in a Stokes flow. Tropea and Yarin [80] mentioned that $\sigma_{\text{drag}}(u)$ can be estimated to be at a maximum equal to 1% when the Stokes number is much smaller than unity. The second source of uncertainty originates from the method used to compute the vector fields (in our case, the direct normalized correlation). During the experiments, the diameter of each particle on the raw images occupies between one to four pixels, and this could lead to a bias error called peak-locking. Van Doorne et al. [81] and Foucault et al. [82] have shown that using a sub-pixel interpolation scheme, suggested by Whittaker [77], increases the accuracy by shifting and deforming the second interrogation window and thus significantly reducing the error due to peak-locking. The optimization of the image particle density within each interrogation window, the in-plane loss of particle pairs and the out of plane loss of particle pairs, also increases the probability of a valid detection of the particle displacement and thus the reliability of the resulting velocity field to more than 95% [83] so that the associated uncertainty can be formulated as $\sigma_{\text{corr}}(u) = 5\%$. The random error component $\sigma_{\text{re}}(x_i)$ for each of the variables is constructed with a 95% significance interval as shown in Equation 2.12,

$$\sigma_{\text{re}}(x_i) = \frac{t \cdot S(x_i)}{\sqrt{N}} \tag{2.12}$$

where t is the value computed by the inverse t-test of the Student's t-distribution for the

total sample population N at the desired confidence level and $S(x_i)$ is the standard deviation of the quantity. Therefore, using the RSS method, the overall uncertainty for the measured velocity can be computed as:

$$\sigma(u) = \sqrt{\sigma_{\text{drag}}(u)^2 + \sigma_{\text{corr}}(u)^2 + \sigma_{\text{re}}(u)^2} \tag{2.13}$$

For higher-order moments, such as the Reynolds stresses ($\overline{u'u'}$), which are computed by the statistics of multiple velocity samples, the distribution does not necessarily follow a normal distribution. Therefore, the Chi-square (χ^2) test is applied to construct the interval of confidence. According to Sullivan and Verhoosel [84], the statistical uncertainty on higher order moments depends on the amount of data used to estimate the variance and the defined significance level, and can be estimated by Equation 2.14 with the subscripts L and U denoting the lower and upper uncertainty bound respectively:

$$\frac{\sqrt{N-1}}{\chi_L} \cdot \overline{u'u'} \leqslant \overline{u'u'} \leqslant \frac{\sqrt{N-1}}{\chi_U} \cdot \overline{u'u'} \tag{2.14}$$

The individual sources of uncertainty, such as the particle drag, the algorithm for computing the cross-correlation and random error are combined using the RSS method.

For the scalar field measurements obtained using the PLIF technique, the theoretical fluorescence signal depends on the number density of added tracer n_i, the number of photons per laser pulse n_{ph}, the absorption cross-section σ_{abs}, the fluorescence efficiency Φ and the detection efficiency η:

$$S_F \sim n_i \cdot n_{ph} \cdot \sigma_{\text{abs}} \cdot \Phi \cdot \eta \tag{2.15}$$

In addition to the theoretical signal strength, the amount of noise expected in the PLIF signal is important. Only detected photons are considered to calculate the signal-to-noise ratio (SNR) in the process. Assuming that the process for the camera to capture the fluorescent signal strength follows a Poisson distribution [85], having an expectancy-value P, and

the standard deviation σ, which is equal to the square root of P, the SNR can be formulated as:

$$\mathrm{SNR} = \frac{P}{\sigma} = \frac{P}{\sqrt{P}} = \sqrt{P} \tag{2.16}$$

Therefore, the relative error $\sigma_{\mathrm{SNR}}(c)$ for the PLIF signal measurement can be estimated as:

$$\sigma_{\mathrm{SNR}}(c) = \frac{1}{\mathrm{SNR}} \tag{2.17}$$

Finally, the overall uncertainties $\sigma(c)$ for the scalar field measured using PLIF can be expressed as a combination of the relative error $\sigma_{\mathrm{SNR}}(c)$ and the statistical uncertainty $\sigma_{\mathrm{re}}(c)$ using the RSS method:

$$\sigma(c) = \sqrt{\sigma_{\mathrm{SNR}}(c)^2 + \sigma_{\mathrm{re}}(c)^2} \tag{2.18}$$

CHAPTER III

Refractive Index Matching (RIM)

Turbulent mixing in stratified environments represents a challenging task in experimental turbulence research, especially when large density gradients are desired. Researchers have successfully create turbulent buoyant jet with gases, such as shooting Hydrogen or Helium jets into air surrounding, or heating the air jet to create density differences ([44], [8], [86], [87], [88]). There are such tiny changes in Refractive Index (RI) when mixing gases that the differences could be neglected [89]. However, when optical measurement techniques like PIV and PLIF are applied to stratified liquids, it is common practice to combine two aqueous solutions with different density but equal RI to suppress particle image deflections. The achieved RIM limit until very recently was around a 3% density ratio. In the ECMFL group, a novel methodology based on the behavior of excess properties and their change in a multi-component system while mixing was developed by Krohn et al. [22] that allows to achieve RIM for aqueous solutions with much higher density differences. The novel methodology was successfully demonstrated by Krohn et al. using a ternary combination of water, isopropanol and glycerol, for which RIM has been achieved in the presence of density differences of up to 8.6% . This innovative technique allows to systematically identify RIM regions in ternary plots, and could be used to potentially extend the experimental campaigns to even higher density ratios. The technique was successfully employed in this dissertation to perform measurements on buoyant jets in stratified environments.

3.1 Previous Efforts

Optical measurement techniques like PIV and PLIF is a promising flow visualization tool to acquire the temporal evolution of velocity and temperature (or concentration) fields without being intrusive to the flow [90]. However, a variable density or temperature field is usually connected with variable Refractive Index (RI), which limits the applicability of PIV or PLIF to very weakly stratified conditions. This is because changes in RI will result in blurred digital images. Shakouchi et al. [21] used water and a NaCl-water solution to create a density interface and visualized the jet impacting into a two-layer density interface (see Figure 3.1). Looking at the visualization data by Shakouchi, the challenges of applying optical measurements to flows in the presence of density differences in liquids become quite apparent, as demonstrated in Figure 3.1(c). Here, significant blurring of the flow image can be observed as soon as the jet impacts the stratified region.

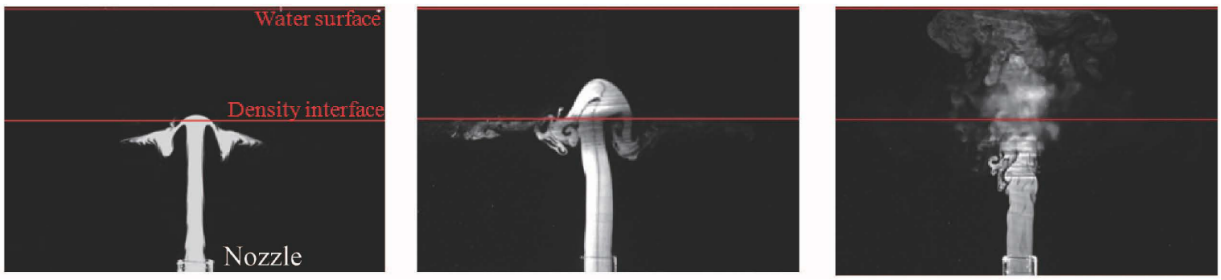

Figure 3.1: Typical behavior of the jet issued into density-stratified fluid: (a) Pattern A (Re = 95); (b) Pattern B (Re = 476); (c) Pattern C (Re = 2378). The red line indicated the sharp interface. Reprinted from [21].

Given these limitations, most of the available experiments have focused on lower Reynolds number (Re) flows, where the Froude Number (Fr) is of the order of 1 and the flow is strongly affected by density stratification, although a significant difference in the dynamics of stratified flows for high-Re conditions has been noticed by Riley and deBruynKops [91]. A few experiments are reported that deal with strongly stratified turbulence. In 2014, Augier et al. [92] generated a density gradient of 20% using water–salt (NaCl) solution and

applied PIV to measure the velocity fields in vertical cross-section, which was sufficiently small according to the publication. The authors ignored the changes in RI and argued that possible influences of RI variations are weak enough due to small-scale mixing in the vertical direction.

When it comes to generating a system with variable density and constant RI in turbulence research using liquids, all methods reported in the scientific literature focus on a combination of two aqueous solutions. However, when density differences in a turbulent flow configuration are desired, it is of paramount importance to keep the RI constant along the gradient of one liquid within the other, i.e., the RI has to remain constant with the changing mixing scalar. Using two binary aqueous solutions, it is, therefore, necessary to investigate the RI across the whole composition diagram (for two binary solutions a ternary diagram is needed), to identify the regions where the RI remains constant along the connecting line of two chosen solutions.

3.2 RIM Technique with Ternary System

Density differences in a flow field can be achieved by either temperature variations or by mixing two miscible solutions having different densities. Density variations are generally related to changes in the Refractive Index (RI). Since the RI determines how much the path of light is refracted when entering a medium, the laser beam used to illuminate the field of view will be bent by the changes of RI when traveling through the flow, causing a distortion of the laser sheet and large uncertainties in locating tracer particles in the PIV raw images. Temperature variations are strongly correlated with changes in RI. Therefore, if optical measurement techniques were to be used in a flow field in the presence of temperature gradients, it would not be possible to obtain unbiased data due to the image distortion. Therefore, the experiments presented in this dissertation have been performed in adiabatic conditions using two miscible solutions characterized by different densities.

Daviero et al. [93] pointed out that the amount of variations in RI that can be tolerated

without incurring into image distortions depends on the beam traverse length and the type of measurement technique: Optical field measurements like PIV and PLIF are generally more sensitive than point measurements using Laser Doppler Velocimetry (LDV). In addition, the light scattered by the seeding particles (for PIV) or emitted by the fluorescent dye (for PLIF) will also be affected, resulting in blurred images for PIV and PLIF measurements. Therefore, differences in RI must be sufficiently small to obtain quantitative information of velocity and concentration fields for the jet flow. Alahyari and Longmire [94] reported that a variation as low as 0.0002 in the refractive index could lead to unusable (blurred) PIV images. As a side note, it is reasonable that previous researches did not perform RIM for gaseous mixtures in the turbulent buoyant jet studies because the differences in RI for mixing Hydrogen or Helium gases with air have a tiny magnitude of 10^{-5} [89]. Therefore, the changing of RI when mixing gases is practically negligible for optical measurement techniques.

By implementing RIM techniques, these challenges have been overcome. According to Daviero et al. [93], the basic idea is to identify two miscible solutions of different density but with the same RI, and such that the RI remains constant with varying mixing scalar. The method was first suggested by McDougall [95] in 1979 using Taylor series expansion to express the refractive index and density as functions of concentrations of two solutes in water. He then applied LDV measurements to several candidates and successfully achieved RIM in the presence of a density difference of 0.015 g/cm^3 (1.5%) with an aqueous combination of Epsom salt and sugar. Later, Hannoun [96] achieved RIM with a density difference of about 0.03 g/cm^3 (3%) using NaCl and ethanol solute pairs. These works, including Daviero et al.'s publication [93], aim at modeling the refractive index variances based on the nonlinear rate of change in density with the assumption for weak polar molecules. However, this relation is no longer valid for water molecules, which are highly polarized. The interaction of molecules with strong differing dipole moments, such as water and Isopropanol, leads to more complex structural properties when mixed.

Inspired by the work done by Touriño et al. [97] and Yahya and Saghir [98] in the field

of petro-chemistry and based on the concept of thermodynamic excess properties that are present when mixing two or more miscible fluids, a novel method was developed and demonstrated in our Experimental and Computational Multiphase Flow Laboratory (ECMFL) by Krohn et al. [22] to achieve a high-density difference of 8.6% using a ternary system. Examining the refractive index matching across the whole composition diagram (a ternary diagram for two binary solutions involved) regions where the refractive index remains constant as function of the mixing scalar (i.e. along the connecting line of two chosen solutions) can be easily identified.

3.2.1 3.16% density difference solutions pair

For the experiments summarized in this dissertation, a combination of two aqueous solutions with sodium sulfate (Na_2SO_4) and glycerol ($H_2O - CH_2OHCHOHCH_2OH$) are used respectively. Measurements of the refractive index and density are performed at a temperature of 293.35 K and atmospheric pressure over the whole composition diagram of the $H_2O - Glycerol - Na_2SO_4$ system. The refractive index is measured with a Sper Scientific 300037 Digital Refractometer with a RI range of $1.3330 < n_D < 1.5318$, which has an accuracy of 0.1% at a resolution of 0.0001. The density measurement is performed using a 50 ml volumetric flask, class A, in combination with a Lianze I2000 digital multi-function scale with an accuracy of 0.1g, resulting in an accuracy of 1% for density measurements.

Figure 3.2 shows the contours of constant refractive index in superposition to the density of the ternary system. Note that parts of the ternary diagram are not filled due to the solubility of Na_2SO_4 in water. The detailed data of measured RI and densities used for Figure 3.2 are given in Table A.1 in Appendix A. The color code represents the density of the ternary mixtures, with blue corresponding to lower density and red to higher density respectively. Because the diagram is an equilateral triangle, the sum of the perpendicular distances L_1, L_2, and L_3 from any point to each side of the diagram is a constant equal to the length of any of the sides L_T. Therefore, the composition of a mixture within the diagram

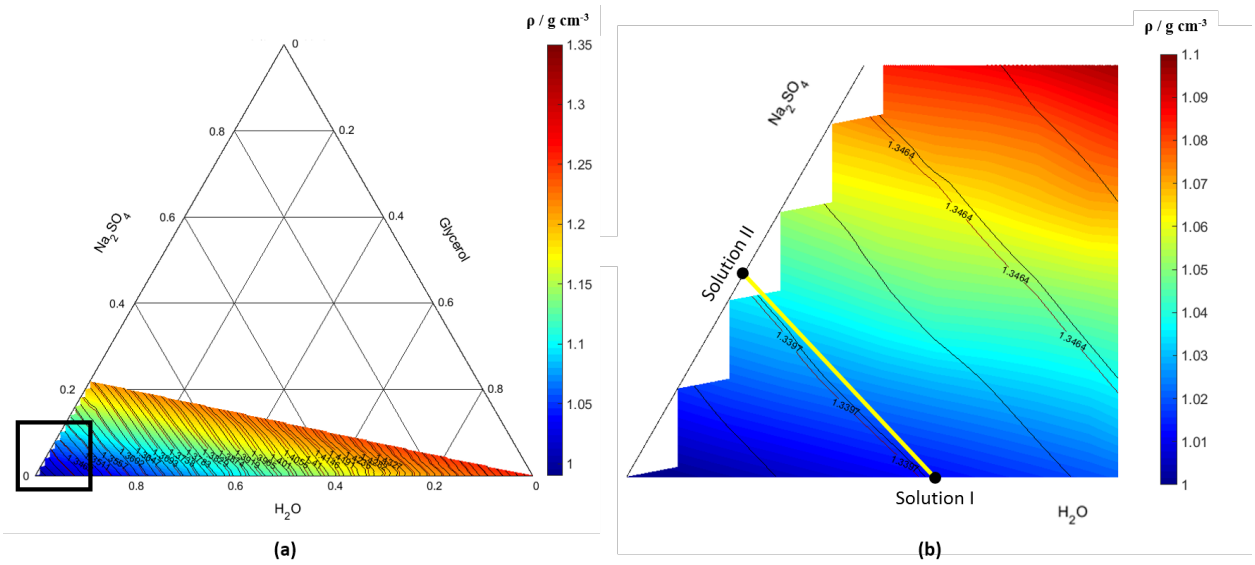

Figure 3.2: Contours of constant refractive index in a superposition of the density (colormap) for the ternary system with $H_2O - Glycerol - Na_2SO_4$: (a) the full plot and (b) the zoom-in view.

can be calculated as:

$$x_1 = \frac{L_1}{L_t}, \; x_2 = \frac{L_2}{L_t}, \; x_3 = \frac{L_3}{L_t} \tag{3.1}$$

As mentioned earlier, to avoid blurring in PIV and PLIF images it is crucial to identify a region in the ternary diagram in which the RI is not changing along the connecting line between two solutions. After zooming in the region indicated by the black box in Figure 3.2(a), a constant RI of 1.3405 (within a deviation of 1×10^{-4}) with a density difference of 3.16% can be achieved along the yellow line connecting the mixtures (I) and (II) in Figure 3.2(b). The corresponding mass fractions for two solutions and their properties at $n_D = 1.3405$ are shown in Table 3.1.

Table 3.1: Nominal mass fractions and properties of the solution pair with a 3.16% density difference.

Solutions	$\boldsymbol{H_2O}$	***Glycerol***	$\boldsymbol{Na_2SO_4}$	$\boldsymbol{\rho}$ / $kg \cdot m^{-3}$	$\boldsymbol{\nu}$ / $m^2 s^{-1}$	$\boldsymbol{n_D}$
I (light)	93.43%	6.57%	0	1012	1.19×10^{-6}	1.3405
II (heavy)	94.90%	0	5.10%	1044	1.10×10^{-6}	1.3405

3.2.2 8.6% density difference solutions pair

To achieve higher density ratios, Krohn et al. [22] applied the novel RIM technique to a mixture of H_2O, Isopropanol ($CH_3CHOHCH_3$) and glycerol. All three liquids are fully miscible among each other, and the two solutions exhibit a large density difference. We have performed measurements of the refractive index and the density at a temperature of 298.15 K and atmospheric pressure over the whole composition diagram of the $H_2O - Glycerol - Isopropanol$ system. The color code for the density is chosen to be white at the density corresponding to pure water, with blue representing lower density and red representing higher density. The detailed data of measured RI and densities used for Figure 3.3 are given in Appendix B Table B.1.

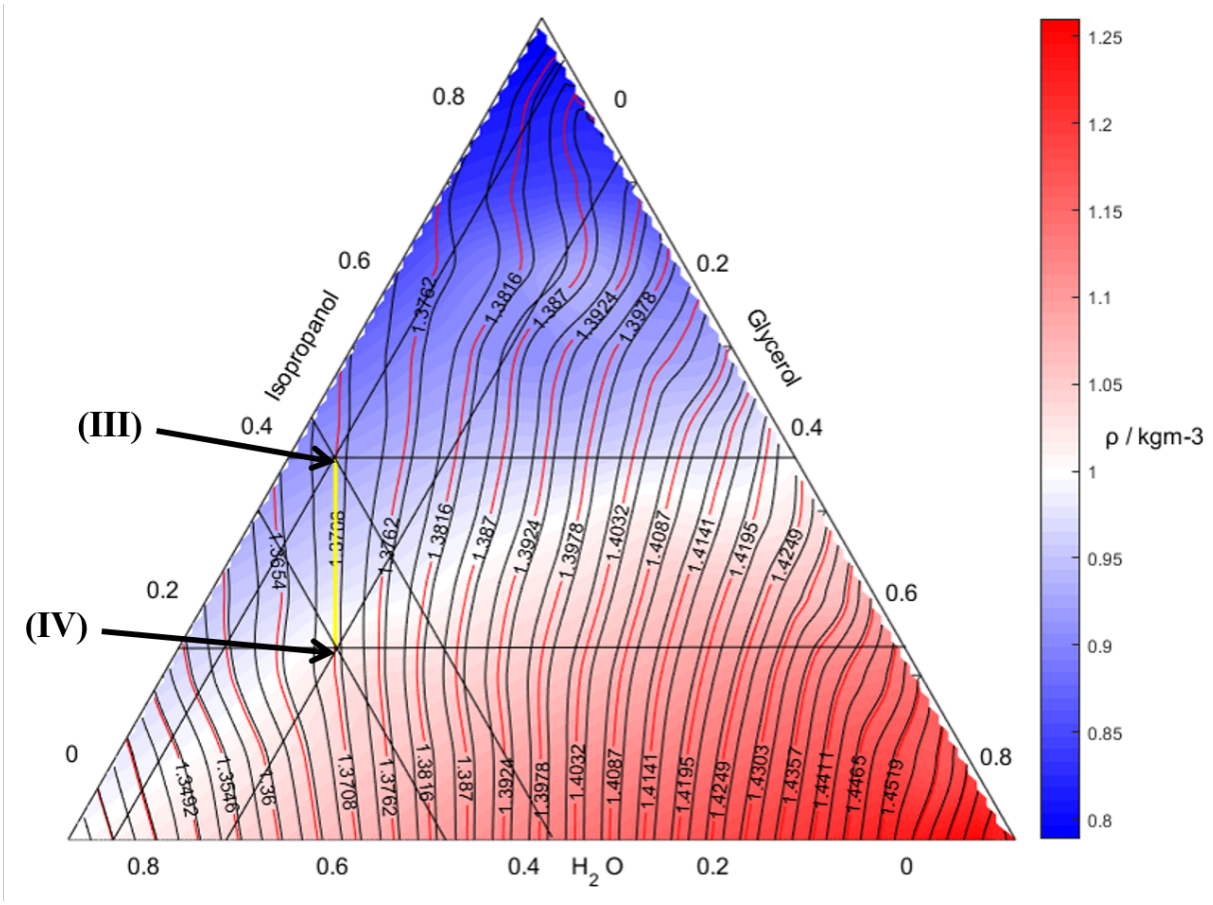

Figure 3.3: Contours of constant RI in a superposition of the density (colormap) for the ternary system with $H_2O - Glycerol - Isopropanol$. Reprint from [22].

It can be observed that mixtures points (III) and (IV) shown in Figure 3.3 lie on a straight line connecting the two points on the ternary diagram. Along this line, a density difference of 8.6% can be realized. The corresponding mass fractions for two solutions and their properties at $n_D = 1.3405$ are shown in Table 3.2.

Table 3.2: Nominal mass fractions and properties of the solution pair with a 8.6% density difference.

Solutions	***H_2O***	***Glycerol***	***Isopropanol***	$\boldsymbol{\rho}$ / $kg \cdot m^{-3}$	$\boldsymbol{\nu}$ / $m^2 s^{-1}$	$\boldsymbol{n_D}$
III (light)	48.20%	5.20%	46.60%	924	4.53×10^{-6}	1.3708
IV (heavy)	60.00%	16.50%	23.50%	1011	4.42×10^{-6}	1.3708

3.3 Proof of Principle

A small-scale experimental setup was conducted as a preliminary test using the 8.6% density difference solutions pair. Only qualitative measurements were performed with the miniDESTROJER facility for the proof-of-principle reported here. The liquid is injected vertically into the tank through the inlet nozzle at a constant nominal inlet velocity of 10.58 m/s. This corresponds to a jet Reynolds number of Re = 5,300. A high-speed PIV system is used to measure the flow field in the vertical mid-plane of the jet. Overall three experiments have been conducted:

(a) A reference case consisting of a non buoyant jet injected in a uniform environment, obtained by injecting solution III into solution III (no differences in density and RI).

(b) A stratified case with the lighter liquid (solution III) being injected into the heavier liquid (solution IV) at 8.6% density difference with RIM.

(c) A stratified case without RIM and a density difference of 8% (here both solutions were slightly altered with a refractive index of $n_D = 1.3712$ for solution III and $n_D = 1.3538$ for solution IV).

Figure 3.4 shows raw images from PIV recordings for the three cases. The jet is injected from the bottom and progresses to the top. In the image (c) of Figure 3.4, where no RIM was applied, particle images are strongly deflected by the mixing interface, especially in the upper part of the image where mixing is more pronounced and therefore strong variation of RI are present in the flow. This effect is not visible in Figure 3.4(b) where the RI is matched, neither in the reference experiment (a), where identical substances are present (and therefore no changes in RI are present in the flow). It is evident that the light traveling through and scattering back from the mixing region of the horizontally established density stratification without RIM is heavily deflected. The resulting PIV images are blurred and cannot be used to obtain velocity measurements.

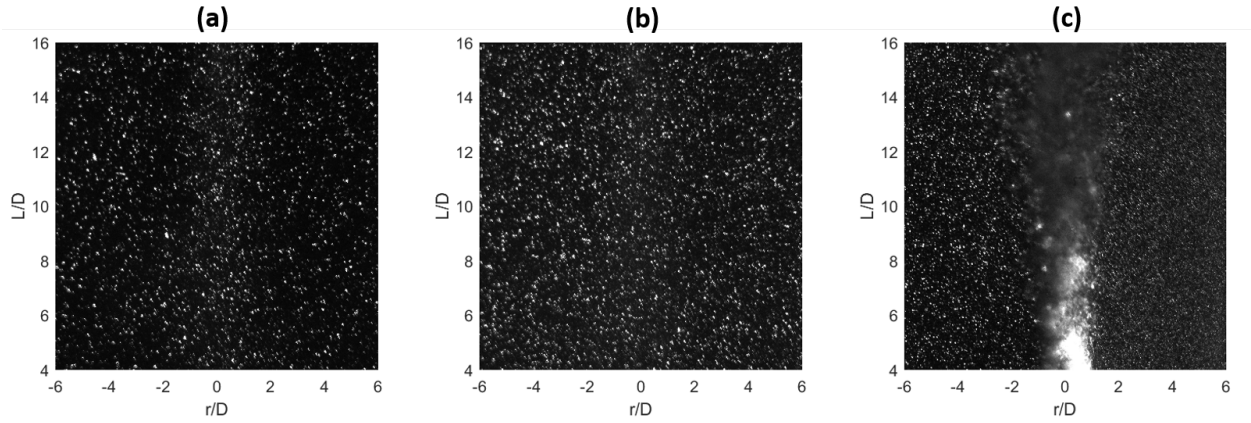

Figure 3.4: Raw PIV images for the three test cases. (a) Reference case of the uniform case with solution III, (b) stratified case with the lighter liquid (solution III) being injected to the heavier liquid (solution IV) at 8.6% density difference with RIM, and (c) stratified case without RIM and a density difference of 8% (here both solutions were slightly altered with a refractive index of $n_D = 1.3712$ for solution III and $n_D = 1.3538$ for solution IV. Reprint from [22].

.

CHAPTER IV

Turbulent Jet in Uniform Environments

Utilizing both the DESTROJER and miniDESTROJER facilities, an experimental study on turbulent round free jets in uniform environments was carried out. The results of the study are presented in this chapter, including flow turbulent statistics as well as the temporal and spatial analysis of the jet mixing behavior. The analyses of the high-resolution experimental database established within this dissertation work are compare with the findings published in the open literature. The jet flow-field coordinate system used throughout this chapter is defined according to Figure 4.1.

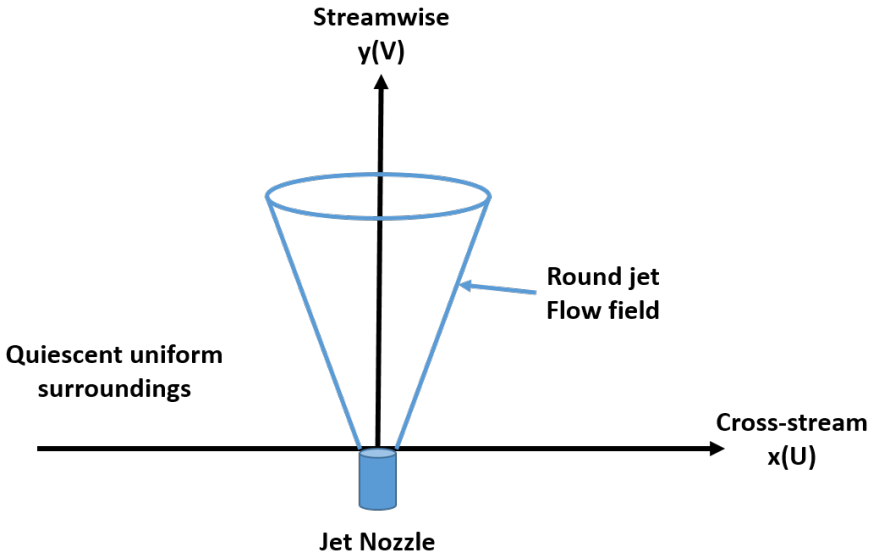

Figure 4.1: Sketch of jet flow in uniform environments and definition of the coordinate system employed for the data analysis.

4.1 Measurement Campaign for Uniform Environment

4.1.1 Uniform jet in the DESTROJER facility using water as working fluid

To create a uniform environment at room temperature and standard pressure, the one-cubic-meter tank of the DESTROJER facility is filled with water. The working fluid is seeded with 10 μm glass hollow sphere particles having a density of 1.10 ± 0.05 grams/cc, and a high-speed PIV system is implemented to visualize and quantify the velocity field. The motor-controlled piston speed is set so that well-defined nominal jet Reynolds numbers in the range between 5,000 to 22,500 can be obtained for this experimental campaign. The experimental test matrix is shown in Table 4.1 including the nominal jet velocities U_0, the water temperature T in the tank and the corresponding Reynolds number (Re).

Table 4.1: Uniform jet inlet velocity and water temperature of the uniform experiments conducted in the DESTROJER facility.

Experimental Cases	$\boldsymbol{U_0}$	$\boldsymbol{\rho}$	$\boldsymbol{T}$	***Re***
$--$	m/s	kg/m^3	$^\circ C$	$--$
T5k	0.38 ± 0.02	998.5 ± 10.0	19.21 ± 0.20	5,000 ± 250
T10k	0.79 ± 0.02	998.5 ± 10.0	19.14 ± 0.20	10,000 ± 250
T15k	1.19 ± 0.02	998.5 ± 10.0	19.21 ± 0.20	15,000 ± 250
T20k	1.60 ± 0.02	998.5 ± 10.0	19.21 ± 0.20	20,000 ± 250
T22k	1.87 ± 0.02	998.6 ± 10.0	18.46 ± 0.20	22,500 ± 250

The high-speed camera is equipped with a Kenko Tokina AT-X M100 PRO D Macro lens (100mm f/2.8) combined with a Nikon TC-201 teleconverter to double the focal length and perform high-spatially resolved recordings for the near-field region of the jet (from 1 to 5 jet-diameter downstream of the jet inlet). The small target shown in Figure 2.3(a) was used for PIV image calibration. Each measurement consists of a total of 8,048 recordings taken in the near-field region of the jet, with acquisition frequencies ranging from 2,000Hz to 10,000Hz depending on the Re number, so that it can be ensured sufficient particle displacement

across consecutive frames. The resulting spatial resolution for the velocity field is equal to $209 \times 209\ \mu m^2$.

For the intermediate jet region (around 10 to 20 jet-diameter downstream of the jet inlet) and for the self-similar region(around 25 to 50 jet-diameter downstream of the jet inlet), a Nikon Nikkor AF 50mm f/1.8 lens alone is used for recording particle images at relatively lower frequencies, ranging from 125 to 800 Hz. The calibration target used for the self-similar region is shown in Figure 2.3(b). About 50,000 images are taken for the measurements in the self-similar region, so that good turbulent statistics are achieved, and the corresponding spatial resolution is $684 \times 684\ \mu m^2$. In the intermediate field of the jet, 20,000 images are recorded and a spatial resolution of $912 \times 912\ \mu m^2$ is achieved. To illustrate and summarize the imaging parameters setup, the experiment Case T20k corresponding to Re = 20,000 is chosen. The PIV imaging parameters are summarized in Table 4.2 for the various regions of interests in the jet flow.

Table 4.2: Detailed imaging parameters for PIV measurements for Experiment Case T20k.

Experimental Case	**T20k (Re = 20,000)**			
Region of Interest	**Near-field for $1 \leq y/D \leq 5$**	**Intermediate field for $10 \leq y/D \leq 20$**	**Self-similar for $25 \leq y/D \leq 36$**	**Self-similar for $37 \leq y/D \leq 50$**
Acquisition Rate	10,000 Hz	810 Hz	460 Hz	260 Hz
Images Recorded	8,048	22,477	47,776	47,975
Interrogation Window Size	64 × 64 (50% overlap) 48 × 48 (75% overlap)	64 × 64 (50% overlap) 32 × 32 (75% overlap)		
Spatial Resolution	209 × 209 μm^2	912 × 912 μm^2	684 × 684 μm^2	684 × 684 μm^2

4.1.2 Uniform jet in the miniDESTROJER facility using aqueous solutions as working fluid

The experimental test matrix performed in the miniDESTROJER facility is summarized in Table 4.3, including the nominal jet velocities U_0, the averaged fluid temperature T, and the corresponding Reynolds number (Re). The working fluids used in the experimental

matrix are the RI-matched solutions mentioned in Chapter III, the corresponding solution # can be found in Table 3.1 & 3.2.

Table 4.3: Uniform jet inlet velocity and fluid temperature of the uniform experiments conducted in the miniDESTROJER facility.

Experimental Cases	U_0	***Solution #***	ρ	T	***Re***
$--$	m/s	kg/m^3	$^\circ C$	$--$	
D029	5.990 ± 0.004	I	1012.0 ± 10.1	20.4 ± 0.1	10,000 ± 7
D030	2.460 ± 0.002	I	1012.0 ± 10.1	20.4 ± 0.1	4,000 ± 2
D031	5.530 ± 0.004	II	1044.0 ± 10.4	20.0 ± 0.1	10,000 ± 7
D032	2.300 ± 0.002	II	1044.0 ± 10.4	20.0 ± 0.1	4,000 ± 2
D045	9.060 ± 0.006	IV	1011.0 ± 10.1	19.2 ± 0.1	4,000 ± 3
D046	4.220 ± 0.003	IV	1011.0 ± 10.1	19.3 ± 0.1	2,000 ± 2
D049	9.060 ± 0.006	III	924.3 ± 9.2	18.4 ± 0.1	4,000 ± 3
D050	4.220 ± 0.003	III	924.3 ± 9.2	18.6 ± 0.1	2,000 ± 2

The measurements have been performed in the self-similar region of the jet (from 45 to 85 jet-diameter downstream of the jet inlet). The PIV measurement system used for this experimental campaign was equipped with a Nikon Nikkor AF 50 mm f/1.8 lens, and a recording frequency of 100 Hz was used. Overall 4,536 images were taken for each case to achieve acceptable statistics of the turbulence quantities, with a spatial resolution of 818 × 818 μm^2. The uniform jet experimental matrix also serves as a reference when comparing to the flow field of buoyant jets in non-uniform environments, which will be discussed in Chapter V.

4.2 Mean Velocity Profiles in the Near-field Region

The jet evolution in the near-field region for Experiment Case T22k (Table 4.1) is reported in Figure 4.2. Here the streamwise mean velocity profiles (left), Turbulent Kinetic Energy (TKE) (middle), and the shear stresses (right) at the downstream locations corresponding to y/D = 1, 2, 3, 4, and 5 are shown. Note that the values of Turbulent Kinetic Energy (TKE)

are approximated because of the 2D nature of the measurements and the application of Equation 2.9. The uncertainties for the mean velocity profiles are presented by uncertainty bars corresponding to a combined uncertainty in the 95% confidence interval, while the two-sided uncertainty intervals are represented by the shaded green area between the upper and lower bounds of the measured TKE and shear stresses profiles, which are plotted in blue dots.

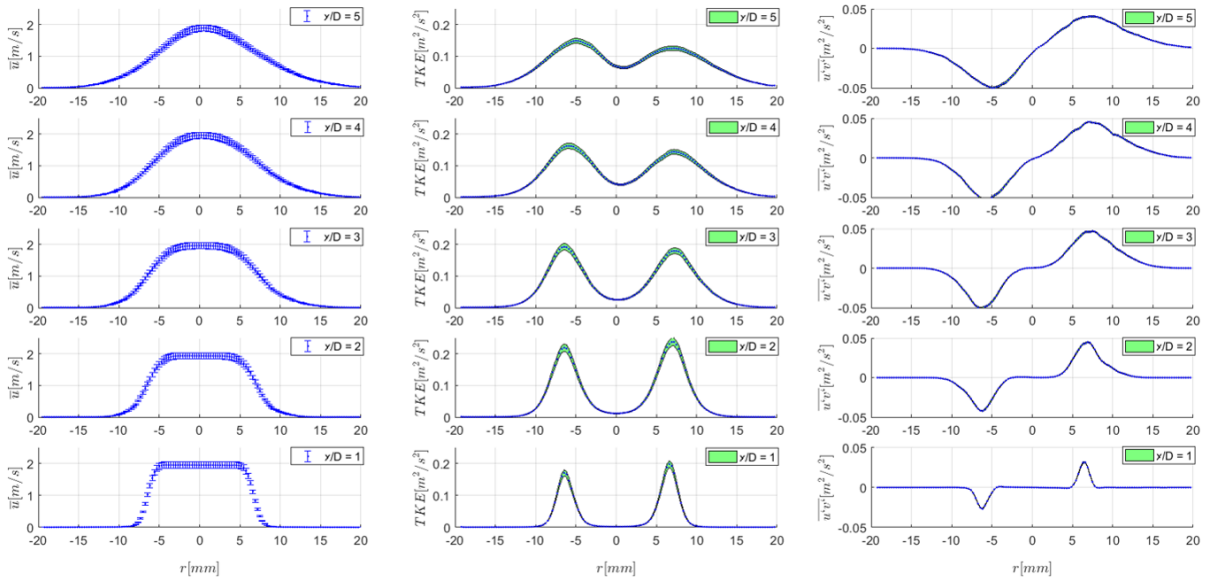

Figure 4.2: Streamwise mean velocity profiles (left), turbulent kinetic energy (middle) and shear stress (right) at different axial distances $y/D = 1, 2, 3, 4, 5$ (from bottom to top) for Experiment Case T22k.

At one jet-diameter downstream of the jet inlet, a top-hat velocity profile can be observed as predicted by Hussein et al. [24] for the potential core of the jet, and turbulence mixing occurs in the shear layer regions, indicated by the maximum turbulent kinetic energy and shear stress at the jet boundary layers ($r = \pm\ 6.35\ mm$). As the downstream distance from the jet inlet increases, the jet velocity develops, expanding from a top-hat shape to form a Gaussian profile with a growth of the shear layer towards the center of the jet. As shown in Figure 4.2, beginning from two jet-diameters downstream of the jet inlet, the turbulent intensity at the centerline increases, and the peaks of the shear stresses increase further

downstream as well. For $2 < y/D < 3$, there is a transition of TKE in which the amplitude first increases along the flow direction and then decays further downstream.

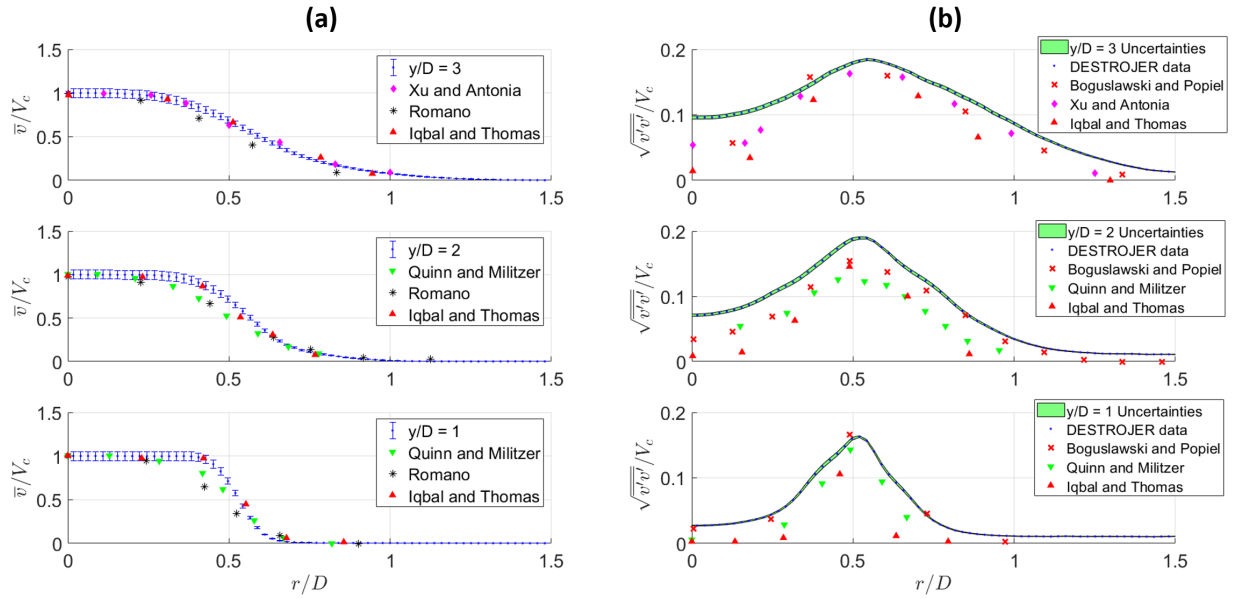

Figure 4.3: Comparisons with the published literature results of (a) normalized streamwise mean velocity profiles, and (b) normalized turbulence intensity of the streamwise velocity at y/D = 1, 2, and 3 for Experiment Case T22k.

The normalized streamwise mean velocity $\overline{v}/V_c$ and the normalized standard deviation of the streamwise velocity $\sqrt{\overline{v'v'}}/V_c$ for Experiment Case T22k are shown in Figure 4.3 together with the experimental data obtained by Xu and Antonia [9], Iqbal and Thomas [10], Quinn and Militzer [7], Romano [99], and Boguslawski and Popiel [100]. Considering the experimental and statistical uncertainties, the streamwise mean velocity profiles, as well as the axial velocity fluctuations are in remarkable agreement with the results found in the open literature, therefore 'validating' the results obtained with the DESTROJER facility.

4.3 Turbulence Statistics in the Jet Self-similar Region

Figure 4.4 shows the jet centerline mean streamwise velocity decay in the self-similar region for the experimental data obtained at the DESTROJER facility using the inlet contraction nozzle, and obtained at the miniDESTROJER using the inlet pipe nozzle. Compared

to the published experimental results with the contraction nozzle studies by Xu and Antonia [9], Wygnanski and Fiedler [23], Panchapakesan and Lumley [101] and Quinn [102], it can be noticed that the DESTROJER data (blue squares in Figure 4.4) are in good agreement with the data published in the literature. However, the pipe nozzle cases measured at the miniDESTROJER facility show a larger decay rate (smaller slope in the V_0/V_{CL} shown in Figure 4.4). According to Equation 1.1 the decay of the centerline velocity for a uniform jet can be expressed as:

$$\frac{V_0}{V_c(x)} = \frac{1}{K_v}\left(\frac{y}{D} - \frac{y_{0,v}}{D}\right) \tag{1.1}$$

Table 4.4 presents the comparison for the decay parameters K_v as well as for the virtual jet origin $y_{0,v}/D$ obtained from a linear curve fitting of the experimental data summarized in Fig. 4.4. The results obtained for the DESTROJER experiments fall within the range of values measured by other researchers using contraction nozzles. The obtained results are also consistent with the observation that using an inlet pipe geometry yields an overall larger value of K_v. The data for the virtual jet origin $y_{0,v}/D$ seems instead to be scattered across the investigated cases.

In the self-similar region of turbulent jet flows the normalized mean velocity profiles and turbulence statistics do not change, regardless of the particular downstream location. To illustrate this, the results obtained for Case T22k for the streamwise mean velocity normalized by the centerline velocity are in Figure 4.5(a) together with uncertainty bars against the non-dimensional coordinates $x/(y/D - y_{0,v}/D)$ for downstream locations $25 \leq y/D \leq 50$. The normalized velocity profiles all collapse to the same Gaussian-shape curve, indicating that from 25 jet-diameters downstream of the jet inlet the jet flow has entered the self-similar region and has become self-preserving. Using the same non-dimensional coordinates, the normal streamwise and radial Reynolds stresses $\overline{v'v'}$ and $\overline{u'u'}$, as well as the shear stress $\overline{u'v'}$, are also plotted at the same downstream locations in Figure 4.5(b). The normalized centerline values for the mean normal streamwise and radial Reynolds stresses measured by Hussein et al. [24] using Laser Doppler Velocimetry (LDV) were equal to 0.076

Table 4.4: Centerline velocity decay parameters compared to other turbulent round jets in uniform environments found in the literature.

Authors/Cases	***Nozzle***	***Technique***	y/D	K_v	$y_{0,v}/D$
Wygnanski and Fiedler (1969) [23]	Contraction	Hot-wire probe	< 50	5.70	3.0
			> 50	5.00	7.0
Panchapakesan and Lumley (1993) [101]	Contraction	Hot-wire probe	30 - 160	6.06	–
Hussein et al. (1994) [24]	Contraction	Hot-wire probe	30 -120	5.80	4.0
Hussein et al. (1994) [24]	Contraction	LDV	30 -120	5.90	2.7
Weisgraber and Liepmann (1998) [103]	Contraction	LDV	17 - 27	6.70	–
Ferdman et al. (2000) [104]	Pipe	Hot-wire probe	≥ 15	6.70	2.5
Mi et al. (2001) [8]	Contraction	Cold wire	0 - 64	4.48	3.5
Xu and Antonia (2002) [9]	Contraction	Hot-wire probe	20 - 75	5.60	3.7
Xu and Antonia (2002) [9]	Pipe	Hot-wire probe	20 - 75	6.50	2.6
Kwon and Seo (2005) [105]	Contraction	PIV	15 - 75	5.50	–
Quinn (2006) [102]	Contraction	Hot-wire probe	18 - 55	6.10	3.65
Fellouah et al. (2009) [106]	Contraction	Hot-wire probe	15 - 29	5.59	2.5
Vouros and Panidis (2013) [25]	Pipe	LDV	0 - 60	5.70	2.65
Sadeghi et al. (2015) [29]	Contraction	Hot-wire probe	10 - 20	6.60	-1.69
T5k	Contraction	PIV	25 - 50	5.45 $\pm$ 0.08	2.88 $\pm$ 0.30
T10k	Contraction	PIV	25 - 50	5.95 $\pm$ 0.09	3.10 $\pm$ 0.36
T15k	Contraction	PIV	25 - 50	5.68 $\pm$ 0.08	2.84 $\pm$ 0.28
T20k	Contraction	PIV	25 - 50	5.76 $\pm$ 0.10	3.67 $\pm$ 0.34
T22k	Contraction	PIV	25 - 50	5.81 $\pm$ 0.07	2.43 $\pm$ 0.26
D029	Pipe	PIV	50 - 80	6.90 $\pm$ 0.03	0.52 $\pm$ 0.29
D030	Pipe	PIV	50 - 80	6.67 $\pm$ 0.03	0.87 $\pm$ 0.23
D031	Pipe	PIV	50 - 80	6.57 $\pm$ 0.04	3.03 $\pm$ 0.59
D032	Pipe	PIV	50 - 80	6.80 $\pm$ 0.03	-0.84 $\pm$ 0.15
D045	Pipe	PIV	50 - 80	6.94 $\pm$ 0.05	-0.17 $\pm$ 0.18
D049	Pipe	PIV	50 - 80	6.85 $\pm$ 0.03	0.40 $\pm$ 0.25

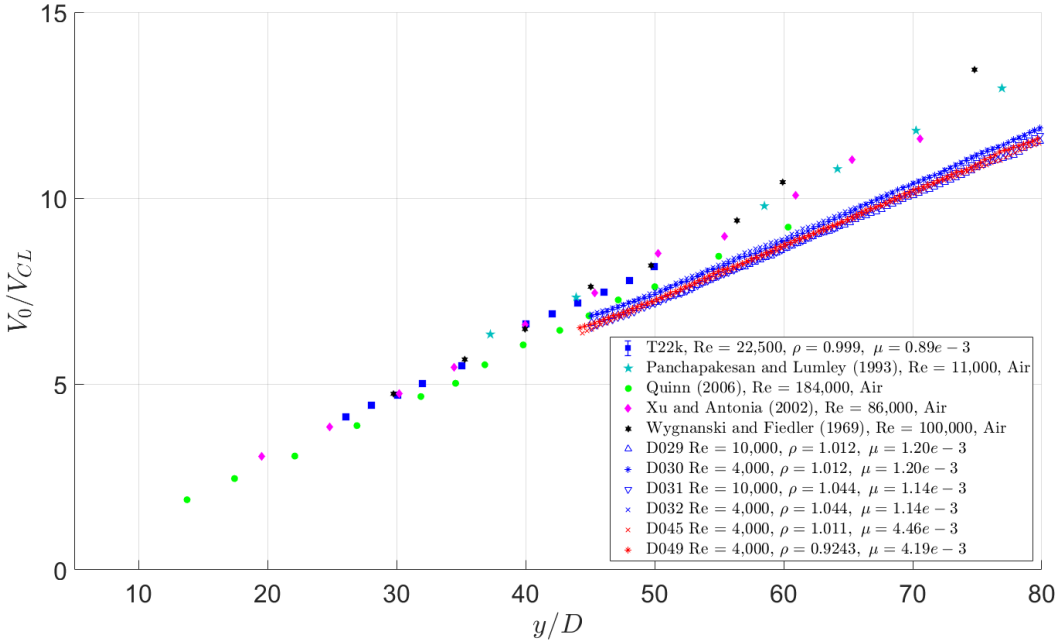

Figure 4.4: Axial decay of the centerline mean streamwise velocity for different cases. Results of the previously published literature are superposed for comparison.

and 0.047 respectively, and 0 for the mean shear stress, which matches very well with the results obtained in this dissertation work.

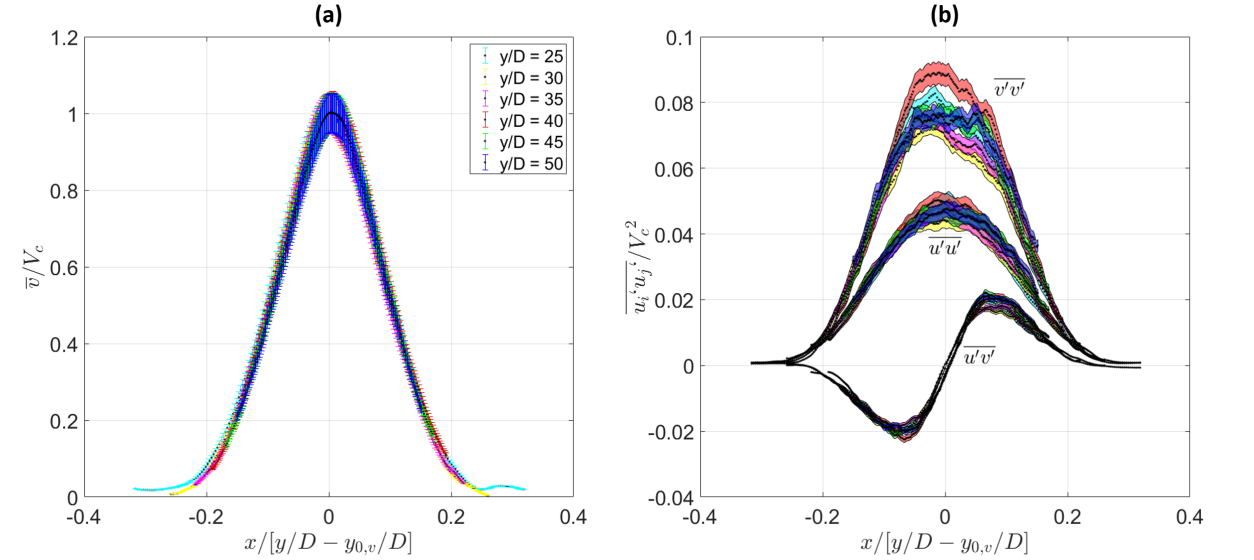

Figure 4.5: Self-similarity behavior of Experiment Case T22k in the self-similar region: (a) scaled streamwise mean velocity profiles collapsing and (b) Reynolds normal and shear stresses collapsing at several downstream locations y/D = 25, 30, 35, 40, 45, and 50.

4.4 Entrainment: Jet Half-width in the Self-similar Region

Entrainment in a turbulent jet flow describes the engulfment of the ambient fluid surrounding the jet flow. This phenomenon contributes to the conservation of the jet momentum flow-rate but leads to an increase in the jet mass flow rate with increasing distance from the jet nozzle. Figure 4.6 shows the normalized jet half-width $r_{1/2}/D$ versus the jet downstream distance y/D for the flow cases measured using both the DESTROJER and the miniDESTROJER facilities. It can be observed that the rates at which $r_{1/2}/D$ increases with y/D are quite similar for all cases, and are in good agreement with the data published by Fellouah and Pollard [11], Mi et al. [8], Xu and Antonia [9], and Quinn and Militzer [7].

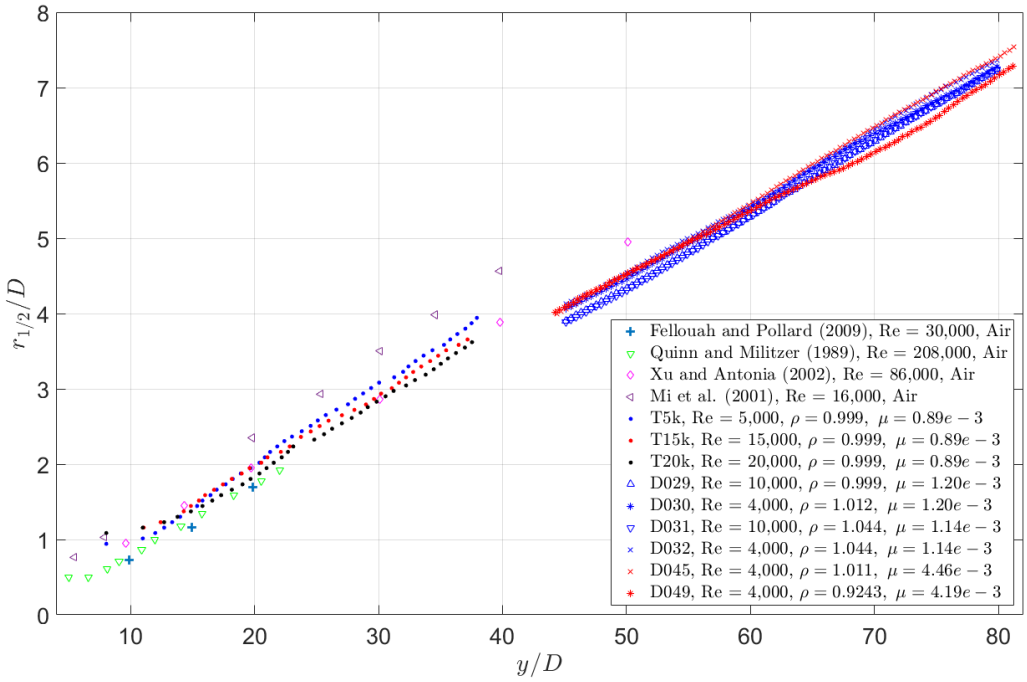

Figure 4.6: Axial evolution of the jet half-width for different Reynolds numbers. Results of data published in the literature by other authors are superposed for comparison.

Table 4.5: Jet half-width spread rate and corresponding constants compared to other turbulent round jets in uniform environments found in the literature.

Authors/Cases	***Nozzle***	***Technique***	K_r	$y_{0,r}/D$
Panchapakesan and Lumley (1993) [101]	Contraction	Hot-wire probe	0.096	–
Hussein et al. (1994) [24]	Contraction	Hot-wire probe	0.094	–
Hussein et al. (1994) [24]	Contraction	LDV	0.102	–
Xu and Antonia (2002) [9]	Contraction	Hot-wire probe	0.095	–
Xu and Antonia (2002) [9]	Pipe	Hot-wire probe	0.086	–
Kwon and Seo (2005) [105]	Contraction	PIV	0.103	–
Fellouah and Pollard (2009) [11]	Contraction	Hot-wire probe	0.097	0.259
Vouros and Panidis (2013) [25]	Pipe	LDV	0.078	–
T5k	Contraction	PIV	0.1060 ± 0.0007	0.132 ± 0.042
T10k	Contraction	PIV	0.0987 ± 0.0006	0.145 ± 0.027
T15k	Contraction	PIV	0.0972 ± 0.0003	0.126 ± 0.037
T20k	Contraction	PIV	0.0995 ± 0.0004	0.138 ± 0.043
T22k	Contraction	PIV	0.0987 ± 0.0006	0.124 ± 0.034
D029	Pipe	PIV	0.0972 ± 0.0002	0.518 ± 0.015
D030	Pipe	PIV	0.0941 ± 0.0004	0.223 ± 0.027
D031	Pipe	PIV	0.0985 ± 0.0004	0.603 ± 0.023
D032	Pipe	PIV	0.0953 ± 0.0005	0.233 ± 0.034
D045	Pipe	PIV	0.0974 ± 0.0004	0.363 ± 0.024
D049	Pipe	PIV	0.0951 ± 0.0008	0.255 ± 0.051

According to Equation 1.2, the spread rate of the jet half-width is linearly proportional to the downstream location beyond the jet potential core region ($y/D \geq 15$):

$$\frac{r_{1/2}}{D} = K_r \left(\frac{y}{D} - \frac{y_{0,r}}{D} \right) \tag{1.2}$$

Therefore, a linear fitting was performed for the results presented in Figure 4.6. The obtained results for K_r and $y_{o,r}/D$ are compared to the date reported in the literature in Table 4.5. Regardless of the nozzle type, it can be observed that the slopes (K_r) obtained for the experiments carried out with both the DESTROJER and the miniDESTROJER facilities are in good agreement with those measured by Fellouah and Pollard [11], Hussein et al. [24], Xu and Antonia [9], Panchapakesan and Lumley [101], and Kwon and Seo [105]. Large discrepancies are observed for $y_{o,r}/D$ instead. This might be due to measurement uncertainties or to the fact that this parameter is more sensitive to the particular inlet nozzle used in the experiments.

4.5 Centerline Streamwise Velocity Skewness and Flatness Factor in the Near-field and Self-similar Regions

To determine the distribution of a stationary signal in space, probability density function (PDF) is often used to describe the variation in signal amplitude. In the computational study of fluid dynamics, PDF could provide valuable information regarding the distribution of a specific quantity amplitude at a certain point. But for the experimental work, the histogram is more suitable to show the distribution of discrete data, like the velocity measurements from PIV. Mi and Nathan [107] mentioned that the distribution of the jet streamwise velocities right after the jet nozzle is almost Gaussian, independent of the inlet conditions of the jet. Using the near-field data from the uniform jet experimental Case T15k with Re = 15,000, Figure 4.7 shows the histograms of the streamwise velocity along the centerline at different downstream locations (from bottom to top: y/D = 1, 3, and 5). It can be noticed

that the streamwise velocity signals at the center of the jet does have an almost Gaussian distribution at y/D = 1 but quickly get skewed at y/D = 3. This shows that the centerline streamwise velocity distribution will be potentially affected by the oscillation of the central unmixed core and the jet's entrainment as the downstream distance increases. Going farther downstream, according to Mi and Nathan [107], the statistical distribution of the centerline streamwise velocity is expected to gradually return to a near Gaussian distribution, because of the mixing between the jet flow and the surrounding ambient fluid, but never truly become Gaussian because of the continuous entrainment of unmixed fresh ambient fluid.

To exam and quantify the departure of the streamwise velocity signal distribution from a Gaussian profile, the skewness and flatness factors (SF and FF) are introduced and estimated as follows:

$$\mathrm{SF} = \frac{\frac{1}{N}\sum_{i=1}^{N}\left(v_i - \bar{v}\right)^3}{\left[\frac{1}{N-1}\sum_{i=1}^{N}\left(v_i - \bar{v}\right)^2\right]^{3/2}} \tag{4.1a}$$

$$\mathrm{FF} = \frac{\frac{1}{N}\sum_{i=1}^{N}\left(v_i - \bar{v}\right)^4}{\left[\frac{1}{N}\sum_{i=1}^{N}\left(v_i - \bar{v}\right)^2\right]^{2}} \tag{4.1b}$$

where N is the overall number of the recorded samples of the instantaneous field and v_i denotes the instantaneous streamwise component of the velocity vector and $\overline{v}$ is the averaged streamwise velocity. Along the centerline, SF and FF are computed for the uniform jet experimental Case T15k and reported in Figure 4.8. According to the probability theory and statistics analysis behind SF and FF, a Gaussian function corresponds to values of 0 and 3, respectively. The plot in Figure 4.8 is discontinuous due to the fact that the measurement spans over different regions of interest (near-field, intermediate field, and self-similar region respectively) and these were taken separately as explained in Chapter II. It can be observed that the values of SF and FF indicates a nearly Gaussian distribution in the near-field of the jet ($y/D \sim 1$) and starts to depart before a distance of 5D downstream the jet inlet, which agrees with the histogram plots shown in Figure 4.7. A local minimum can be seen in both

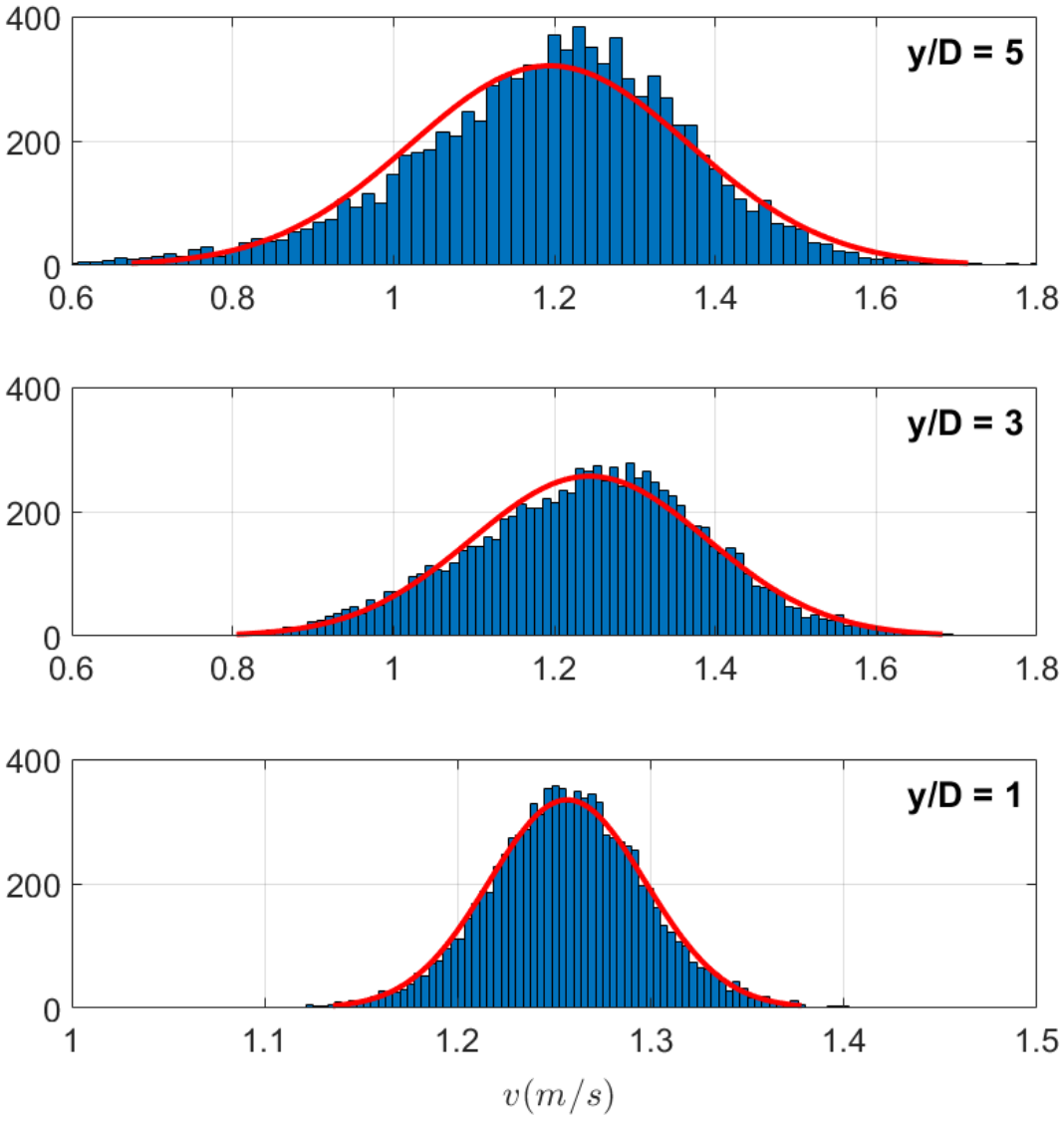

Figure 4.7: Axial evolution of the histogram of the measured streamwise velocities at the center of the jet in the near-field (from bottom to top: y/D = 1, 3, and 5) for Experimental Case T15k. The histogram is plotted in blue with the red curve denoting a Gaussian distribution.

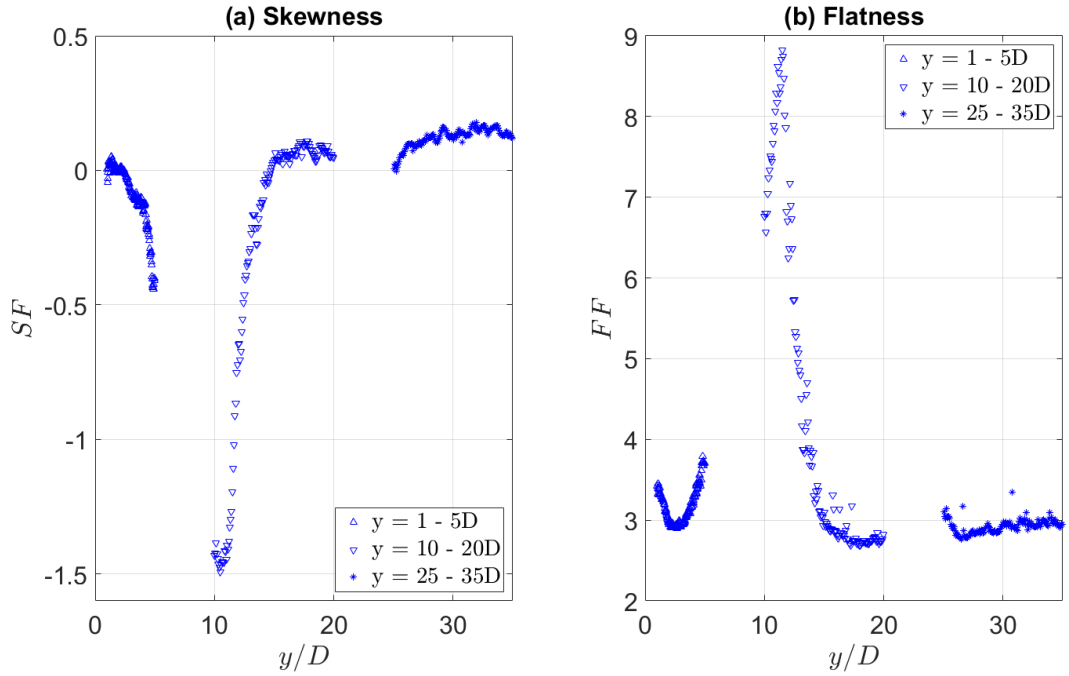

Figure 4.8: Axial evolution along the centerline of (a) skewness factor and (b) flatness factor for streamwise velocity in Experimental Case T15k.

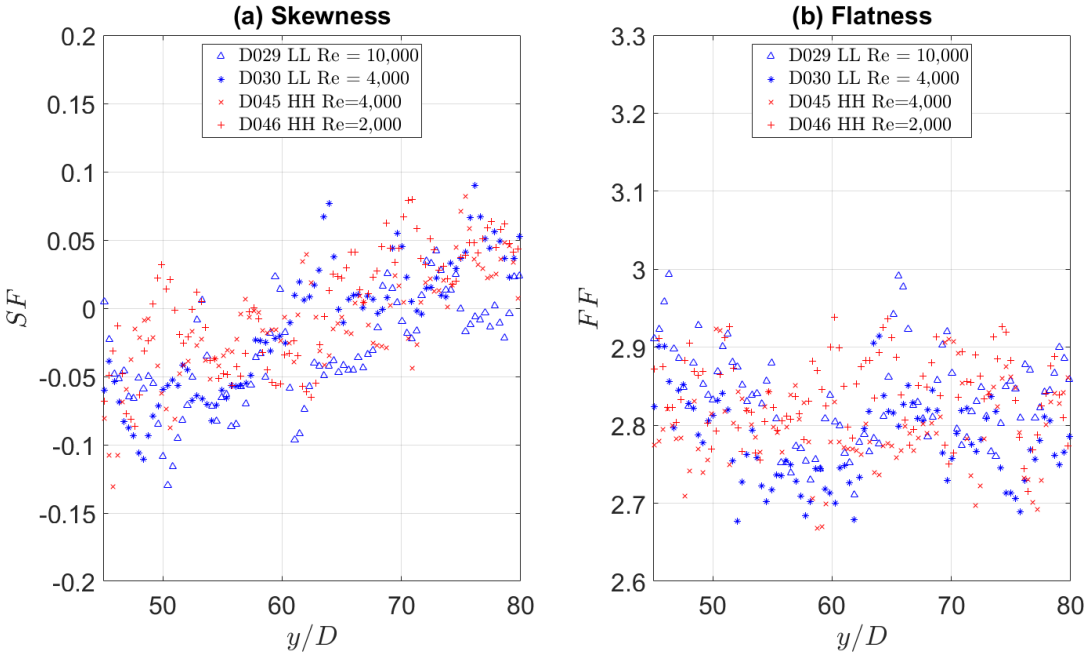

Figure 4.9: Axial evolution along the centerline of (a) skewness factor and (b) flatness factor for streamwise velocity with uniform experimental cases D029, D030, D045, and D046.

the SF and FF plots at $y/D \approx 10$. This means that this particular location is intermittently occupied by the high-velocity 'unmixed' jet fluid, the low-velocity 'unmixed' ambient fluid and the 'mixed' fluid within the shear layers, leading to highly skewed PDF of the streamwise velocity. As the downstream distance y increases, the SF and FF approach the asymptotic values corresponding to a Gaussian distribution (i.e. SF=0, FF =3). Similar observations can be drawn by analyzing the results for the uniform jet cases D029, D030, D045 and D046 measured at the miniDESTROJER facility in the self-similar region ($45 \leq y/D \leq 80$), reported in Figure 4.9.

4.6 Triple Velocity Correlation

The triple velocity correlations ($\overline{u_i' u_j' u_k'}$) represent fluxes of the Reynolds stresses, and their gradients appear as diffusion terms in the Reynolds stress transport equations. Given Equation 2.5, the streamwise velocity triple correlation $\overline{v'v'v'}$ can be calculated as:

$$\overline{v'v'v'} = \frac{1}{N-1}\sum_{i=1}^{N}(v_i - \overline{v})^3 \tag{4.2}$$

The triple correlation $\overline{v'u'v'}$ (or simpler as $\overline{u'v'^2}$) instead is computed as:

$$\overline{v'u'v'} = \overline{u'v'^2} = \frac{1}{N-1}\sum_{i=1}^{N}(u_i - \overline{u})(v_i - \overline{v})^2 \tag{4.3}$$

With the coordinate definitions (v for the axial velocity, and u for radial velocity) shown in Figure 4.1, Figure 4.10 and 4.11 show the radial profiles of the normalized streamwise velocity triple correlation $\overline{v'v'v'}/V_c^3$ as well as the streamwise transport of shear stresses $\overline{u'v'^2}/V_c^3$ for the uniform cases conducted in the miniDESTROJER facility at downstream locations y/D = 50, 60, 70 and 80, respectively. It can be noticed that all the cases with Re larger than 4,000 show similar magnitudes and trends on both figures, except for the uniform cases D046 and D050 with Re = 2,000. The lower Re cases have larger peak values when

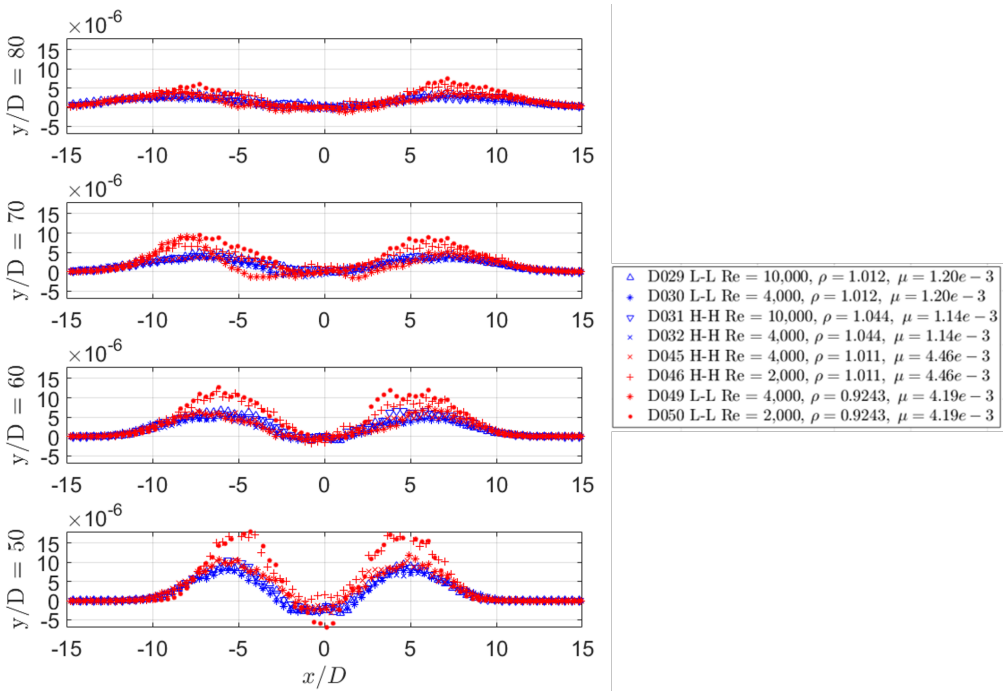

Figure 4.10: Radial profiles of the normalized streamwise velocity triple correlation $\overline{v'v'v'}/V_c^3$ for all the uniform cases conducted in the miniDESTROJER facility at downstream locations y/D = 50, 60, 70 and 80, respectively.

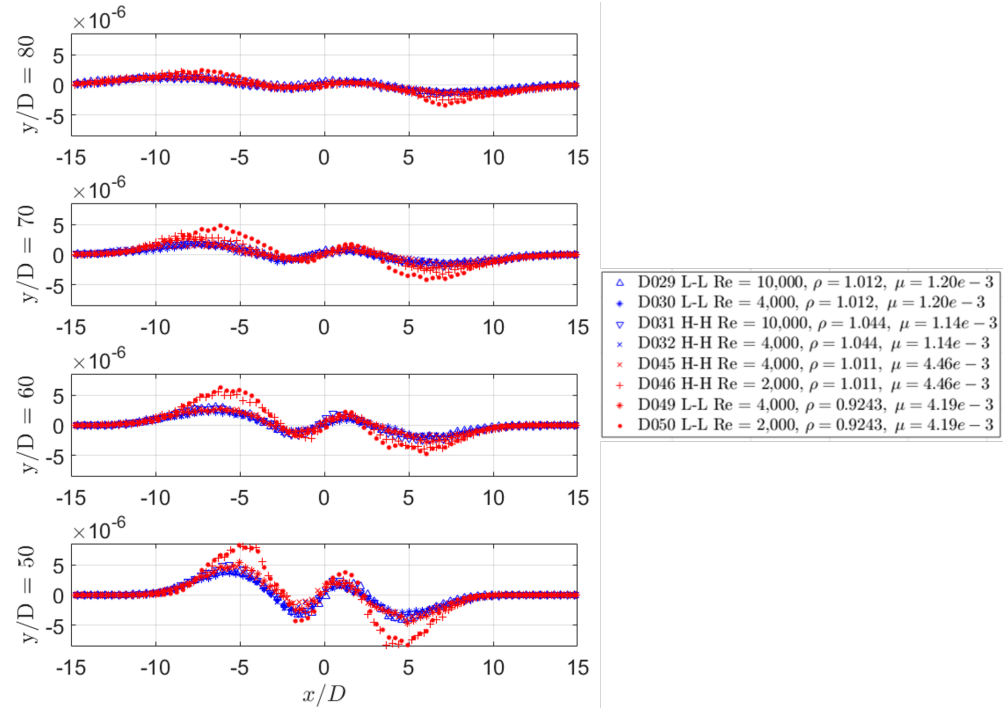

Figure 4.11: Radial profiles of the normalized streamwise transport of shear stresses $\overline{u'v'^2}/V_c^3$ for all the uniform cases conducted in the miniDESTROJER facility at downstream locations y/D = 50, 60, 70 and 80, respectively.

compared to the cases at higher Reynolds number, indicating a higher flux of the Reynolds normal stresses during the mixing process with the surroundings.

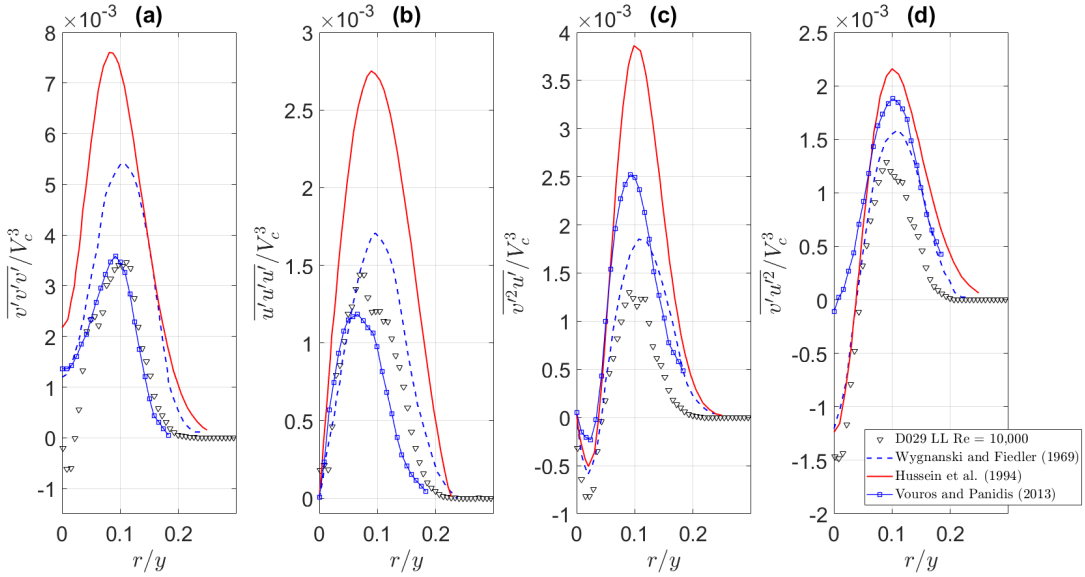

Figure 4.12: Radial profiles of the non-dimensional third-order velocity moments. Experimental data of Wygnanski and Fiedler (1969) [23], Hussein et al. (1994) [24], and Vouros and Panidis (2013) [25] are plotted in superposition for comparison.

Shown in Figure 4.12 are the radial profiles of the normalized triple velocity correlations at y/d = 60 normalized by the centerline velocity. The measured data are compared to the experimental data published by Wygnanski and Fiedler (1969) using hot-wire anemometry (Re = 100,000) [23], Hussein et al. (1994) using LDV (Re = 100,000) [24], and Vouros and Panidis (2013) using LDV (Re = 5,500) [25]. These third-order velocity moments of the axial and radial velocity component represent the transport of the shear and normal stresses due to the velocity fluctuations components in the axial and radial direction respectively. They all present low values on the centerline, and increase in the radial direction with a peak close to the center of the shear layer. In Figure 4.12(a), the measurements for the uniform case D029 has the lowest centerline value for the streamwise velocity triple correlation $\overline{v'v'v'}/V_c^3$ than the other compared cases. This indicates a strong backward transport of the streamwise normal stress. However, the locations of the peaks are similar for all the experiments. As for the radial velocity triple correlation $\overline{u'u'u'}/V_c^3$ in Figure 4.12(b), the D029 data, together

with the measurements done by Wygnanski and Fiedler [23], Hussein et al. [24], and Vouros and Panidis [25], presents close-to-zero values at the jet center due to the symmetry. The $\overline{u'u'u'}/V_c^3$ values increases then in the radial direction, with a peak close to the center of the jet shear layer. The $\overline{v'^2u'}/V_c^3$ term shown in Figure 4.12(c) starts from zero on the centerline due to symmetry, attains small negative values at the central area and increases to significantly larger positive values close to the center of the shear layer location, with similar peak locations for all cases as well. The $\overline{v'u'^2}/V_c^3$ term in Figure 4.12(d) has negative values around the jet central region, increases in the radial direction to a peak close to the centre of the shear layer and returns to zero values at a larger radial distance. This almost matches perfectly with the data presented Wygnanski and Fiedler [23] and Hussein et al. [24], but with a smaller peak magnitude.

4.7 Lumley Triangle

The Lumley triangle (Figure 4.13) introduced by Lumley and Newman [108] is a two-dimensional map of the second and third invariants of the normalized Reynolds stress anisotropy tensor b_{ij} and used to visualize the anisotropy of turbulence at any given point in a flow domain. The Lumley triangle is also used to analyze whether the computational results obtained with a turbulence model are realizable, meaning that the normal Reynolds stresses are always produced to be positive and the Shear Reynolds stresses satisfy the Schwartz inequality. The normalized anisotropy tensor b_{ij} is defined as:

$$b_{ij} = \frac{\overline{u_i'u_j'}}{2k} - \frac{\delta_{ij}}{3}, \text{ where } k = \frac{\overline{u_n'u_n'}}{2} \tag{4.4}$$

The diagonalization of b_{ij} provides three eigenvalues, i.e. λ_1, λ_2, and λ_3. The trace of the tensor b_{ij} (first invariant) is by definition equal to zero. Therefore b_{ij} can be fully characterized by the second and third invariants only, which are functions of the b_{ij} eigenvalues λ_i:

$$II = a_{ij}b_{ji}/2 = \lambda_1^2 + \lambda_1\lambda_2 + \lambda_2^2 \tag{4.5a}$$

$$III = a_{ij}b_{jk}b_{ki}/3 = -\lambda_1\lambda_2\left(\lambda_1 + \lambda_2\right) \tag{4.5b}$$

The anisotropic state of turbulence (i.e. how much the three normal Reynolds stresses differ from each other) in relation to the Lumley triangle is illustrated in Figure 4.13 and Figure 4.14. In the latter, the second and third invariant of b_{ij} are replaced using variables η, ξ, respectively:

$$\eta^2 = II/3 \tag{4.6a}$$

$$\xi^3 = III/2 \tag{4.6b}$$

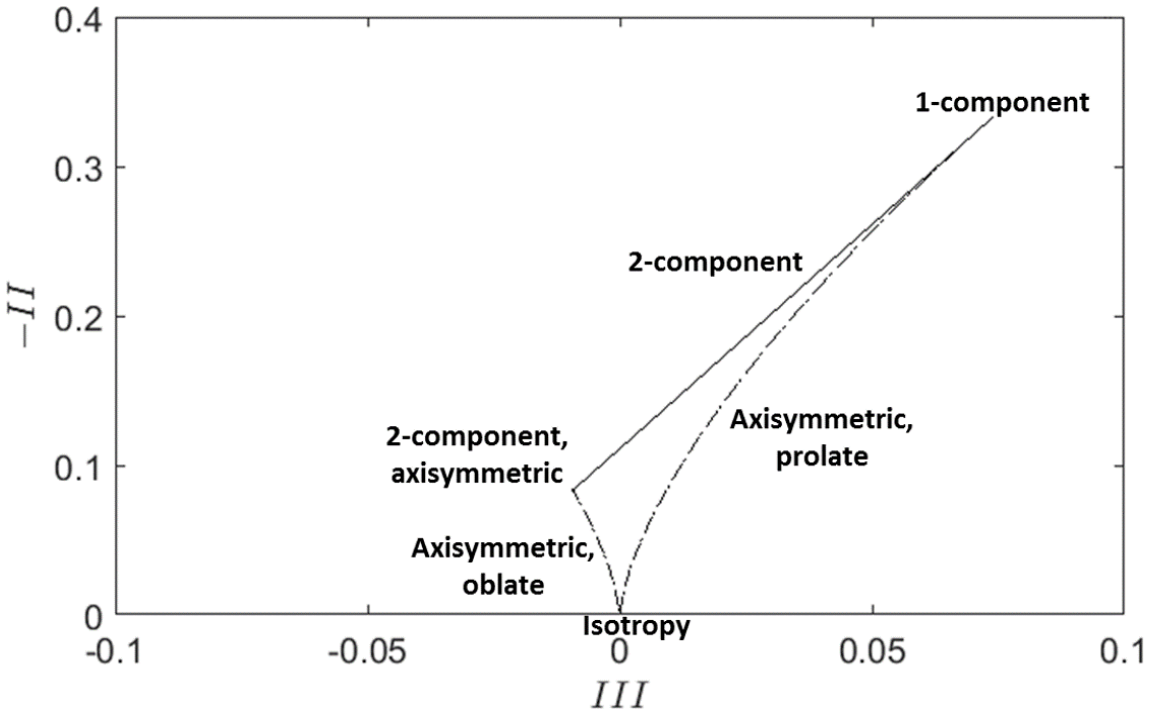

Figure 4.13: Demonstration of Lumley triangle with the second and third principal components of turbulent anisotropy with the limiting states for each boundary locations.

The mapping reported in Figure 4.14 stretches the lower left quadrant of the Lumley triangle,

providing a detailed view of the region near the isotropic origin (representing a turbulent state in which the normal Reynolds stresses are all equal to 2k/3). The Lumley triangle can be used to evaluate trajectories of return to isotropy (Choi and Lumley [109]).

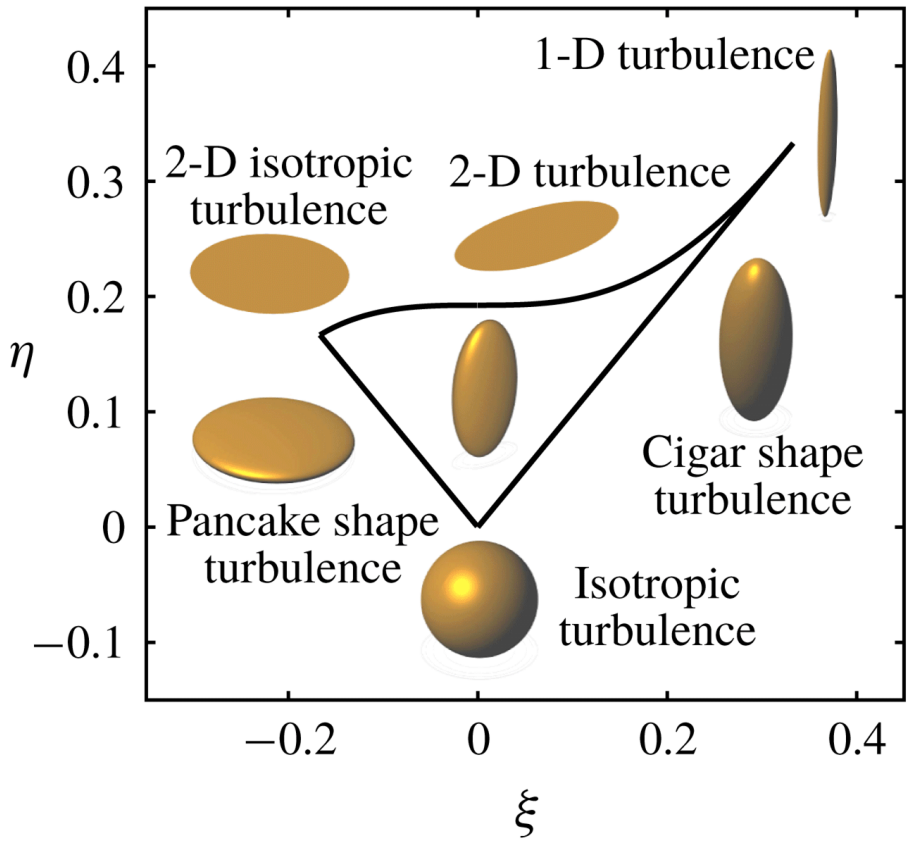

Figure 4.14: Demonstration of turbulence triangle showing limits of the invariants η and ξ with characteristic spheroids representing the shape of the turbulence. Reprinted from [26].

As discussed in Appendix E, verification experiments have been performed at both experimental facilities to ensure that the jet flow is axisymmetric with respect to the vertical axis. Because of azimuthal symmetry, when calculating the components of the anisotropic tensor along the jet centerline, it can be assumed that the normal stresses in the spanwise and radial direction are equal. Figure 4.15 shows the trajectory in the Lumley triangle plane of the b_{ij} state along the centerline of the jet for $1 \leq y/D \leq 50$ and for different Reynolds numbers ranging from 5,000 to 22,500, with the experimental details mentioned in Table 4.1. Regardless of the Reynolds number, all cases start from the upper left, indicating a pancake-

shape turbulence in the near-field. Then, moving along the flow-field toward the self-similar region, the turbulence state transitions into a oblate axisymmetric shape, maintaining the status until decaying to isotropy. Therefore, the phenomenology of the turbulent jet flow field along the centerline can be illustrated in Figure 4.16.

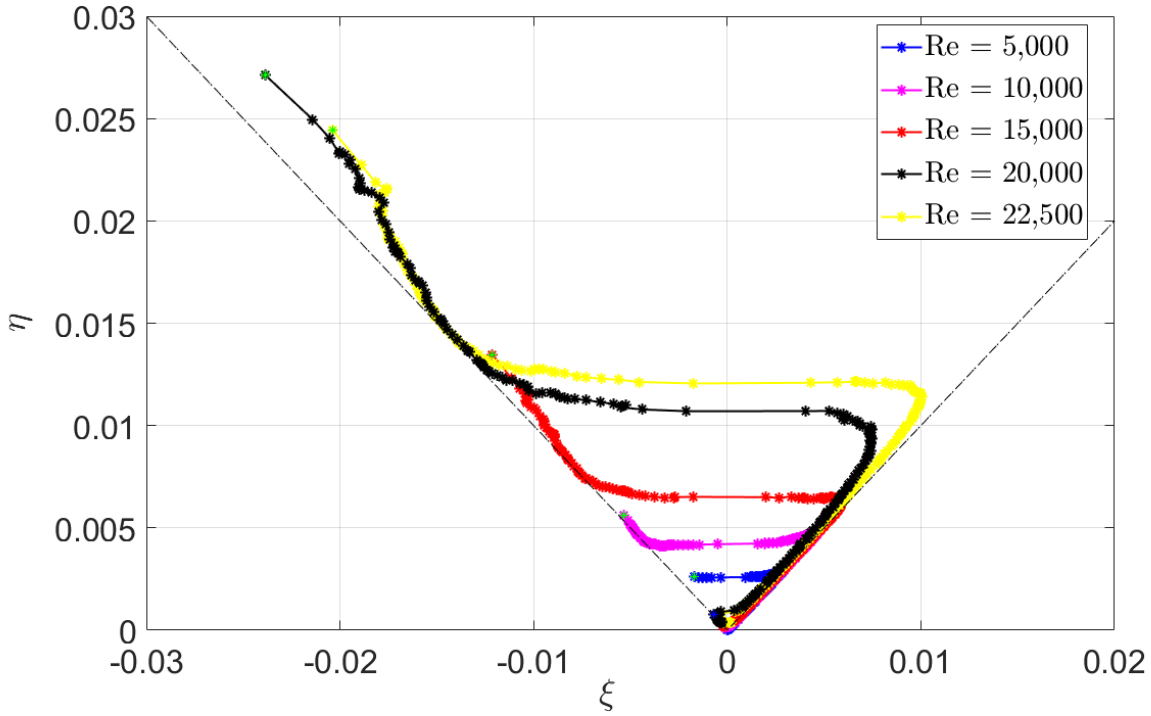

Figure 4.15: Turbulence triangle plot of the jet flow field for different Reynolds number cases from 5,000 to 22,500.

4.8 Structural Dynamics

In this section, the analysis on the structural dynamics performed by Krohn et al. [27] using the database established in this dissertation is reported here for completeness. The Power Spectral Density (PSD) for the streamwise velocity measurements was computed at various downstream positions along the jet centerline. The spectra of the near-field results are shown in Figure 4.17, normalized by the Kolmogorov length scale η_κ and associated

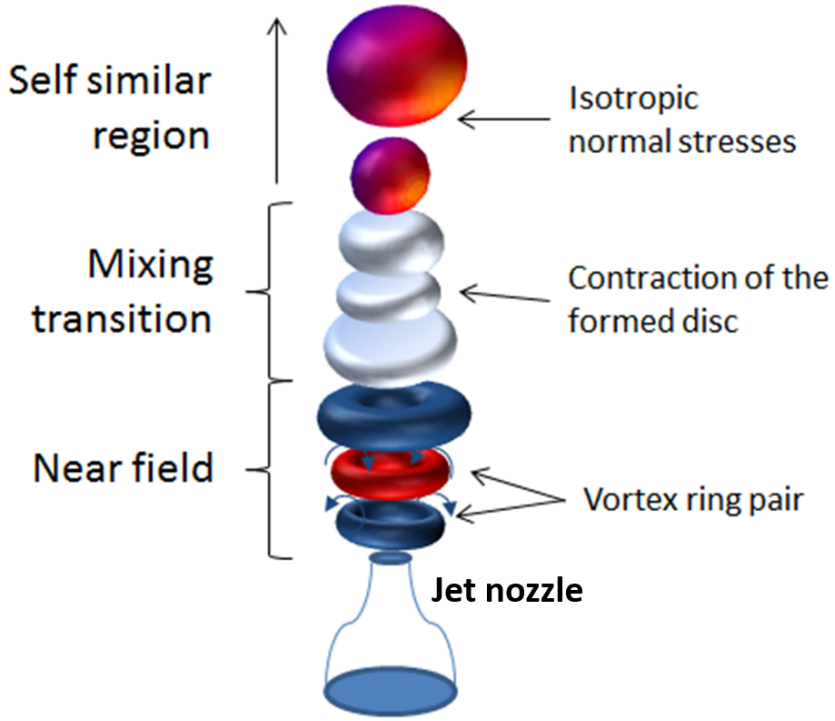

Figure 4.16: Illustration of the hypothetical dynamics of a turbulent round free jet flow field. Reprinted from Krohn et al. [27].

velocity scale v_κ, defined as

$$\eta_\kappa = \left(\frac{\nu^3 D}{\bar{v}^3}\right)^{1/4} \tag{4.7a}$$

$$v_\kappa = \left(\frac{\nu\pi^3}{D}\right)^{1/4} \tag{4.7b}$$

where $\bar{v}$ is the streamwise component of the mean velocity at the location where the PSD is computed, ν is the kinematic viscosity of the fluid and D is the hydraulic diameter of the jet nozzle. In this section, the uniform jet experimental Case T15k with Re = 15,000 is chosen for conducting the investigation. At the center of the nozzle exit, the Kolmogorov length scale is $\eta_\kappa = 9.59\ \mu m$, and the corresponding velocity scale is $v_\kappa = 0.105\ m/s$. Figure 4.17 shows the resulting spectra for different downstream distances along the centerline of the jet in Figure 4.17(a) and different radial locations across the jet at y/D = 2 shown in Figure 4.17(b). Within the potential core of the jet ($1 < y/D < 3$), we observe a departure from the -5/3 slope of the energy cascade that is associated with the range of frequencies in which the energy cascade is dominated by inertial transfer, while the -7 slope characterizes the dissipative range where viscous forces dominate. The spatial development of the spectra clearly indicates that the near field is dominated by a shear-layer vortex rollup that eventually evolves to a broad frequency distribution. At y/D = 3, the velocity spectra evolve to display a turbulence cascade with one peak remaining at a Strouhal number St = 0.512, which was close to St = 0.485 found by St = 0.479 found by Fellouah [11] (y/D = 3 and Re = 30,000), St = 0.4 found by Mi et al. [8] (y/D = 3 and Re = 16,000), and Jung et al. [110] (y/D = 4 and Re = 117,600). At these positions, the formation of coherent structures is apparent with the increased energy content at these peak frequencies. The vortex rollup frequency remains consistent along the radial direction until the center of the shear layer. With increased distance from the core, deceleration due to friction with fluid in rest occurs to shift the rollup frequency toward the right in the spectra (in Figure 4.17(b) for x/D = 3/4 and 1).

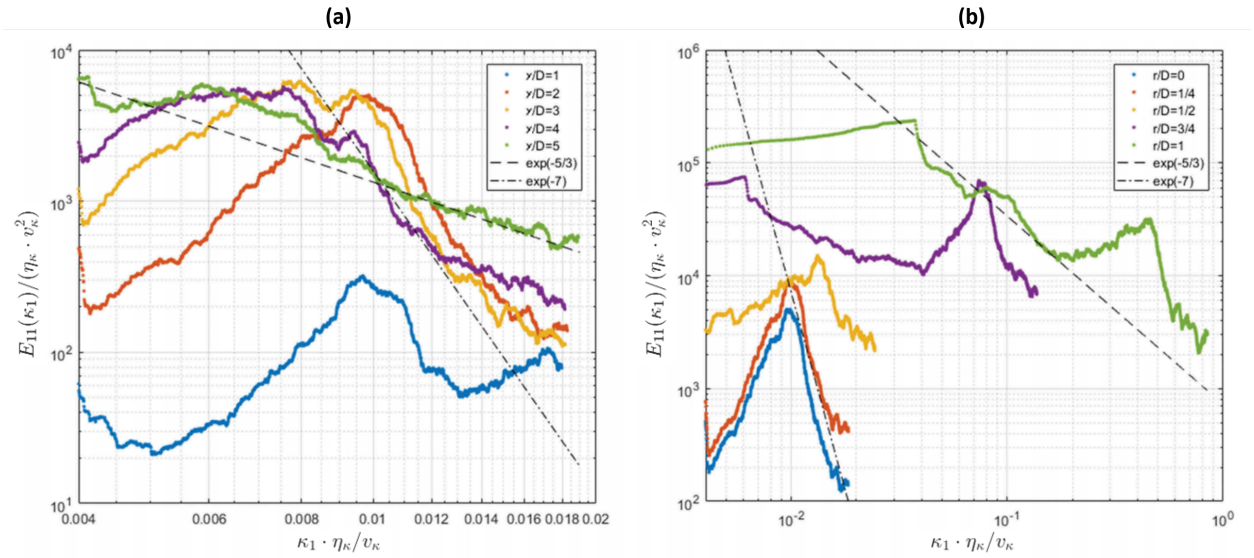

Figure 4.17: Power Spectral Density for Case T15k: (a) at the jet centerline for different downstream distances y/D, and (b) at y/D = 2 for different radial distances x/D. The dashed line represents the $\kappa^{-5/3}$ slope of the inertial subrange, and the dotted dashed line represents the dissipative range with κ^{-7}. Reprinted from Krohn et al. [27].

Given the fact of the single turbulent round free jet experiments, coherent structures of the flow field are analyzed by two-point spatial correlations of variances of velocities and shear stress in this section. The two-point spatial correlations equation for Reynolds stresses and shear stress need to be modified from Equation 1.4 as follows:

$$R_{f',f'} = \frac{\overline{f'_x f'_0}}{\sqrt{\overline{f'_0 f'_0} \cdot \overline{f'_x f'_x}}} \tag{4.8}$$

where the subscripts indicate the variance of the reference point (denoted 0) and in the whole flow field (denoted x). The variance itself is defined for the streamwise component as:

$$f' = v'v' - \overline{v'v'} \tag{4.9}$$

Similar equations apply for the radial component and the shear stress component. Figure 4.18 shows the resulting structures for reference points at the same locations where the spectral analysis in Figure 4.17(a) was performed. In the left column of Figure 4.18,

the spatial autocorrelation of the streamwise normal stresses $R_{v'v',v'v'}$ is shown for various downstream distances in the near-field of the jet. Within the potential core of the flow ($1 < y/D < 3$), we observe a paired structure that spans radially across the jet.

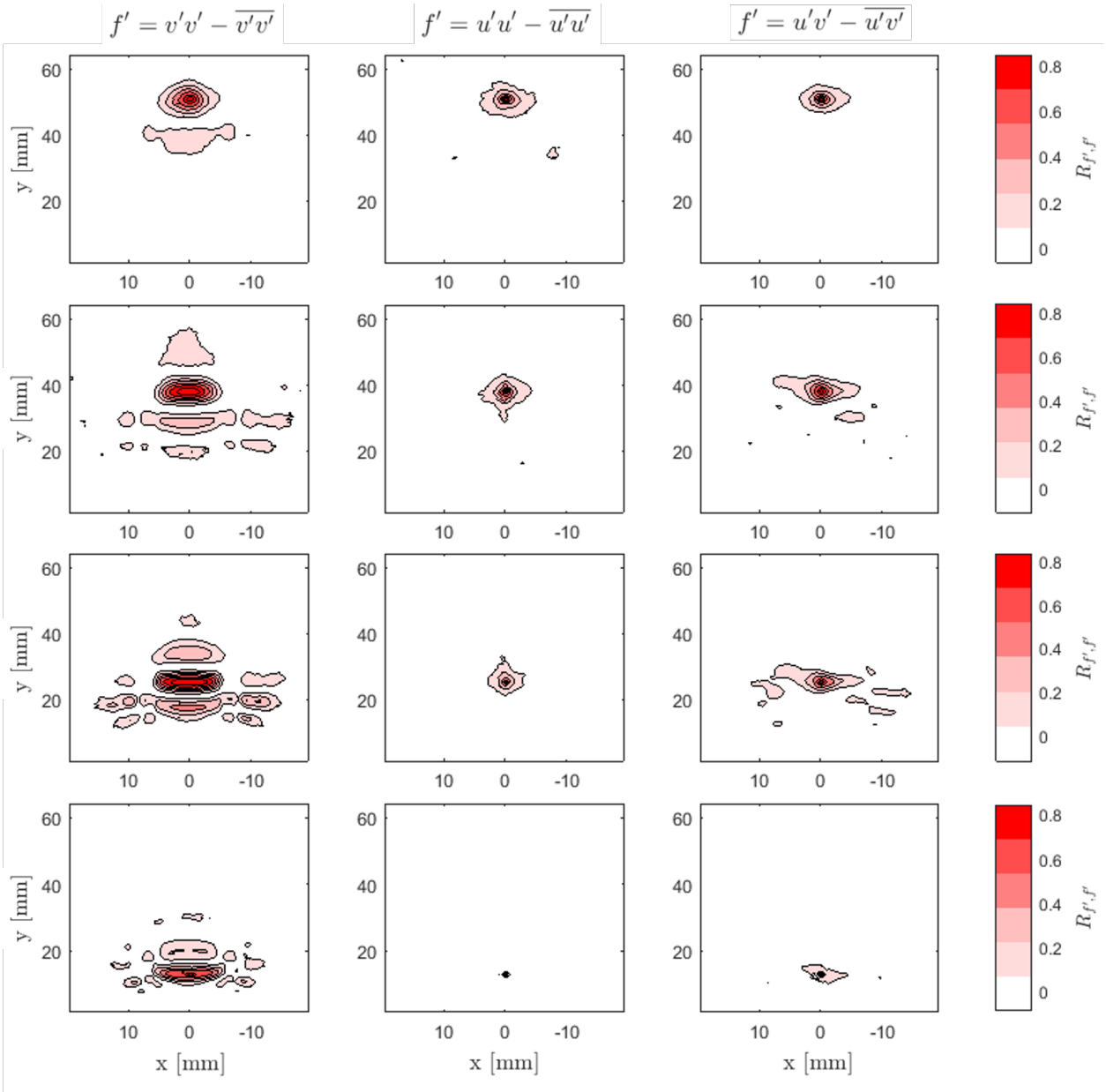

Figure 4.18: Two-point autocorrelations of variances of velocities. The reference points are along the jet centerline for various downstream distances (bottom to top row: y/D = 1, 2, 3, and 4): left column:$R_{v'v',v'v'}$; middle column: $R_{u'u',u'u'}$; and right column: $R_{u'v',u'v'}$. Reprinted from Krohn et al. [27].

The secondary structure reflects the potential core confined by the vortex ring that evolves

due to shear on the boundaries of the jet. At a location of y/D = 2, we observe two secondary maxima in the streamwise direction. They indicate how alternating vortex ring pairs are formed around the core. It is at this location where on the outer boundary of the shear layer the streamwise fluctuations show coherence to the core structure exactly half a period behind due to entraining fluid. Farther downstream at y/D = 4, the core of the vortex ring collapses as shown by a more and more circular structure, which is no more correlated to the outer region of the jet. The correlation depth of the cross-stream spatial autocorrelation at y/D = 1 is found to be extremely small within 1 mm. At this point, the flow is extremely anisotropic and momentum fluctuations are strongly streamwise oriented within the potential core. This dynamic is also reflected by the coherent field of shear (right column). While internal cross-stream friction develops with the development of vortex rings, shear within the core also occurs. Beyond the tip of the core downstream, local shear and both fluctuating components of velocity span an almost circular penetration depth that defines the starting point of the intermediate field of the jet. It is this lack of friction within the core that leads to a dissipative transport of eddy scales within the energy spectrum, and as friction develops, small neighboring structures begin to interact, merge, and form larger structures, which in turn change the distribution of scales in the spectrum. This can be observed in Figure 4.17(b) where the slope of the spectrum departs from -7 (illustrated by the straight red line) across the boundaries of the potential core toward the -5/3 slope (illustrated by the straight blue line).

Figure 4.19 shows two-point autocorrelations of variances of velocities of the jet. The reference points are at y/D = 2 for various radial distances (bottom to top row: x/D = 0, 1/4, 1/2, and 3/4). The left column shows the streamwise variance autocorrelation $R_{v'v',v'v'}$, the middle column shows the cross-stream variance autocorrelation $R_{u'u',u'u'}$, and the right column shows the shear stress autocorrelation $R_{u'v',u'v'}$. We observe a symmetric correlation of both sides of the jet. While the correlation depth within the core and the inner side of the shear layer at x/D = 1/4 shows similar structures as the jet centerline (at x/D = 0) for

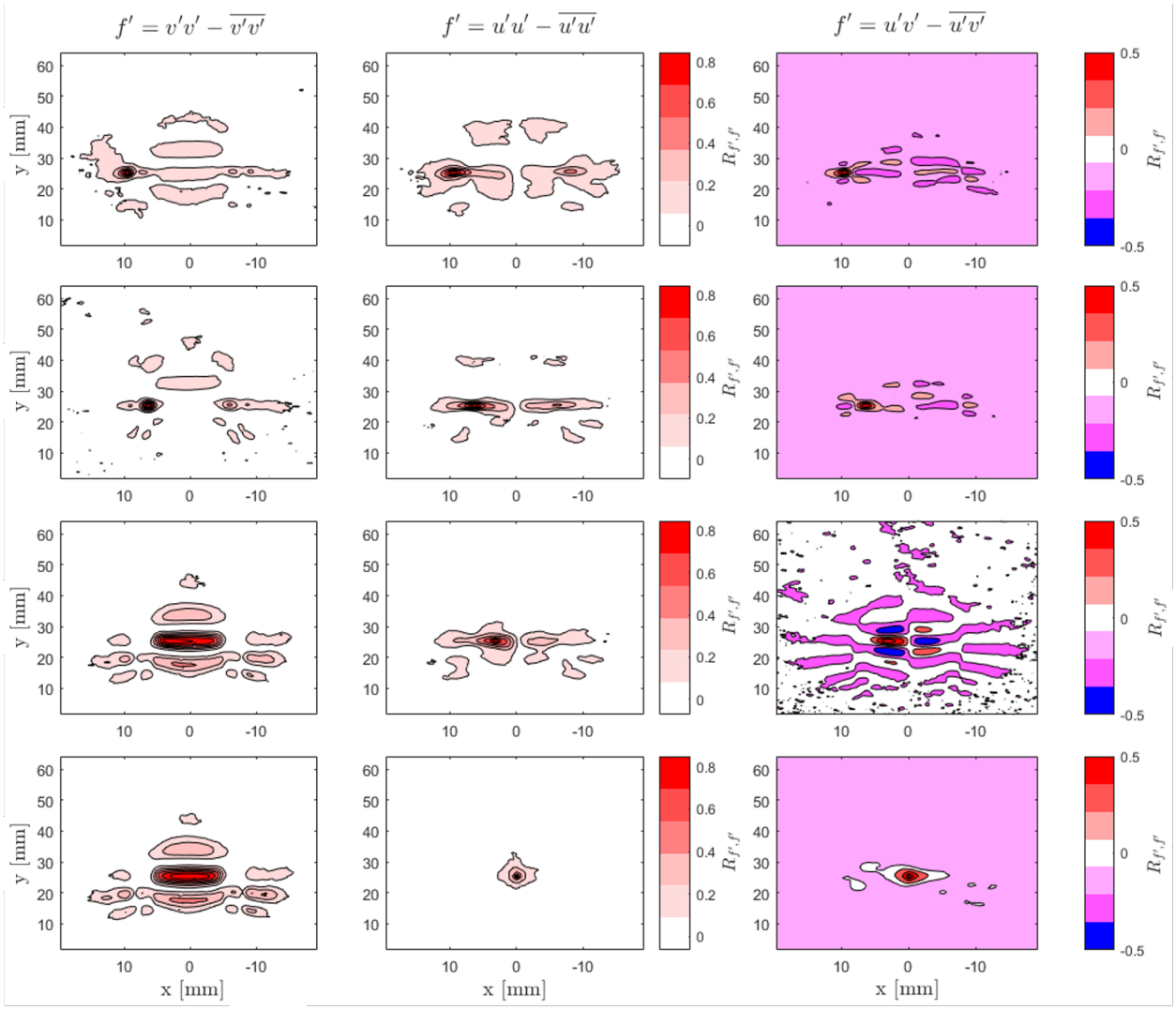

Figure 4.19: Two-point autocorrelations of variances of velocities. The reference points are at y/D = 2 for various radial distances (bottom to top row: x/D = 0, 1/4, 1/2, and 3/4): left column:$R_{v'v',v'v'}$; middle column: $R_{u'u',u'u'}$; and right column: $R_{u'v',u'v'}$. Reprinted from Krohn et al. [27].

streamwise autocorrelations, the cross-stream structure spans considerably more deeply into the shear region, which leads to more internal friction and thus larger structures to form. The situation aggravates in the core of the shear layer at x/D = 1/2, where the cross-stream structure dominates the streamwise in size. This inflection is evident in the spectrum of Figure 4.17(b). Here, the spectrum already slopes at -5/3. Focusing on the correlation at the outer region of the jet shear layer (x/D = 3/4), large structures dominate and at this point are fully infused by viscous effects. At x/D = 1/2, the shear stress correlation field reflects the complex structure of three vortex rings by paired co-correlated and anti-correlated regions that are alternating anti-symmetric across the layer.

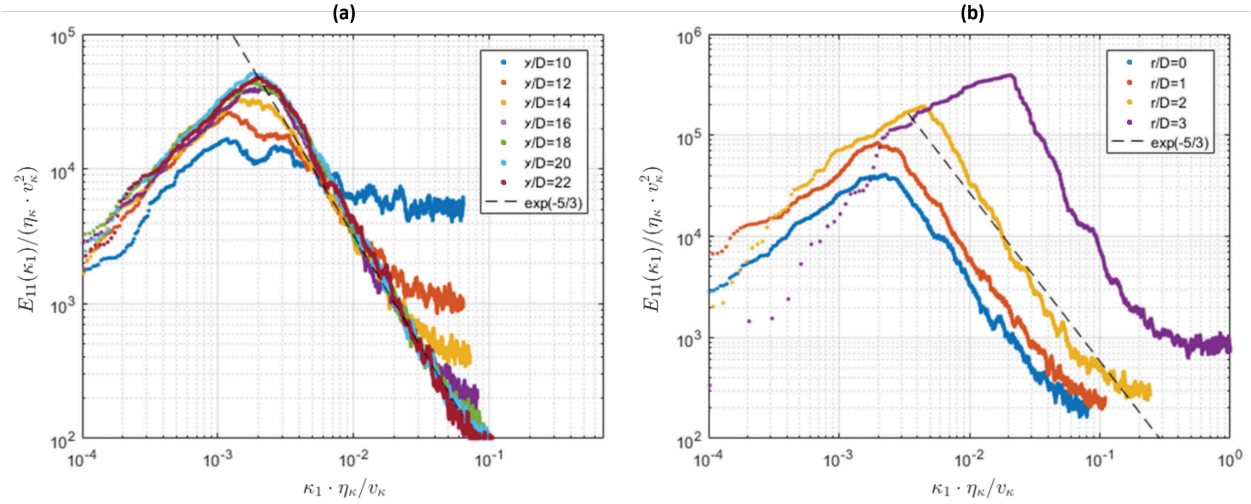

Figure 4.20: Power Spectral Density: (a) at the jet centerline for different downstream distances y/D and (b) at y/D = 16 for different radial distances x/D. The dashed line represents the $\kappa^{-5/3}$ slope of the inertial subrange. Reprinted from Krohn et al. [27].

Figure 4.20 shows the spectral analysis for various streamwise distances at the centerline (Figure 4.20(a)) and various radial distances at y/D = 16 (Figure 4.20(b)) in the mixing transition of the jet. The analysis of the potential core revealed a viscous transfer of scales within the energy spectra beyond the core. Figure 4.20 supports this theory. We also observe decay in large-scale structures toward the outer limits of the jet (visible in the primary peaks of the spectra). While the transport of scales follows a -5/3 slope toward the whole intermediate field, the change in penetration depth of coherent structures shows a mini-

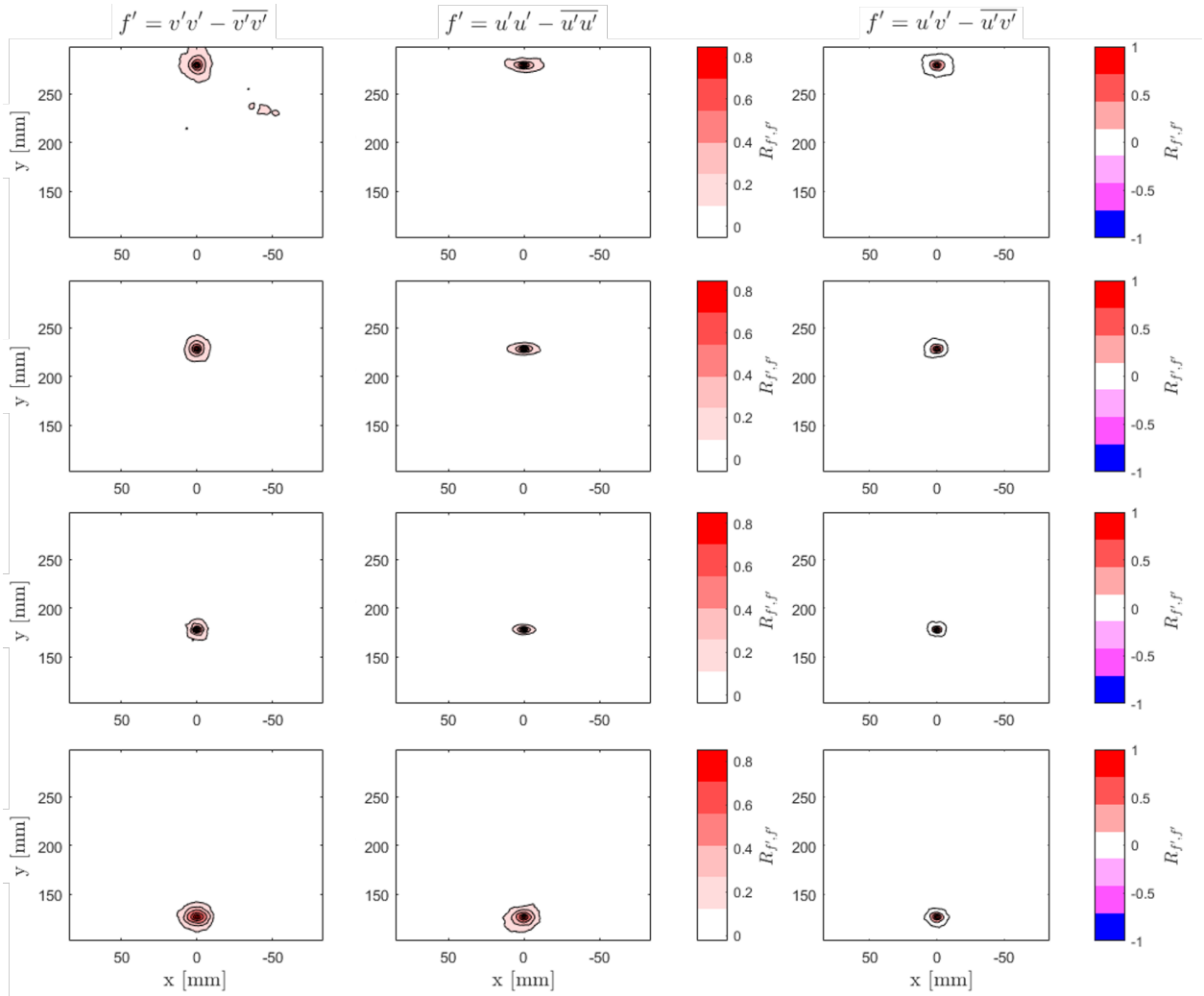

Figure 4.21: Two-point autocorrelations of variances of velocities. The reference points are along the jet centerline for various downstream distances (bottom to top row: y/D = 10, 14, 18, and 22): left column:$R_{v'v',v'v'}$; middle column: $R_{u'u',u'u'}$; and right column: $R_{u'v',u'v'}$. Reprinted from Krohn et al. [27].

mum. Figure 4.21 shows this phenomenon where two-point autocorrelations of variances of velocities of the jet are given. The reference points are at x/D = 0 for various downstream distances (from bottom to top row: y/D = 10, 14, 18, and 22). The left column shows the streamwise variance autocorrelation $R_{v'v',v'v'}$, the middle column shows the cross-stream variance autocorrelation $R_{u'u',u'u'}$, and the right column shows the shear stress autocorrelation $R_{u'v',u'v'}$. At y/D = 14, all three autocorrelations show a minimum in penetration depth, which increases farther downstream, concluding that the mixing transition ends with this minimum since all structures keep growing farther within the self-similar region.

With focus on the inflection at y/D = 14, Figure 4.22 shows two-point autocorrelations for various radial distances (bottom to top row: x/D = 0, 1, 2, and 3). From the core of the jet toward radially away from the core, we observe a vertically elongated streamwise structure that is growing in size in conjunction with a spanwise elongated structure of radial variances, while shear covariant structures remain symmetric and circular. Together with the Lumley Triangle study shown in Figure 4.15 and the hypothetical illustration of a turbulent round free jet flow field shown in Figure 4.16, the investigations of the coherent structures confirm that the initially formed vortex ring pairs, which surround and thus limit the potential core of the jet in the near-field, roll up and merge farther downstream. The transported friction within the vortices toward the potential core of the jet affects the rate at which energy is transported across different scales from a dissipative to a viscous behavior. Once the structural extent of the vortex pairs (illustrated in red and blue) overcomes the singularity of the core, which is the potential core here, a disk-shape momentum structure evolves. This coherent momentum structure collapses toward an energetically more favorable symmetry: a sphere, which is where we detected the minimum extent of the penetration depth across the core (shown in Figure 4.21). The shear field structure within the core of the collapsing vortex ring pair structures is found to be symmetric, which confirms that the detected disk structure shears toward the centerline in order to form a sphere.

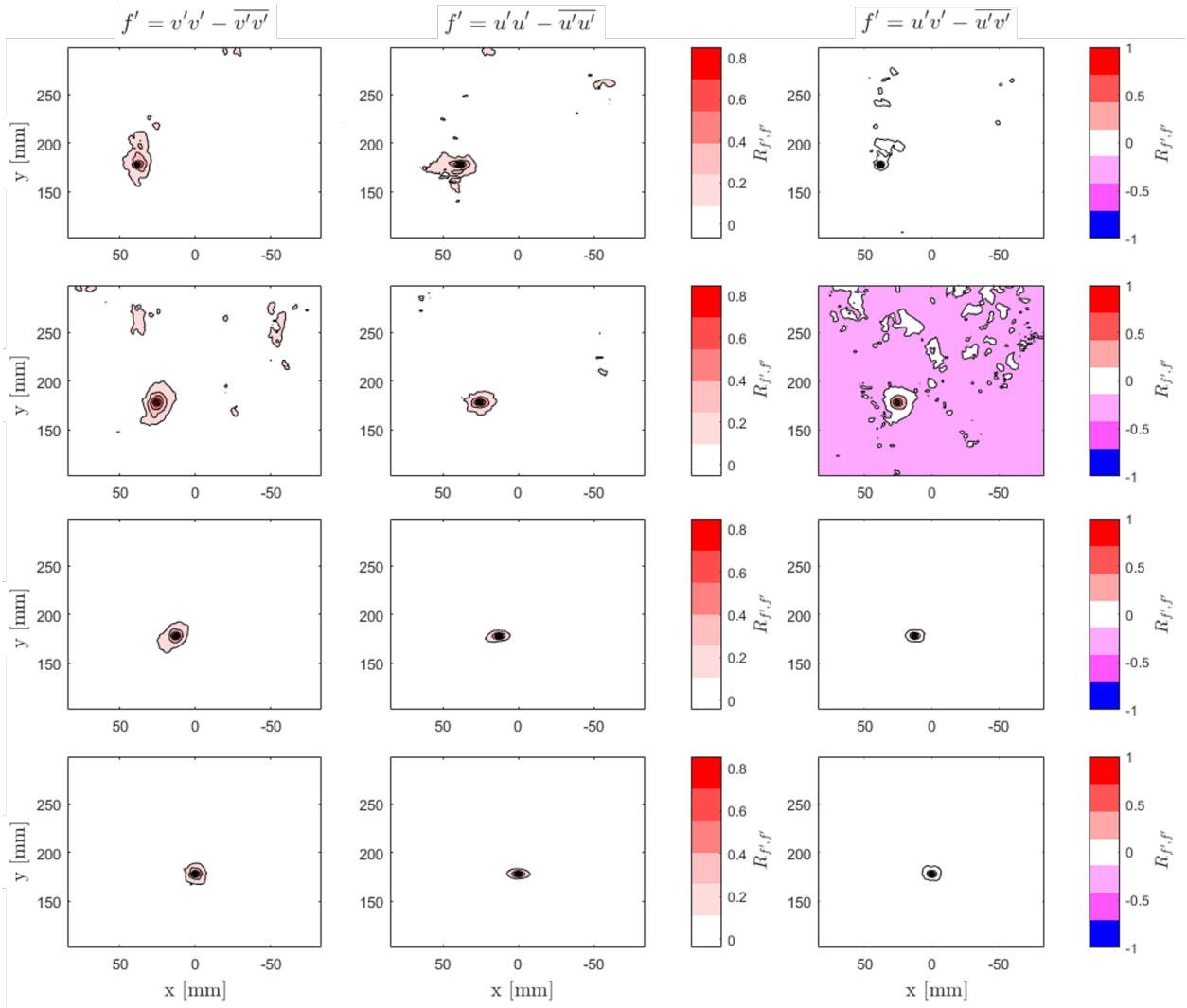

Figure 4.22: Two-point autocorrelations of variances of velocities. The reference points are at y/D = 14 for various radial distances (bottom to top row: x/D = 0, 1, 2, and 3): left column:$R_{v'v',v'v'}$; middle column: $R_{u'u',u'u'}$; and right column: $R_{u'v',u'v'}$. Reprinted from Krohn et al. [27].

CHAPTER V

Turbulent Buoyant Jet in Stratified Environments

This chapter is focused on the investigation of buoyant jets in stratified environments. A high-resolution experimental database for this type of flows has been established employing the novel RIM technique developed by Krohn et al. [22] and discussed in Chapter III. Synchronized PIV/PLIF measurements have been carried out at the miniDESTROJER facility to obtain both the instantaneous velocity- and scalar-fields.

Unlike jets in a uniform environment, buoyant jets can be characterized by the competing effects of the momentum carried with the jet flow and the buoyancy forces between jet and surroundings. For buoyant jets in the presence of positive density gradients in the flow direction (so-called positively buoyant jet), the momentum and buoyancy forces act both in the same direction, with buoyancy forces increasingly dominating the flow as the jet gets farther away from the origin. For buoyant jets in the presence of negative density gradients (so-called negatively buoyant jets), the buoyancy forces oppose the momentum in the jet flow until the streamwise velocity decays to zero and flow reversal will take place. The flow behavior is more complex when a lighter jet is injected into a two-layer stratified environment which denser fluid at the bottom and lighter fluid at the top. The jet flow will first mix with the denser fluid, behaving as a positively buoyant jet, to then behave as a negatively buoyant jet when impacting with the top layer, since the fluid in the jet flow has become heavier due to the mixing with the lower fluid.

In this chapter, the mixing processes of turbulent buoyant jets will be investigated, and the results will be compared to the reference uniform jets discussed in the previous chapter. Similar to Chapter IV, the coordinate system of the jet flow-field is defined and illustrated in Figure 5.1.

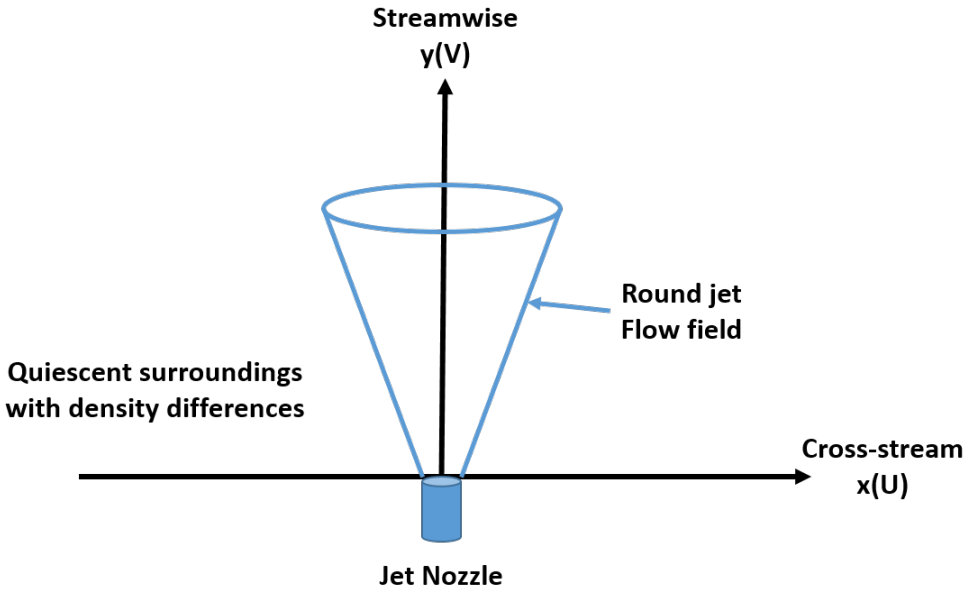

Figure 5.1: Sketch of jet flow in a stratified environment and definition of the coordinates for the data analyses.

5.1 Measurement Campaign for Non-Uniform Environments

Turbulent buoyant flows are commonly characterized by the Reynolds number (Re) and densimetric Froude Number (Fr) with the velocity scale U and the length scale L (the jet diameter for this work):

$$Re = \frac{UL}{\nu} \tag{5.1a}$$

$$Fr = \frac{U}{\sqrt{g \cdot \Delta\rho \cdot L}} \tag{5.1b}$$

where ν is the kinematic viscosity, $\Delta\rho$ is the density gradient and g is the gravitational

acceleration. Xiang et.al [111] mentioned that Reynolds number could get extremely large in many geophysical and engineering applications due to the large values that the product UL can assume. The time (L/U) scales associated with the inlet turbulence are usually three orders of magnitude smaller than those associated with buoyancy forces exerted by the nature. However, if there is no more energy input into the system, the length scale increases while velocity decreases, resulting in a buoyancy-dominated flow. In this chapter, the test cases which are part of the experimental campaign will be characterized by the Reynolds number as well as the Froude Number Fr_0 estimated at the jet inlet location. The initial fluid level present in the miniDESTROJER tank is kept equal to 250 $\pm$ 1 mm for the entire experimental campaign.

5.1.1 Buoyant Jet with 3.16% density difference

Two types of experiments have been conducted for buoyant jets, one in which a lighter (heavier) fluid is injected into a heavier (lighter) environment, as illustrated in Figure 5.2(a), and a second experimental configuration in which a fluid is injected into a stratified environment, as shown in Figure 5.2(b). During the preparation of the two-layer environment, the initial upper boundary for the heavier solution is set to be located at 125 $\pm$ 1 mm downstream of the nozzle exit, then the lighter solution is gently poured from the top of the tank until the desired fluid level is reached. Due to the natural diffusion process, there will inevitably be a stratification zone at the boundary between the higher and lighter solution. The thickness of the stratification zone will be quantified within the the 10-90 percentile range and provided as initial conditions for each experimental run.

Utilizing the miniDESTROJER facility and the 3.16% solutions pairs with Sodium Sulfate and Glycerol mentioned in Section 3.2.1, the experimental campaign summarized in Table 5.1 was executed. In the table, the experiments conditions are reported for nominal jet velocity U_0, averaged fluid temperature T, Reynolds number (Re) and densimetric Froude Number (Fr), and solutions density differences .

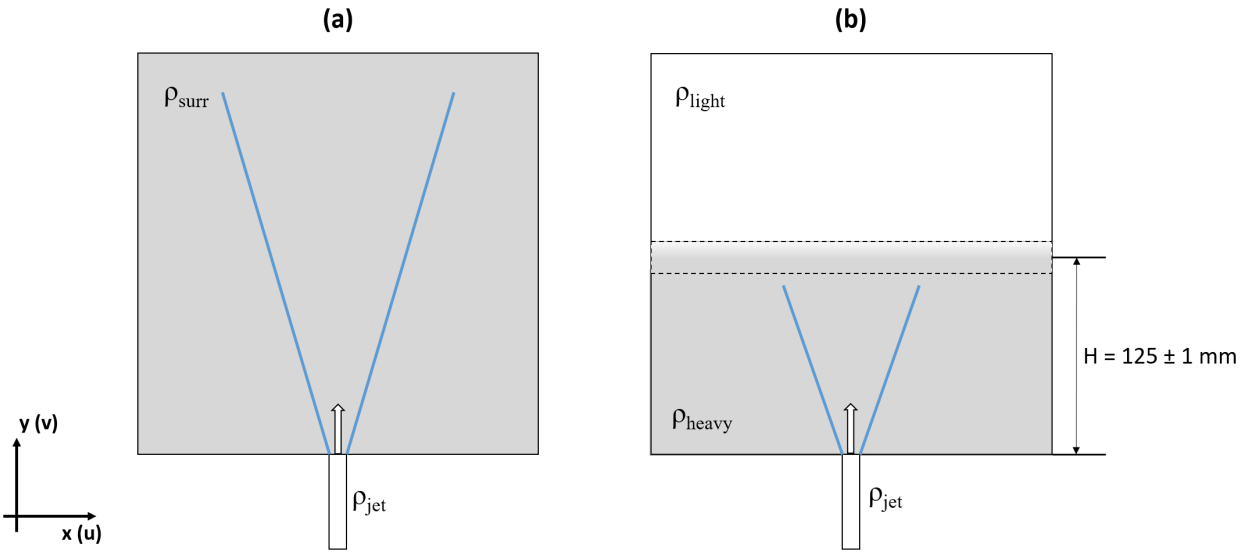

Figure 5.2: Initial conditions for the setup of (a) positively or negatively buoyant jet, and (b) the two-layer stably stratified environment, with ρ_{light} denoting the density for lighter fluid and ρ_{heavy} denoting the density for heavier fluid.

Table 5.1: Buoyant jet inlet velocity and fluid temperature of the experiments conducted for 3.16% density differences.

Cases	$\boldsymbol{U_0}$	$\boldsymbol{\rho_{jet}}$	$\boldsymbol{\rho_{surr}}$	$\boldsymbol{\Delta\rho}$	$\boldsymbol{T}$	$\boldsymbol{Re}$	$\boldsymbol{Fr_0}$
$--$	m/s	kg/m^3	kg/m^3	$--$	$^\circ C$	$--$	$--$
D033	5.990 ± 0.004	1012 ± 10.1	1044.0 ± 10.4	+3.16%	20.4 ± 0.1	10,000 ± 7	240.49 ± 0.16
D034	2.460 ± 0.002	1012 ± 10.1	1044.0 ± 10.4	+3.16%	20.4 ± 0.1	4,000 ± 2	92.34 ± 0.06
D035	5.530 ± 0.004	1044 ± 10.4	1012.0 ± 10.1	-3.16%	20.0 ± 0.1	10,000 ± 7	225.50 ± 0.15
D036	2.300 ± 0.002	1044 ± 10.4	1012.0 ± 10.1	-3.16%	20.5 ± 0.1	4,000 ± 2	93.79 ± 0.06
D042	5.990 ± 0.004	1012 ± 10.1	Sharp Interface	–	18.1 ± 0.1	10,000 ± 7	240.49 ± 0.16
D043	2.460 ± 0.002	1012 ± 10.1	Sharp Interface	–	19.0 ± 0.1	4,000 ± 2	92.34 ± 0.06

5.1.2 Buoyant Jet with 8.6% density difference solutions

Mixtures of water, Isopropanol, and Glycerol were used as working fluids for the experimental database at higher density differences (8.6%), so that RIM could be achieved, as explained in Chapter III. Details on the experimental campaign parameters are summarized in Table 5.2. Because Isopropanol is volatile, it was not possible to establish a stable two-layer stratification, therefore this experimental matrix includes only positively and negatively buoyant jets injected in uniform environments.

Table 5.2: Buoyant jet inlet velocity and fluid temperature of the experiments conducted for a 8.6% density difference.

Cases	$\boldsymbol{U_0}$	$\boldsymbol{\rho_{jet}}$	$\boldsymbol{\rho_{surr}}$	$\boldsymbol{\Delta\rho}$	$\boldsymbol{T}$	$\boldsymbol{Re}$	$\boldsymbol{Fr_0}$
$--$	m/s	kg/m^3	kg/m^3	$--$	$^\circ C$	$--$	$--$
D047	9.060 ± 0.006	1011 ± 10.1	924.3 ± 9.2	-8.6%	19.3 ± 0.1	4,000 ± 3	220.87 ± 0.15
D048	4.220 ± 0.003	1011 ± 10.1	924.3 ± 9.2	-8.6%	19.7 ± 0.1	2,000 ± 2	102.88 ± 0.07
D051	9.060 ± 0.006	924.3 ± 9.2	1011.0 ± 10.1	+8.6%	18.5 ± 0.1	4,000 ± 3	211.19 ± 0.14
D052	4.220 ± 0.003	924.3 ± 9.2	1011.0 ± 10.1	+8.6%	18.8 ± 0.1	2,000 ± 2	98.37 ± 0.07

5.2 Turbulent Statistics of Positively and Negatively Buoyant jets

In this section, positively and negatively buoyant jets in the presence of 3.16% and 8.6% density differences will be compared to reference cases of uniform jets. With reference to the working fluids Solution I and II mentioned in Table 3.1, the cases that will be discussed in the following sections include:

- Uniform Case **D029**: Solution I being injected into Solution I;
- Uniform Case **D031**: Solution II being injected into Solution II;
- Positively Buoyant Case **D033**: Solution I being injected into Solution II at 3.16% density difference with RIM;

- Negatively Buoyant Case **D035**: Solution II being injected into Solution I at 3.16% density difference with RIM.

5.2.1 Mean velocity, scalar transport and TKE in the self-similar region

Figure 5.3 shows the streamwise mean velocity field obtained for buoyant and non-buoyant jets at Re = 10,000. In particular, in Figure 5.3(a) the streamwise mean velocity field for the uniform case D029 (light fluid injected into light environment) is plotted in shading, while the superimposed isolines correspond to the positively buoyant jet case D033 (light fluid injected into the heavy environment). In Figure 5.3(b), the uniform case D031 with heavy fluid and the negatively buoyant jet case D035 are compared instead. Compared to the reference uniform cases (D029 and D031), it can be noticed that the streamwise velocity magnitude is suppressed when injecting the light solution into the heavy environment while it appears to be slightly amplified when the heavy fluid is injected into light surroundings.

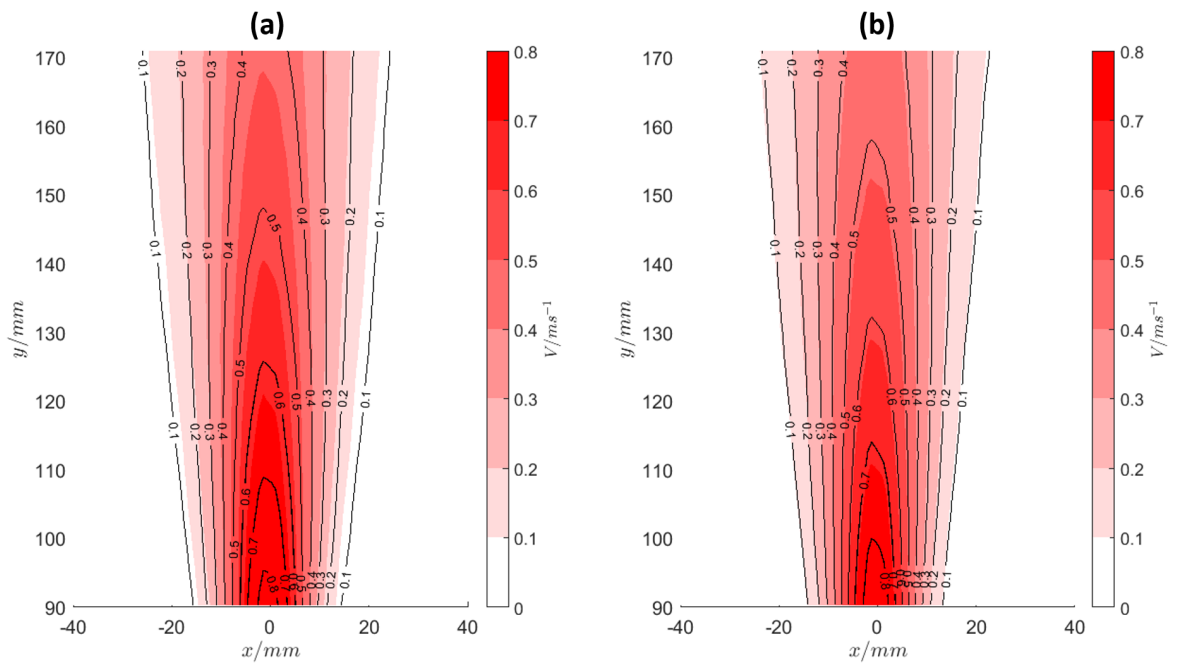

Figure 5.3: Fields of streamwise mean velocity: (a) D029 for uniform jet in shading vs. D033 for positively buoyant jet in isolines, and (b) D031 for uniform jet in shading vs. D035 for negatively buoyant jet in isolines.

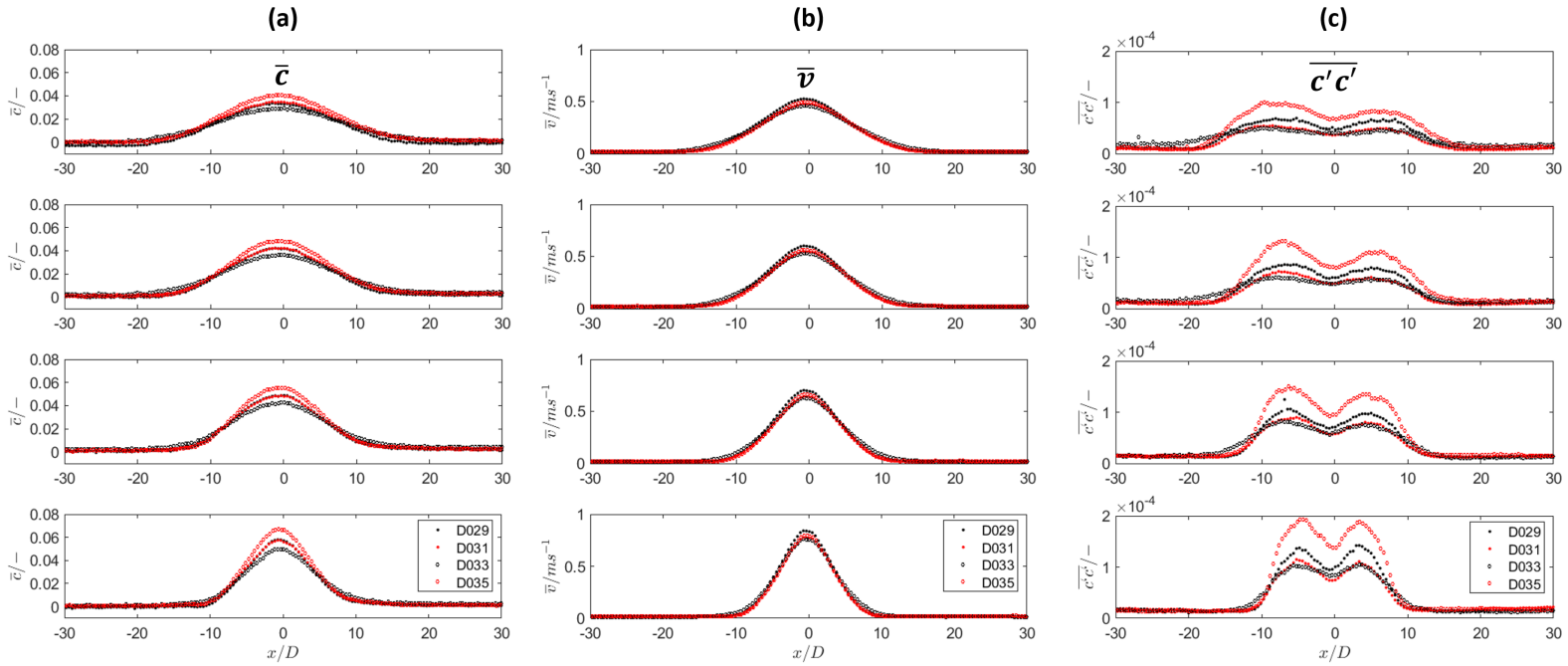

Figure 5.4: Radial profiles of (a) mean transport scalar, (b) streamwise mean velocity and (c) transport scalar variance extracted at y/D = 50, 60, 70 and 80 (from bottom to top).

To better visualize these effects, the radial profiles of the evolution of the transport scalar and the streamwise mean velocity along the vertical axis of the jet are reported in Figure 5.4. In Figure 5.4(a)&(b), both mean scalar and streamwise velocity profiles follow the same trend, with Gaussian-shape profiles that spread and decay as the jet travels further downstream the jet inlet. The entrainment from the surrounding fluid causes a decrease in the core concentration and of the streamwise velocity as well. Enhanced mixing is observed when the light solution is injected into the heavy environment, while mixing is suppressed when the heavy solution gets injected into the light environment. The streamwise mean velocity exhibits interesting trends: when injecting the light solution into the heavy environment, a strong deceleration of the streamwise centerline velocity is observed with increasing downstream distance comparing to the reference uniform jet case; more momentum is carried with the heavy solution when it gets injected into the light environment instead, resulting in less deceleration compared to the corresponding uniform jet case (heavy fluid injected into heavy environment). Radial profiles of Turbulent Kinetic Energy (TKE) normalized by the jet inlet velocities for these cases are, therefore, plotted in Figure 5.5 to verify with the mixing behavior. It can be noticed that the magnitudes for the normalized TKE profiles are surprisingly similar for all the cases, except for a wider span in the radial direction for the positively buoyant jet case D033.

The radial profiles for the scalar variance at different downstream locations are shown in Figure 5.4(c). Here it can be observed that the scalar variances across the mixing zone increase with increasing y/D for all cases. It can be shown that the double peaks in the radial profiles of the scalar variance are caused by two shear layers, which are present on both sides of the jet matching the locations of the two maxima in TKE plots shown in Figure 5.5. Comparing the two reference cases, i.e. D029 and D031, the cases of heavy liquid injecting into a heavy environment exhibit a lower scalar variance due to the overall lower turbulent intensities. With respect to the uniform case for the light solution injection, injecting the light solution into a heavy environment results in a lower amplitude of the scalar

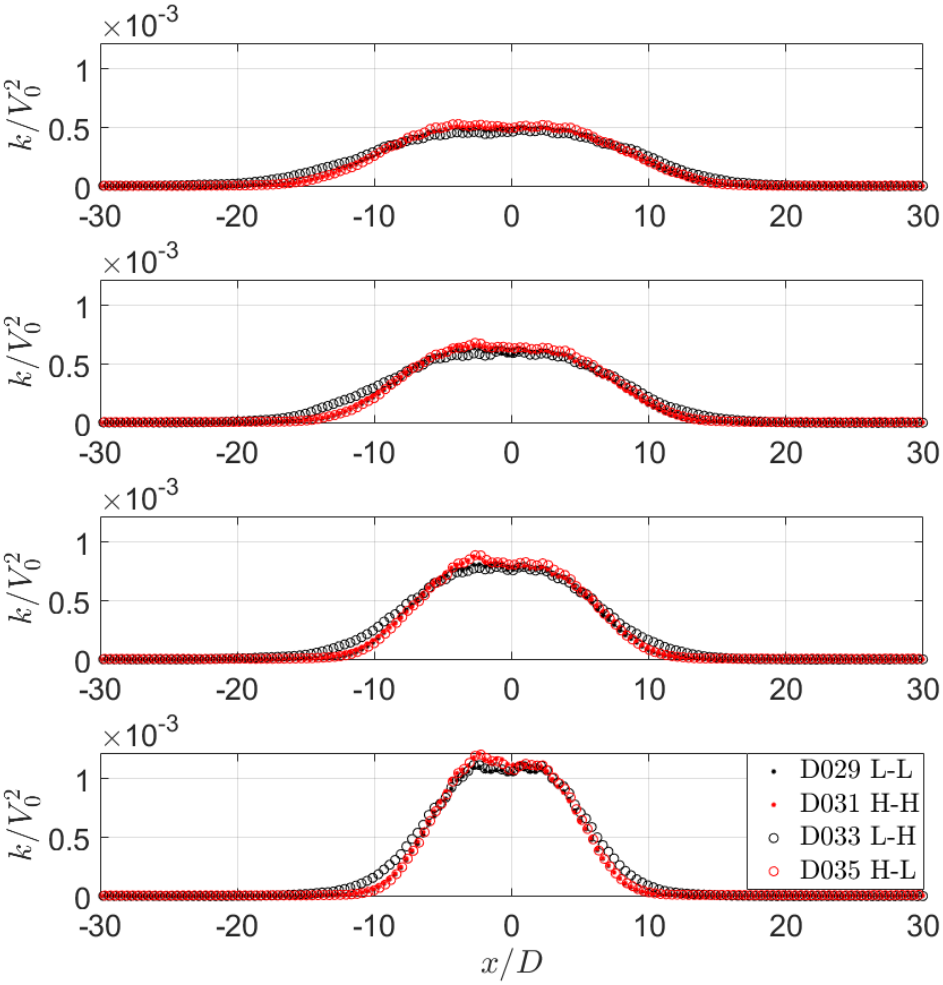

Figure 5.5: Radial profiles of the normalized Turbulent Kinetic Energy extracted at y/D = 50, 60, 70 and 80 (from bottom to top).

variance, as well as larger crosswise jet spreading. This might originate in the increased entrainment with the accelerated light fluid exposing enhanced shears to the surrounding. The observed behavior agrees with the findings reported by Krohn et al. ([112], [113]) for the jet near- and intermediate-field ($5 \leq y/D \leq 15$), and is due to the acceleration caused by the buoyant forces. This also implies that the same effect is present in the jet self-similar region ($50 \leq y/D \leq 80$). However, the amplitudes of the scalar variance are larger for the heavy into light cases, indicating that the mixing process is still undergoing. Findings are in conjunction with less mixing for the case of heavy fluid injected into light fluid and enhanced mixing when injecting light fluid into heavy fluid, as shown for the mean transport scalar plot (Figure 5.4a).

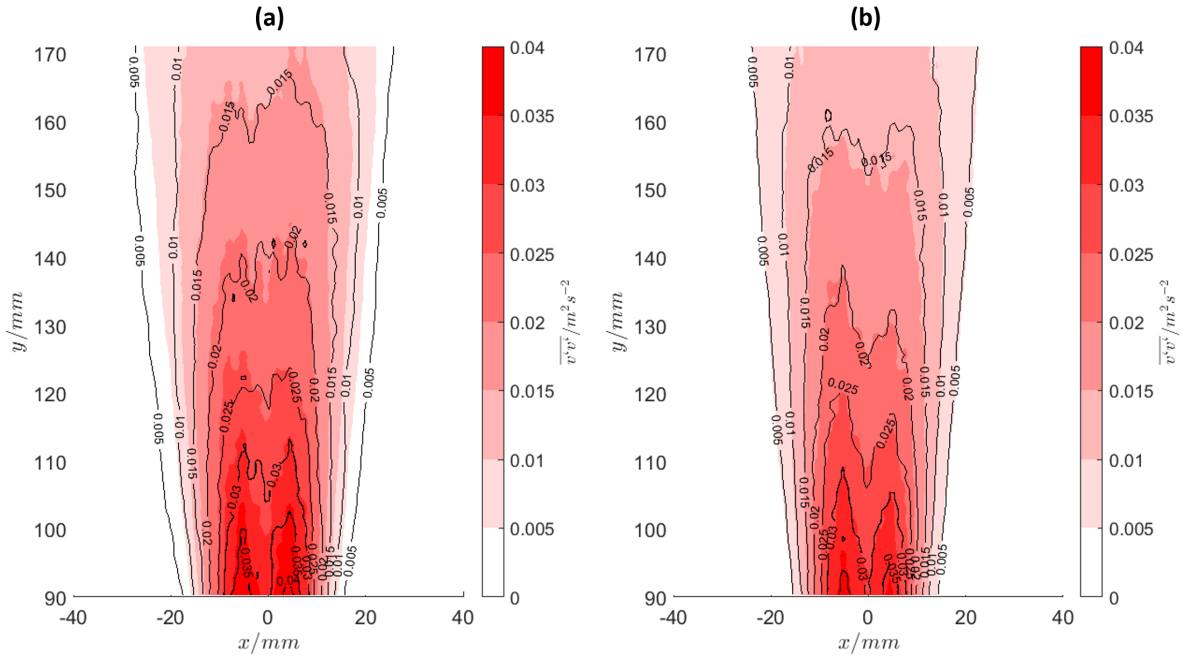

Figure 5.6: Fields of streamwise velocity variance: (a) D029 for uniform jet in shading vs. D033 for positively buoyant jet in isolines, and (b) D031 for uniform jet in shading vs. D035 for negatively buoyant jet in isolines.

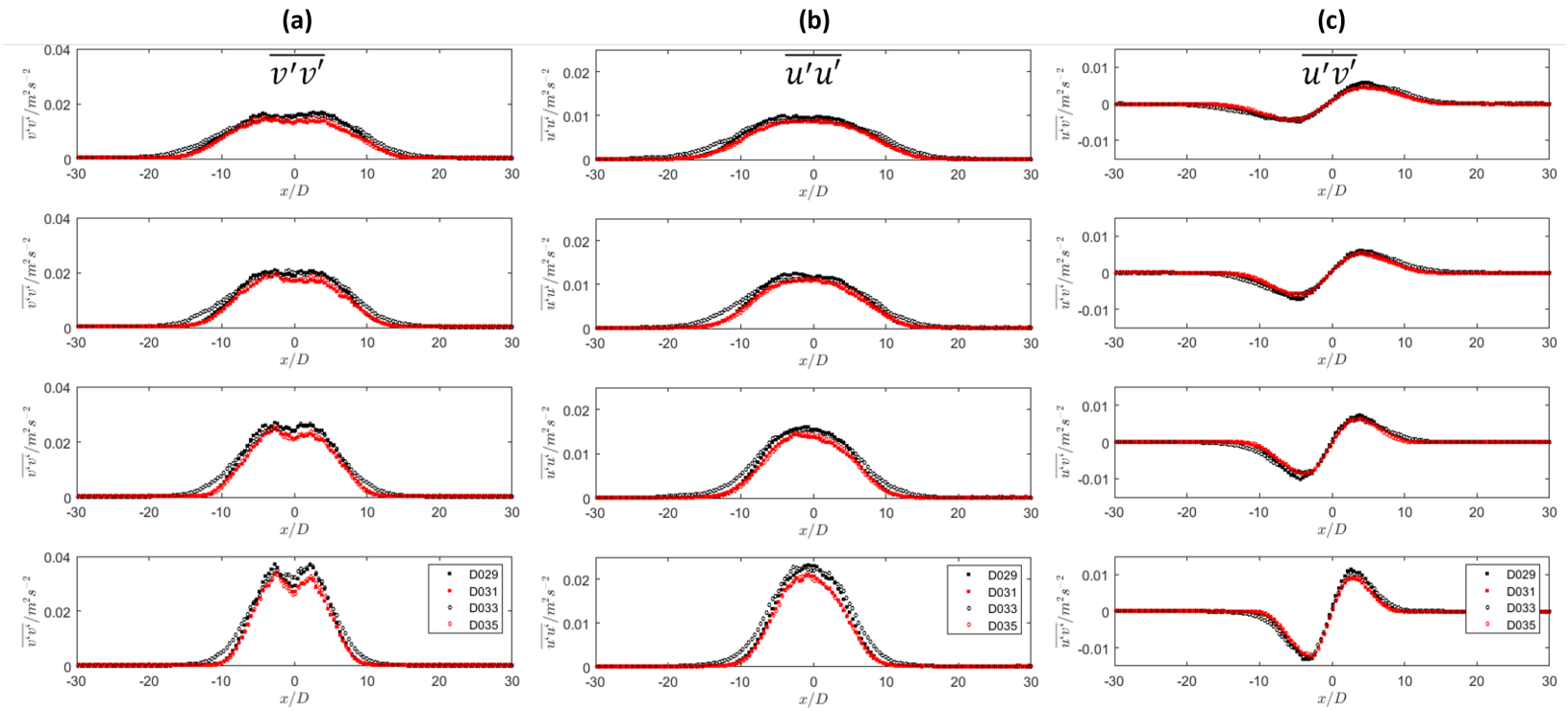

Figure 5.7: Radial profiles of (a) streamwise velocity variance, (b) crosswise velocity variance, and (c) shear stress extracted at y/D = 50, 60, 70 and 80 (from bottom to top).

Figure 5.6 shows the streamwise velocity variance fields for the four cases with Re = 10,000. Again, the reference cases for uniform jets are plotted in shading, while the corresponding buoyant jet cases are represented in isolines. In Figure 5.6(a) the uniform case D029 is compared to the positively buoyant jet case D033, while in Figure 5.6(b) the uniform case D031 is compared to the negatively buoyant jet case D035. In terms of magnitudes, both the reference and density difference cases show almost the same values. For different downstream locations, Figure 5.7 confirms that in the self-similar region of the jet flow the streamwise and crosswise velocity variances appear to be unaffected by the presence of density differences. Together with the TKE profiles shown in Figure 5.4, this indicates that the turbulent momentum transfer is almost identical with or without the presence of density differences. The same effect can be observed in the shear fields. Here positive shears on the left side and negative shears on the right side indicate the directions of entrainment.

5.2.2 Turbulent fluxes, eddy viscosity, and diffusivity in the self-similar region

With the investigations on the velocity and scalar field, turbulent fluxes can be computed according to Equation 2.7 and 2.8, which provides information on both the direction and magnitude of the turbulent transport of the scalar field. Figure 5.8 shows the comparison of the crosswise and streamwise turbulent fluxes. It can be noticed that the turbulent fluxes in the radial direction $\overline{u'c'}$ are much smaller, as expected, than in the streamwise direction $\overline{v'c'}$. The crosswise fluxes follow the gradient of the mean transport scalar. The positive flux amplitude on the left of the core and the negative flux amplitude on the right implies the influx and engulfment of the surrounding fluid into the jet correspondingly. Because of the reduced streamwise velocity fluctuations and decreased scalar fluctuations, it can be observed that the amplitude of both the crosswise and streamwise turbulent fluxes are lower for the light into heavy case, when compared to the reference uniform case with light solution. More pronounced differences can be observed for the streamwise fluxes. Opposite behavior for the reference case is observed if the heavy fluid is injected into the light fluid.

Therefore, as indicated in Figure 5.8, turbulent fluxes are suppressed when injecting the light liquid into the heavy environment and enhanced when the heavy liquid is injected into light surroundings.

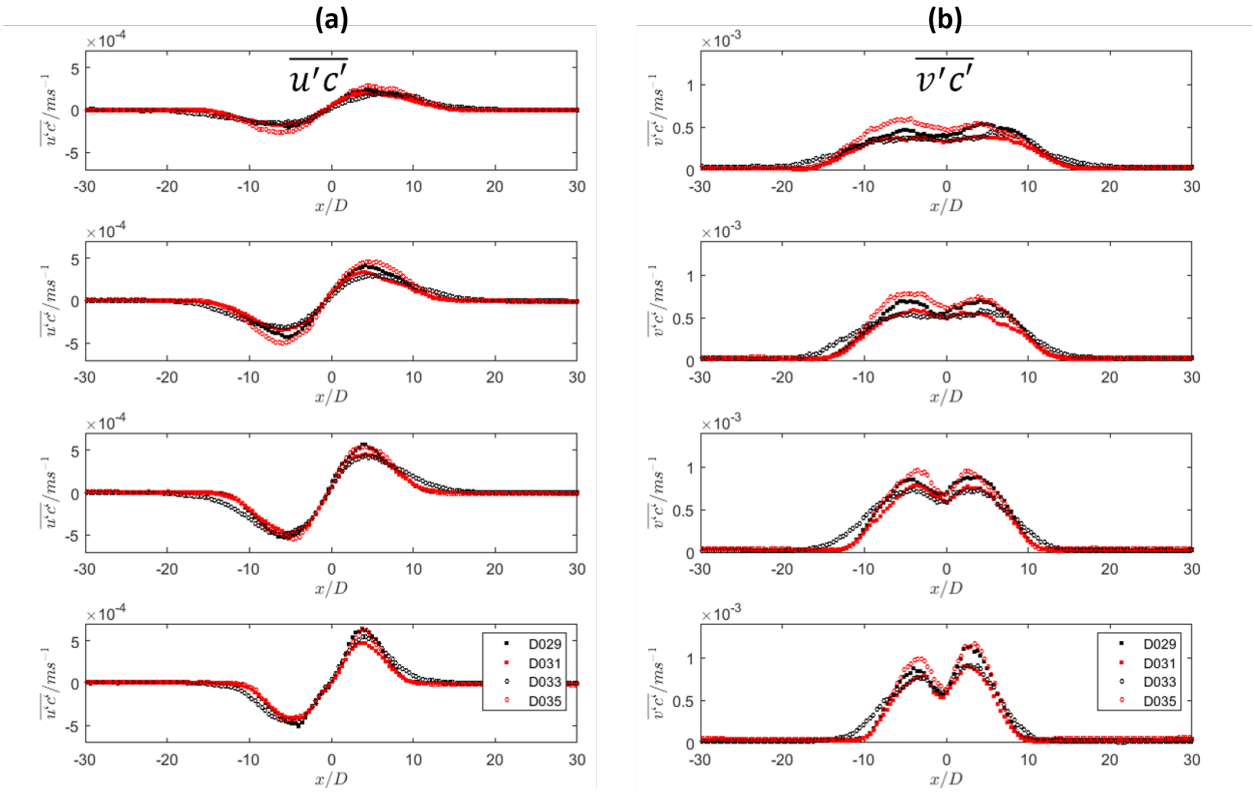

Figure 5.8: Radial profiles of (a) crosswise turbulent flux and (b) streamwise turbulent flux extracted at y/D = 50, 60, 70 and 80 (from bottom to top).

According to Equation 1.6 with the proper arrangement of terms, the turbulent eddy viscosity ν_t can be evaluated along the flow field using Equation 5.2, where u and x denote the radial velocity and radial direction respectively, while v and y denote the streamwise velocity and direction respectively (see also Figure 5.1):

$$\nu_t = -\overline{u'v'} / \left(\frac{\partial \bar{u}}{\partial y} + \frac{\partial \bar{v}}{\partial x} \right) \tag{5.2}$$

In Figure 5.9(a) the turbulent eddy viscosity estimated according to Equation 5.2 are plotted for different downstream locations. It can be noticed that all cases show positive turbulent

viscosities. Both the reference cases and the heavy into light cases exhibits similar values and trends, while a larger turbulent eddy viscosity is observed in the region surrounding the jet for the case of light liquid injected into the heavy environment (D033).

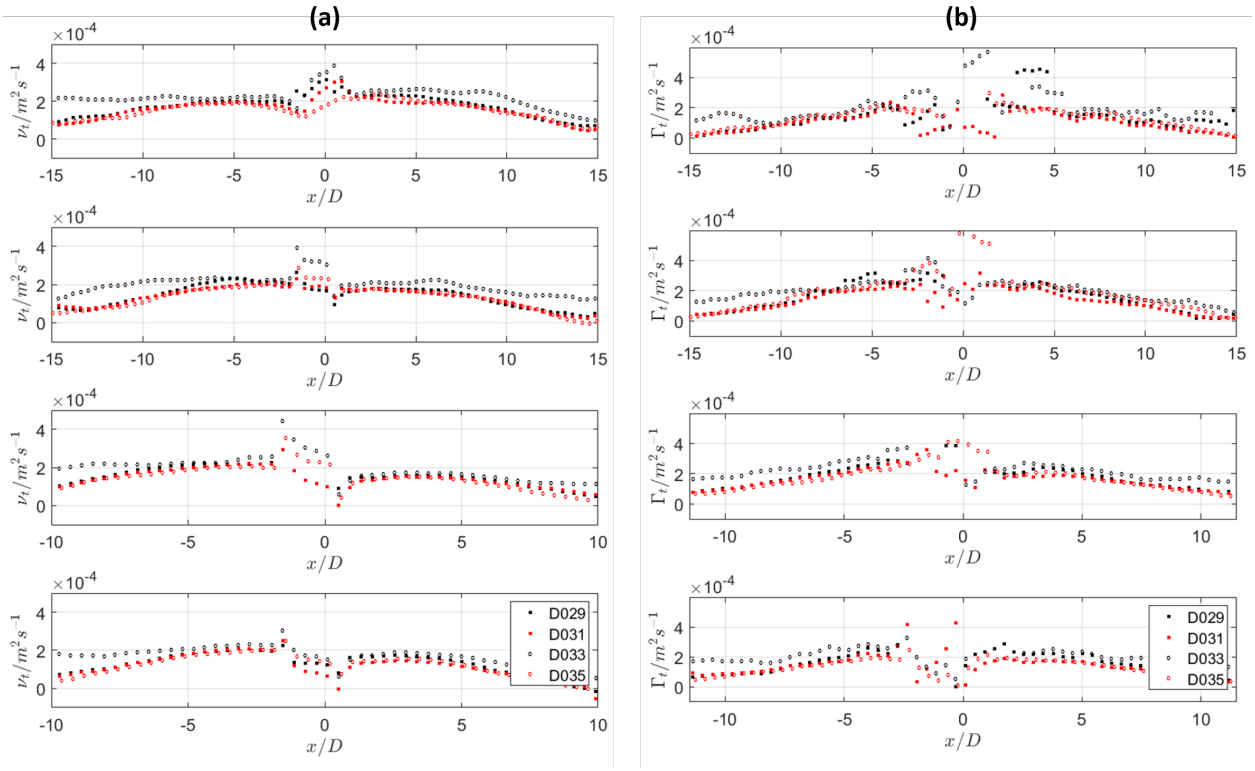

Figure 5.9: Radial profiles of (a) turbulent eddy viscosity and (b) turbulent diffusivity extracted at L/D = 50, 60, 70 and 80 (from bottom to top)

Similarly, the turbulent diffusivity, estimated using Equation 1.7, can be evaluated as: Equation 5.3, taking into account the turbulent flux and scalar gradient in crosswise direction,

$$\Gamma_t(\mathrm{x}) = -\overline{u'c'}/\frac{\partial \bar{c}}{\partial x} \tag{5.3}$$

The turbulent diffusivity for species mixing was analyzed accordingly and the results are plotted on the right in Figure 5.9(b) at different locations downstream of the jet inlet. The center region of the jet shows larger values and propagates out radially. Compared to the surrounding region, the reason why the center of the jet has strong variations in Figure 5.9 is that the scalar gradient at the denominator of Equation 5.3 has small values. For all

the experimental cases, with or without density difference, the turbulent diffusivities in the crosswise direction presents similar magnitude and trend, only slightly larger for light liquid injected into the heavy environment with the marker of black circles.

5.2.3 Scalar field characterization in the self-similar region

In the self-similar region of a free jet, profiles of mean flow quantities and turbulence statistics do not change with the downward location, when normalized using an appropriate parameter (e.g. centerline velocity, etc.). In other words, as the jet propagates freely in the media, for example, the velocity profiles decay but the shapes of these profiles remain the same. In Section 4.3, it has been shown that the normalized mean velocity and shears stress collapse onto each other from 25 jet-diameters away from the jet inlet. This behaviour should still hold when investigating the scalar transport of a turbulent round free buoyant jet.

After performing Gaussian fitting of the mean transport scalar profiles, $\Theta_c(y)$ is defined to be the value of the transport scalar along the jet centerline for a given downstream location y. Θ_c decays with the reciprocal of the downstream distance from a virtual origin $y_{0,c}$:

$$\frac{C_0}{\Theta_c} = K_c \left(\frac{y}{D} - \frac{y_{o,c}}{D} \right) \tag{5.4}$$

where C_0 denotes the scalar quantity at the jet inlet and K_c is the decay constant. To characterize the spreading of the jet scalar field, the scalar half-radius $r_{c,1/2)}(y)$ is introduced and defined as the radial location at which the local mean scalar is equal to half its value at the centerline according to the Gaussian fitting of the mean transport scalar profiles. In the jet self-similar region, the scalar half-radius can be expressed by a linear relation as a function of the downstream coordinate:

$$\frac{r_{c,1/2}}{D} = K_{r,c} \left(\frac{y}{D} - \frac{y_{0,rc}}{D} \right) \tag{5.5}$$

where $K_{r,c}$ is the spreading rate of $r_{c,1/2)}(y)$ and $y_{0,rc}$ is the virtual origin associated with the half-radius according to the definition.

The experimental cases of the uniform jets and positively/negatively buoyant jets are fitted according to Equation 5.4 and 5.5 in the range $45 \leq y/D \leq 85$. The decay constant K_c, the spreading rate $K_{r,c}$, and the two virtual origins are obtained and compared in Table 5.3 with experiments found in the published literature (experiments in References [8], [86], [87], [88] and [114] were performed with gas jets, while the experiments reported in References [115] and [116] were conducted in water), corresponding to buoyant free jets generated from pipe nozzles injecting into a quiescent environment with a density ratio of $\rho_{\text{jet}}/\rho_{\text{surr}}$. The centerline decay constant K_c of scalar quantities varies from 0.184 to 0.429 in the comparison table, and the virtual origin $y_{o,c}$ associated with the scalar transport also exhibits large variations as well. The deviations in results could arise from the differences in Reynolds numbers, density ratios, or viscosities between gases and liquids shown in Table 5.3. It turns out that our experiments tend to have a larger decay rate compared to the other experiments reported in Table 5.3, which could point out to a faster intermixing process between the two fluid solutions. The spreading rate $K_{r,c}$ shows a better agreement across different experiments for round jets, with all measurements resulting in values close to 0.1.

According to the self-similarity hypothesis, the normalized scalar fluctuations should reach asymptotically to the same value in the far-field of the jet flow. The streamwise evolution of the normalized centerline scalar fluctuations $\sqrt{\overline{c'c'}}/\Theta_c$ are plotted along the jet centerline and shown in Figure 5.10. The results are compared with the results obtained by Birch et al. [86], Lockwood and Moneib [87], Wilson and Danckwerts [114], and Nakamura et al. [116]. The 'asymptotic' values of $\sqrt{\overline{c'c'}}/\Theta_c$ are reported in Table 5.3, ranging from 0.181 to 0.225. Also, Figure 5.10 shows that the previous investigations by Birch et al. [86] and Lockwood and Moneib [87] have not achieved an asymptotic value. All our experiments agree with the normalized scalar fluctuations what Wilson and Danckwerts [114] and Nakamura et al. [116] measured. It can also be noticed that, compared to other experiments conducted for

this section, Reference Cases D031 (heavy liquid into heavy surroundings) shows a relatively lower magnitude (about 15% lower) of normalized scalar fluctuations but the trend has not yet reached its asymptotic value. Given this, experiments should be performed in the future to investigate the field further downstream into the fully developed self-similar region in order to verify the self-similarity hypothesis.

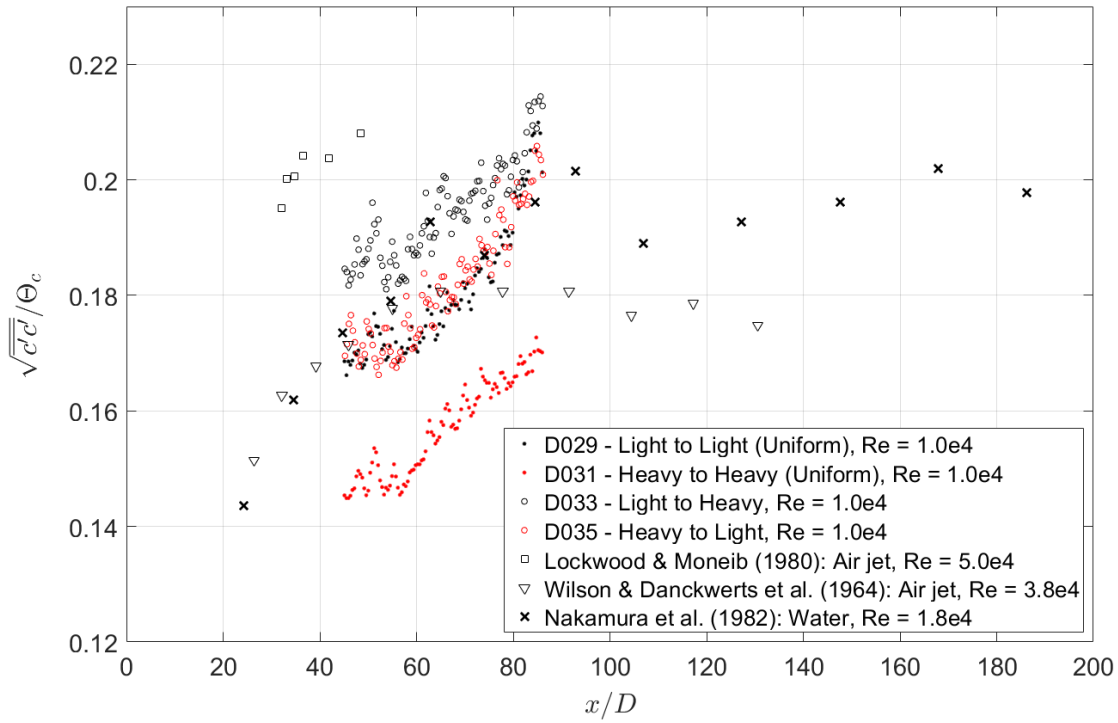

Figure 5.10: Centerline distributions of the normalized scalar fluctuations from $45 \leq y/D \leq 85$. Experimental results of the previously published literature are plotted in superposition for comparison.

Table 5.3: Scalar measurements comparisons for an axisymmetric jet with a pipe-shape outlet.

Authors/Cases	***Re***	$\boldsymbol{\rho_{jet}/\rho_{surr}}$	***Technique***	***y/D***	$\boldsymbol{K_c}$	$\boldsymbol{y_{o,c}}$	$\boldsymbol{K_{r,c}}$	$\boldsymbol{y_{0,rc}}$	$\boldsymbol{\sqrt{\overline{c'c'}}/\Theta_c}$
Wilson and Danckwerts(1964) [114]	38,000	1.000	Hot-wire	30 - 140	–	–	–	–	0.181
Birch et al. (1978) [86]	16,000	0.560	Raman scattering	0 - 70	0.225	5.80	0.097	0	–
Lockwood and Moneib (1980) [87]	50,400	0.540	Thermal-couple	0 - 50	0.184	2.00	0.132	2.00	–
Nakamura et al. (1982) [116]	5,000	1.000	PLIF	30 - 300	–	–	–	–	0.202
Dahm and Dimotakis (1990) [115]	5,000	1.000	PLIF	0 - 300	0.185	–	–	–	0.225
Richards and Pitts (1993) [88]	25,000	1.552	Rayleigh scattering	20 - 60	0.208	2.10	0.116	10.50	–
Mi et al. (2001) [8]	16,000	0.850	Cold-wire	0 - 70	0.216	4.73	0.102	1.30	–
D029	10,000	1.000	PLIF	45 - 85	0.364	4.34	0.074	5.12	0.208
D031	10,000	1.000	PLIF	45 - 85	0.360	2.53	0.075	4.77	0.170
D033	10,000	0.969	PLIF	45 - 85	0.429	3.73	0.088	5.13	0.213
D035	10,000	1.032	PLIF	45 - 85	0.309	2.90	0.077	7.44	0.200

5.3 Turbulent Statistics of Buoyant Jets in Two-Layer Stratified Environments

In this section, the experimental data for buoyant jets in a two-layer stratified environment are discussed. The jet impinging the stratified layer will behave as a positively buoyant jet until it reaches the sharp density interface, therefore the previous experiments on positively buoyant jets in uniform environments are used for comparison. The experimental tests discuss in this section includes the following cases, using Solution I and II mentioned in Table 3.1 as working fluids:

- Positively Buoyant Jet **D033**: Solution I being injected into Solution II at 3.16% density difference at Re = 10,000;
- Positively Buoyant Jet **D034**: Solution I being injected into Solution II at 3.16% density difference at Re = 4,000;
- Sharp Density Interface **D042**: Solution I being injected on a density interface created by Solution I and II at Re = 10,000;
- Sharp Density Interface **D043**: Solution I being injected on a density interface created by Solution I and II at Re = 4,000.

5.3.1 Mean velocity and scalar transport

Figure 5.11 shows the streamwise mean velocity fields for the two experimental pairs D033/D042 with Re = 10,000 and D034/D043 with Re = 4,000 respectively. The experimental data for buoyant jets injected into a two-layers stratified environment are compared with the corresponding buoyant jet injected into a uniform environment. In Figure 5.11(a), the streamwise mean velocity field for D042 is plotted in shading with the superimposed isolines corresponding to D033. It can be noticed that when the Reynolds number is equal to 10,000, the velocity fields of the jets are similar independently from the presence of a

sharp density interface. However, the positively buoyant jet has a slightly wider spreading than the jet impinging with the stratified interface. With the sharp density interface, the mixing process seems to get suppressed. Figure 5.11(b) shows the comparison for the runs with Re = 4,000 (D034 and D043). It is obvious that the buoyant jet behavior in a uniform environment is very different compared to the case with the two-layer stratification: negative streamwise velocities can be found in the contour plot of case D043, meaning there is a downward current in the jet flow when a two-layer stratification is impacted by a low Re-number jet. This confirms the theory mentioned at the beginning of the chapter: after the momentum carried by jet starts to decay as the downstream distances increase, buoyancy effects start to dominate. In the two-layer stratified environment, the lighter fluid jet will entrain and mix with the denser liquid once it leaves the nozzle, increasing the overall jet density as the jet moves downstream of the jet nozzle. After it passes the density interface, the jet becomes a negatively buoyant jet, with the buoyant force acting in the opposite direction as the momentum force.

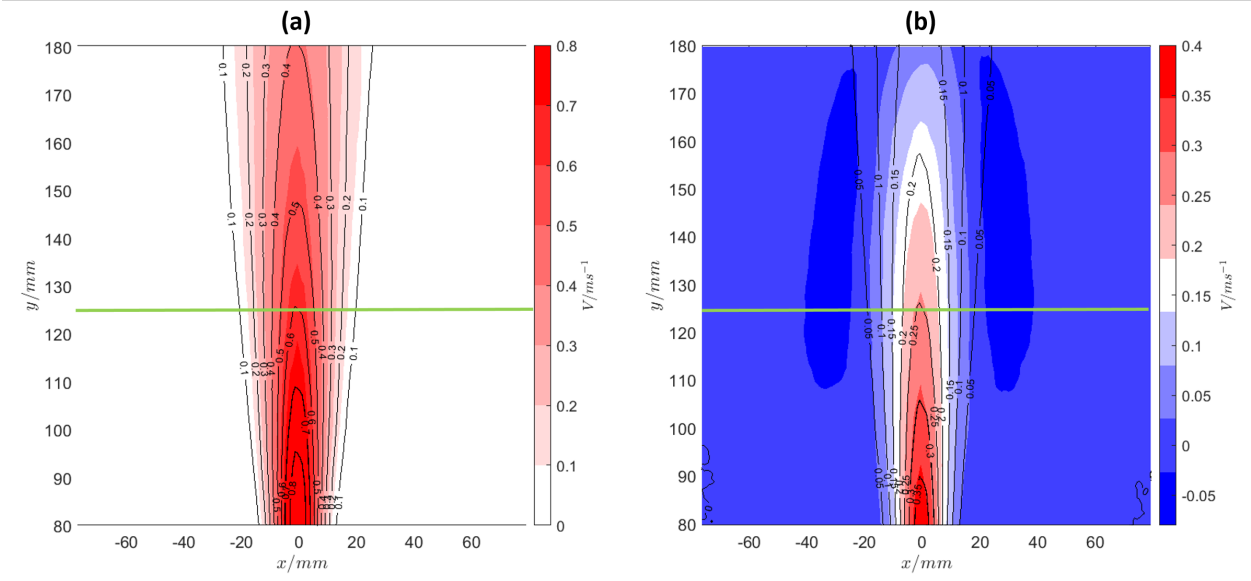

Figure 5.11: Fields of streamwise mean velocity: (a) D033 for positively buoyant jet in isolines vs. D042 for two-layer stratified setup in shading with Re = 10,000, and (b) D034 for positively buoyant jet in isolines vs. D043 for two-layer stratified setup in shading with Re = 4,000. The green line at y = 125mm indicates the two-layer interface location.

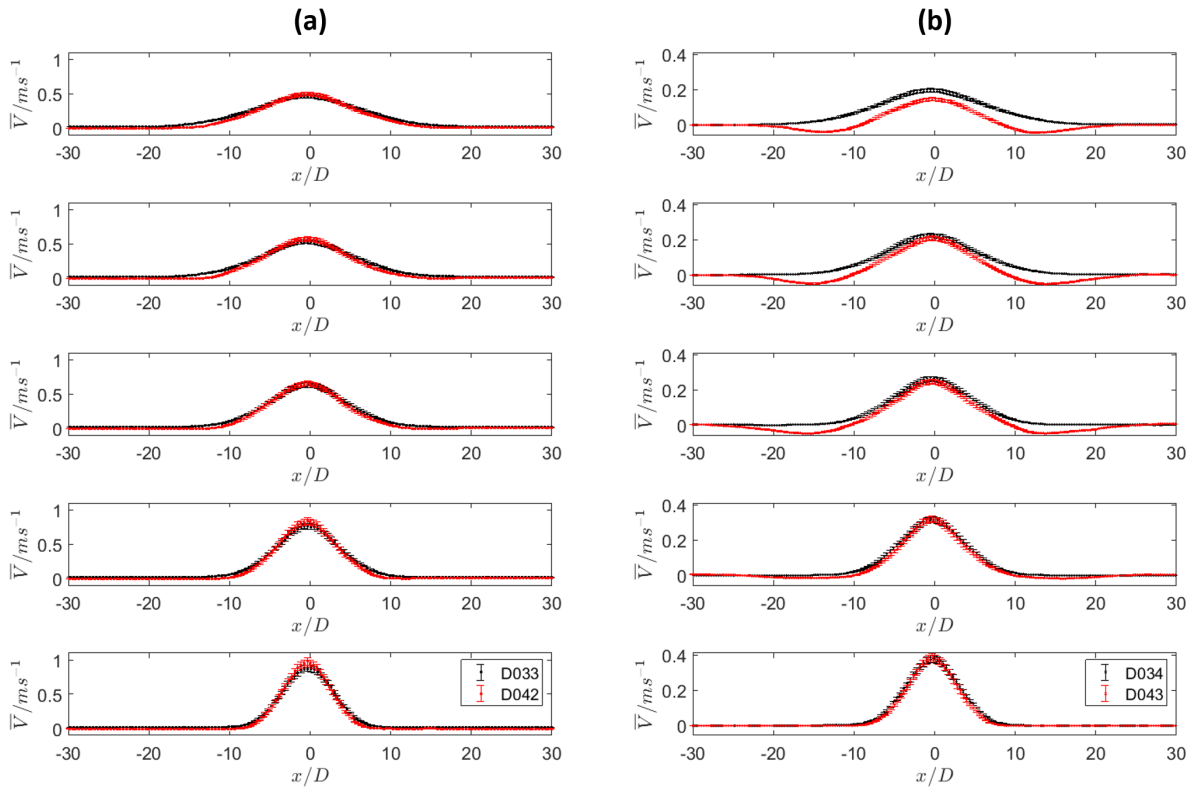

Figure 5.12: Radial profiles of mean streamwise velocity at y/D = 40, 50, 62.5, 70 and 80 (from bottom to top) for the comparisons between (a) D033 and D042 with Re = 10,000, and (b) D034 and D043 with Re = 4,000.

As mentioned previously, after the momentum carried by jet starts to decay as the downstream distances increase, buoyancy effects start to dominate. In the two-layer stratified environment, the lighter fluid jet will entrain and mix with the denser liquid once it leaves the nozzle, leading to an increase of the overall jet density as the jet moves downstream of the jet nozzle. After it passes the density interface, the jet becomes a negatively buoyant jet, with the buoyant force acting in the opposite direction of the momentum force. To better visualize these effects, Figure 5.12 shows the radial profiles of the evolution of the streamwise mean velocity along the vertical axis of the jet at downstream locations of y = 80, 100, 125 (the interface), 140, and 160 mm respectively (corresponding to y/D = 40, 50, 62.5, 70 and 80). In Figure 5.12(a), with the higher Reynolds number Re = 10,000, the streamwise velocity profiles for both jets follow the same trend, with Gaussian-shape profiles that spread and decay as the jet travels further downstream. It can also be noticed that the positively buoyant jet does have wider streamwise velocity profiles after the stratified interface is crossed (the interface is located at y =125 mm, corresponding to y/D = 62.5). The entrainment from the surrounding fluid causes a small decrease in the streamwise velocity as well. Therefore, enhanced mixing is observed for the positively buoyant jet with a higher Reynolds number compared to the jet in the presence of a sharp density interface.

Interesting trends are presented in Figure 5.12(b), where the runs for Re = 4,000 are reported. Before the jet reaches the stratified interface located at y/D = 62.5 (y = 125 mm), the velocity profiles do behave similarly in both cases of the uniform denser environment (D034) and two-layer stratified environment (D043) since both flows consist of the positively buoyant jet with the same inlet conditions. However, as already seen in Figure 5.11(b), the streamwise mean velocity profiles for the jet in the two-layer stratified environment exhibit negative values while the center of the jet is still moving upward. While the centerline jet velocity decreases as the downstream distance increases, the spreading of the reverse flow also decreases. This indicates that the jet does exhibit a finite penetration depth within the fluid domain at which location the centerline velocity decays to zero, and the fluid previously

entrained by the jet start moving downward, due to the prevalence of the buoyancy forces.

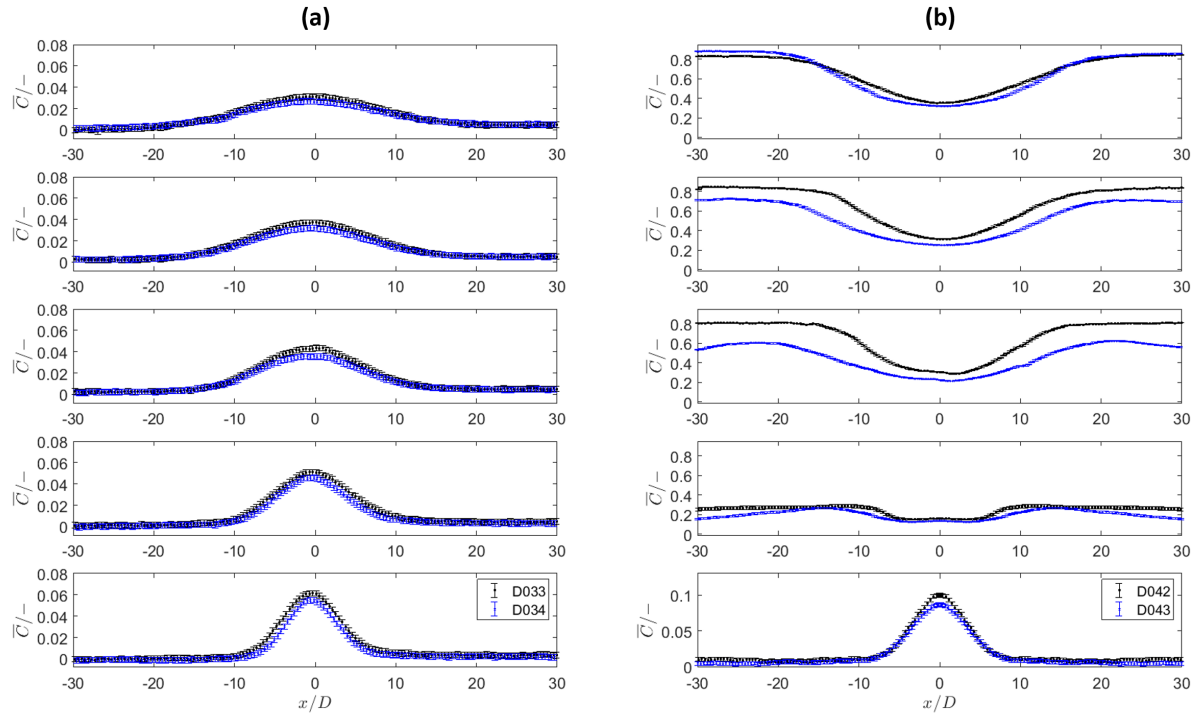

Figure 5.13: Radial profiles of mean concentration at y/D = 40, 50, 62.5, 70 and 80 (from bottom to top) for comparisons between (a) D033 in black dots and D034 in blue crosses, and (b) D042 in black dots and D043 in blue crosses.

The radial profiles of the evolution of the transport scalar at different downstream locations are shown in Figure 5.13. For the positively buoyant jet, the jet's mean scalar transport has Gaussian-shape profiles, spreading and decaying as the jet travels further downstream for both Reynolds numbers of 10,000 and 4,000 respectively shown in Figure 5.13(a). For the positively buoyant jet D033 with Re = 10,000, the maximum mean scalar transportation is about 10.4% larger than the case D034 with Re = 4,000 at the jet centerline with y = 80 mm (40D away from the inlet). The same behavior can be observed in Figure 5.13(b) for the jets in the presence of a two-layer stratified interface, at locations below the sharp density layer (e.g., at y = 80 mm), where the jet behaves still as a positively buoyant jet. Shown in Figure 5.13(b), compared to the jet with a higher momentum at Re = 10,000 (D042) for which the mixing is happening at the jet central region, it can be seen that for the case D043

with Re = 4,000 most of the mixing processes happen and propagate outward at location y/D = 62.5 after the jet has penetrated the two-layer interface and come back down to the sharp layer. This is consistent with the wider negative mean velocity spreading shown in Figure 5.11(b) for case D043.

5.3.2 Shear stresses and turbulent kinetic energy (TKE)

In Figure 5.14, the shear stresses normalized by the square of the inlet velocity for the four runs with the same scale at y = 100, 125, 140 and 160mm (y/D = 50, 62.5, 70 and 80) are plotted in pairs of the same Reynolds number for (a) D033 v.s. D042 with Re = 10,000, and (b) D034 v.s. D043 with Re = 4,000 to illustrate the influences of the sharp density interface. The normalized shear stress radial profiles appear to be unaffected in the self-similar region of the jet flow for all cases, meaning the shear stresses induced by the turbulent jet momentum is almost identical for different inlet velocities with or without the presence of the sharp density interface.

The results for the turbulent kinetic energy normalized by the square of the inlet velocity with the same scale are reported in Figure 5.15 for (a) D033 and D042 with Re = 10,000 and (b) D034 and D043 with Re = 4,000. In Figure 5.15(a), it can be shown that the positively buoyant jet D033 has a slightly larger spreading of TKE compared to the jet with a sharp layer setup in D034 with Re = 10,000, indicating the mixing is suppressed when the density interface is present. This agrees with the velocity contour plot shown in Figure 5.11(a). For the cases with lower Reynolds number (Re = 4,000) shown in Figure 5.15(b), the normalized TKE shows a larger value at y = 160mm (80D away from the nozzle) compared to the other cases because the flow gets more turbulent due to the mixing from the upcoming jet with the reversed flow from the top. In Figure 5.15(b), it can be shown that the buoyant jet impacting on the sharp interface with a lower Reynolds number Re = 4,000 has a larger turbulent kinetic energy in the surrounding regions ($|x/D| \geq 10$), mainly caused by the reverse flow coming from the top and starting to disturb and propagate outward. This

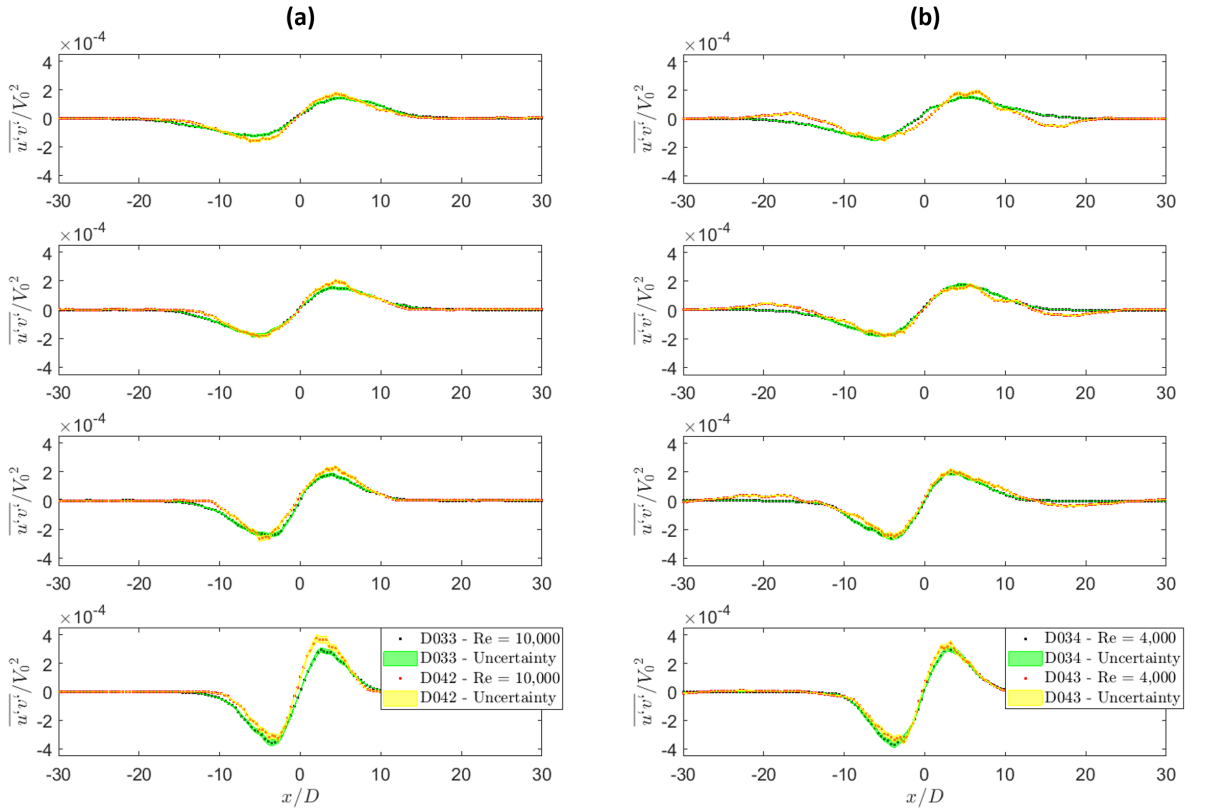

Figure 5.14: Normalized shear stress at downstream locations y/D = 40, 50, 62.5, 70 and 80 (from bottom to top) between (a) D033 and D042 with Re = 10,000, and (b) D034 and D043 with Re = 4,000.

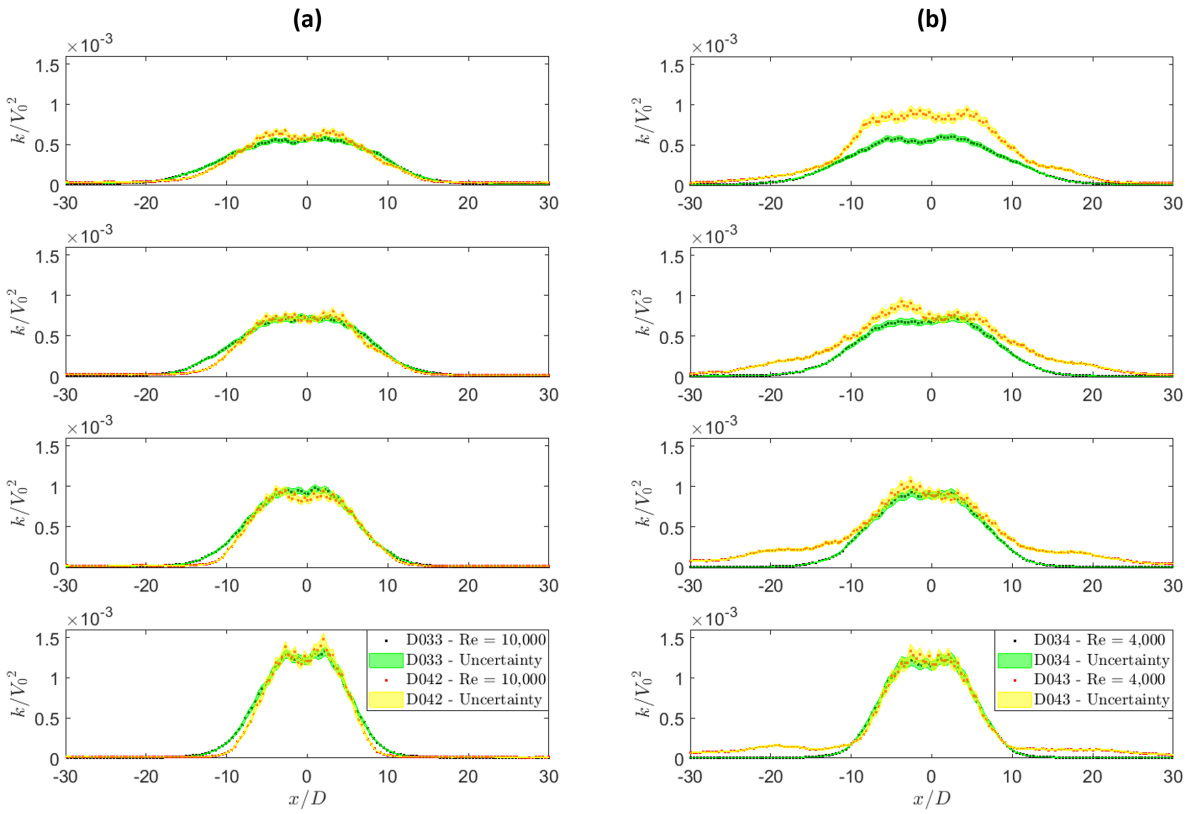

Figure 5.15: Normalized turbulent kinetic energy at downstream locations y/D = 40, 50, 62.5, 70 and 80 (from bottom to top) between (a) D033 and D042 with Re = 10,000, and (b) D034 and D043 with Re = 4,000.

means that the reverse flow in D043 introduces more turbulence to the downstream location where the density interface exists, the mixing process at y = 125mm (62.5D away from the inlet) behaving more turbulent in the surrounding regions ($|x/D| \geq 10$) than the positively buoyant jet flow (D034) with the same Reynolds number of 4,000.

5.3.3 Penetration depth

Figure 5.16 shows time snapshots of the PLIF measurement of the jet impacting the sharp density interface with Re = 4,000. Because of the lower jet momentum compared to the buoyancy force, this is the only case in the experimental campaign discussed here in which the jet has a finite maximum penetration depth and reversed flow can be observed. It can also be observed that by using the RIM technique, excellent image contrast is obtained when compared to the results by Shakouchi et al. [21] reported in Figure 3.1, for which RIM was not employed. According to the PLIF measurements as well as the velocity fields, the maximum penetration depth for the case D043 can be estimated to be 192 ± 1 mm. Ansong et al. [39] mentioned a theoretical solution for the penetration of a turbulent buoyant jet impinging into a two-layer stratified environment, as stated in Equation 5.6:

$$Z_{\max} = \left(\frac{2}{5}\right)^{1/6} \left(\frac{3}{2} - \mu\tilde{F}\right)^{1/2} H \tag{5.6}$$

where H is the distance of the jet inlet from the stratified interface, $\mu \approx 0.8$ is an empirical constant proposed by Abraham [117], and $\tilde{F} = V_i^2 / \left[(\rho_i - \rho_{\text{upper}})\, gH/\rho_{\text{jet}}\right]$ in which V_i is the streamwise centerline jet velocity at the stratified interface and ρ_{upper} is the fluid density of the upper layer. According to Figure 5.12, the average jet velocity at the stratified interface is $V_i = 0.249 \pm 0.013\ m/s$. Assuming the density of the flow is proportional to the scalar measurement, the density at the interface is estimated to be $\rho_i = 1.037 \pm 0.006\ kg/m^3$. This results in a value of $\mu\tilde{F} > 3/2$, an consequently in an imaginary value for $Z_{\max}$. Gustafsson and Larsen [118], warns that the correlation of Equation 5.6 might fail because it assumes

a continuous and instantaneous redistribution of density difference within the jet as the density changes at the fringe of the jet. Since there is still very limited literature available for high-resolution velocity- and scalar-field measurements of a buoyant jet impacting a two-layer stably stratified environment with reverse flow, the theoretical formulation of the penetration depth for such scenario is still not settled. The experimental setup used in this dissertation could be employed in the future to gather additional data and develop a better correlation for the penetration depth.

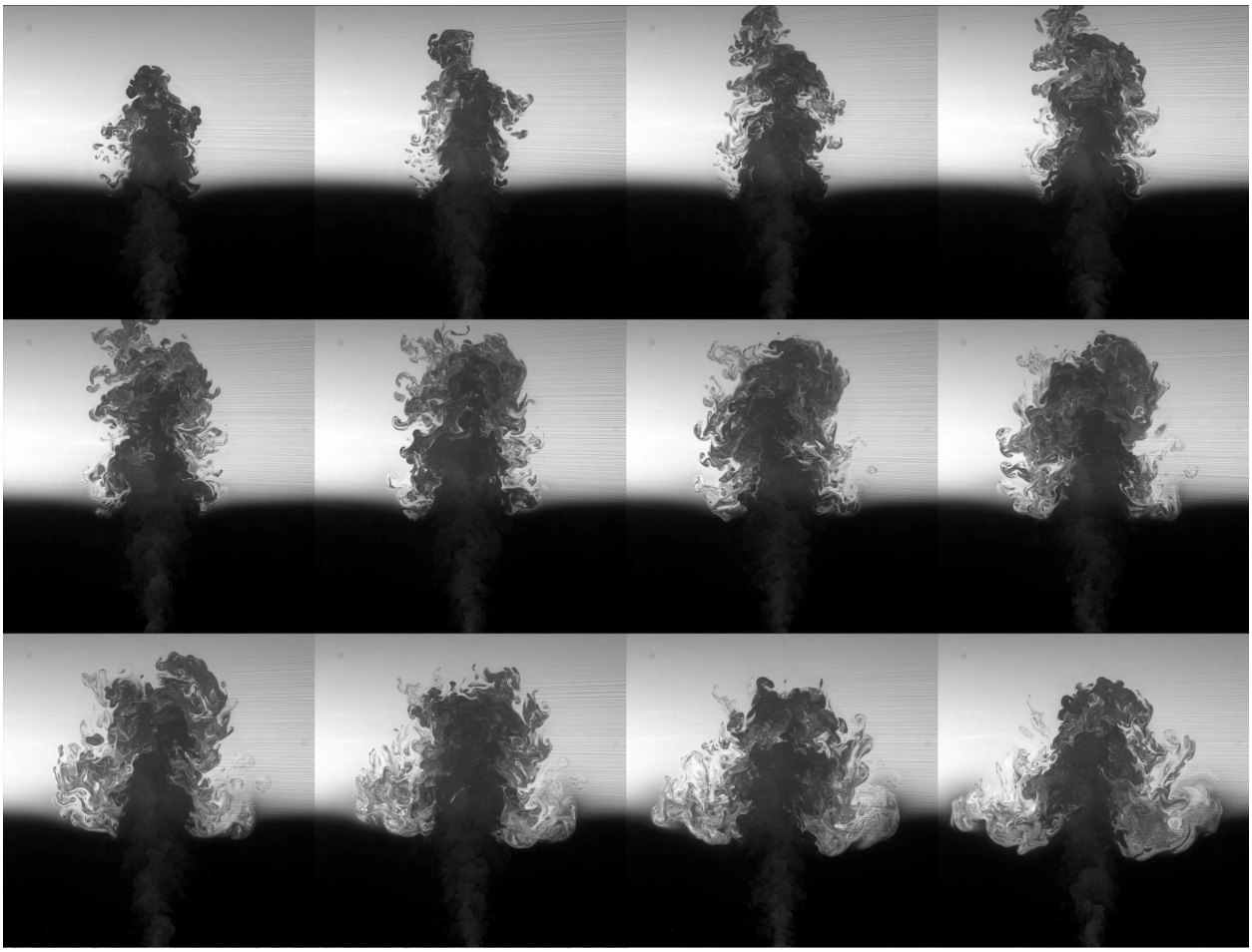

Figure 5.16: Snapshots of PLIF measurements with a time-step of 0.04 seconds between each photo from left to right, up to bottom.

5.4 Centerline Profiles Decay for Streamwise Velocity

In chapter 1 it has been discussed that the centerline streamwise velocity decay can be expressed by the following relationship:

$$\frac{V_0}{V_c(x)} = \frac{1}{K_v}\left(\frac{y}{D} - \frac{y_{0,v}}{D}\right) \tag{1.1}$$

The mean streamwise velocity decay normalized by the inlet velocity along the centerline from downstream locations y/D = 45 to 80 is plotted in Figure 5.17 for all the uniform cases measured at the miniDESTROJER facility . Two separate clusters of lines can be clearly identified, an upper cluster corresponding to the uniform turbulent cases with Re = 10,000 and 4,000, and the lower cluster corresponding to lower Reynolds number of 2,000. For each line cluster, a dashes curve is fitted to represent the average of the cluster. These are used as the reference for the comparison with the cases involving density differences (DD) reported in Figure 5.18.

In Table 5.4 a summary is presented of the fitted parameters for the decay constant K_v and jet virtual origin $y_{0,v}/D$ of Equation 1.1. It can be noticed that the negatively buoyant jets have a relatively closer decay constant compared with the uniform cases. However, for the positively buoyant jet with Re = 10,000 and 4,000 as well as the jet impinging the two-layer stratified layer with Re = 10,000 exhibit noticeably smaller values of K_v, indicating a faster decaying jet centerline mean streamwise velocity. Similar as the comparison shown in Table 4.4, the virtual jet origin $y_{0,v}/D$ still seems to be scattered across all the cases presented here, except for the positively and negatively buoyant jets, which present a larger $y_{0,v}/D$ value when the Reynolds number is as low as 2,000. This could be interpreted as a different decay mechanism for low Re jet flows.

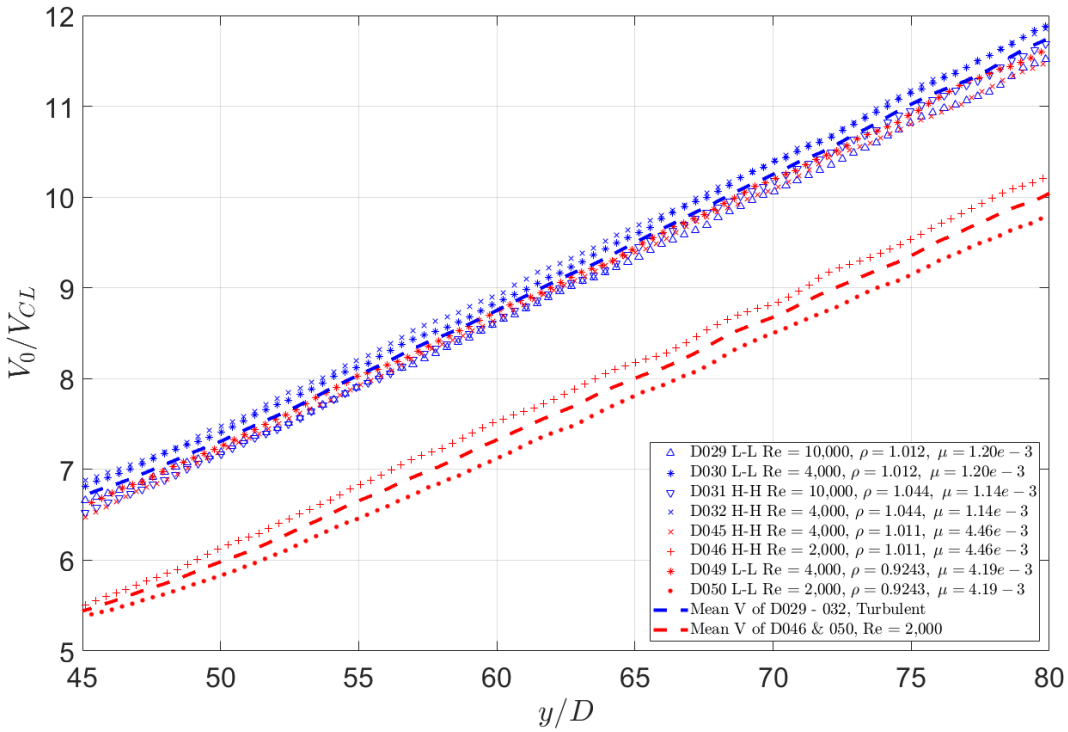

Figure 5.17: Normalized centerline streamwise velocity decay from downstream locations y/D = 45 to 80 for all uniform cases conducted in miniDESTROJER facility. Legend specifies the case details for fluid properties, and L stands for lighter fluid, H for heavier.

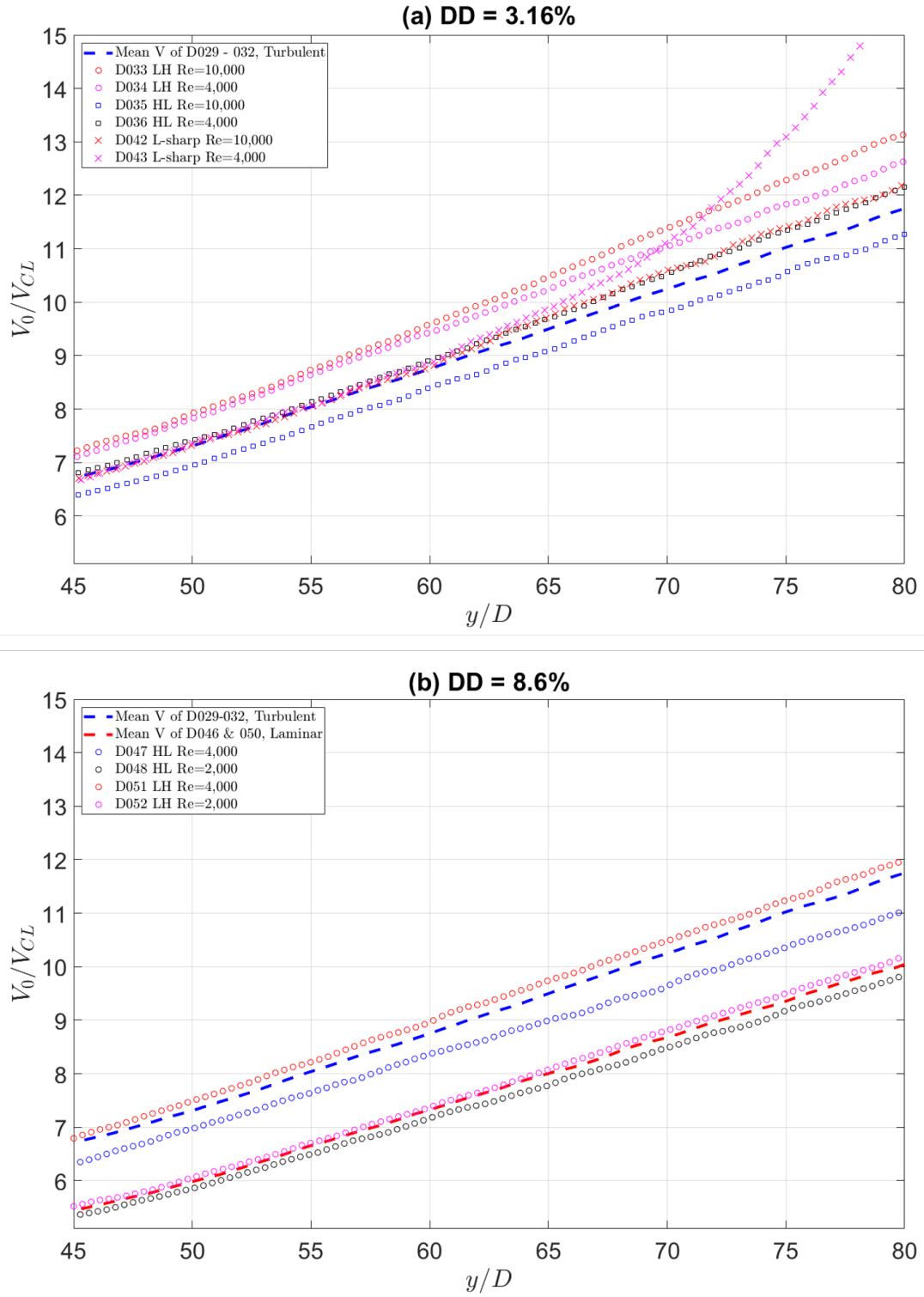

Figure 5.18: Normalized centerline streamwise velocity decay compared with the uniform references from downstream locations y/D = 45 to 80 for (a) 3.16 % density difference cases and (b) 8.6 % density difference cases.

Table 5.4: Comparison for the centerline streamwise velocity decay constant and virtual jet origins between the turbulent buoyant jet cases and the uniform jet cases.

Cases	***Re***	$\boldsymbol{\Delta\rho}$	$\boldsymbol{K_v}$	$\boldsymbol{y_{0,v}/D}$
Uniform	$\geq$ 4,000	0	6.826 $\pm$ 0.032	0.044 $\pm$ 0.288
Uniform	2,000	0	7.446 $\pm$ 0.033	5.361 $\pm$ 0.274
D033	10,000	+3.16%	5.754 $\pm$ 0.037	4.567 $\pm$ 0.399
D034	4,000	+3.16%	6.270 $\pm$ 0.020	0.861 $\pm$ 0.185
D035	10,000	-3.16%	7.003 $\pm$ 0.034	1.175 $\pm$ 0.302
D036	4,000	-3.16%	6.410 $\pm$ 0.050	2.539 $\pm$ 0.479
D042	10,000	Sharp Interface	5.981 $\pm$ 0.040	6.884 $\pm$ 0.443
D047	4,000	-8.6%	7.413 $\pm$ 0.022	-1.721 $\pm$ 0.187
D048	2,000	-8.6%	7.651 $\pm$ 0.047	5.081 $\pm$ 0.353
D051	4,000	+8.6%	6.689 $\pm$ 0.018	-0.131 $\pm$ 0.145
D052	2,000	+8.6%	7.305 $\pm$ 0.048	5.815 $\pm$ 0.393

5.5 Centerline Profiles Decay for TKE

Starting with the Navier-Stokes (NS) equations, assuming sufficiently high Reynolds number, Kolmogorov [119] derived an exact relationship between the second- and third-order moments of the longitudinal velocity increment assuming homogeneous, isotropic turbulence. However, in normal laboratory conditions the assumption of very large Re is not always practical to achieve, therefore, the global isotropy assumption would fail. In this light, Danaila et al. [120] revisited the hypotheses and derived a generalized scale-by-scale energy equation along the centerline of a turbulent round jet with the local isotropy assumption:

$$\begin{aligned} &- \left\langle (\delta v)(\delta q)^2 \right\rangle + 2\nu \frac{\mathrm{d}}{\mathrm{d}l} \left\langle (\delta q)^2 \right\rangle - \frac{V}{l^2} \int_0^l s^2 \frac{\partial}{\partial y} \left\langle (\delta q)^2 \right\rangle \mathrm{d}s \\ &\qquad - 2 \frac{\partial V}{\partial y} \frac{1}{l^2} \int_0^l s^2 \left(\left\langle (\delta v)^2 \right\rangle - \left\langle (\delta u)^2 \right\rangle \right) \mathrm{d}s = \frac{4}{3} \langle \varepsilon \rangle l \end{aligned} \tag{5.7}$$

where $\delta v = v(y+l) - v(y)$ that l is defined to be the spacing in the streamwise direction y, V is the mean streamwise velocity, $\langle(\delta q)^2\rangle$ $(= \langle(\delta v)^2\rangle + \langle(\delta u)^2\rangle + \langle(\delta w)^2\rangle)$ is the total turbulent energy structure function, $\langle\varepsilon\rangle$ is the mean dissipation rate of turbulent kinetic energy, and ν is the kinematic viscosity. One possible equilibrium similarity solution of Equation 5.7 is a power-law of the form:

$$\langle q^2 \rangle = K_k (y - y_{o,k})^m \tag{5.8}$$

where $\langle q^2 \rangle = \langle v^2 \rangle + 2\langle u^2 \rangle$ along the jet centerline, $y_{o,k}$ is the virtual origin for the TKE decay, m is the power-law exponent and K_k is a constant of proportionality. It can be noticed that $k = 2\langle q^2 \rangle$ according to the definition of TKE (Equation 2.9) in the thesis.

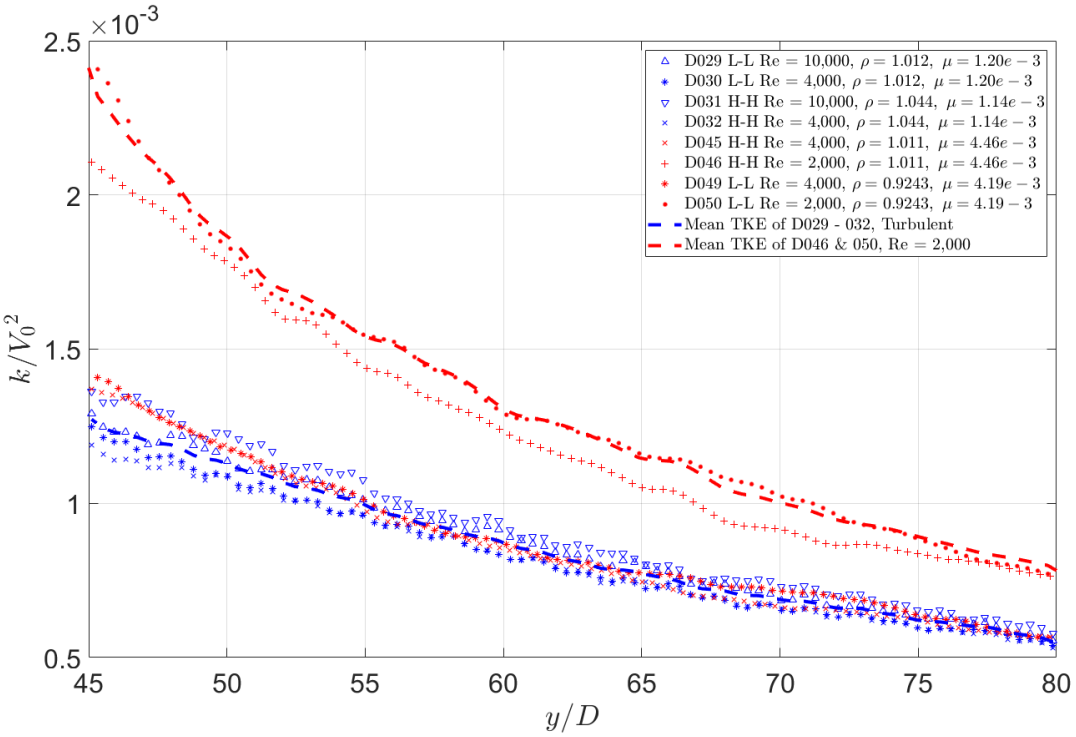

Figure 5.19: Normalized centerline TKE decay from downstream locations y/D = 45 to 80 for all uniform cases conducted in miniDESTROJER facility. Legend specifies the case details for fluid properties, and L stands for lighter fluid, H for heavier.

In Figure 5.19, the centerline TKE decay normalized by the inlet velocity from downstream locations y/D = 45 to 80 is plotted for all the uniform cases measured at the miniDESTROJER facility. Due to the differences in the Reynolds number, there are two

separate clusters of lines, as expected: the upper cluster corresponds to the uniform turbulent cases with Re = 10,000 and 4,000, and the lower cluster correspond to a Reynolds number of 2,000. For each line cluster, a dashes curve is fitted to represent the average of the uniform cases. These are used as reference for the comparison with the cases involving density differences (DD), presented in Figure 5.20.

According to Equation 5.8, a power-law curve fitting is applied to the TKE variations along the centerline for turbulent buoyant jets with density differences, together with the uniform jet cases. The fitting parameters are summarized in Table 5.5. We notice a remarkable agreement for the power-law exponent m across all cases, taking into account the fitting uncertainties. The decay rate constant K_k, instead, presents large uncertainties.

Table 5.5: The centerline TKE power-law fitted parameters comparison between the turbulent buoyant jet cases and the uniform jet cases as well as the uniform jet data from Sadeghi et al. (2015) [29].

Cases	***Re***	$\boldsymbol{\Delta\rho}$	$\boldsymbol{K_k}$	$\boldsymbol{m}$
Sadeghi et al. (2015) [29]	50,000	0	3.29	-1.83
Uniform	$\geq$ 4,000	0	3.036 $\pm$ 2.402	-1.73 $\pm$ 0.405
Uniform	2,000	0	3.620 $\pm$ 3.265	-1.782 $\pm$ 0.264
D033	10,000	+3.16%	9.986 $\pm$ 21.576	-1.958 $\pm$ 0.801
D034	4,000	+3.16%	3.398 $\pm$ 5.909	-1.760 $\pm$ 0.656
D035	10,000	-3.16%	6.034 $\pm$ 7.133	-1.862 $\pm$ 0.444
D036	4,000	-3.16%	7.668 $\pm$ 14.016	-1.924 $\pm$ 0.680
D042	10,000	Sharp Interface	15.656 $\pm$ 56.052	-2.095 $\pm$ 1.335
D047	4,000	-8.6%	3.678 $\pm$ 2.341	-2.049 $\pm$ 0.617
D048	2,000	-8.6%	6.376 $\pm$ 7.072	-1.883 $\pm$ 0.439
D051	4,000	+8.6%	5.932 $\pm$ 8.934	-1.917 $\pm$ 0.575
D052	2,000	+8.6%	3.822 $\pm$ 2.080	-1.803 $\pm$ 0.217

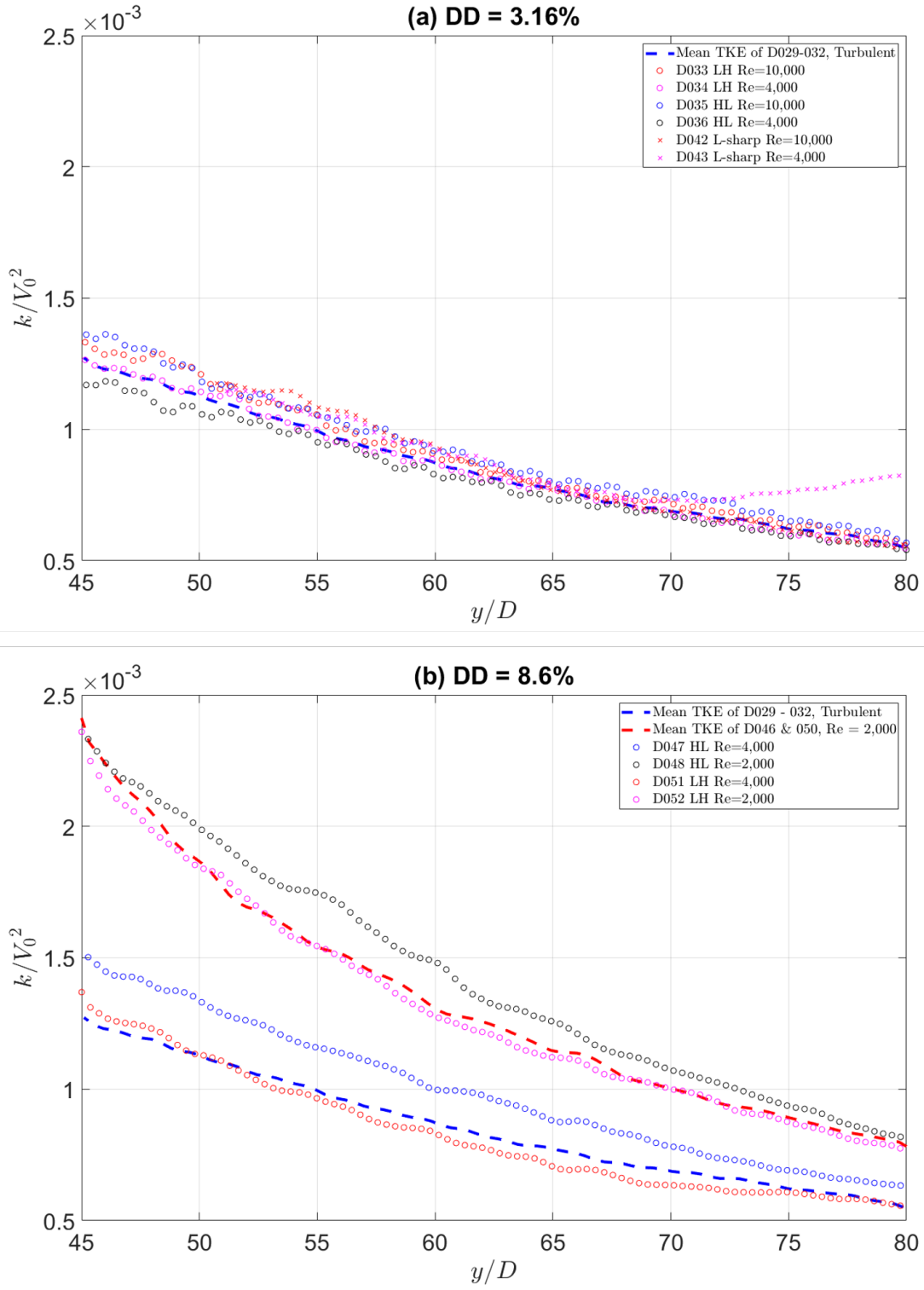

Figure 5.20: Normalized centerline TKE decay compared with the uniform references from downstream locations y/D = 45 to 80 for (a) 3.16 % density difference cases and (b) 8.6 % density difference cases.

5.6 Entrainment in the Self-similar Regions

According to Equation 1.2, in Section 4.4 we have discussed that, for turbulent uniform jets, there exists a linear relationship between the spread rate of the jet half-width and the downstream locations beyond the jet potential core region ($y/D \geq 15$) .

$$\frac{r_{1/2}}{D} = K_r \left(\frac{y}{D} - \frac{y_{0,r}}{D} \right) \tag{1.2}$$

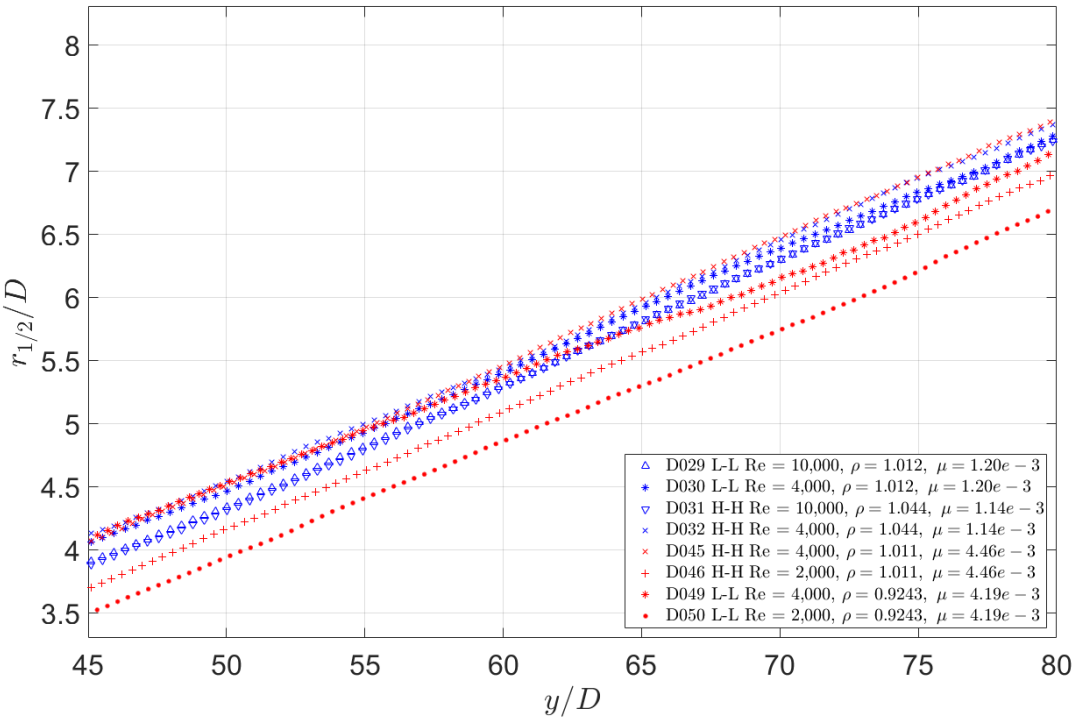

Figure 5.21: Axial evolution of the jet half-width for all uniform cases conducted in miniDESTROJER facility. Legend specifies the case details for fluid properties, and L stands for lighter fluid, H for heavier.

The axial evolution of the jet half-width from downstream locations y/D = 45 to 80 is plotted in Figure 5.21 for all the uniform cases measured at the miniDESTROJER facility. It has been shown in Table 4.5 that the inlet conditions of Re and the jet nozzle types have fewer effects on the spreading rate of the jet half-width. There is also no remarkable difference that can be observed in Figure 5.21 with regards to the $r_{1/2}/D$ increasing slope.

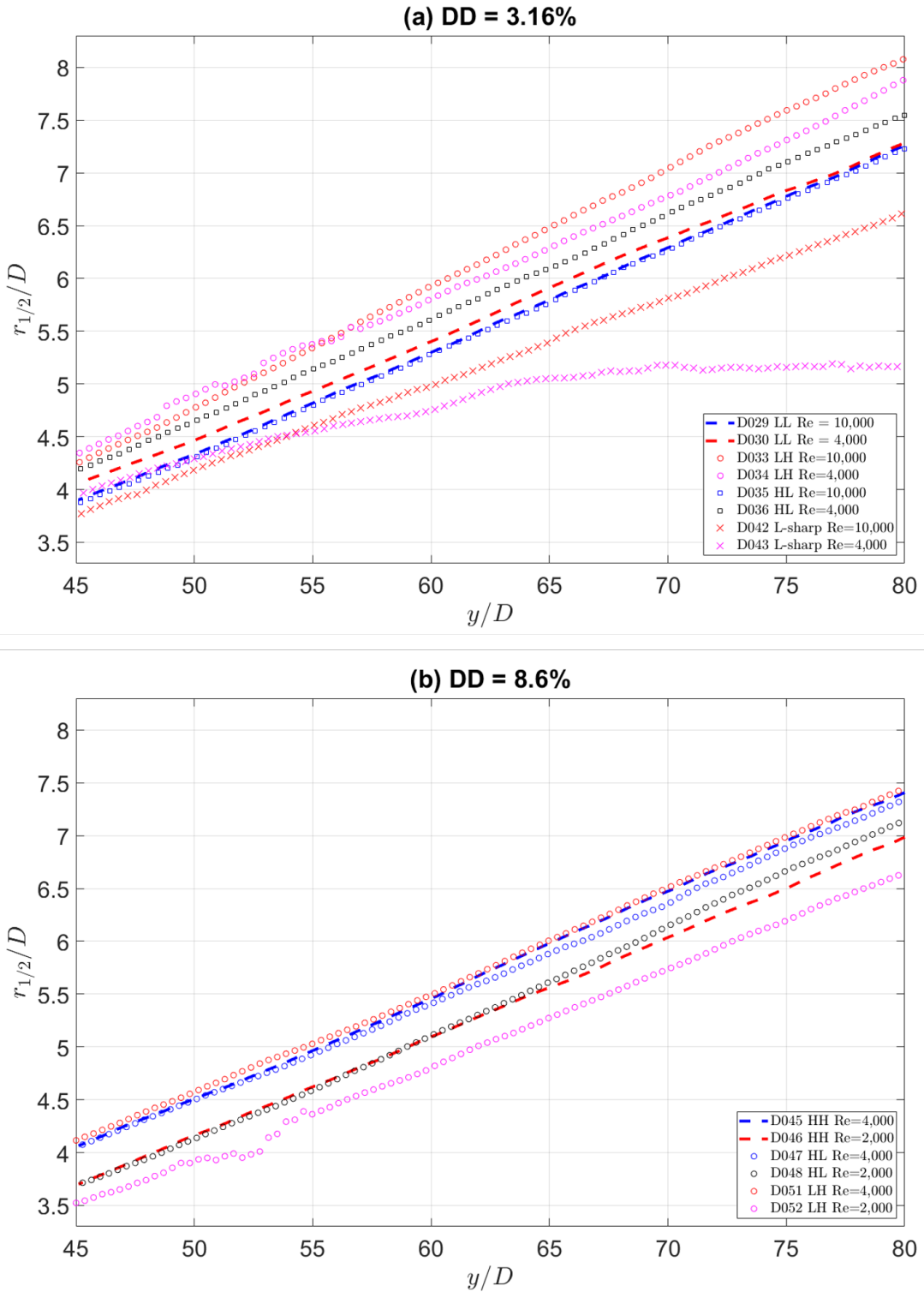

Figure 5.22: Axial evolution of the jet half-width compared with the uniform references from downstream locations y/D = 45 to 80 for (a) 3.16 % density difference cases and (b) 8.6 % density difference cases.

Therefore, selected uniform cases are used as the reference for the comparison with the cases involving density differences (DD), and presented in Figure 5.22.

The data are then fitted to estimate the parameters in Equation 1.2. The obtained results are summarized in Table 5.6, including the constant K_r and the jet virtual origin for the jet half-width $y_{0,r}/D$, to investigate the effect of density on the entrainment of a turbulent round jet. The values of K_r present no significant difference between the uniform jets and buoyant jets with respect to the inlet Reynolds number. The only exception is found for the positively buoyant jet case D033 and the jet impinging the two-layer stratified environment. The larger K_r for D033 agrees with the previous findings, indicating an enhanced mixing process with a larger entrainment rate. In the two-layer stratified case (corresponding to a positively buoyant jet before the sharp interface), the smaller value of K_r indicates an overall confined entrainment process due to the presence of the stratified layer. No clear trend is observed for the virtual jet origin of the jet half-width $y_{0,r}/D$.

Table 5.6: Comparison of jet half-width spread rate and corresponding constants between the turbulent buoyant jet cases and the uniform jet cases.

Cases	***Re***	$\boldsymbol{\Delta\rho}$	$\boldsymbol{K_r}$	$\boldsymbol{y_{0,r}/D}$
Uniform	$\geq$ 4,000	0	0.0946 ± 0.0005	0.2808 ± 0.0290
Uniform	2,000	0	0.0927 ± 0.0002	0.5874 ± 0.0151
D033	10,000	+3.16%	0.1119 ± 0.0004	0.8018 ± 0.0253
D034	4,000	+3.16%	0.0983 ± 0.0008	0.0652 ± 0.0504
D035	10,000	-3.16%	0.0974 ± 0.0003	0.5552 ± 0.0160
D036	4,000	-3.16%	0.0976 ± 0.0002	0.2307 ± 0.0132
D042	10,000	Sharp Interface	0.0814 ± 0.0003	-0.1078 ± 0.0169
D047	4,000	-8.6%	0.0947 ± 0.0005	0.2528 ± 0.0292
D048	2,000	-8.6%	0.1005 ± 0.0005	0.9002 ± 0.0328
D051	4,000	+8.6%	0.0962 ± 0.0004	0.2448 ± 0.0225
D052	2,000	+8.6%	0.0913 ± 0.0007	0.6543 ± 0.0438

5.7 Centerline Streamwise Velocity Skewness and Flatness Factor in the Self-similar Regions

In order to investigate the effect of density variations on the centerline streamwise velocity PDF in the self-similar region, the skewness factor (SF) and flatness factor (FF) are both plotted in Figure 5.23 and compared with the uniform jet cases D029 and D046 (plotted in dashes).

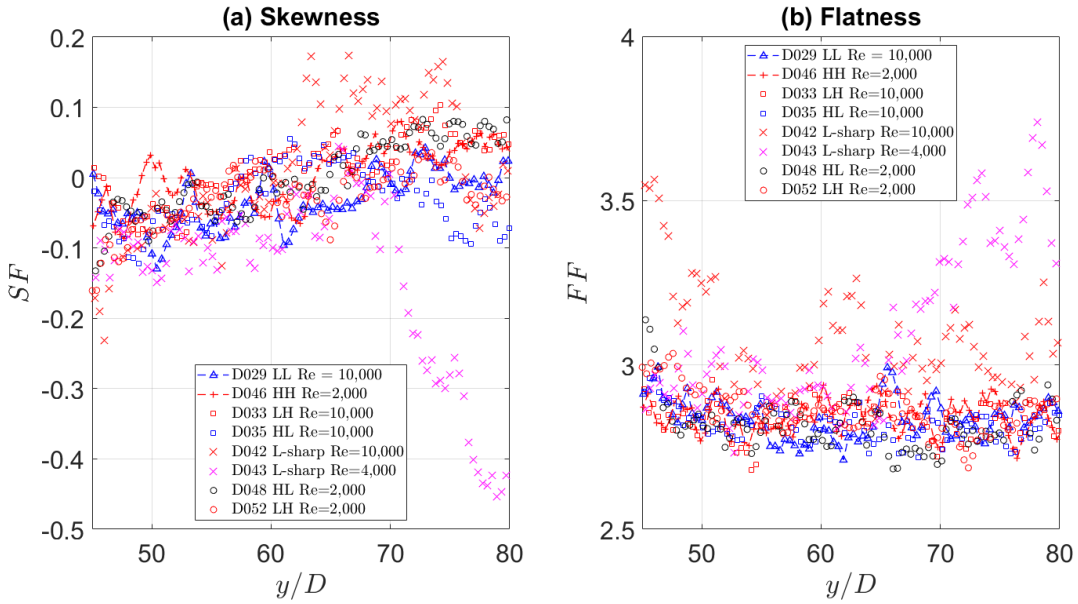

Figure 5.23: Axial evolution along the centerline of (a) skewness factor and (b) flatness factor for streamwise velocity.

It can be noticed that SF and FF follow a similar trend for positively and negatively buoyant jet, as well as for the uniform jets. However, different trends are found for the jets impinging a two-layer stratified interface, especially for case D043 with Re = 4,000. The reason for the deviation is due to the reversed flow observed in Figure 5.11, leading to higher values of skewness as well as oscillatory behaviour ($y/D \geq 70$).

5.8 Triple Velocity Correlation

In this section, the triple velocity correlations for the uniform turbulent jets presented in Section 4.6 are compared to the results obtained for positively and negatively buoyant jet (cases D033 and D035 respectively). The normalized third-order velocity moments for the density difference cases at y/d = 60 are shown in Figure 5.24.

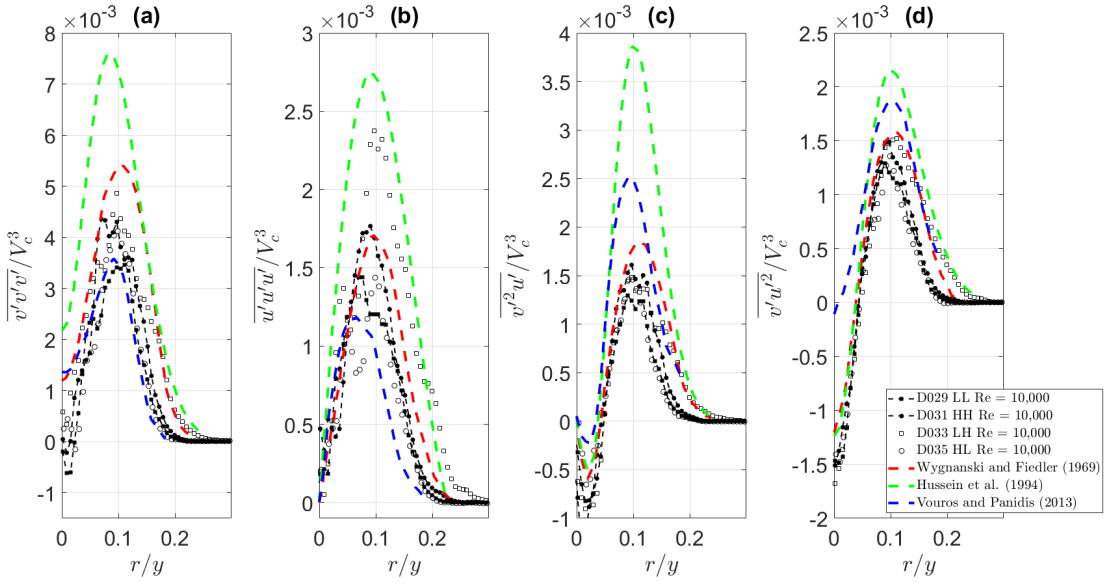

Figure 5.24: Radial profiles of the non-dimensional third-order velocity moments for the positively and negatively buoyant jet. Experimental data of Wygnanski and Fiedler (1969) [23], Hussein et al. (1994) [24], Vouros and Panidis (2013) [25], as well as the uniform cases D029 and D031 are plotted in superposition for comparison.

There is no remarkable difference observed for the streamwise velocity triple correlation $\overline{v'v'v'}$, as well as for the streamwise transport for the shear and normal stresses $\overline{v'^2u'}/V_c^3$ and $\overline{v'u'^2}/V_c^3$, as illustrated in Figure 5.24(a), (c) and (d). However, in Figure 5.24(b) it can be seen that the normalized radial velocity triple correlation $\overline{u'u'u'}/V_c^3$ of the positively buoyant jet case D033 yields a peak value which is almost double the ones from the corresponding uniform case D029, indicating an enhancing radial transport behavior of the radial normal stresses, therefore, an enhanced mixing process in the radial direction. And the opposite behavior can be noticed when comparing the negatively buoyant jet case with its corresponding uniform case D031. This agrees with the conclusion we obtained in Section 5.2.

CHAPTER VI

Computational Fluid Dynamics (CFD) Simulations

In this chapter, the CFD validation study conducted by Mao et al. [28] is presented. The study was aimed at assessing the performance of RANS models using the experimental results obtained with the miniDESTROJER facility. The computer software ANSYS ICEM-CFD (version 18.1) is used to generate the computational mesh, and the commercial code STAR-CCM+ (version 13.04) is used to perform the CFD simulations. The novel experimental data from the RIM optical fluid measurements is used to assess the predictive capability of the Realizable $k-\epsilon$ (RKE) model and RST model for turbulent round buoyant jets and identify the reasons for discrepancies. The profiles of both first-order and second-order turbulence flow statistics in the self-similar region are investigated and compared with the high-resolution experimental database.

6.1 Geometry, Boundary Conditions, and Mesh

A sketch of the round-jet flow in polar-cylindrical coordinates for the CFD investigations is shown in Figure 6.1. A density difference with a ratio of 3.16% is achieved by mixing two miscible solutions with different densities. Experiments have been conducted for four cases, with detailed fluid properties shown in Table 6.1, where the jet fluid properties are denoted with the subscript $_{jet}$, and the surrounding environment has the subscript $_{surr}$. Given the specified flow rates, all four cases have the same jet nominal Reynolds number (Re) equal to

10,000.

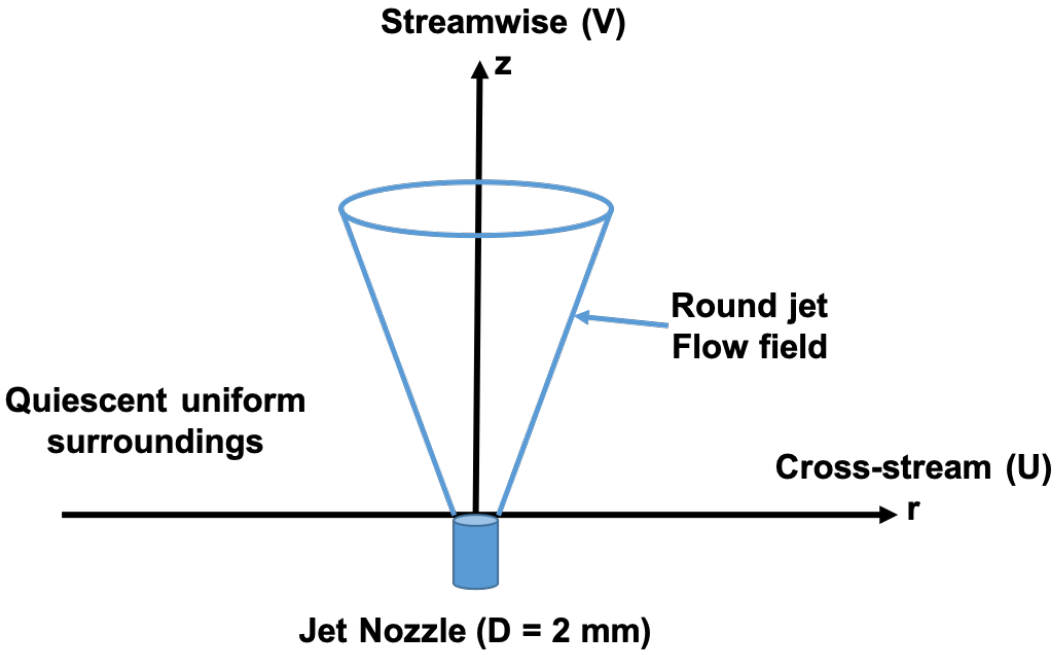

Figure 6.1: Sketch of jet flow with the definition of the coordinates for the CFD study.

Table 6.1: Fluid properties test matrix for CFD simulation setup.

CFD Cases	***Flow rate $\dot{m}$***	***$\Delta\rho$***	***ρ_{jet}***	***ρ_{surr}***	***μ_{jet}***	***μ_{surr}***
$--$	kg/s	$--$	kg/m^3	kg/m^3	$Pa \cdot s$	$Pa \cdot s$
D029	0.0190	0	1012	1012	0.001184	0.001184
D031	0.0181	0	1044	1044	0.001139	0.001139
D033	0.0190	+3.16%	1012	1044	0.001184	0.001139
D035	0.0181	-3.16%	1044	1012	0.001139	0.001184

Consistent with the geometry of the miniDESTROJER facility, the CFD computational domain consists of a 30 $\times$ 30 $\times$ 25 cm^3 box, with an inlet section of 2 mm in diameter extruded by a total length of 5mm. At the inlet, a fully developed flow boundary condition was imposed and numerical schemes were set to be second order, the walls were set to no-slip boundary conditions, and the top of the tank was set as a pressure outlet boundary condition. The computational mesh was generated with the computer software ANSYS

ICEM-CFD and consists of a conformal, structured hexahedral mesh with 13.3 Million cells. Because of the nature of the experiment, the mesh was refined along the jet trajectory. The mesh is fine enough to capture the flow structures according to the PIV measurements. In addition, by taking advantage of the symmetry of the experiment, 2D-axisymmetric simulations were executed as well, to reduce the computational time. The mesh generated for the 2D-axisymmetric simulations was made by only keeping the cells at the mid-plane of the geometry. In this manner, the same cell distribution is maintained between the 3D and 2D simulations (at the mid-plane). Pre-test simulations have shown that the 2D-axisymmetric simulation provides an almost identical profile to that of the 3D simulation. Snapshots of the mesh are shown in Figure 6.2.

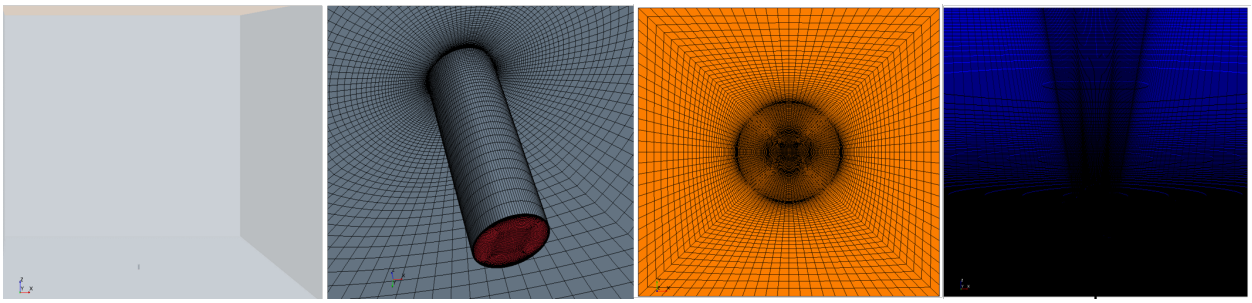

Figure 6.2: Geometry and mesh presentation in STAR-CCM+ (from left to right: geometry, inlet, top view, cross-section view). Reprinted from [28].

It is noticeable that in the experiment, the tank top was higher than the level of tank fluid, which resulted in a slight increase of fluid level due to the accumulation of injected fluid through the jet. Due to the long distance between the area of interest and the tank top, and in view of the relatively small surface level increase (roughly 4 mm in comparison with 250 mm of water level), the influence of the outlet boundary condition on the jet can be assumed to be negligible. Simulations were performed using the RKE and the RST turbulence models. While for the RKE model, steady-state simulations were sufficient to achieve convergence, transient simulations had to be performed when using the RST model in order to achieve satisfactory convergence of the numerical solution. The transient simulation was stopped once steady-state conditions were achieved. The comparison between simulations

and experimental data are discussed in the next section.

6.2 CFD Results and Comparison

Radial profiles of quantities of interest are compared in the jet self-similar region at four downstream locations, namely $z/D = 50,\ 60,\ 70,\ 80$ away from the jet exit. In addition to the mean velocity field and the turbulent statistics, the production term of the turbulence kinetic equation is also compared with experimental data to gain deeper insight into the performance of the turbulence models investigated in this section.

6.2.1 Streamwise velocity profiles

Figure 6.3 shows the streamwise velocity contour downstream of the $z/D = 45$ location for the four runs summarized in Table 6.1. From the contour plots in Figure 6.3, it can be clearly seen that, as the jet penetrates further through the surrounding fluid, center velocity decreases due to the dissipation of momentum and jet spreading. In addition, the RST model predicts larger jet center velocity compared to the RKE model for all four cases, regardless of the density differences. In comparison with experiments, it is clear that the RST model has a better match than the RKE model, especially in the jet center. One noticeable difference between the two uniform cases and the two cases with density differences is that the latter has a negative streamwise velocity in the surrounding field. This could come from the enhanced mixing process between jets and surroundings.

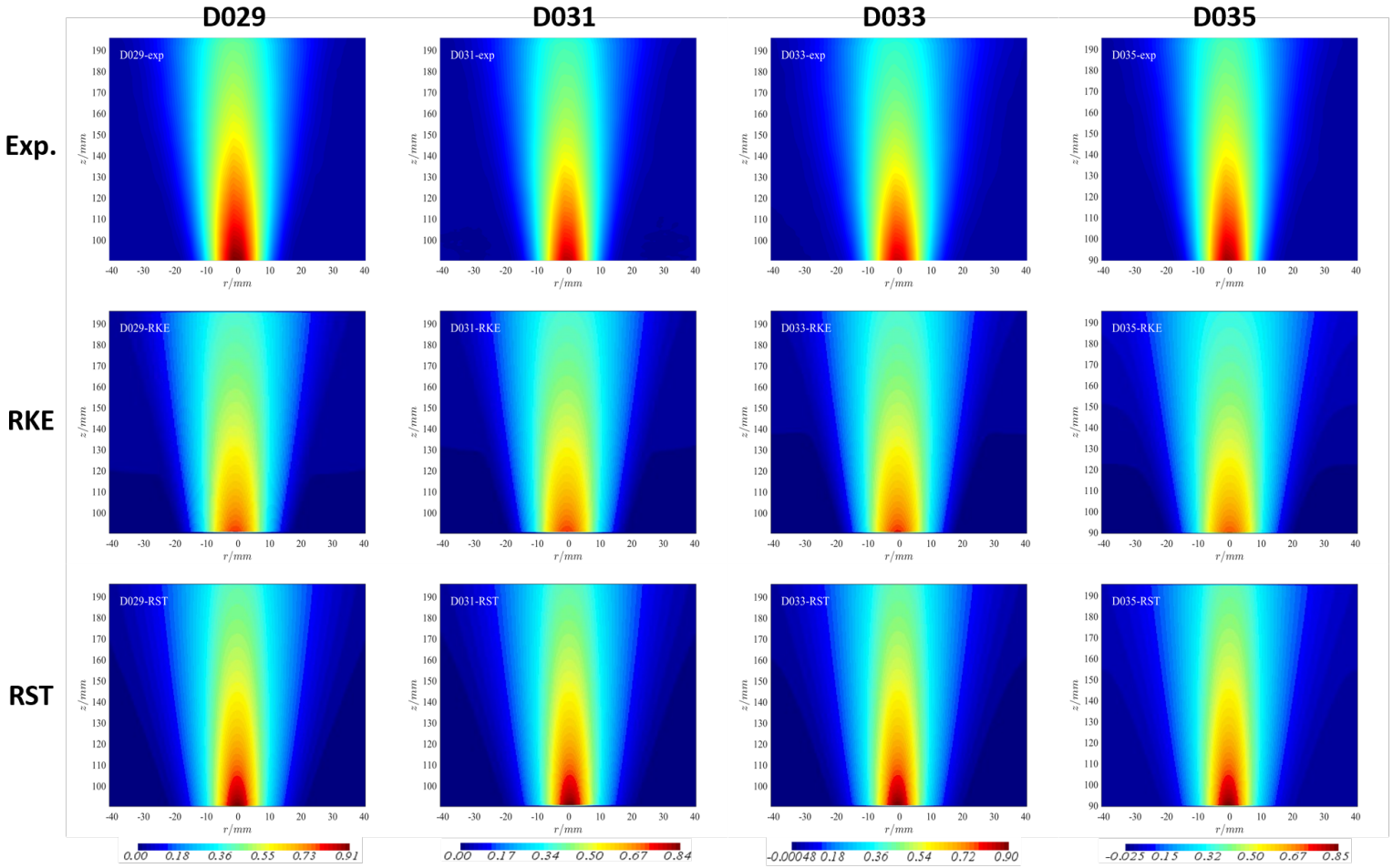

Figure 6.3: Streamwise velocity contours (top row: Experimental results, middle row: RKE model, bottom row: RST model). Reprinted from [28]

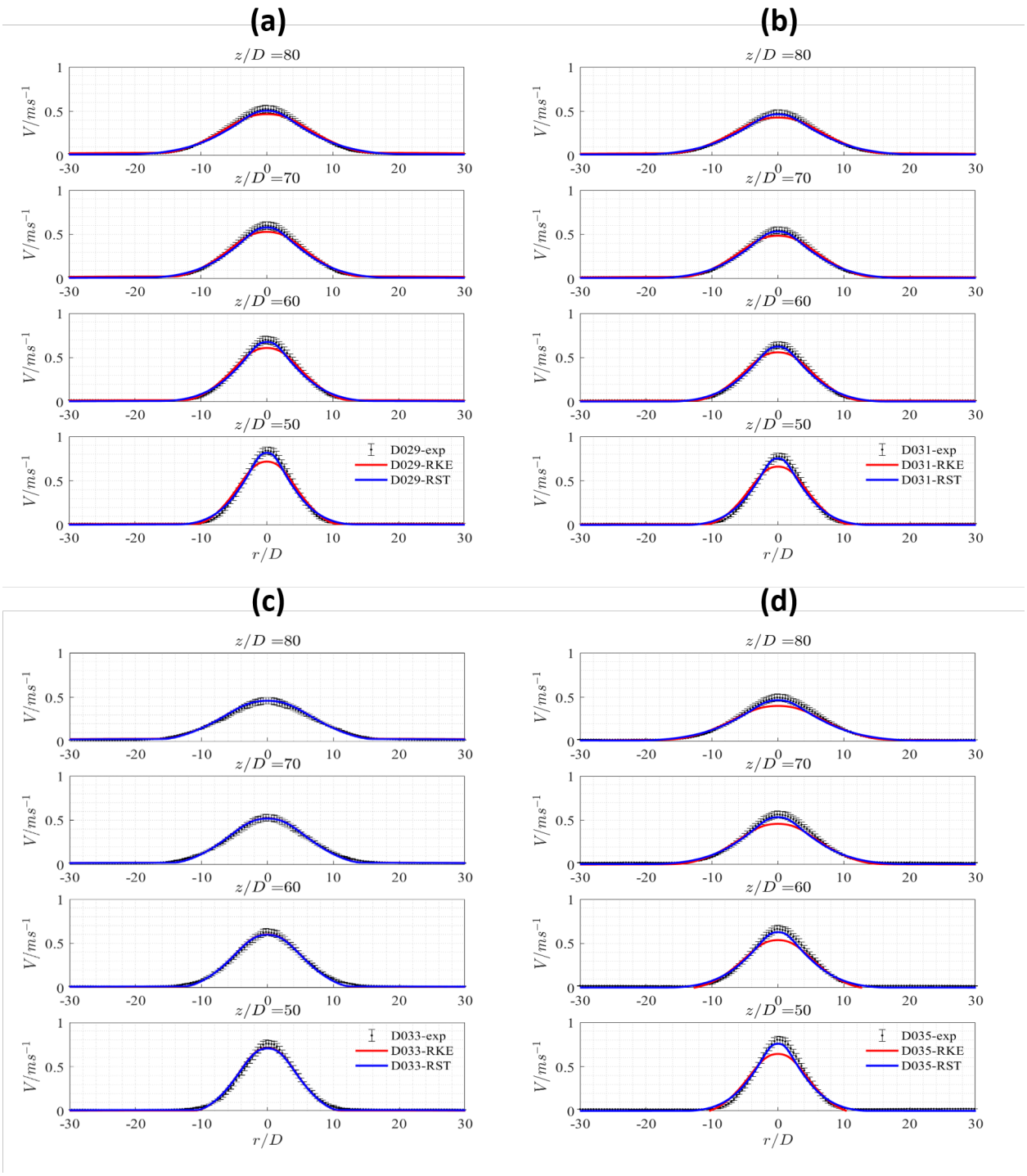

Figure 6.4: Streamwise velocity profiles at $z/D = 50,\ 60,\ 70,\ 80$ (from bottom to top) away from the jet exit for cases: (a) D029, (b) D031, (c) D033 and (d) D035. Reprinted from [28].

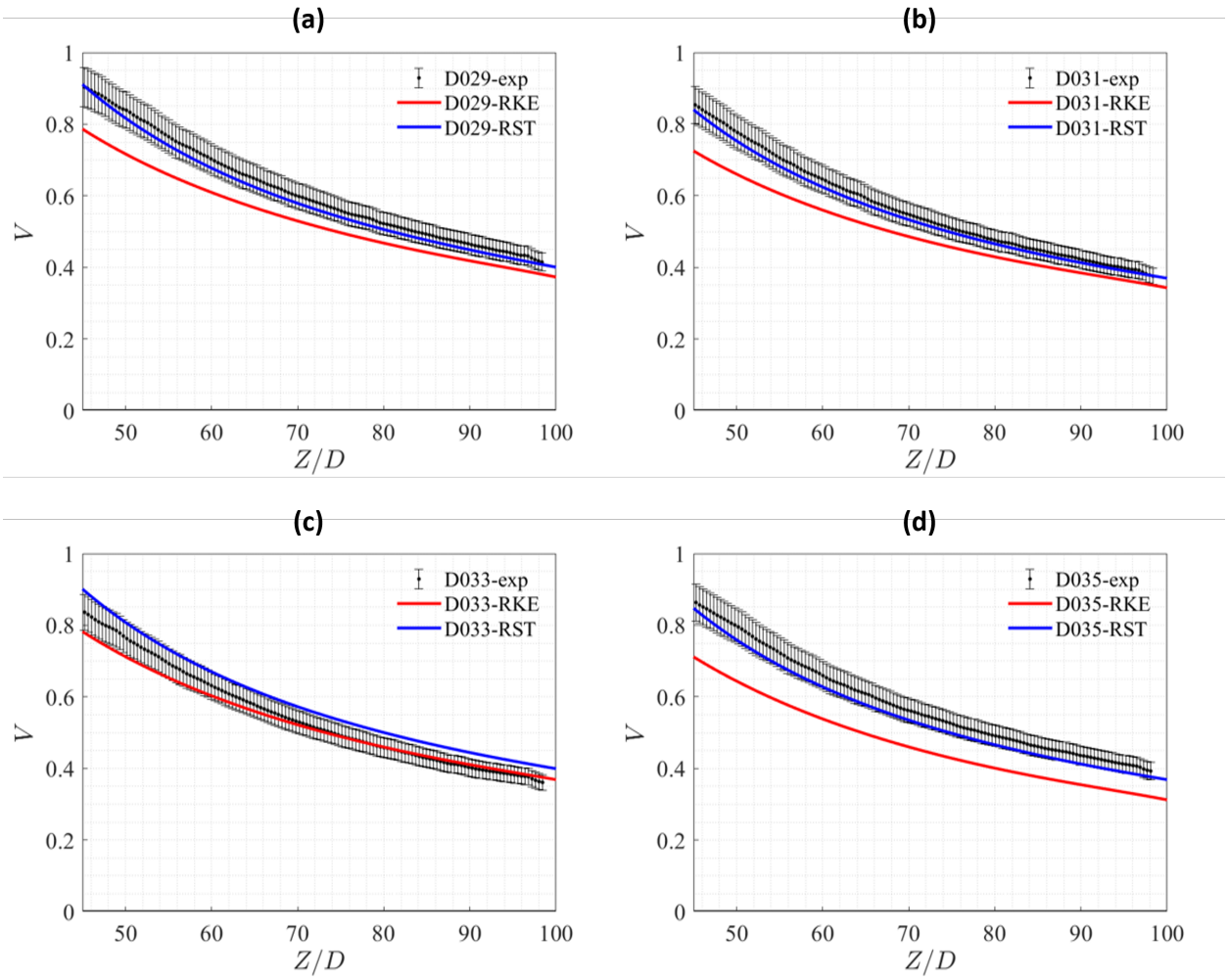

Figure 6.5: Centerline velocity decay profiles for cases: (a) D029, (b) D031, (c) D033 and (d) D035. Reprinted from [28].

In addition, as z/D increases, downstream from the nozzle, the discrepancy between simulation and experimental results tends to get smaller regardless of the density difference mentioned in Mao et al. [28]. A more clear look on this can be obtained through the plot of the decay of centerline velocity. As is shown in Figure 6.5, the discrepancy gets smaller when the jet is away from the inlet. It is known that moving further away downstream of the nozzle inlet, most momentum has been dissipated and the dissipation rate consequently slows down. Intuitively, one might conclude that the overprediction of the spreading rate of the streamwise velocity arises from the underestimation of turbulence dissipation (more spreading indicates less mixing and less TKE, therefore less dissipation).

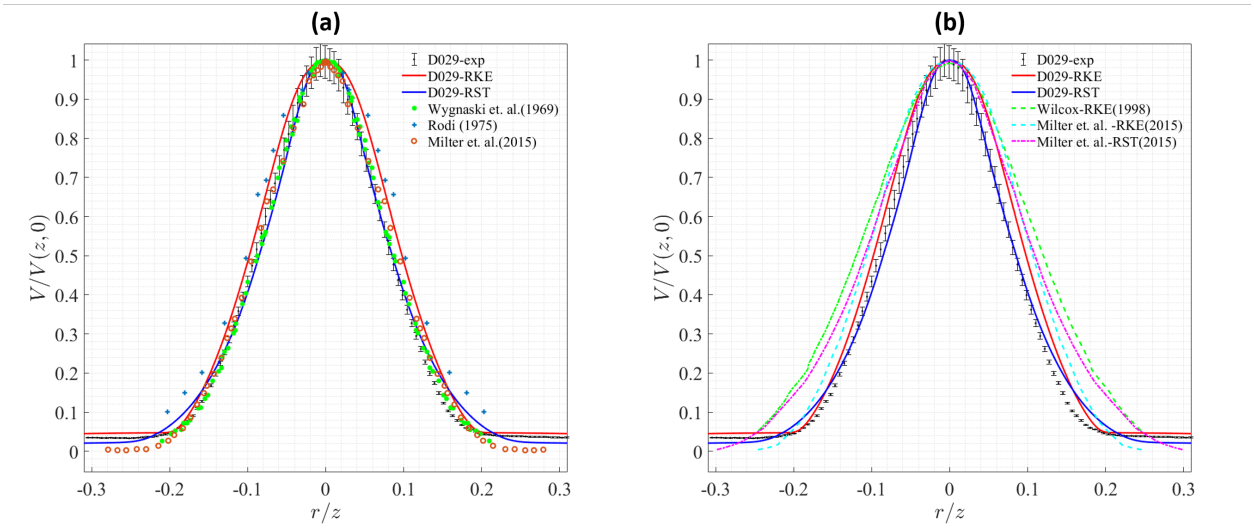

Figure 6.6: Normalized velocity profiles in comparison with results from the literature of (a) experimental data, and (b) simulation results. Reprinted from [28].

In Figure 6.6, the normalized velocity profiles for case D029 (both experiment and simulations) are compared with results published in the open literature. In Figure 6.6(a) the experimental data published by Miltner et al. [66], Wygnanski and Fiedler [23], and Rodi [121]) are included. With exception of Rodi's data [10], all other experimental data including the D029 case measured within this dissertation work, are in good agreement. It can be observed that the CFD RST model is in good agreement with the experimental data shown in Figure 6.6(b), while the RKE model predicts a broader profile, which means that the

velocity decay rate is overpredicted according to Mao et al. [28]. Similar simulations have also been conducted by Wilcox [62] and Miltner et al. [66] for uniform jets and their results are shown in Figure 6.6(b). However, since they used a uniform mass flow inlet condition, it is noticeable that simulations given by Miltner et al. [66] show even broader profiles are witnessed for the RKE model.

6.2.2 Reynolds stress, turbulent kinetic energy, and turbulent eddy viscosity

To investigate the reasons for the discrepancy observed between the experimental data and the RKE model, we focus our attention on turbulence parameters. From Equation 1.5b, it is clear that Reynolds stresses affect the velocity spread (through a diffusion term). Reynolds stresses are composed of shear stresses ($\overline{u_i' u_j'}$) and normal stresses. The radial profiles of the shear stress obtained for the four runs are compared to experimental data in Figure 6.7. It can be seen that the obtained shear stress profiles are in good agreement with the experimental data, even for cases in which density differences are involved. This is in agreement with the conclusion from the experiments conducted by Qin et al. [122] that the turbulence momentum transfer is almost identical regardless of the density effect.

While for the RST model transport equations are solved for the individual Reynolds stresses, in the RKE model the turbulence eddy viscosity assumption is adopted as closure for the Reynolds stresses:

$$-\overline{u_i' u_j'} = \nu_t \left(\frac{\partial U_i}{\partial x_j} + \frac{\partial U_j}{\partial x_i} \right) - k\delta_{ij} \tag{6.1}$$

where ν_t is the turbulent eddy viscosity, $k = \frac{1}{2}\overline{u_i' u_i'}$ is the turbulent kinetic energy. Equation 6.1 can be used to compute the turbulent eddy viscosity for the experimental data. Based on the Reynolds stresses computed by the RKE model and as measured in the experiments, the combination of accurately predicted shear stress profiles and underpredicted streamwise velocity profiles makes it obvious that turbulence eddy viscosity must be over-

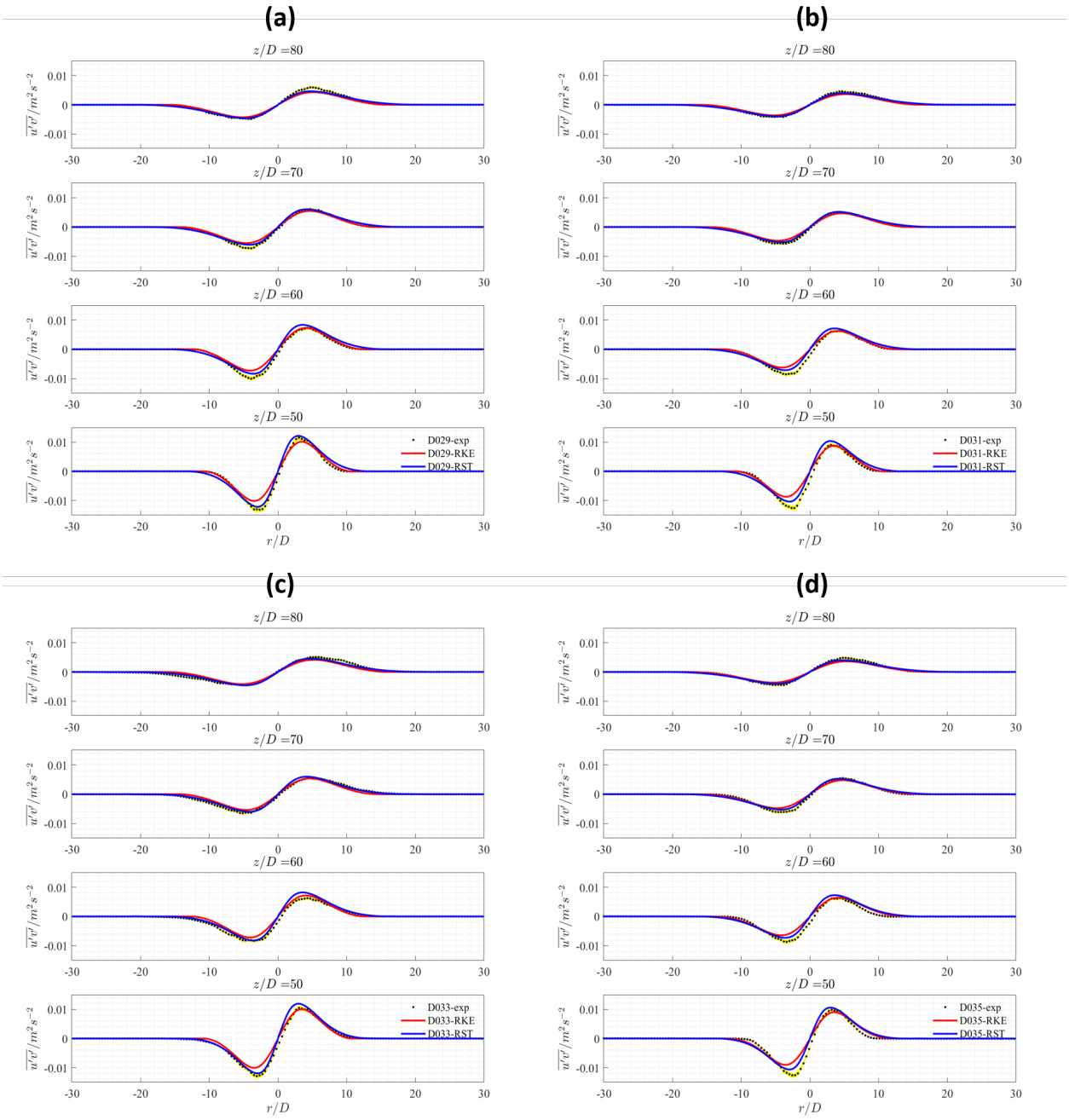

Figure 6.7: Shear stress profiles at $z/D = 50,\ 60,\ 70,\ 80$ (from bottom to top) away from the jet exit for cases: (a) D029, (b) D031, (c) D033 and (d) D035. Reprinted from [28].

predicted, as demonstrated in Figure 6.8. Similar to the streamwise velocity profiles, the eddy viscosity profiles also deviate in the jet center region, while exhibiting relatively good agreement off jet center.

In the RKE model, two additional transport equations are solved for the turbulent kinetic energy k and the turbulent dissipation rate ϵ respectively, and the eddy viscosity is given by:

$$\nu_t = C_\mu \frac{k^2}{\epsilon} = 0.09 \frac{k^2}{\epsilon} \tag{6.2}$$

In the current PIV/PLIF experiments, only two-dimensional data were acquired for the r-z plane (mid-plane of the jet flow, z denotes for the streamwise direction and r for radial). While the turbulence kinetic energy can be extracted from the experimental data, the turbulence dissipation rate is not, being a term that would require measurements of the out-of-plane velocity component as well. Defining the 'pseudo' turbulent kinetic energy $\tilde{k}$ in two-dimensions as:

$$\tilde{k} = \frac{1}{2}\left(\overline{u'u'} + \overline{v'v'}\right) \tag{6.3}$$

where $\overline{v'v'}$ and $\overline{u'u'}$ are the normal stresses in the streamwise and radial direction respectively, the predicted 'pseudo' turbulent kinetic energy for both models is compared to the experimental data in Figure 6.9. It can be clearly seen that the RKE model underestimates the turbulent kinetic energy in the center region, while exhibits reasonably good agreement in the shear layer. This is different from the results published by Aziz et al. [65], who found that the standard $k - \epsilon$ model to give a lower value in the center and higher value in the shear layer. The RST model instead tends to overestimate the turbulence kinetic energy, especially at locations closer to the jet inlet. Using Case D029 and D035 as the comparison, the centerline turbulent kinetic energy decay from both models, are plotted and presented in Figure 6.10. It shows that the RST model has larger centerline turbulent kinetic energy compared to the experimental results. In addition, the decay rate of the centerline turbulent kinetic energy for RST model is larger than the results from RKE model as well as results

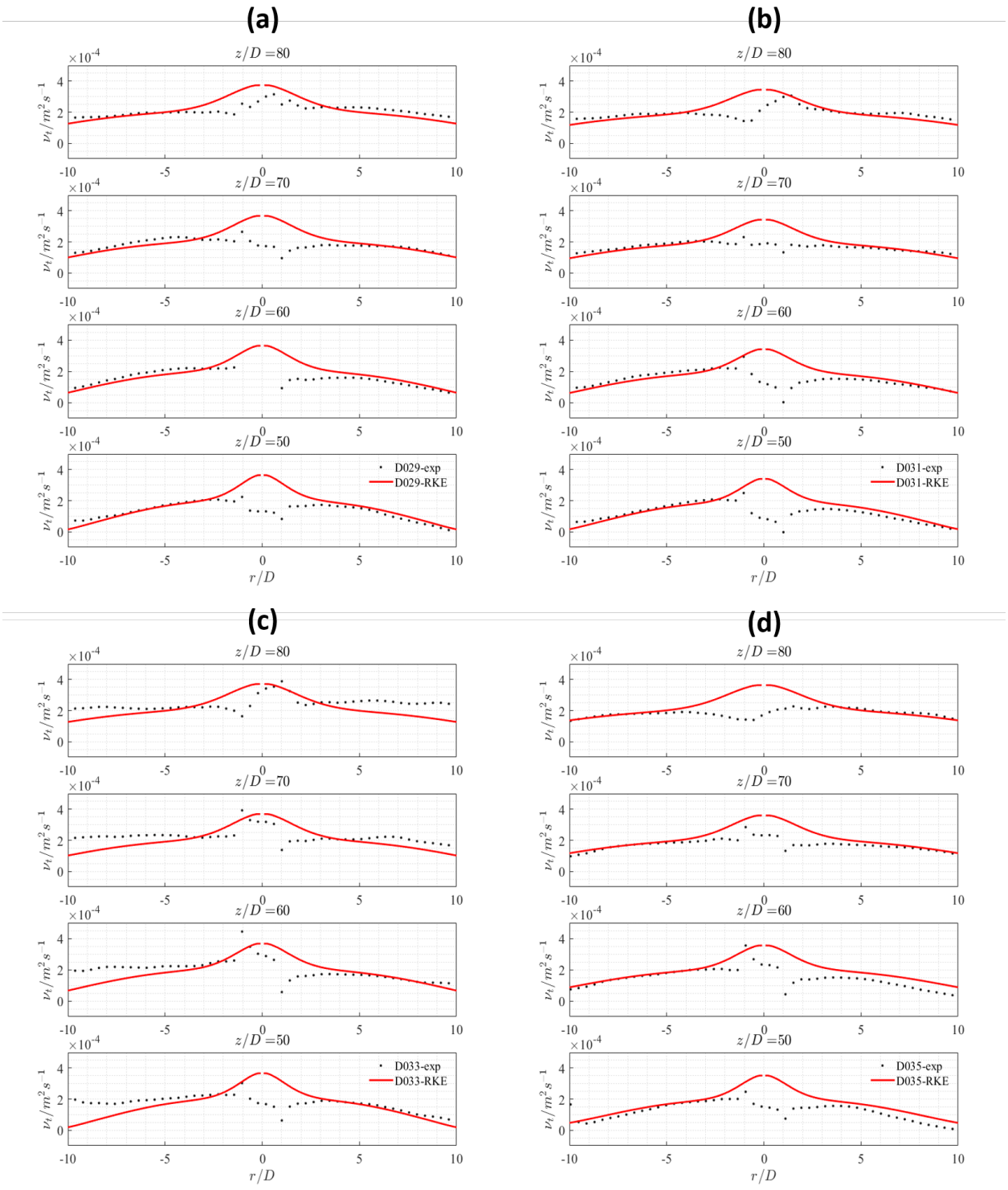

Figure 6.8: Turbulent eddy viscosity profiles at $z/D = 50,\ 60,\ 70,\ 80$ (from bottom to top) away from the jet exit for cases: (a) D029, (b) D031, (c) D033 and (d) D035. Reprinted from [28].

from the experiments.

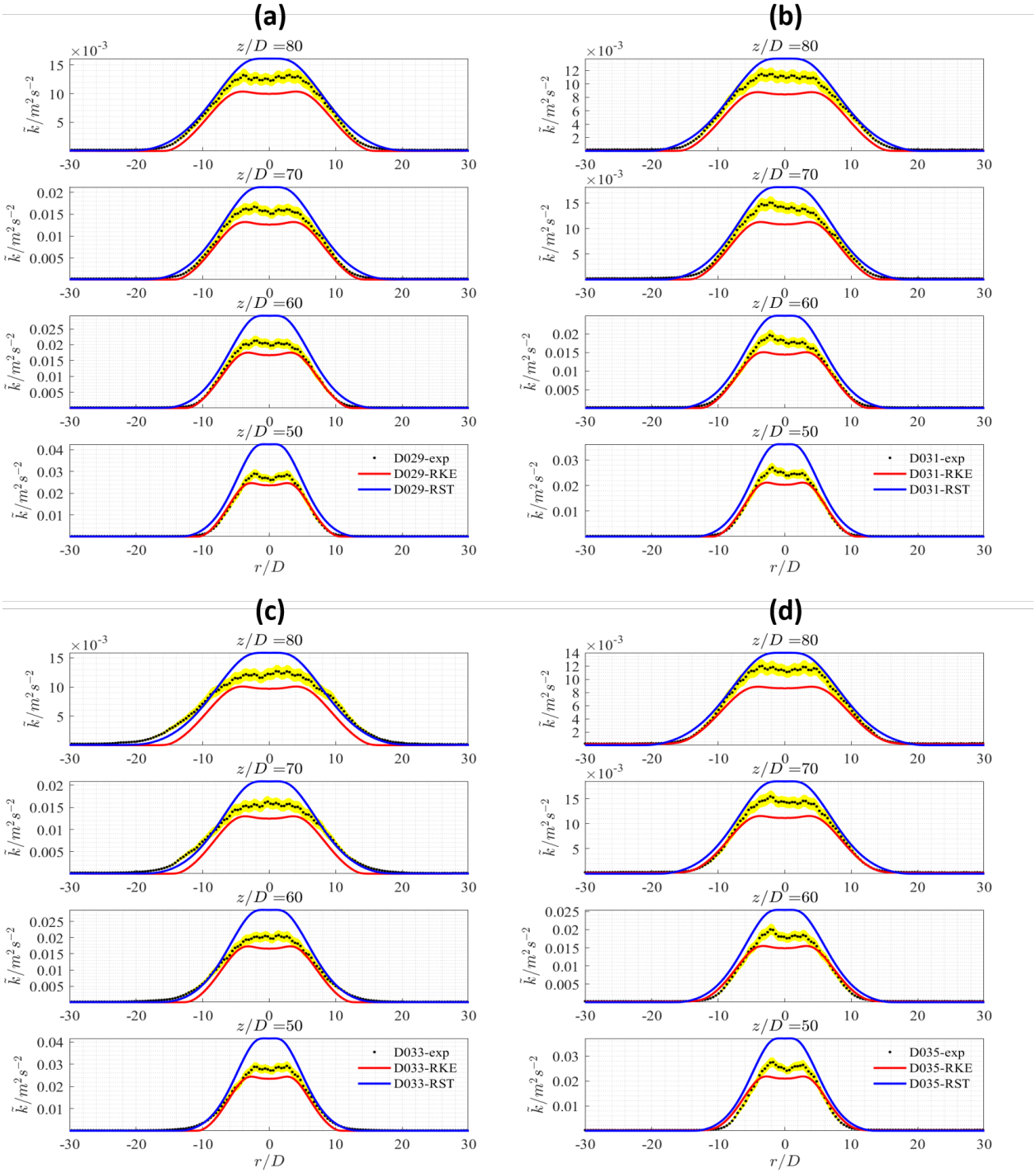

Figure 6.9: 'Pseudo' turbulent kinetic energy $\tilde{k}$ profiles at $z/D = 50,\ 60,\ 70,\ 80$ (from bottom to top) away from the jet exit for cases: (a) D029, (b) D031, (c) D033 and (d) D035. Reprinted from [28].

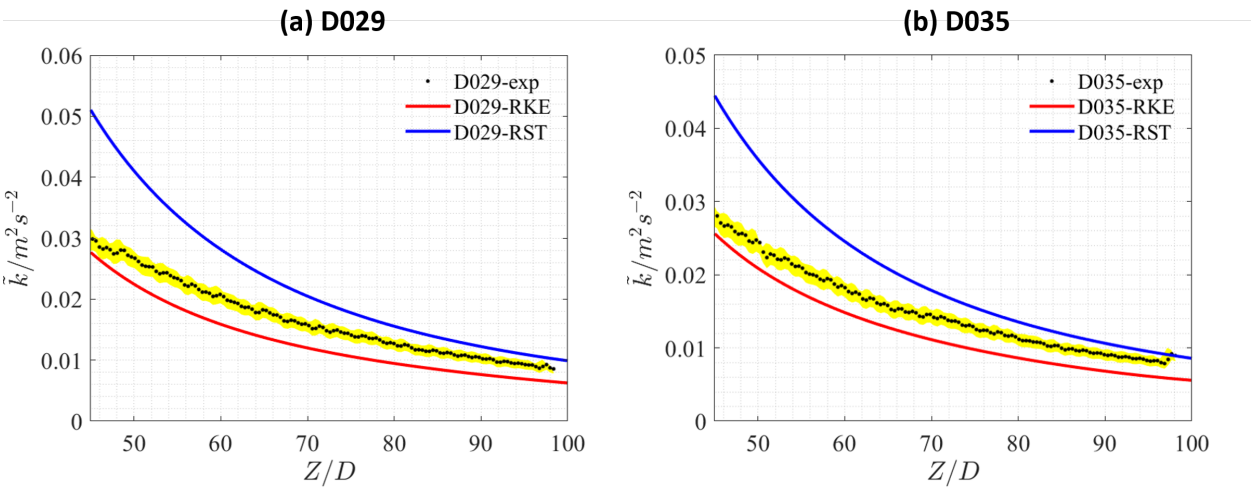

Figure 6.10: The decay of turbulent kinetic energy $\tilde{k}$ along the centerline for (a) D029 and (b) D035. Reprinted from [28].

6.2.3 Turbulent kinetic energy production

In the previous section, it has been demonstrated that the RKE model tends to underpredict the turbulent kinetic energy. In order to investigate the major reason for the under-prediction of the turbulent kinetic energy, it is necessary to have a deeper look at the production terms appearing in the transport equation for the turbulent kinetic energy. As turbulent flows are always dissipative, the production of turbulence is essential to sustain turbulence kinetic energy. The production term of turbulent kinetic energy in Einstein notation is expressed as:

$$P_k = -\overline{u_i' u_j'} \frac{\partial U_i}{\partial x_j} \tag{6.4}$$

For round jet in cylindrical coordinate (with z denoting the streamwise direction, and r the radial direction respectively), Equation 6.4 can be rewritten as:

$$P_k = -\overline{u_z' u_r'} \left(\frac{\partial U_r}{\partial x_z} + \frac{\partial U_z}{\partial x_r} \right) - \overline{u_z' u_z'} \frac{\partial U_z}{\partial x_z} - \overline{u_r' u_r'} \frac{\partial U_r}{\partial x_r} \tag{6.5}$$

The comparison between simulation results and experiments for turbulence production is presented in Figure 6.11. Double peaks in the radial profiles of P_k are observed in both

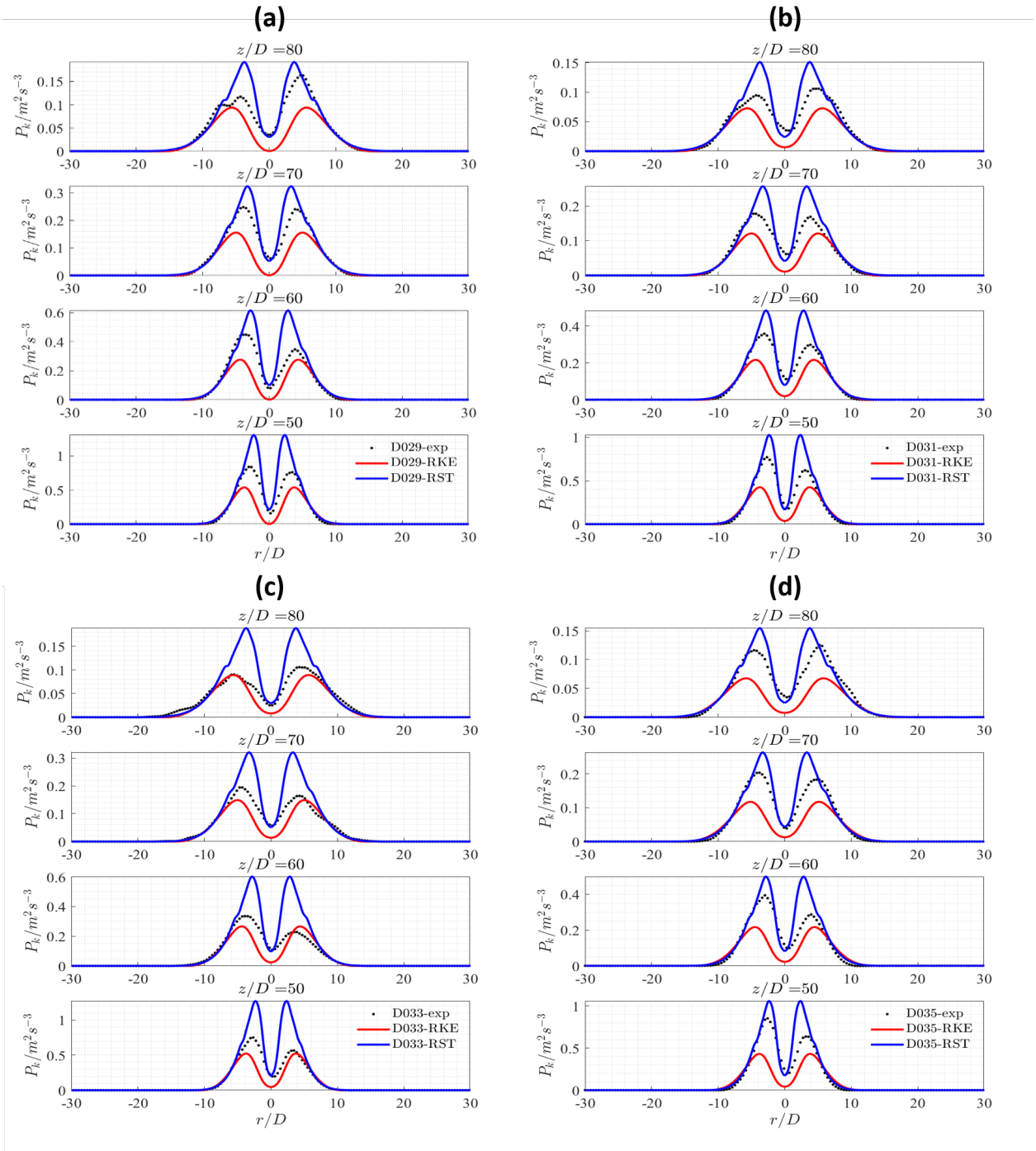

Figure 6.11: Turbulent production profiles at $z/D = 50,\ 60,\ 70,\ 80$ (from bottom to top) away from the jet exit for cases: (a) D029, (b) D031, (c) D033 and (d) D035. Reprinted from [28].

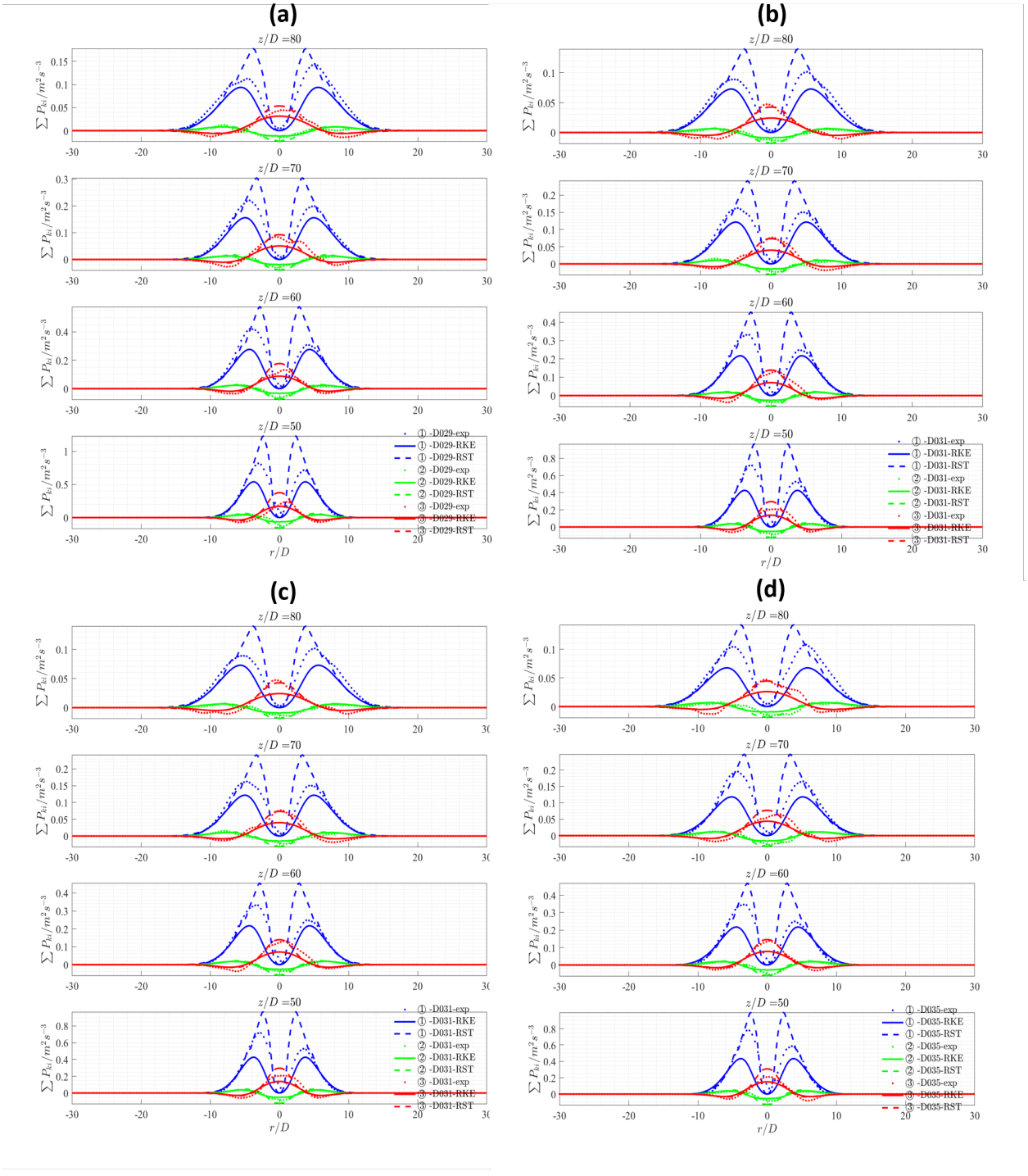

Figure 6.12: Budgets of turbulent production profiles at z/D = 50, 60, 70, 80 (from bottom to top) away from the jet exit for cases: (a) D029, (b) D031, (c) D033 and (d) D035. Reprinted from [28].

simulations and experiments. This is caused by the two shear layers present on both sides of the jet. It can be observed that for all the four runs, turbulence production is well predicted by both the RKE and RST models in the shear layer region, while in the jet center region the RST model over-estimates turbulence production, and the RKE model underestimates turbulence production. As the turbulent production given by the RKE model is always lower than experimental values, it is then understandable why the RKE model under-predicts turbulence kinetic energy profiles as inferred above. The good agreement of turbulence production in the center region given by the RST model indicates that the overestimation of turbulence kinetic energy in the center region is due to the underestimation of turbulence dissipation.

Since the production term can be expanded into three individual terms which are composed of various products of velocity gradient and Reynolds stresses, as shown in Equation 6.5, the contribution from each term can be illustrated by plotting them separately (see Figure 6.12, where the radial profiles of each term of P_k are shown for all experimental runs at different axial locations). The circled numbers in the legend represent the contribution to P_k in the same order as shown in Equation 6.5. It can be seen that the product of the shear stress with the mean strain rate tensor is the main contributor to the turbulence production in the shear layer. In the jet center, instead, the main contributor is the product of the streamwise normal stress with the gradient of the mean streamwise velocity along the axial direction. For the RKE model, each dominant term has a smaller magnitude compared to experimental values, the total of which accounts for the underprediction of turbulence production. On the contrary, the RST model results in larger values for each dominant term, therefore yielding overprediction of turbulence production.

6.2.4 Impact of RKE model parameters

The results discussed in the previous sections have demonstrated that the RKE model tends to underestimate turbulence production as well as TKE in the jet self-similar region

(Mao et al. [28]). To test whether a change in turbulence production and dissipation would result in improved predictions, we consider the turbulence dissipation transport equation implemented in STAR-CCM+ without temperature gradient:

$$\frac{\partial \rho\epsilon}{\partial t} + \frac{\partial \left(\rho\epsilon U_j\right)}{\partial x_j} = \frac{\partial}{\partial x_i}\left[\left(\mu + \frac{\mu_t}{\sigma_\epsilon}\right)\frac{\partial \epsilon}{\partial x_j}\right] + C_{\varepsilon 1}\frac{\epsilon}{k}\left(P_k + C_{\varepsilon 3}\frac{\mu_t}{\rho Pr_t}\frac{\partial \rho}{\partial x_i}\cdot g_i\right) - C_{\varepsilon 2}\rho f_2\frac{\epsilon^2}{k} \quad (6.6)$$

where Pr_t is the turbulent Prandtl number, $\mu_t = \rho\nu_t = \rho C_\mu k^2/\epsilon$ with $C_\mu = 0.09$, $\sigma_\epsilon = 1.3$, f_2 is a damping function and the default model coefficients $C_{\varepsilon 1}$, $C_{\varepsilon 2}$ and $C_{\varepsilon 3}$ are not universal since they have been tuned based on a limited set of flow conditions. Their values are critical for calculating the dissipation rate and therefore determine the accuracy of the RKE model. To investigate the influence of their values on the simulation results, case D029 was taken as reference and the values of $C_{\varepsilon 1}$ and $C_{\varepsilon 2}$ where modified, while $C_{\varepsilon 3}$ was kept as default value since the results discussed in Jiaxin's et al. paper [28] have shown that the RKE model underpredicts turbulence kinetic energy regardless of density differences.

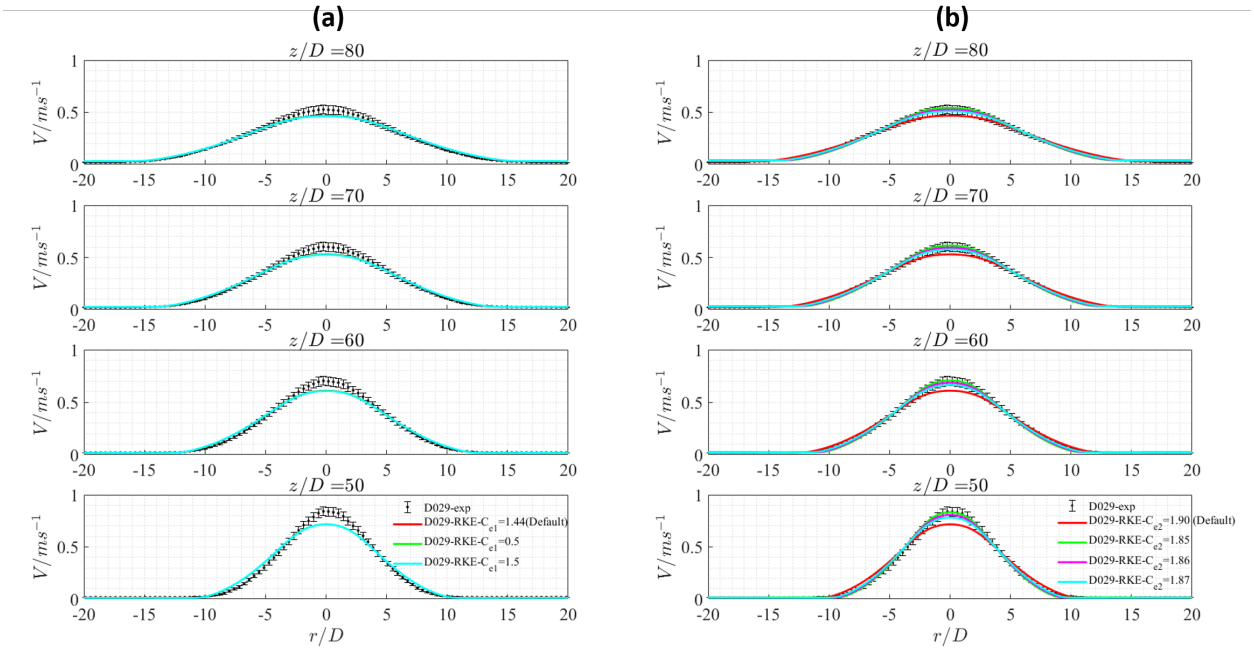

Figure 6.13: Streamwise velocity profiles for case D029 at z/D = 50, 60, 70, 80 (from bottom to top) by modified model coefficients for (a) $C_{\varepsilon 1}$ and (b) $C_{\varepsilon 2}$. Reprinted from [28].

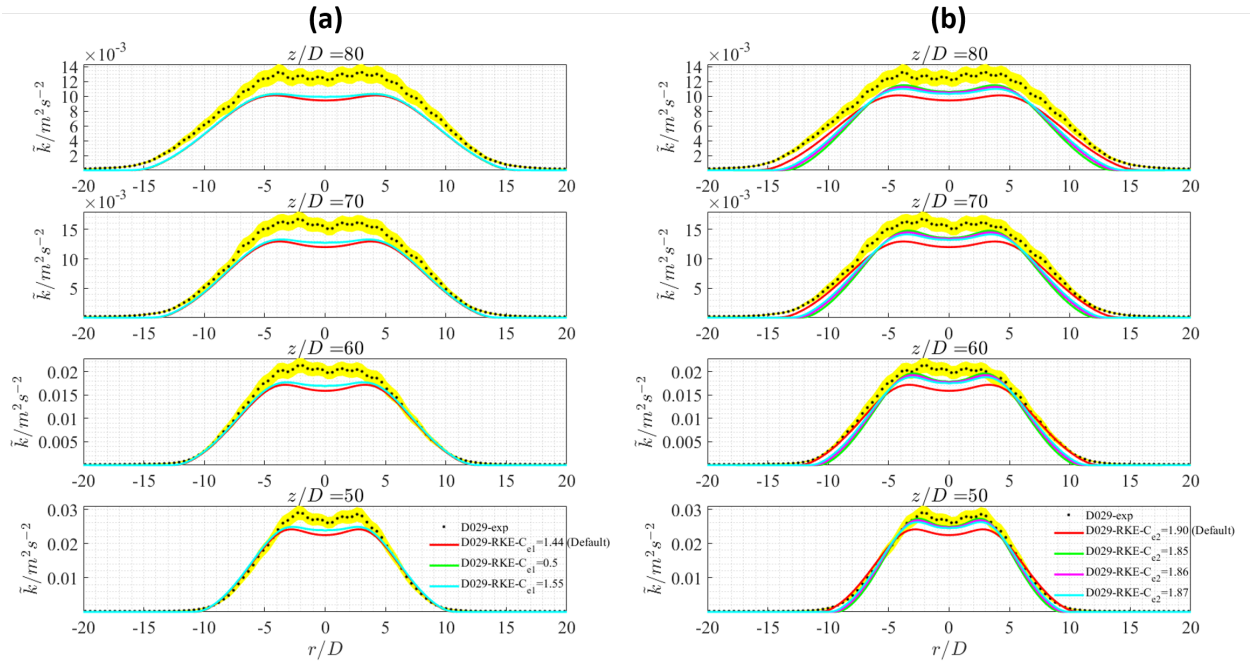

Figure 6.14: Turbulent kinetic energy profiles for case D029 at $z/D = 50,\ 60,\ 70,\ 80$ (from bottom to top) by modified model coefficients for (a) $C_{\varepsilon 1}$ and (b) $C_{\varepsilon 2}$. Reprinted from [28].

In Figure 6.13 and Figure 6.14, the streamwise velocity and turbulent kinetic energy profiles are reported for case D029, with varying model coefficients. It can be observed that $C_{\varepsilon 1}$ does not affect the mean velocity profiles while having a slight improvement in turbulent kinetic energy in the jet center. This can be expected from Equation 6.6 since $C_{\varepsilon 1}$ is responsible for magnifying turbulence production. Turbulence production predicted by RKE is fairly small in the center region according to Figure 6.11, which contributes less to the transport equation. As a result, $C_{\varepsilon 1}$ made a slight influence on reducing dissipation. $C_{\varepsilon 2}$ instead is decisive for accurate predictions. Compared to default value 1.90, slightly small $C_{\varepsilon 2}$ shows good agreement of velocity and turbulent kinetic energy profiles for all the locations. From this experience, it can be seen that the RKE model is very sensitive to $C_{\varepsilon 2}$ and the selection of its value is of importance (Mao et al. [28]). This conclusion is consistent with the findings by Lai et al. [59] and Thiesset et al. [123], who both agreed that a lower value for $C_{\varepsilon 2}$ is needed, even though the two research groups' results do not agree on the specific value.

6.3 Summary of the findings

The performance of the RKE model and the RST model has been assessed by Mao et al. [28] against high-resolution experimental data for turbulent round jets with and without density differences. It is observed that, although the standard RKE model can predict well shear stresses, it tends to underestimate streamwise velocity and turbulence kinetic energy in the jet center region. A deeper analysis of the turbulence production terms indicates that the RKE model also underestimates turbulence production. The RST model, instead, results in good agreement for mean streamwise velocity profiles and shear stress, while it overestimates turbulence kinetic energy in the center region. No difference in model performance for the turbulence quantities has been observed comparing results for uniform density and cases with density differences. This should be further investigated for cases with higher density differences when the buoyancy effect is even stronger.

The streamwise velocity profiles are better predicted in cases where the light fluid is injected into heavy fluid, compared to the case in which heavy fluid is injected into the light fluid. In addition, the model coefficients of the turbulence dissipation equation for the RKE model were modified to investigate their effects on the simulation results. It was found that the RKE model is very sensitive to the coefficient $C_{\varepsilon 2}$ and its value has a critical effect on the model accuracy.

CHAPTER VII

Conclusions and Future Work

In this chapter, the research work done for this dissertation is summarized. Based on the findings, suggestions for future experimental and computational work are offered as well.

7.1 Conclusions

This dissertation is aimed at investigating and characterizing turbulent round free jets interactions with uniform and stratified environments, by establishing a high-resolution high-fidelity database. Two experimental facilities DESTROJER and miniDESTROJER have been designed and built, with the jet flow generated by a servo-engine-driven piston to achieve a precisely controllable and repeatable inlet velocity profile. High-fidelity synchronized Particle Image Velocity (PIV) and Planar Laser-induced Fluorescence (PLIF) have been used to measure the jet velocity and scalar fields and associated turbulence statistics. A novel Refractive Index Matching (RIM) technique developed by Krohn et al. [22] using a ternary system has been employed in this dissertation to achieve RI matching with liquid flows in the presence of much higher density differences than what previously reported in the open literature, allowing therefore the use of PIV and PLIF for the investigation of buoyant jets interaction with uniform and stratified environments up to density variations of 8.6%.

The turbulent jets in uniform environments have been measured using PIV in the near-, intermediate and far-field regions, and have been characterized in terms of the mean flow

field and turbulence statistics (i.e., the mean streamwise velocity field, Reynolds and shear stress profiles, etc.). The measured centerline mean streamwise velocity decay constants and the jet virtual origins are found to be in good agreement with the results published in the existing literature. Normalized by the virtual jet origins, the profiles of the normalized jet streamwise mean velocity as well as the streamwise and radial normal stress are found to be independent of the downstream location, supporting the finding of self-similarity behavior of a turbulent round free jet in the far-field region. The normalized centerline values for the mean normal streamwise and radial Reynolds stresses also match well with the data published in the literature by Hussein et al. [24]. Also with regard to the flow entrainment, the experimental data measured at the DESTROJER and miniDESTROJER facilities are found to be in fair agreement with previous studies. Statistical analyses of the instantaneous velocity along the jet centerline for uniform and buoyant jets have been conducted, looking at the skewness and flatness factors of the measured signal. The two parameters have been used to investigate the deviation of the instantaneous velocity from a Gaussian distribution, showing that for uniform jets the deviation from a Gaussian distribution starts occurring at y/D of 1 in the near-field region, with a return to a nearly Gaussian distribution at y/D of $\simeq$15, corresponding to the intermediate field region. A truly Gaussian distribution however is never achieved even in the far-field region, because of the mixing between the jet flow and the surrounding ambient fluid. Third-order terms such as triple velocity correlations are also experimentally estimated to gain insight in the transport of Reynolds and shear stresses in turbulent jet flows. It has been found that the magnitudes of the triple velocity correlations increases with the decreasing of Re, which indicates a stronger diffusion effect with lower-Re jet flows. Also with regards to the triple velocity correlation, the experimental results have been found to be in reasonable agreement with previously published data. Lastly, spatial and temporal analyses of the turbulent jet mixing behavior in uniform environments have been conducted using the Lumley Triangle representation and Power Spectral Density (PSD) methods, providing insights into the mixing structures of a turbulent uniform jet.

The behaviour of buoyant jets in the presence of uniform environments and two-layer stratification has been investigated experimentally as well, and the results have been compared with the behaviour of reference uniform jets. By analyzing the the mean scalar and the scalar variance fields, enhancement of the mixing process was found for positively buoyant jets, while suppression of mixing was found for the negatively buoyant jets. Differences however were not observed in the TKE as well as the normal and shear stresses profiles, which were found to be insensitive to the presence or absence of density differences. Analysis of the triple velocity correlations yields that positively buoyant jets exhibit an enhanced transport of the radial normal Reynolds stresses in the radial direction, yielding enhanced mixing in the radial direction. In addition, turbulent eddy viscosity and diffusivity, are estimated from the experimental data based on the gradient diffusion approximation. It was found that positively buoyant jets exhibit higher magnitudes of both eddy viscosity and eddy diffusivity when compared to uniform and negatively buoyant jets. The measured experimental data for buoyant jets spreading rate and decay constants are also found to be in good agreement with previously published data. It has also been found that, when a buoyant jet impinges on a two-layer stratified interface, downstream current is observed for relatively low Re numbers, when the jet momentum is not sufficiently high to compete with the negative buoyant forces. The jet penetration height has also been measured and compared with an existing theoretical solution derived by Ansong et al. [39]. However, due to the simplified assumptions used in the analytical derivation, namely that there will be a continuous and instantaneous redistribution of density difference within the jet as the density changes at the fringe of the jet, the analytical solution is not able to capture the experimental data presented in this dissertation. The centerline streamwise velocity decay constants have been found to show little dependence on the presence of density differences. The power-law decay relation for the centerline TKE with respect to the downstream location proposed by Danaila et al. [120] was validated using this dissertation experimental data. Finally, the skewness factor and flatness factor of the instantaneous velocity along the jet centerline have been analyzed

for buoyant jets as well, showing no significant difference for the positively and negatively buoyant jets, with the exception of buoyant jets in the presence of stratified layers, for which large deviation have been observed after 70 jet-diameter with Re = 4,000. This is to be expected, since that location corresponds to the jet penetration depth.

Finally, the experimental database established in this dissertation was used to assess Computational Fluid Dynamics (CFD) models predictive capabilities when simulating uniform and buoyant jets. Both the Realizable $k-\epsilon$ (RKE) and the Reynolds Stress Transport (RST) models were analyzed. The mean streamwise velocity profiles were well predicted by the RST model, while the RKE model has been found to largely underestimates the velocity in the jet central region. With respect to the Turbulent Kinetic Energy, it was found that the RKE model underestimates the TKE along the jet centerline, while the RST model over-predicts it. The analysis of the Turbulent Kinetic Energy transport equation production terms has shown that the RKE model underestimates the TKE production while RST does the opposite. Investigation of various products of velocity gradient and Reynolds stresses also shows that the gradient of the streamwise velocity in the crosswise direction contributes the most to the turbulent kinetic energy production. Lastly, the impact of model coefficients of the turbulent dissipation equation for the RKE model was investigated.

7.2 Future Work

In this dissertation a high-resolution high-fidelity experimental database was established for turbulent round free jets in both uniform and stratified environments, with well-defined initial and boundary conditions. While the novel experimental database could be used to derive new correlations and improve the computational models, additional experimental data over a wider range of Reynolds number (Re) would be beneficial.

A large number of publications on uniform jets are reported in the open literature, however limited data still exists on buoyancy-driven turbulent jet flows (most of the data available in the literature has been obtained using gases as working fluids and for very high Reynolds

number). Utilizing the mentioned novel Refractive Index Matching (RIM) technique and the traditional optical fluid measurement methods, new possibilities have been brought to the scientific community to achieve high density difference using liquids as working fluids. When the density stratification is present, more sophisticated studies are worthwhile to investigate the interactions and forces of attraction between the molecules at the interface of two fluids, i.e., the interfacial tension. With the idea of the ternary plot system, it is also worthwhile investigating the feasibility of matching the Refractive Index between two fluid pairs and a specific transparent solid material. In this light, optical fluid measurements will be made possible for visualizing the fluid flow inside a more complex geometry, such as the axial flow passing through spacer grids or wire-wrapping nuclear fuel bundles.

On the computational side, the CFD-grade high-resolution experimental data measured within this dissertation could be used to validate and further develop Large Eddy Simulations (LES) subgrid-scale models. These models are most often based on the assumption of local isotropy, which breaks down in the presence of stratified environments.

APPENDICES

APPENDIX A

Database for RIM Study of $H_2O - \boldsymbol{Glycerol} - Na_2SO_4$ Ternary System

The following Table A.1 provides the full refractive indices and densities measurements for $H_2O - Glycerol - Na_2SO_4$ ternary system at atmospheric pressure and 293.35 K. The refractive index is measured with a Sper Scientific 300037 Digital Refractometer with a RI range of $1.3330 < n_D < 1.5318$, which has an accuracy of 0.1% at a resolution of 0.0001. The density measurement is performed using a 50 ml volumetric flask, class A in combination with a Lianze I2000 digital multi-function scale, with an accuracy of 0.1g, which results in an uncertainty within 1% for density measurement.

H_2O	$Glycerol$	Na_2SO_4	n_D	ρ
x_1	x_2	x_3	$-$	g/cm^3
1.00	0.00	0.00	1.3330	0.9980
0.99	0.01	0.00	1.3342	1.0005
0.98	0.02	0.00	1.3353	1.0028
0.97	0.03	0.00	1.3365	1.0051
0.96	0.04	0.00	1.3376	1.0074

Continued on next page

Table A.1 – *Continued from previous page*

H_2O	$Glycerol$	Na_2SO_4	n_D	ρ
x_1	x_2	x_3	$-$	g/cm^3
0.95	0.05	0.00	1.3388	1.0097
0.94	0.06	0.00	1.3400	1.0120
0.93	0.07	0.00	1.3412	1.0144
0.92	0.08	0.00	1.3424	1.0167
0.91	0.09	0.00	1.3436	1.0191
0.90	0.10	0.00	1.3448	1.0215
0.88	0.12	0.00	1.3472	1.0262
0.86	0.14	0.00	1.3496	1.0311
0.84	0.16	0.00	1.3521	1.0360
0.82	0.18	0.00	1.3547	1.0409
0.80	0.20	0.00	1.3572	1.0459
0.76	0.24	0.00	1.3624	1.0561
0.72	0.28	0.00	1.3676	1.0664
0.68	0.32	0.00	1.3730	1.0770
0.64	0.36	0.00	1.3785	1.0876
0.60	0.40	0.00	1.3841	1.0984
0.56	0.44	0.00	1.3897	1.1092
0.52	0.48	0.00	1.3954	1.1200
0.48	0.52	0.00	1.4011	1.1308
0.44	0.56	0.00	1.4069	1.1419
0.40	0.60	0.00	1.4129	1.1530
0.36	0.64	0.00	1.4189	1.1643
0.32	0.68	0.00	1.4249	1.1755

Continued on next page

Table A.1 – *Continued from previous page*

H_2O	$Glycerol$	Na_2SO_4	n_D	ρ
x_1	x_2	x_3	$-$	g/cm^3
0.28	0.72	0.00	1.4310	1.1866
0.24	0.76	0.00	1.4370	1.1976
0.20	0.80	0.00	1.4431	1.2085
0.16	0.84	0.00	1.4492	1.2192
0.12	0.88	0.00	1.4553	1.2299
0.08	0.92	0.00	1.4613	1.2404
0.04	0.96	0.00	1.4674	1.2508
0.00	1.00	0.00	1.4735	1.2611
1.00	0.00	0.01	1.3335	1.0002
0.99	0.00	0.01	1.3345	1.0071
0.98	0.00	0.02	1.3359	1.0160
0.97	0.00	0.03	1.3376	1.0252
0.96	0.00	0.04	1.3390	1.0340
0.95	0.00	0.05	1.3406	1.0436
0.94	0.00	0.06	1.3418	1.0520
0.93	0.00	0.07	1.3435	1.0619
0.92	0.00	0.08	1.3450	1.0700
0.91	0.00	0.09	1.3464	1.0808
0.90	0.00	0.10	1.3477	1.0900
0.88	0.00	0.12	1.3509	1.1100
0.86	0.00	0.14	1.3539	1.1300
0.84	0.00	0.16	1.3561	1.1480
0.82	0.00	0.18	1.3595	1.1705

Continued on next page

Table A.1 – *Continued from previous page*

H_2O	$Glycerol$	Na_2SO_4	n_D	ρ
x_1	x_2	x_3	$-$	g/cm^3
0.80	0.00	0.20	1.3620	1.1907
0.78	0.00	0.22	1.3643	1.2106
0.89	0.10	0.01	1.3464	1.0320
0.79	0.20	0.01	1.3591	1.0580
0.69	0.30	0.01	1.3717	1.0800
0.59	0.40	0.01	1.3852	1.1040
0.49	0.50	0.01	1.3993	1.1340
0.39	0.60	0.01	1.4141	1.1620
0.29	0.70	0.01	1.4286	1.1940
0.88	0.10	0.02	1.3482	1.0400
0.78	0.20	0.02	1.3602	1.0620
0.68	0.30	0.02	1.3731	1.0920
0.58	0.40	0.02	1.3867	1.1160
0.48	0.50	0.02	1.4013	1.1440
0.38	0.60	0.02	1.4158	1.1720
0.86	0.10	0.04	1.3508	1.0580
0.76	0.20	0.04	1.3630	1.0820
0.66	0.30	0.04	1.3770	1.1140
0.56	0.40	0.04	1.3911	1.1400
0.84	0.10	0.06	1.3542	1.0760
0.74	0.20	0.06	1.3668	1.1020
0.64	0.30	0.06	1.3802	1.1280
0.94	0.04	0.02	1.3409	1.0260

Continued on next page

Table A.1 – *Continued from previous page*

H_2O	$Glycerol$	Na_2SO_4	n_D	ρ
x_1	x_2	x_3	$-$	g/cm^3
0.92	0.04	0.04	1.3441	1.0460
0.90	0.04	0.06	1.3469	1.0620
0.88	0.04	0.08	1.3498	1.0780
0.86	0.04	0.10	1.3527	1.1000
0.92	0.06	0.02	1.3431	1.0300
0.90	0.06	0.04	1.3462	1.0480
0.88	0.06	0.06	1.3492	1.0680
0.86	0.06	0.08	1.3518	1.0860
0.84	0.06	0.10	1.3549	1.1060
0.90	0.08	0.02	1.3456	1.0340
0.88	0.08	0.04	1.3488	1.0520
0.86	0.08	0.06	1.3515	1.0700
0.84	0.08	0.08	1.3546	1.0920
0.82	0.08	0.10	1.3577	1.1100

Table A.1: Refractive indices and densities measurements for $H_2O - Glycerol - Na_2SO_4$ ternary system at atmospheric pressure and 293.35 K.

APPENDIX B

Database for RIM Study of $H_2O - Glycerol - Isopropanol$ Ternary System

The following Table B.1 provides the full refractive indices and densities measurements for $H_2O - Glycerol - Isopropanol$ ternary system at atmospheric pressure and 298.15 K. The refractive index is measured with a Sper Scientific 300037 Digital Refractometer with a RI range of $1.3330 < n_D < 1.5318$, which has an accuracy of 0.1% at a resolution of 0.0001. The density measurement is performed using a 50 ml volumetric flask, class A in combination with a Lianze I2000 digital multi-function scale, with an accuracy of 0.1g, which results in an uncertainty within 1% for density measurement.

H_2O	$Glycerol$	$Isopropanol$	n_D	ρ
x_1	x_2	x_3	$-$	g/cm^3
1.0000	0.0000	0.0000	1.3330	0.9980
0.9950	0.0050	0.0000	1.3336	0.9994
0.9900	0.0100	0.0000	1.3342	1.0005
0.9800	0.0200	0.0000	1.3353	1.0028
0.9700	0.0300	0.0000	1.3365	1.0051

Continued on next page

Table B.1 – *Continued from previous page*

H_2O	$Glycerol$	$Isopropanol$	n_D	ρ
x_1	x_2	x_3	$-$	g/cm^3
0.9600	0.0400	0.0000	1.3376	1.0074
0.9500	0.0500	0.0000	1.3388	1.0097
0.9400	0.0600	0.0000	1.3400	1.0120
0.9300	0.0700	0.0000	1.3412	1.0144
0.9200	0.0800	0.0000	1.3424	1.0167
0.9100	0.0900	0.0000	1.3436	1.0191
0.9000	0.1000	0.0000	1.3448	1.0215
0.8800	0.1200	0.0000	1.3472	1.0262
0.8600	0.1400	0.0000	1.3496	1.0311
0.8400	0.1600	0.0000	1.3521	1.0360
0.8200	0.1800	0.0000	1.3547	1.0409
0.8000	0.2000	0.0000	1.3572	1.0459
0.7600	0.2400	0.0000	1.3624	1.0561
0.7200	0.2800	0.0000	1.3676	1.0664
0.6800	0.3200	0.0000	1.3730	1.0770
0.6400	0.3600	0.0000	1.3785	1.0876
0.6000	0.4000	0.0000	1.3841	1.0984
0.5600	0.4400	0.0000	1.3897	1.1092
0.5200	0.4800	0.0000	1.3954	1.1200
0.4800	0.5200	0.0000	1.4011	1.1308
0.4400	0.5600	0.0000	1.4069	1.1419
0.4000	0.6000	0.0000	1.4129	1.1530
0.3600	0.6400	0.0000	1.4189	1.1643

Continued on next page

Table B.1 – *Continued from previous page*

H_2O	$Glycerol$	$Isopropanol$	n_D	ρ
x_1	x_2	x_3	$-$	g/cm^3
0.3200	0.6800	0.0000	1.4249	1.1755
0.2800	0.7200	0.0000	1.4310	1.1866
0.2400	0.7600	0.0000	1.4370	1.1976
0.2000	0.8000	0.0000	1.4431	1.2085
0.1600	0.8400	0.0000	1.4492	1.2192
0.1200	0.8800	0.0000	1.4553	1.2299
0.0800	0.9200	0.0000	1.4613	1.2404
0.0400	0.9600	0.0000	1.4674	1.2508
0.0000	1.0000	0.0000	1.4735	1.2611
0.8985	0.0000	0.1015	1.3419	0.9806
0.8009	0.0000	0.1991	1.3511	0.9668
0.7027	0.0000	0.2973	1.3583	0.9485
0.6001	0.0000	0.3999	1.3638	0.9258
0.5064	0.0000	0.4936	1.3679	0.9039
0.3948	0.0000	0.6052	1.3718	0.8772
0.3076	0.0000	0.6924	1.3742	0.8566
0.2213	0.0000	0.7787	1.3760	0.8361
0.1016	0.0000	0.8984	1.3774	0.8069
0.0009	0.0000	0.9991	1.3772	0.7808
0.7997	0.1000	0.1003	1.3530	1.0060
0.6997	0.2000	0.1003	1.3655	1.0320
0.5997	0.3000	0.1003	1.3780	1.0560
0.4997	0.4000	0.1003	1.3910	1.0800

Continued on next page

Table B.1 – *Continued from previous page*

H_2O	$Glycerol$	$Isopropanol$	n_D	ρ
x_1	x_2	x_3	$-$	g/cm^3
0.3997	0.5000	0.1003	1.4052	1.1040
0.2997	0.6000	0.1003	1.4190	1.1280
0.1997	0.7000	0.1003	1.4333	1.1560
0.0997	0.8000	0.1003	1.4487	1.1760
0.6993	0.1000	0.2007	1.3633	0.9920
0.5993	0.2000	0.2007	1.3728	1.0280
0.4993	0.3000	0.2007	1.3859	1.0380
0.3993	0.4000	0.2007	1.3982	1.0560
0.2993	0.5000	0.2007	1.4108	1.0780
0.1993	0.6000	0.2007	1.4235	1.1040
0.1020	0.7000	0.1980	1.4383	1.1260
0.5990	0.1000	0.3010	1.3677	0.9720
0.4990	0.2000	0.3010	1.3786	0.9920
0.3990	0.3000	0.3010	1.3906	1.0160
0.2990	0.4000	0.3010	1.4016	1.0320
0.1990	0.5000	0.3010	1.4142	1.0560
0.1030	0.6000	0.2970	1.4263	1.0600
0.5010	0.1000	0.3990	1.3723	0.9520
0.4010	0.2000	0.3990	1.3819	0.9760
0.3010	0.3000	0.3990	1.3931	0.9920
0.2010	0.4000	0.3990	1.4051	1.0120
0.1040	0.5000	0.3960	1.4165	1.0080
0.4007	0.1000	0.4993	1.3755	0.9280

Continued on next page

Table B.1 – *Continued from previous page*

H_2O	$Glycerol$	$Isopropanol$	n_D	ρ
x_1	x_2	x_3	$-$	g/cm^3
0.3007	0.2000	0.4993	1.3855	0.9460
0.2050	0.3000	0.4950	1.3973	0.9500
0.1050	0.4000	0.4950	1.4081	0.9660
0.3060	0.1000	0.5940	1.3788	0.9100
0.2060	0.2000	0.5940	1.3896	0.9100
0.1060	0.3000	0.5940	1.4000	0.9240
0.2070	0.1000	0.6930	1.3794	0.9000
0.1070	0.2000	0.6930	1.3875	0.9340
0.1080	0.1000	0.7920	1.3838	0.8480
0.0090	0.1000	0.8910	1.3886	0.8180
0.0080	0.2000	0.7920	1.3914	0.8500
0.0070	0.3000	0.6930	1.4001	0.8940
0.0060	0.4000	0.5940	1.4089	0.9320
0.0050	0.5000	0.4950	1.4206	0.9840
0.0040	0.6000	0.3960	1.4287	1.0300
0.0030	0.7000	0.2970	1.4407	1.0800
0.0020	0.8000	0.1980	1.4518	1.1430
0.0010	0.9000	0.0990	1.4626	1.1800
0.0100	0.0000	0.9900	1.3765	0.7860

Table B.1: Refractive indices and densities measurements for $H_2O - Glycerol - Isopropanol$ ternary system at atmospheric pressure and 298.15 K.

APPENDIX C

Preliminary RIM study in Replica Facility

Due to the cost of the chemicals and potentially hazardous waste for the testing, a scaled acrylic replica ($11 \times 11 \times 11\ cm^3$) of the original DESTROJER facility was designed and manufactured as shown in Figure C.1. The jet inlet diameter is scaled to 1.1 mm.

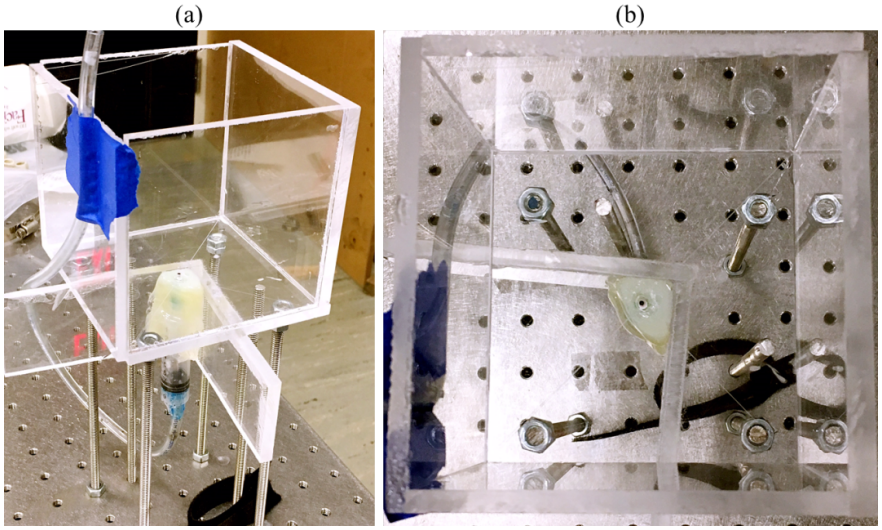

Figure C.1: A scaled replica ($11 \times 11 \times 11\ cm^3$) of the square tank (a) leveled on the optics table, and (b) its top view with the scaled jet nozzle on the bottom.

The jet is powered by a syringe pump. However, due to its volumetric flow rate settings, the syringe pump can only provide an initial jet velocity of 0.5 m/s at maximum, resulting in a Reynolds number of 547. Even though this is classified as a laminar flow, the raw particle

images from PIV measurements can still be useful to tell whether there is a mismatch of RI for the stratified environment test.

To demonstrate the fundamental differences between the RI-matched and RI-not-matched cases, sodium chloride (NaCl) and isopropanol solutions are used to create the stratified layers, and both of them are made to have a refractive index of 1.3424 at 20.5 °C. After seeding the solutions with the fluorescent glass hollow particles and forming the stratified layers in the small replica tank, Figure C.2 shows the raw particle images without the jet for two cases: (a) the refractive index of NaCl solution on the bottom matches prefect with the isopropanol solution on the top; (b) the mismatched refractive index for the NaCl on the bottom and the pure water on the top. The red line indicates the separation of the stratified layers due to the density differences. For the well-matched refractive index case, the raw PIV images have particles with shape contrast and pixel occupations as those images for uniform environment measurements before, while the light scatted by the particles gets bent and the image gets blurred due to the defocus for the mismatched case. It can be illustrated that how vital the matching of refractive indexes is for the valid PIV measurements.

Figure C.3 shows the raw and processed images when the jet with the same NaCl solution as the bottom part is impacting the stratified layers, and in Figure C.3(a) the matched case remains to have a good contrast for particles and background, resulting in a continuous velocity field, but Figure C.3(b) has lots of blurred regions due to the mismatched refractive index, leading to many empty spaces in the velocity vector field.

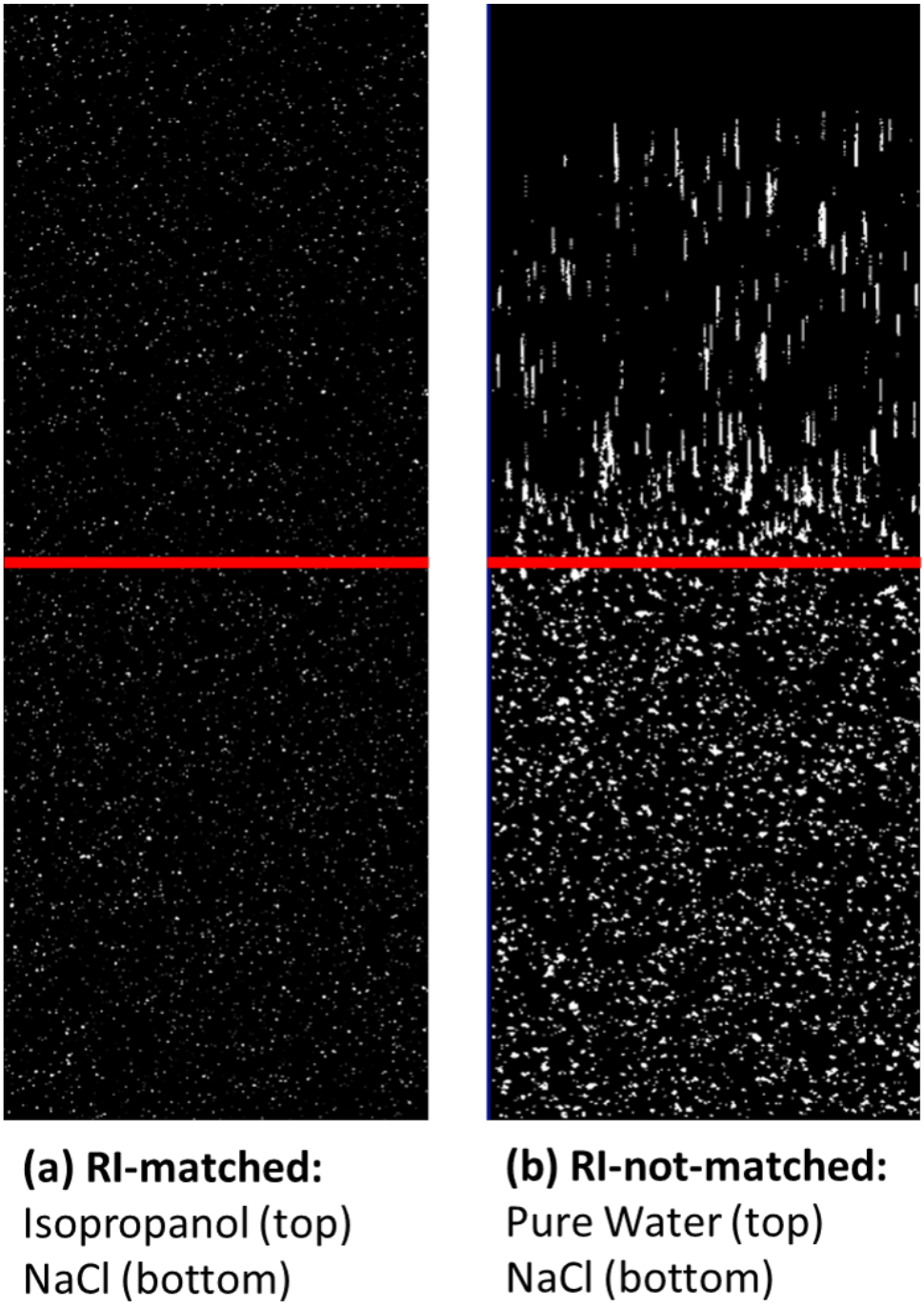

Figure C.2: Stratified layers with (a) matched refractive index at 1.3424 for 5%wt NaCl and 10%wt isopropanol solutions and (b) unmatched refractive index for 5%wt NaCl solution and pure water.

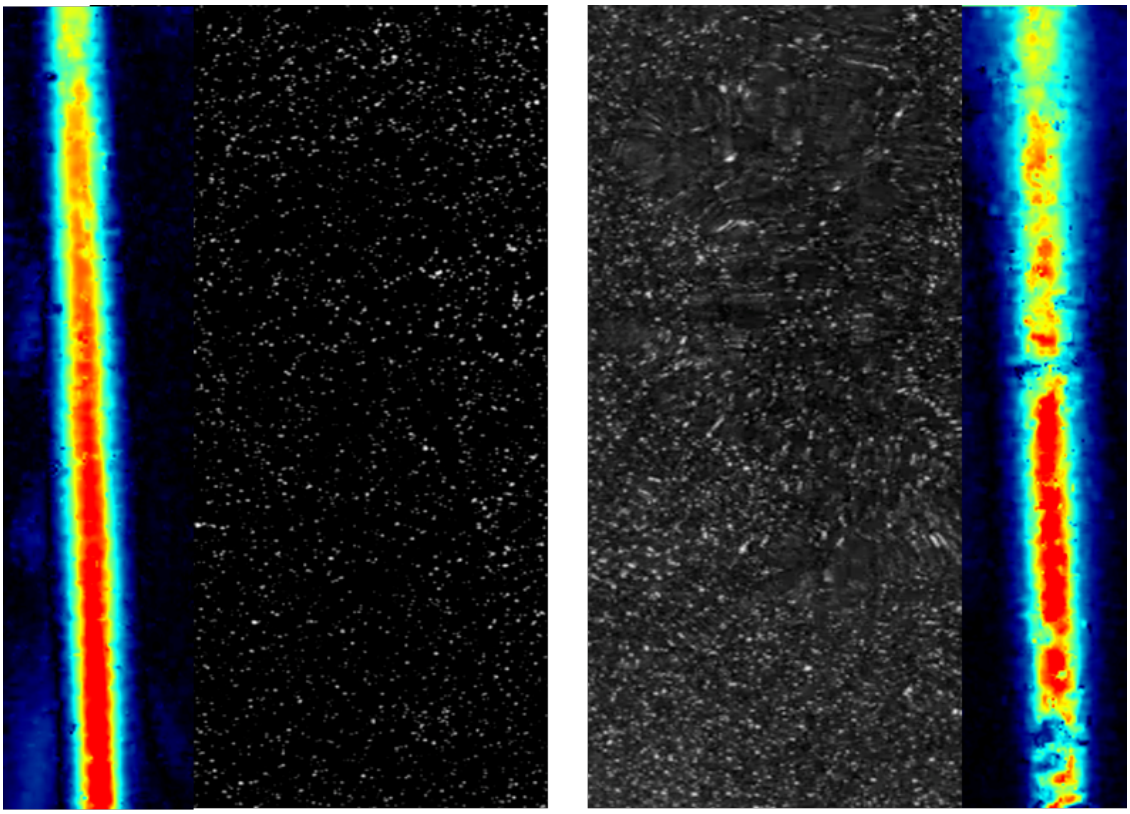

Figure C.3: PIV measurements of (a) matched refractive case and (b) unmatched refractive index case. The processed instantaneous velocity fields are shown for the corresponding raw images.

APPENDIX D

Data Convergence

The statistical convergence of the measured quantities (including the mean velocities and higher-order fluctuations like Reynolds stresses) was tested for each of the conducted experiments. Convergence was analyzed as follows: the ensemble average of a measured quantity (for example, the streamwise mean velocity $\overline{u}$) is computed by random sampling the collected velocity vectors at given locations from the complete time-series (in terms of the overall number of the recorded instantaneous fields N, see Equation 2.4 to compute the time-averages. The random sampling procedure helps to represent the spread of the quantity of interest. In Figure D.1, the scattering plot in black dots shows the resulting convergence of the uniform case D029 for mean streamwise velocity, Reynolds and shear stresses at 60 jet-diameter away on the centerline of the jet, while the red line indicates the converged value in the end. Keeping the arrangement of plots and measurement location the same, Figure D.2 shows the positively buoyant jet when lighter fluid shoot into heavier surrounding, Figure D.3 is for the negatively buoyant jet (heavier jet into lighter surrounding), and Figure D.4 shows the lighter jet impinging the sharp density interface. For all the cases, the convergence plots of the measured quantities illustrate a range of $\pm$ 5% of its final converged values.

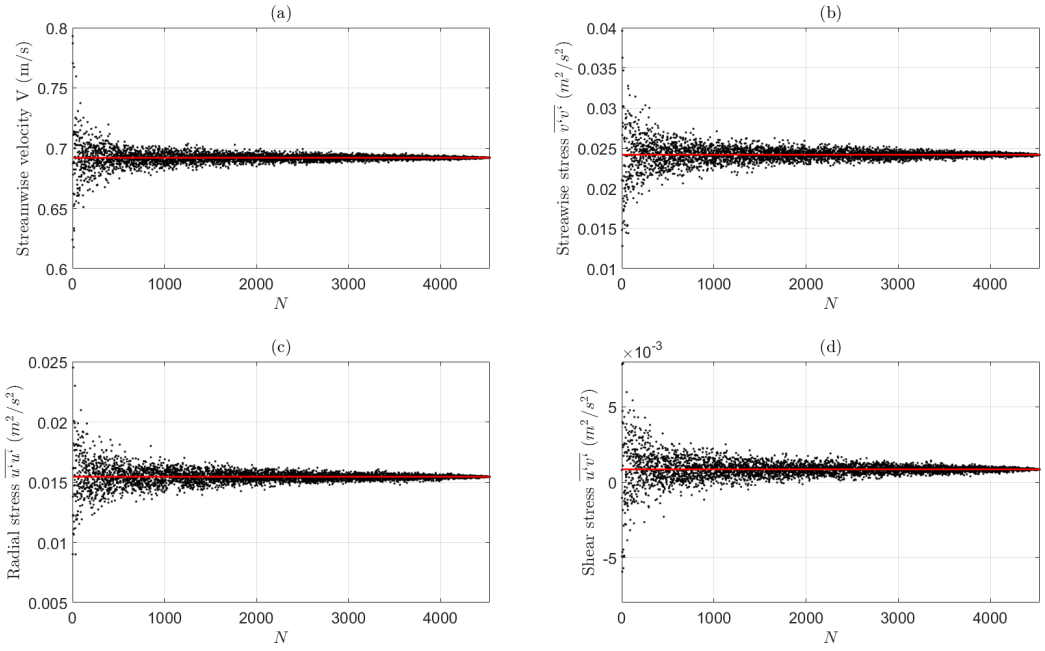

Figure D.1: Convergence plots for uniform case D029: (a) Mean streamwise velocity, (b) Streamwise stress $\overline{v'v'}$, (c) Radial stress $\overline{u'u'}$ and (d) Shear stress $\overline{u'v'}$.

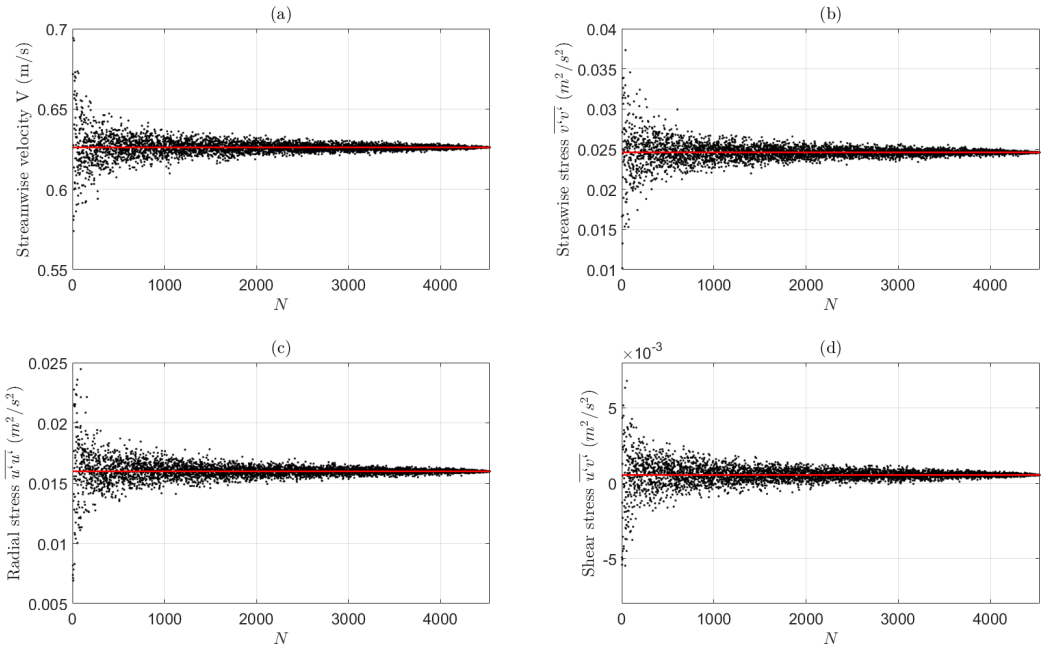

Figure D.2: Convergence plots for stratified case D033 (L-H): (a) Mean streamwise velocity, (b) Streamwise stress $\overline{v'v'}$, (c) Radial stress $\overline{u'u'}$ and (d) Shear stress $\overline{u'v'}$.

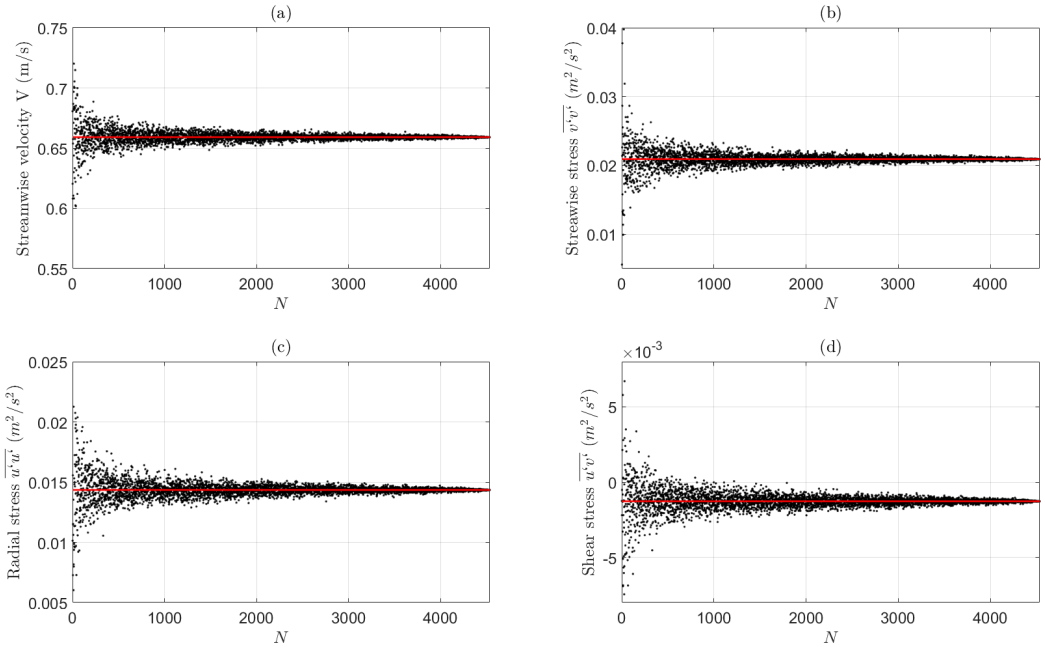

Figure D.3: Convergence plots forstratified case D035 (H-L): (a) Mean streamwise velocity, (b) Streamwise stress $\overline{v'v'}$, (c) Radial stress $\overline{u'u'}$ and (d) Shear stress $\overline{u'v'}$.

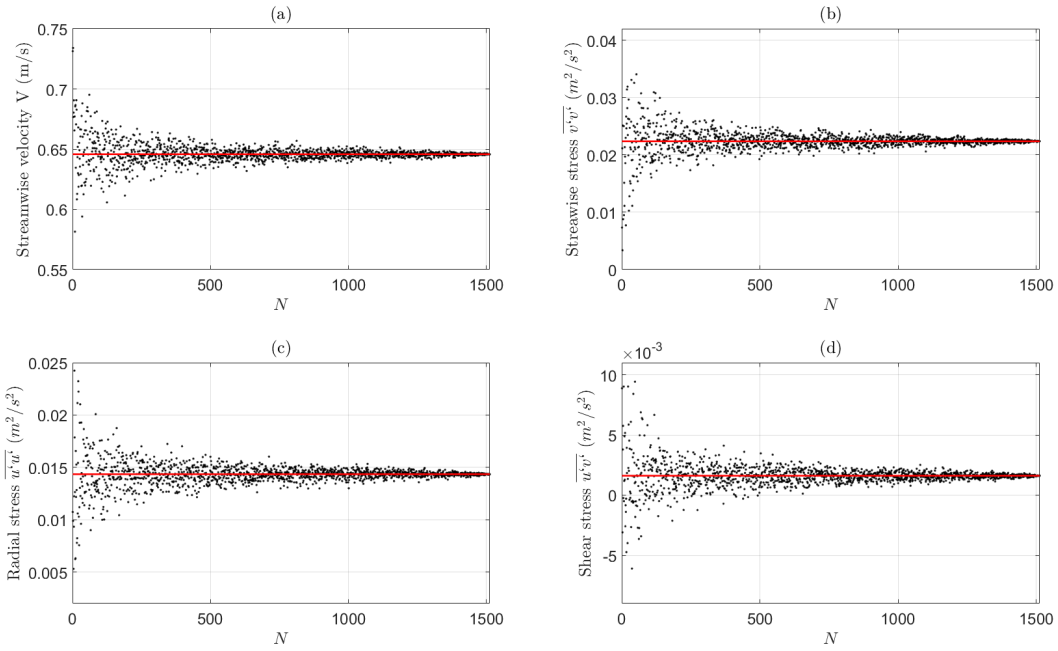

Figure D.4: Convergence plots for stratified case D042 (L-Sharp): (a) Mean streamwise velocity, (b) Streamwise stress $\overline{v'v'}$, (c) Radial stress $\overline{u'u'}$ and (d) Shear stress $\overline{u'v'}$.

APPENDIX E

Nozzle Symmetric Validation

To verify whether the nozzle is symmetric or not, two perpendicular imaging planes were chosen and their average velocity fields, as well as Reynolds stresses, were compared and discussed. As shown in Figure E.1, PIV laser and camera system are set up for different orientations of laser direction (SE and SW indicated the laser pointing direction) and corresponding imaging planes. Detailed experimental parameters for two perpendicular imaging planes at Re = 10,000 in near-field was summarized in Table E.1. Filming 9054 images and in total about 23-second measure duration could lead to a well converged near-field flow pattern.

Table E.1: Experimental parameters used in the symmetric test.

Laser Facing	$\boldsymbol{U_0}$	***Temperature***	***Image Rate***	***Measure Duration***
$--$	m/s	$^{\circ}C$	Hz	s
SW	0.79 ± 0.02	19.35 ± 0.2	400	22.64
SE	0.79 ± 0.02	20.58 ± 0.2	400	22.64

The axial time-average velocities obtained at different downstream locations x/D = 1, 2, and 3 were shown in Figure E.2 for x-y and y-z imaging planes, together with averaged normal and shear stresses and Reynolds stresses. For the axial time-average velocity in the

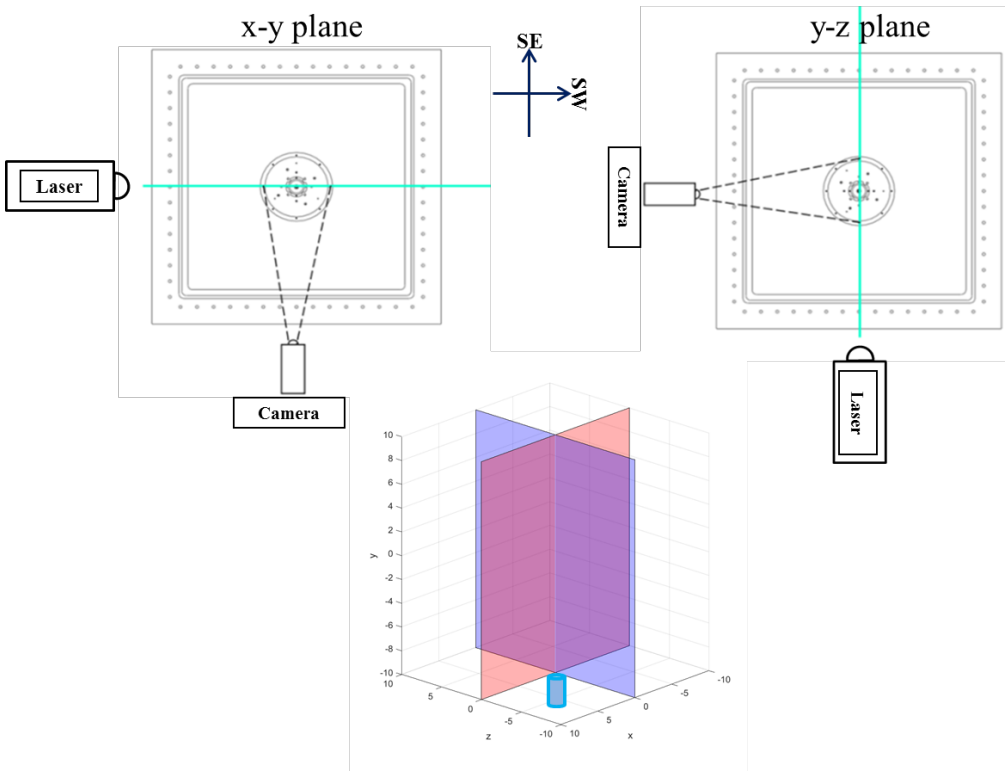

Figure E.1: Illustration of laser and camera planes for the symmetric test, and for the different color planes plotted at the bottom; red indicates x-y imaging plane and blue is y-z imaging plane.

first row (u component), which is along the jet flow direction, velocity profiles for this two planes at each location agreed with each other very well. As for the velocity component in the second row which is perpendicular to jet flow directions (v component), it is reasonable that the repeatability for those will not be as good as the axial velocities because most fluid particles are dominated by the jet axial momentum and will not move across the jet. Shown in the third and fourth row in Figure E.2, streamwise and radial normal stresses τ_{xx} and τ_{yy} also indicated a good match. Also, for Reynolds shear stresses τ_{xy} in the last row, data from both x-y and y-z plane showed a perfect match at the trend and peak values as well. In conclusion, shown in Figure E.2, the agreements in velocities and stresses profiles for two perpendicular planes across the nozzle indicated that the jet flow created in the DESTROJER facility could be considered as symmetric. The same procedures have also been applied to the miniDESTROJER facility with the final conclusion to be a symmetric jet as well.

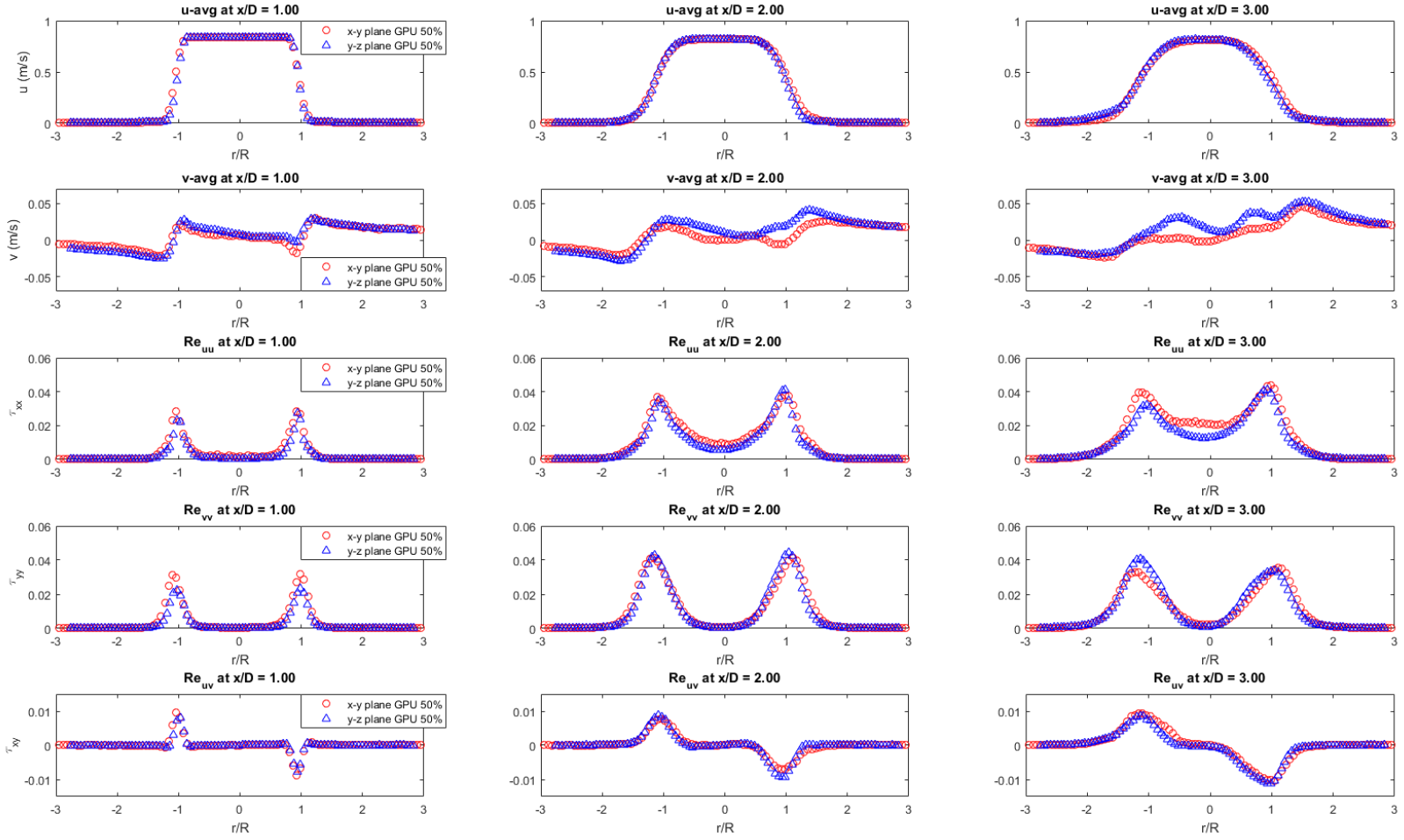

Figure E.2: Average velocities and Reynolds stresses at different downstream locations x/D = 1 (left), 2 (middle), and 3 (right) for x-y and y-z imaging planes.

BIBLIOGRAPHY

BIBLIOGRAPHY

[1] FrenchKheldar. Turbulent jet. https://www.flickr.com/photos/frenchkheldar/2295921232/in/photostream/. Accessed: 2020–05–19. viii, 2

[2] Charism Sayat. Erupting volcano in Philippines. https://abcnews.go.com/International/erupting-volcano-philippines-forces-evacuation-thousands-villagers/story?id=52576060. Accessed: 2020–05–19. viii, 2

[3] Raeky. Sodium-Cooled Fast Reactor. https://commons.wikimedia.org/wiki/File:Sodium_fast_reactor.jpg. Accessed: 2020–05–19. viii, 4

[4] Venugopal Koikal Varma, David Eugene Holcomb, Fred J Peretz, Eric Craig Bradley, Dan Ilas, AL Qualls, and Nathaniel M Zaharia. Ahtr mechanical, structural, and neutronic preconceptual design. Technical report, Oak Ridge National Lab.(ORNL), Oak Ridge, TN (United States), 2012. viii, 5

[5] Mrinal Kaushik, Rakesh Kumar, and G Humrutha. Review of computational fluid dynamics studies on jets. *American Journal of Fluid Dynamics*, 5(3A):1–11, 2015. viii, 7

[6] CG Ball, H Fellouah, and A Pollard. The flow field in turbulent round free jets. *Progress in Aerospace Sciences*, 50:1–26, 2012. viii, 9

[7] WR Quinn and J Militzer. Effects of nonparallel exit flow on round turbulent free jets. *International Journal of Heat and Fluid Flow*, 10(2):139–145, 1989. viii, 9, 16, 52, 56

[8] J Mi, DS Nobes, and GJ Nathan. Influence of jet exit conditions on the passive scalar field of an axisymmetric free jet. *Journal of Fluid Mechanics*, 432:91–125, 2001. viii, 8, 9, 38, 54, 56, 70, 94, 96

[9] Gu Xu and Robert Antonia. Effect of different initial conditions on a turbulent round free jet. *Experiments in Fluids*, 33(5):677–683, 2002. viii, 9, 52, 53, 54, 56, 57, 58

[10] MO Iqbal and FO Thomas. Coherent structure in a turbulent jet via a vector implementation of the proper orthogonal decomposition. *Journal of Fluid Mechanics*, 571:281–326, 2007. viii, 9, 52

[11] Hachimi Fellouah and Andrew Pollard. The velocity spectra and turbulence length scale distributions in the near to intermediate regions of a round free turbulent jet. *Physics of Fluids*, 21(11):115101, 2009. viii, 9, 10, 11, 56, 57, 58, 70

[12] idealsimulations. Turbulence Models In CFD. https://www.idealsimulations.com/resources/turbulence-models-in-cfd. Accessed: 2020–05–19. viii, 13

[13] André Bakker. Turbulence Models for Applied Computational Fluid Dynamics. http://www.bakker.org/dartmouth06/engs150/10-rans.pdf. Accessed: 2020–05–19. viii, 14

[14] LaVision®. Particle image velocimetry. https://www.piv.de/piv/measurement_principle/index.php. Accessed: 2020–05–19. viii, 19

[15] BFA Wieneke. *PIV Uncertainty Quantification and Beyond*. PhD thesis, Delft University of Technology, 2017. ix, 23

[16] LaVision®. Product manual – sheet optics (divergent). http://www.lavision.de/en/downloads/manuals/laser-accessories.php. Accessed: 2020–05–19. ix, 23

[17] LaVision®. Laser induced fluorescence. https://www.smart-piv.com/en/techniques/lif-plif/index.php. Accessed: 2020–05–19. ix, 25

[18] Zaereth. Rhodamine6G Chloride. http://en.wikipedia.org/wiki/File:Rhodamine6G_Chloride.JPG. Accessed: 2020–05–19. ix, 26

[19] M Sakai, T Ohmori, and M Fujii. Two-color picosecond time-resolved infrared super-resolution microscopy. *Handai Nanophotonics*, 3:189–195, 2007. ix, 26

[20] Johne Jesus Mol Peixoto, Weslei Viana Gabriel, Ciro Azevedo Silva, Leticia Queiroz Ribeiro, Carlos Antonio da Silva, Itavahn Alves da Silva, and Varadarajan Seshadri. Analysis of jet behavior and surface fluctuations in the meniscus of fluid in a physical model of a beam blank mold and cfd modelling. In *8th International Symposium on High-Temperature Metallurgical Processing*, pages 89–99. Springer, 2017. ix, 27

[21] Shogo Shakouchi, Shota Fukue, Tomomi Uchiyama, et al. Investigation of the behavior of a jet issued into two-layer density-stratified fluid. *Journal of Flow Control, Measurement & Visualization*, 3(01):1, 2014. ix, 39, 105

[22] Benedikt Krohn, Annalisa Manera, and Victor Petrov. A novel method to create high density stratification with matching refractive index for optical flow investigations. *Experiments in Fluids*, 59(4):66, 2018. ix, 38, 42, 44, 46, 79, 139

[23] Israel Wygnanski and Ho Fiedler. Some measurements in the self-preserving jet. *Journal of Fluid Mechanics*, 38(3):577–612, 1969. x, xiii, 53, 54, 64, 65, 118, 126

[24] Hussein J Hussein, Steven P Capp, and William K George. Velocity measurements in a high-reynolds-number, momentum-conserving, axisymmetric, turbulent jet. *Journal of Fluid Mechanics*, 258:31–75, 1994. x, xiii, 8, 51, 53, 54, 57, 58, 64, 65, 118, 140

[25] Alexandros P Vouros and Th Panidis. Turbulent properties of a low reynolds number, axisymmetric, pipe jet. *Experimental thermal and fluid science*, 44:42–50, 2013. x, xiii, 54, 57, 64, 65, 118

[26] Xiaoliang He, Sourabh V Apte, Justin R Finn, and Brian D Wood. Characteristics of turbulence in a face-centred cubic porous unit cell. *Journal of Fluid Mechanics*, 873:608–645, 2019. x, 67

[27] Benedikt Krohn, Sunming Qin, John Downing, Victor Petrov, and Annalisa Manera. An experimental study of local self-similarity in the mixing transition of a turbulent free jet. *Nuclear Science and Engineering*, 193(1-2):171–184, 2019. x, xi, 32, 68, 69, 71, 72, 74, 75, 76, 78

[28] Jiaxin Mao, Sunming Qin, , Victor Petrov, and Annalisa Manera. Rans simulations of turbulent round jets in the presence of density difference and comparison with high-resolution experimental data. In *The 19th International Topical Meeting on Nuclear Reactor Thermalhydraulics (NURETH-19)*. American Nuclear Society, 2011. xiii, 119, 121, 123, 124, 125, 126, 127, 128, 130, 131, 132, 133, 134, 136, 137, 138

[29] Hamed Sadeghi, Philippe Lavoie, and Andrew Pollard. Self-preservation of the transport equations in a free round turbulent jet. In *Ninth International Symposium on Turbulence and Shear Flow Phenomena (TSFP-9)*, pages 8B–1. the University of Melbourne, 2015. xv, 54, 112

[30] Ching Jen Chen and Wolfgang Rodi. Vertical turbulent buoyant jets: a review of experimental data. *Nasa STI/Recon Technical Report A*, 80, 1980. 3

[31] PF Linden. The interaction of a vortex ring with a sharp density interface: a model for turbulent entrainment. *Journal of Fluid Mechanics*, 60(3):467–480, 1973. 3

[32] RP Cleaver, MR Marshal, and PF Linden. The build-up of concentration within a single enclosed volume following a release of natural gas. *Journal of hazardous materials*, 36(3):209–226, 1994. 3

[33] Wolfgang Rodi. *Turbulent buoyant jets and plumes: HMT: the science & applications of heat and mass transfer. Reports, reviews & computer programs*, volume 6. Elsevier, 2014. 3

[34] Richard W Mott and Andrew W Woods. On the mixing of a confined stratified fluid by a turbulent buoyant plume. *Journal of fluid mechanics*, 623:149–165, 2009. 3

[35] L Dehmani, Doan Kim-Son, and L Gbahoue. Turbulent structure of an axisymmetric plume penetrating a strong density stratification. *International journal of heat and fluid flow*, 17(5):452–459, 1996. 3

[36] YJP Lin and PF Linden. The entrainment due to a turbulent fountain at a density interface. *Journal of Fluid Mechanics*, 542:25–52, 2005. 3

[37] PD Friedman and J Katz. Rise height for negatively buoyant fountains and depth of penetration for negatively buoyant jets impinging an interface. *J. Fluids Eng.*, 122(4):779–782, 2000. 3

[38] Lynn J Bloomfield and Ross C Kerr. Turbulent fountains in a stratified fluid. *Journal of Fluid Mechanics*, 358:335–356, 1998. 3

[39] Joseph K Ansong, Patrick J Kyba, and Bruce R Sutherland. Fountains impinging on a density interface. *Journal of Fluid Mechanics*, 595:115–139, 2008. 3, 105, 141

[40] WD Baines. Entrainment by a plume or jet at a density interface. *Journal of Fluid Mechanics*, 68(2):309–320, 1975. 3

[41] Evgeny V Ermanyuk and J-B Flór. Taylor–couette flow in a two-layer stratified fluid: instabilities and mixing. *Dynamics of atmospheres and oceans*, 40(1-2):57–69, 2005. 3

[42] Estelle Guyez, J-B Flor, and Emil J Hopfinger. Turbulent mixing at a stable density interface: the variation of the buoyancy flux–gradient relation. *Journal of Fluid Mechanics*, 577:127–136, 2007. 3

[43] Domenico Paladino, Michele Andreani, Robert Zboray, and Jörg Dreier. Toward a cfd-grade database addressing lwr containment phenomena. *Nuclear engineering and design*, 253:331–342, 2012. 3

[44] E Deri, B Cariteau, and D Abdo. Air fountains in the erosion of gaseous stratifications. *International journal of heat and fluid flow*, 31(5):935–941, 2010. 4, 38

[45] Hsun-Chia Lin, Sheng Zhang, David Diamond, Stephen Bajorek, Richard Christensen, Yujun Guo, Graydon Yoder, Shanbin Shi, Qiuping Lv, and Xiaodong Sun. Phenomena identification and ranking table study for thermal hydraulics for advanced high temperature reactor. *Annals of Nuclear Energy*, 124:257–269, 2019. 5

[46] James C Laurence. Intensity, scale, and spectra of turbulence in mixing region of free subsonic jet. Technical report, National Advisory Committee for Aeronautics (NACA): Lewis Flight Propulsion Lab. Cleveland, OH, United States, 1956. 6

[47] GJ Nathan, J Mi, ZT Alwahabi, GJR Newbold, and DS Nobes. Impacts of a jet's exit flow pattern on mixing and combustion performance. *Progress in Energy and Combustion Science*, 32(5-6):496–538, 2006. 8

[48] P Hrycak, S Jachna, and DT Lee. A study of characteristics of developing, incompressible, axi-symmetric jets. *Letters in Heat and Mass Transfer*, 1(1):63–71, 1974. 8

[49] William K George and R Arndt. The self-preservation of turbulent flows and its relation to initial conditions and coherent structures. *Advances in turbulence*, 3973, 1989. 8

[50] Stephen B Pope. *Turbulent flows*. IOP Publishing, 2001. 8

[51] Andrey Nikolaevich Kolmogorov. The local structure of turbulence in incompressible viscous fluid for very large reynolds numbers. *Cr Acad. Sci. URSS*, 30:301–305, 1941. 10

[52] Henry A Becker and TA Massaro. Vortex evolution in a round jet. *Journal of fluid mechanics*, 31(3):435–448, 1968. 11

[53] Paul E Dimotakis, Richard C Miake-Lye, and Dimitris A Papantoniou. Structure and dynamics of round turbulent jets. *The Physics of fluids*, 26(11):3185–3192, 1983. 11

[54] Stephen K Robinson. Coherent motions in the turbulent boundary layer. *Annual Review of Fluid Mechanics*, 23(1):601–639, 1991. 11

[55] Walter Tollmien. Berechnung turbulenter ausbreitungsvorgänge. *ZAMM-Journal of Applied Mathematics and Mechanics/Zeitschrift für Angewandte Mathematik und Mechanik*, 6(6):468–478, 1926. 12

[56] Han Zhang, Yabing Li, Jianjun Xiao, and Thomas Jordan. Large eddy simulations of the all-speed turbulent jet flow using 3-d cfd code gasflow-mpi. *Nuclear Engineering and Design*, 328:134–144, 2018. 12

[57] Sasan Salkhordeh, Sagnik Mazumdar, Anirban Jana, and Mark L Kimber. Reynolds number dependence of higher order statistics for round turbulent jets using large eddy simulations. *Flow, Turbulence and Combustion*, 102(3):559–587, 2019. 12

[58] Mukul Bisoi, Manab Kumar Das, Subhransu Roy, and Devendra Kumar Patel. Large eddy simulation of three-dimensional plane turbulent free jet flow. *European Journal of Mechanics-B/Fluids*, 65:423–439, 2017. 12

[59] Chris CK Lai and Scott A Socolofsky. Budgets of turbulent kinetic energy, reynolds stresses, and dissipation in a turbulent round jet discharged into a stagnant ambient. *Environmental Fluid Mechanics*, 19(2):349–377, 2019. 12, 137

[60] Zhiyan Wang, Muhsin M Ameen, Sibendu Som, and John Abraham. Assessment of large-eddy simulations of turbulent round jets using low-order numerical schemes. *SAE International Journal of Commercial Vehicles*, 10(2017-01-0575):572–581, 2017. 12

[61] Ping Wang, Jochen Fröhlich, Vittorio Michelassi, and Wolfgang Rodi. Large-eddy simulation of variable-density turbulent axisymmetric jets. *International Journal of Heat and Fluid Flow*, 29(3):654–664, 2008. 12

[62] David C Wilcox et al. *Turbulence modeling for CFD*, volume 2. DCW industries La Canada, CA, 1998. 15, 127

[63] Christian Heschl, Kiao Inthavong, Wolfgang Sanz, and Jiyuan Tu. Nonlinear eddy viscosity modeling and experimental study of jet spreading rates. *Indoor air*, 24(1):93–102, 2014. 16

[64] Shahriar Ghahremanian and Bahram Moshfegh. Evaluation of rans models in predicting low reynolds, free, turbulent round jet. *Journal of Fluids Engineering*, 136(1), 2014. 16

[65] TN Aziz, JP Raiford, and AA Khan. Numerical simulation of turbulent jets. *Engineering applications of computational fluid mechanics*, 2(2):234–243, 2008. 16, 129

[66] Martin Miltner, Christian Jordan, and Michael Harasek. Cfd simulation of straight and slightly swirling turbulent free jets using different rans-turbulence models. *Applied thermal engineering*, 89:1117–1126, 2015. 16, 126, 127

[67] Niloy Das, SM Rakibul Islam, Sayeed Mohammed, and Mohammad Nasim Hasan. Numerical study of turbulent round free jet. In *AIP Conference Proceedings*, volume 1980, page 040026. AIP Publishing LLC, 2018. 16

[68] Ehsan Faghani, Simin Dokht Saemi, Reza Maddahian, and Bijan Farhanieh. On the effect of inflow conditions in simulation of a turbulent round jet. *Archive of Applied Mechanics*, 81(10):1439–1453, 2011. 16

[69] V Petrov and A Manera. Validation of STAR-CCM+ for bouyancy driven mixing in a PWR reactor pressure vessel. In *The 14th International Topical Meeting on Nuclear Reactor Thermalhydraulics (NURETH-14)*. Canadian Nuclear Society, 2011. 16

[70] Daniel Nunez. *High-Resolution Experiments of Momentum- and Buoyancy-Driven Flows for the Validation and Advancement of Computational Fluid Dynamics Codes*. PhD thesis, University of Michigan, 2019. 16

[71] MS Hossain and W Rodi. A turbulence model for buoyant flows and its application to vertical buoyant jets. In *Turbulent buoyant jets and plumes*, pages 121–178. Elsevier, 1982. 17

[72] Wolfgang Rodi. *Turbulence models and their application in hydraulics*. CRC Press, 1993. 17

[73] Zhenghua Yan and Göran Holmstedt. A two-equation turbulence model and its application to a buoyant diffusion flame. *International Journal of Heat and Mass Transfer*, 42(7):1305–1315, 1999. 17

[74] Jude Worthy, V Sanderson, and P Rubini. Comparison of modified k-ϵ turbulence models for buoyant plumes. *Numerical Heat Transfer: Part B: Fundamentals*, 39(2):151–165, 2001. 17

[75] Markus Raffel, Christian E Willert, Fulvio Scarano, Christian J Kähler, Steve T Wereley, and Jürgen Kompenhans. *Particle image velocimetry: a practical guide*. Springer, 2018. 18

[76] LaVision®. DaVis 8.4. `https://www.lavision.de/en/downloads/software/index.php`. 2017. 32

[77] ET Whitaker. On the functions which are represented by the expansion of interpolating theory. In *Proceedings of the Royal Society of Edinburgh*, volume 35, pages 181–194, 1915. 32, 35

[78] Peter AM Kalt, Cristian H Birzer, and Graham J Nathan. Corrections to facilitate planar imaging of particle concentration in particle-laden flows using mie scattering, part 1: Collimated laser sheets. *Applied optics*, 46(23):5823–5834, 2007. 32

[79] SJ Kline and FA McClintock. Describing uncertainties in single-sample experiments. *Mechanical Engineering*, 75:3–8, 1953. 35

[80] Cameron Tropea and Alexander L Yarin. *Springer handbook of experimental fluid mechanics*. Springer Science & Business Media, 2007. 35

[81] Casimir WH van Doorne. *Stereoscopic PIV on transition in pipe flow*. PhD thesis, Universiteit Delft, 2004. 35

[82] JM Foucaut, B Miliat, N Perenne, and M Stanislas. Characterization of different piv algorithms using the europiv synthetic image generator and real images from a turbulent boundary layer. In *Particle Image Velocimetry: Recent Improvements*, pages 163–185. Springer, 2004. 35

[83] Richard D Keane and Ronald J Adrian. Theory of cross-correlation analysis of piv images. *Applied scientific research*, 49(3):191–215, 1992. 35

[84] Michael Sullivan and JCM Verhoosel. *Statistics: Informed decisions using data*. Pearson New York, 2013. 36

[85] Benedikt Krohn. *Turbulent Structures in a Planar Horizontal Gas Mixing Layer Under the Influence of High Density Gradients*. PhD thesis, ETH Zurich, 2018. 36

[86] AD Birch, DR Brown, MG Dodson, and JR Thomas. The turbulent concentration field of a methane jet. *Journal of Fluid Mechanics*, 88(3):431–449, 1978. 38, 94, 96

[87] FC Lockwood and HA Moneib. Fluctuating temperature measurements in a heated round free jet. *Combustion Science and Technology*, 22(1-2):63–81, 1980. 38, 94, 96

[88] Cecilia D Richards and William M Pitts. Global density effects on the self-preservation behaviour of turbulent free jets. *Journal of Fluid Mechanics*, 254:417–435, 1993. 38, 94, 96

[89] Microelectronics Heat Transfer Laboratory. Fluid Properties Calculator. `http://www.mhtl.uwaterloo.ca/old/onlinetools/airprop/airprop.html`. Accessed: 2020–05–19. 38, 41

[90] Lara Adrian, Ronald J Adrian, and Jerry Westerweel. *Particle image velocimetry*. 30. Cambridge university press, 2011. 39

[91] James J Riley and Stephen M DeBruynkops. Dynamics of turbulence strongly influenced by buoyancy. *Physics of Fluids*, 15(7):2047–2059, 2003. 39

[92] Pierre Augier, Paul Billant, Maria-Eletta Negretti, and J-M Chomaz. Experimental study of stratified turbulence forced with columnar dipoles. *Physics of Fluids*, 26(4):046603, 2014. 39

[93] GJ Daviero, PJW Roberts, and K Maile. Refractive index matching in large-scale stratified experiments. *Experiments in fluids*, 31(2):119–126, 2001. 40, 41

[94] A Alahyari and Ellen K Longmire. Particle image velocimetry in a variable density flow: application to a dynamically evolving microburst. *Experiments in Fluids*, 17(6):434–440, 1994. 41

[95] Trevor J Mcdougall. On the elimination of refractive-index variations in turbulent density-stratified liquid flows. *Journal of Fluid Mechanics*, 93(1):83–96, 1979. 41

[96] Imad Hannoun. Matching the refractive index [in] density stratified flows. Technical report, California Institute of Technology, 1985. 41

[97] A Touriño, M Hervello, V Moreno, G Marino, and M Iglesias. Change of refractive indices in ternary mixtures containing chlorobenzene-n-hexane-(n-heptane or n-octane) at 298.15 k. *Journal–Serbian Chemical Society*, 69(6):461–476, 2004. 41

[98] Mohammed Yahya and M Ziad Saghir. Prediction and experimental measurement of refractive index in ternary hydrocarbon mixtures. *Journal of Chemical & Engineering Data*, 60(8):2329–2342, 2015. 41

[99] G Romano. The effect of boundary conditions by the side of the nozzle of a low reynolds number jet. *Experiments in fluids*, 33(2):323–333, 2002. 52

[100] L Bogusławski and Cz O Popiel. Flow structure of the free round turbulent jet in the initial region. *Journal of Fluid Mechanics*, 90(3):531–539, 1979. 52

[101] Nagangudy R Panchapakesan and John L Lumley. Turbulence measurements in axisymmetric jets of air and helium. part 1. air jet. *Journal of Fluid Mechanics*, 246:197–223, 1993. 53, 54, 57, 58

[102] WR Quinn. Upstream nozzle shaping effects on near field flow in round turbulent free jets. *European Journal of Mechanics-B/Fluids*, 25(3):279–301, 2006. 53, 54

[103] TH Weisgraber and D Liepmann. Turbulent structure during transition to self-similarity in a round jet. *Experiments in Fluids*, 24(3):210–224, 1998. 54

[104] E Ferdman, MV Otugen, and S Kim. Effect of initial velocity profile on the development of round jets. *Journal of Propulsion and Power*, 16(4):676–686, 2000. 54

[105] Seok Jae Kwon and Il Won Seo. Reynolds number effects on the behavior of a non-buoyant round jet. *Experiments in fluids*, 38(6):801–812, 2005. 54, 57, 58

[106] H Fellouah, CG Ball, and A Pollard. Reynolds number effects within the development region of a turbulent round free jet. *International Journal of Heat and Mass Transfer*, 52(17-18):3943–3954, 2009. 54

[107] J Mi and GJ Nathan. Statistical properties of turbulent free jets issuing from nine differently-shaped nozzles. *Flow, turbulence and combustion*, 84(4):583–606, 2010. 58, 59

[108] John L Lumley and Gary R Newman. The return to isotropy of homogeneous turbulence. *Journal of Fluid Mechanics*, 82(1):161–178, 1977. 65

[109] Kwing-So Choi and John L Lumley. The return to isotropy of homogeneous turbulence. *Journal of Fluid Mechanics*, 436:59–84, 2001. 67

[110] Daehan Jung, Stephan Gamard, and William K George. Downstream evolution of the most energetic modes in a turbulent axisymmetric jet at high reynolds number. part 1. the near-field region. *Journal of Fluid Mechanics*, 514:173–204, 2004. 70

[111] X Xiang, TJ Madison, P Sellappan, and GR Spedding. The turbulent wake of a towed grid in a stratified fluid. *Journal of Fluid Mechanics*, 775:149–177, 2015. 81

[112] Benedikt Krohn, Sunming Qin, Annalisa Manera, and Victor Petrov. Refractive index matching for optical flow investigation with high density stratification. In *ASME 2018 5th Joint US-European Fluids Engineering Division Summer Meeting*. American Society of Mechanical Engineers Digital Collection, 2018. 88

[113] Benedikt Krohn, Sunming Qin, Victor Petrov, and Annalisa Manera. Coherent structures and correlation fields in the mixing transition of a turbulent round free jet. In *ASME 2018 5th Joint US-European Fluids Engineering Division Summer Meeting*. American Society of Mechanical Engineers Digital Collection, 2018. 88

[114] RAM Wilson and PV Danckwerts. Studies in turbulent mixing—ii: A hot-air jet. *Chemical Engineering Science*, 19(11):885–895, 1964. 94, 96

[115] Werner JA Dahm and Paul E Dimotakis. Mixing at large schmidt number in the self-similar far field of turbulent jets. *Journal of Fluid Mechanics*, 217:299–330, 1990. 94, 96

[116] I Nakamura, Y Sakai, and M Miyata. A study on the fluctuation concentration field in a turbulent jet: On the measurement of the concentration fluctuation intensity and the self-preservation. *Nagoya University Faculty Engineering Memoirs*, 34, 1982. 94, 96

[117] Gerrit Abraham. *Jet diffusion in stagnant ambient fluid*. PhD thesis, Food and Agriculture Organization of the United Nations, 1963. 105

[118] Bengt Gustafsson and Ian Larsen. Jet diffusion in stagnant stratified waters. *Water Research*, 4(5):353–361, 1970. 105

[119] Andrei Nikolaevich Kolmogorov. Dissipation of energy in the locally isotropic turbulence. *Proceedings of the Royal Society of London. Series A: Mathematical and Physical Sciences*, 434(1890):15–17, 1991. 110

[120] L Danaila, RA Antonia, and Paolo Burattini. Progress in studying small-scale turbulence using 'exact' two-point equations. *New Journal of Physics*, 6(1):128, 2004. 110, 141

[121] W Rodi. A review of experimental data of uniform density free turbulent boundary layers. *Journal of Fluid Mechanics*, 1:79–165, 1975. 126

[122] Sunming Qin, Benedikt Krohn, Victor Petrov, and Annalisa Manera. Velocity and scalar fields of a turbulent buoyant jet in the self-similar region. *Nuclear Technology*, 206(2):307–321, 2020. 127

[123] F Thiesset, RA Antonia, and L Djenidi. Consequences of self-preservation on the axis of a turbulent round jet. *Journal of Fluid Mechanics*, 748, 2014. 137